

**On the light and iron dependent coupling of carbon fixation  
and photosynthetic electron transport in Arctic and  
Subarctic marine phytoplankton**

by

Nina Schuback

MSci, The University of Glasgow, 2010

A THESIS SUBMITTED IN PARTIAL FULFILLMENT OF  
THE REQUIREMENTS FOR THE DEGREE OF

DOCTOR OF PHILOSOPHY

in

THE FACULTY OF GRADUATE AND POSTDOCTORAL STUDIES  
(Oceanography)

THE UNIVERSITY OF BRITISH COLUMBIA  
(Vancouver)

September 2016

© Nina Schuback, 2016

## Abstract

---

Marine phytoplankton primary productivity, the photosynthetic conversion of CO<sub>2</sub> into organic carbon by microscopic photosynthetic algae in the surface ocean, plays a fundamental role in ecosystem dynamics and global biogeochemical cycles. Consequently, the ability to accurately measure, monitor and predict environmental influences on this process over a range of spatial and temporal scales is crucial. The work presented in this thesis evaluates the application of fast repetition rate fluorometry (FRRF) for instantaneous, high resolution estimates of phytoplankton primary productivity. Results from both laboratory experiments and field work in Arctic and Subarctic marine waters show that the conversion factor required to derive carbon-based primary productivity estimates from FRRF-derived rates of electron transport in photosystem II (ETR) varies significantly in response to the interacting effects of iron and light availability (Chapter 2), over diurnal cycles (Chapter 3), and in response to nitrogen and light availability under low temperatures (Chapter 4). At a photo-physiological level, a high conversion factor is observed under conditions of excess excitation energy, where the amount of light energy absorbed in the pigment antenna exceeds the capacity for downstream metabolic processes, i.e. carbon fixation. Phytoplankton employ numerous mechanisms to alleviate excess excitation energy after charge separation, and these processes are postulated to be responsible for the increased de-coupling of ETR and carbon fixation. Consistent with this hypothesis, a strong correlation was observed between the derived conversion factor and the dissipation of excess excitation energy before charge separation, which can be estimated as non-photochemical quenching (NPQ). Because NPQ can be estimated from FRRF measurements, it can be used as a proxy for the magnitude and variability of the conversion factor between carbon fixation and ETR, and this approach holds potential to significantly improve carbon-based primary productivity estimates from FRRF measurements. The work presented in this thesis advances our understanding of the coupling between light absorption, photo-chemistry, and carbon fixation in response to various environmental gradients. The experimental approach taken demonstrates how an appreciation of photo-physiological processes of photosynthesis is critical for improved estimates of phytoplankton primary productivity at regional scales.

## Preface

---

Chapter 2 has been published as:

Schuback N, Schallenberg C, Duckham C, Maldonado MT, Tortell PD (2015) Interacting Effects of Light and Iron Availability on the Coupling of Photosynthetic Electron Transport and CO<sub>2</sub>-Assimilation in Marine Phytoplankton. *PLoS ONE* *10*, e0133235.

The experiments of this study were designed by NS with help from MTM and PDT. NS, CS and CD conducted field work; NS was responsible for analysis of field samples and the lab culturing component of the study. Data interpretation and writing of the manuscript was done by NS with help from MTM and PDT.

Chapter 3 has been published as:

Schuback N, Flecken M, Maldonado MT, Tortell PD (2016) Diurnal Variation in the Coupling of Photosynthetic Electron Transport and CO<sub>2</sub>-assimilation in Iron-limited Phytoplankton in the NE Subarctic Pacific. *Biogeosciences* *13*, 1019–1035.

The experiments of this study were designed by NS with help from MTM and PDT. NS and MF conducted field work and analyzed all samples. Data interpretation and writing of the manuscript was done by NS with help from MTM and PDT.

Chapter 4 has been submitted for publication as:

Schuback N, Hoppe CJM, Tremblay JE, Maldonado MT, Tortell PD (2016) Primary productivity and the coupling of photosynthetic electron transport and carbon fixation in the Arctic Ocean.

Under review.

The experiments of this study were designed by NS with help from MTM and PDT. NS, CJMH and PDT conducted field work and analyzed samples. Data interpretation and writing of the manuscript was done by NS with help from CJMH, MTM and PDT.

## Table of Contents

---

|   |              |
|---|--------------|
| <b>Abstract.....</b>  | <b>ii</b>    |
| <b>Preface.....</b>   | <b>iii</b>   |
| <b>Table of Contents .....</b>  | <b>iv</b>    |
| <b>List of Tables .....</b>   | <b>ix</b>    |
| <b>List of Figures.....</b>   | <b>x</b>     |
| <b>List of Symbols .....</b>  | <b>xiii</b>  |
| <b>List of Abbreviations .....</b>  | <b>xv</b>    |
| <b>Acknowledgements .....</b>   | <b>xviii</b> |
| <b>Chapter 1: Introduction .....</b>  | <b>1</b>     |
| 1.1    Global significance of aquatic photosynthesis.....   | 1            |
| 1.2    Photosynthesis and primary production.....   | 2            |
| 1.3    Environmental controls on marine photosynthesis.....   | 3            |
| 1.3.1    Light.....   | 4            |
| 1.3.2    Parameters modulating the response to light .....  | 5            |
| 1.4    Quantifying phytoplankton photosynthesis .....   | 5            |
| 1.4.1    Incubation based rate measurements .....   | 6            |
| 1.4.2    Active chlorophyll a fluorescence .....  | 6            |
| 1.4.3    Photosynthesis vs light curves .....   | 9            |
| 1.5    Study regions .....  | 9            |
| 1.6    Thesis objective and structure.....  | 10           |
| 1.6.1    Chapter specific summaries .....   | 10           |
| 1.7    Figures.....   | 12           |
| <b>Chapter 2: Interacting effects of light and iron availability on the coupling of<br/>photosynthetic electron transport and CO<sub>2</sub>-assimilation in marine phytoplankton .....</b> | <b>16</b>    |
| 2.1    Summary.....   | 16           |
| 2.2    Introduction.....  | 17           |
| 2.3    Methods.....   | 19           |
| 2.3.1    Iron addition experiment.....  | 19           |
| 2.3.2    Laboratory culturing .....   | 20           |

|  |  |           |
|--|--|-----------|
| 2.3.3  | Station sampling.....  | 21        |
| 2.3.4  | [chl <sub>a</sub> ] .....  | 21        |
| 2.3.5  | Carbon assimilation .....  | 21        |
| 2.3.6  | Chl <sub>a</sub> fluorescence parameters and ETR <sub>RCII</sub> .....   | 22        |
| 2.3.7  | PvsE curves.....   | 25        |
| 2.3.8  | Derivation of conversion factor .....  | 25        |
| 2.4  | Results.....   | 27        |
| 2.4.1  | Effect of iron addition on phytoplankton community composition, photo-physiology, ETR <sub>RCII</sub> and CO <sub>2</sub> -assimilation in the NE Subarctic Pacific..... | 27        |
| 2.4.2  | Effects of iron limitation on photo-physiology and rates of ETR <sub>RCII</sub> and CO <sub>2</sub> -assimilation in mono-specific phytoplankton cultures .....          | 30        |
| 2.5  | Discussion.....  | 31        |
| 2.5.1  | Magnitude of the observed conversion factor.....   | 31        |
| 2.5.2  | Interacting effects of iron and light on the conversion factor $\Phi_{e:C}/n_{PSII}$ .....   | 33        |
| 2.5.3  | Iron limitation increases ETR <sub>RCII</sub> .....  | 35        |
| 2.5.4  | Link to NPQ <sub>NSV</sub> .....   | 36        |
| 2.5.5  | A possible approach towards improved prediction of CO <sub>2</sub> -assimilation from FRRF data.....   | 37        |
| 2.6  | Conclusions.....   | 38        |
| 2.7  | Tables and figures .....   | 40        |
| <b>Chapter 3: Diurnal variation in the coupling of photosynthetic electron transport and carbon fixation in iron-limited phytoplankton in the NE Subarctic Pacific .....</b> |  | <b>51</b> |
| 3.1  | Summary.....   | 51        |
| 3.2  | Introduction.....  | 52        |
| 3.3  | Methods.....   | 54        |
| 3.3.1  | Study site and water-column hydrography .....  | 54        |
| 3.3.2  | Sample collection.....   | 55        |
| 3.3.3  | [chl <sub>a</sub> ] and HPLC .....   | 55        |
| 3.3.4  | Absorption spectra .....   | 56        |
| 3.3.5  | FRRF-derived photophysiological parameters and ETR <sub>RCII</sub> .....   | 57        |
| 3.3.6  | Carbon fixation .....  | 59        |

|  |   |           |
|--|---|-----------|
| 3.3.7  | Spectral correction and curve-fitting .....   | 59        |
| 3.3.8  | Derivation of conversion factor .....   | 60        |
| 3.3.9  | Relative changes in $1/n_{\text{PSII}}$ .....   | 61        |
| 3.4  | Results.....  | 62        |
| 3.4.1  | Physical and chemical characteristics of the water-column during the experiment .                   | 62        |
| 3.4.2  | Phytoplankton community composition .....   | 62        |
| 3.4.3  | Diurnal changes in rates of carbon fixation and $\text{ETR}_{\text{RCII}}$ .....                    | 62        |
| 3.4.4  | Relative changes in $1/n_{\text{PSII}}$ .....   | 64        |
| 3.4.5  | Photo-regulatory changes.....   | 64        |
| 3.5  | Discussion.....   | 66        |
| 3.5.1  | Diurnal changes in carbon fixation.....   | 66        |
| 3.5.2  | Diurnal changes in $\text{ETR}_{\text{RCII}}$ and the conversion factor $K_c/n_{\text{PSII}}$ ..... | 67        |
| 3.5.3  | Diurnal changes in photo-physiology at the level of PSII .....                                      | 69        |
| 3.5.4  | Linking $K_c/n_{\text{PSII}}$ and $\text{NPQ}_{\text{NSV}}$ .....                                   | 71        |
| 3.6  | Conclusion .....  | 73        |
| 3.7  | Tables and figures.....   | 75        |
| <b>Chapter 4: Primary productivity and the coupling of photosynthetic electron transport and carbon fixation in the Arctic Ocean .....</b> |   | <b>85</b> |
| 4.1  | Summary.....  | 85        |
| 4.2  | Introduction.....   | 85        |
| 4.3  | Methods.....  | 87        |
| 4.3.1  | Sample collection.....  | 87        |
| 4.3.2  | [chl <sub>a</sub> ] and HPLC .....  | 88        |
| 4.3.3  | Absorption spectra .....  | 89        |
| 4.3.4  | <sup>14</sup> C – uptake.....   | 90        |
| 4.3.5  | FRRF photo-physiology and $\text{ETR}_{\text{RCII}}$ .....  | 91        |
| 4.3.6  | Spectral correction .....   | 93        |
| 4.4  | Results and Discussion .....  | 94        |
| 4.4.1  | Hydrographic properties and phytoplankton community composition .....                               | 95        |
| 4.4.2  | Variability in <sup>14</sup> C-uptake rates .....   | 96        |
| 4.4.3  | Light absorption and photo-physiology in PSII.....  | 98        |

|   |   |            |
|---|---|------------|
| 4.4.4   | Absorption spectra .....  | 98         |
| 4.4.5   | Diagnostic pigment ratios .....   | 99         |
| 4.4.6   | FRRF derived photo-physiology .....   | 100        |
| 4.4.7   | Light-dependent rates of charge separation in RCII .....  | 101        |
| 4.4.8   | Coupling of $ETR_{RCII}$ and $^{14}C$ -uptake .....   | 102        |
| 4.4.9   | Using NPQ estimates to improve carbon based primary production from FRRF measurements in the Arctic Ocean ..... | 104        |
| 4.5   | Conclusion .....  | 107        |
| 4.6   | Tables and figures .....  | 108        |
| <b>Chapter 5: General discussion.....</b>               |   | <b>126</b> |
| 5.1   | Evolutionary considerations.....  | 126        |
| 5.2   | NPQ as an integrator for physiological state .....  | 127        |
| 5.3   | Linking the molecular to the global scale .....   | 129        |
| 5.4   | Potentials and limitations of induced ChlF approaches in oceanography .....                                     | 130        |
| 5.4.1   | FRRF and productivity .....   | 131        |
| 5.4.2   | FRRF and iron limitation .....  | 133        |
| 5.5   | Future directions .....   | 134        |
| 5.5.1   | Spectral correction .....   | 134        |
| 5.5.2   | Uncertainties in $^{14}C$ -uptake experiments .....   | 135        |
| 5.5.3   | Confirmation of alternative electron flow pathways .....  | 136        |
| <b>References.....</b>                                  |   | <b>137</b> |
| <b>Appendices.....</b>                                  |   | <b>161</b> |
| Appendix A : Supplementary material for chapter 2 ..... |   | 161        |
| A.1   | Spectral distribution of light sources and phytoplankton absorption spectra .....                               | 161        |
| A.2   | Phytoplankton assemblage composition .....  | 163        |
| A.3   | Volume normalized rates of $CO_2$ -assimilation .....   | 164        |
| Appendix B : Supplementary material for chapter 4 ..... |   | 165        |
| B.1   | Final pigment ratio matrices from CHEMTAX analysis of HPLC pigments.....  | 165        |
| B.2   | Phytoplankton assemblage composition .....  | 166        |
| B.3   | $P_{vsE}$ curves for $^{14}C$ -uptake .....   | 167        |
| B.4   | $P_{vsE}$ curves for $ETR_{RCII}$ .....   | 168        |

|     |   |     |
|-----|---|-----|
| B.5 | Phytoplankton absorption spectra .....                                    | 169 |
| B.6 | Spectral distribution of light and phytoplankton absorption spectra ..... | 170 |

## List of Tables

---

|  |     |
|--|-----|
| Table 2.1: Effect of iron limitation on photo-physiology in two mono-specific phytoplankton cultures grown in the laboratory. ....   | 40  |
| Table 3.1: Parameters measures at each time-point during the diurnal experiment. ....  | 75  |
| Table 3.2 :Phytoplankton pigments used for the derivation of diagnostic pigment ratios. ....   | 76  |
| Table 4.1: Physical and hydrological characteristics of sampling stations.....   | 108 |
| Table 4.2: Depth-specific hydrological variables for ML and sub-ML samples for each station.<br>.....  | 109 |
| Table 4.3: Relative taxonomic composition of the phytoplankton assemblage as inferred from CHEMTAX analysis of HPLC pigments.....  | 110 |
| Table 4.4: P <sub>v</sub> sE curve fit parameters for ETR <sub>RCII</sub> and <sup>14</sup> C-uptake, and the derived conversion factor between these rates. See next page for full legend. .... | 111 |
| Table 4.5: Diagnostic light absorption parameters and pigment ratios. See next page for full legend.....   | 113 |
| Table 4.6: Photo-physiological parameters derived from FRRF measurements. ....   | 115 |
| Table B1: Final pigment ratio matrices from CHEMTAX analysis of HPLC pigments.....   | 165 |

## List of Figures

---

|   |    |
|---|----|
| Figure 1.1: Schematic representation of the photosynthetic light reactions in eukaryotic organisms. ....  | 12 |
| Figure 1.2: The biophysical model underlying the derivation of ChlF yields and parameters from FRRF measurements. ....  | 13 |
| Figure 1.3: Representative PvsE curve for short term $^{14}\text{C}$ -uptake rates. ....  | 15 |
| Figure 2.1: Map of sampling stations along the Line-P transect in the NE Subarctic Pacific. ....  | 41 |
| Figure 2.2: Response of <i>chl a</i> biomass and photo-physiology during the on-board iron addition experiment. The experiment was conducted with a phytoplankton assemblage sampled at station P20. ....   | 42 |
| Figure 2.3: Response of rates of $\text{CO}_2$ -assimilation ( $\text{mol C mol chl a}^{-1} \text{ s}^{-1}$ ) and $\text{ETR}_{\text{RCII}}$ ( $\text{mol e}^- \text{ mol RCII}^{-1} \text{ s}^{-1}$ ) during the iron addition experiment at station P20. .... | 43 |
| Figure 2.4: Time-course of $\alpha$ (a-c) and $P_{\text{max}}$ (d-f) of $\text{CO}_2$ -assimilation, $\text{ETR}_{\text{RCII}}$ and the derived conversion factor $\Phi_{\text{e:C/nPSII}}$ during the iron addition experiment at station P20. ....            | 44 |
| Figure 2.5: Light dependency of ChlF-derived parameters from FRRF measurements on day three after iron addition and in the iron-limited control treatment. ....   | 45 |
| Figure 2.6. Changes in the light dependency of the conversion factor $\Phi_{\text{e:C/nPSII}}$ (a-e) and $\text{NPQ}_{\text{NSV}}$ (f-j) over the course of the iron addition experiment. ....  | 46 |
| Figure 2.7: Relationship between the conversion factor $\Phi_{\text{e:C/nPSII}}$ and $\text{NPQ}_{\text{NSV}}$ values during the iron addition experiment. ....   | 47 |
| Figure 2.8: Conceptual diagram visualizing the concept of excess excitation energy and its dissipation before and after charge separation in RCII. ....   | 48 |
| Figure 2.9: Rates of $\text{CO}_2$ -assimilation ( $\text{mol C mol chl a}^{-1} \text{ hr}^{-1}$ ) derived from FRRF measurements plotted against rates measured by $^{14}\text{C}$ -assimilation experiments. ....   | 50 |
| Figure 3.1: Diurnal variation in rates and light dependency of $\text{ETR}_{\text{RCII}}$ , carbon fixation and the derived conversion factor $K_{\text{c/nPSII}}$ . ....   | 77 |
| Figure 3.2: Diurnal changes in capacities and efficiencies of $\text{ETR}_{\text{RCII}}$ and carbon fixation and the derived conversion factor $K_{\text{c/nPSII}}$ . ....  | 78 |
| Figure 3.3: Diurnal changes in $\text{ETR}_{\text{RCII}}$ , carbon fixation and $K_{\text{c/nPSII}}$ derived for <i>in situ</i> light intensities at 5 m depth. ....  | 80 |

|   |     |
|---|-----|
| Figure 3.4: Relative changes in the components of our conversion factor $K_C/n_{PSII}$ over the diurnal cycle. ....   | 81  |
| Figure 3.5: Diurnal changes in pigment ratios. ....   | 82  |
| Figure 3.6: Diurnal changes in PSII photo-physiological parameters derived from FRRF measurements. ....   | 83  |
| Figure 3.7: Correlation between the conversion factor $K_C/n_{PSII}$ and the expression of $NPQ_{NSV}$ . .  | 84  |
| Figure 4.1: Map of stations sampled. See Table 4.1 and 4.2 for hydrological characteristics of the stations at the time of sampling. At stations HB1, HB2 and BB1.5 water was sampled from within the mixed layer only, using the ships underway water supply (7 m depth). At all other stations two samples were taken from the rosette of which one was within the mixed layer (50 % surface PAR) and one under the mixed layer (targeting the deep <i>chl a</i> maximum, if present). .. | 116 |
| Figure 4.2: Parameter derived from $^{14}C$ -uptake vs E curves. ....   | 117 |
| Figure 4.3: Relationship between surface water (ML) nitrate ( $NO_3+NO_2$ ) concentrations and $^{14}C$ -uptake $P_{max}^{chl a}$ and $\alpha^{chl a}$ . ....   | 118 |
| Figure 4.4: Co-variation of $\alpha^{chl a}$ and $P_{max}^{chl a}$ . ....   | 119 |
| Figure 4.5: Diagnostic absorption parameters and pigment ratios. ....   | 120 |
| Figure 4.6: Comparison of FRRF-derived photo-physiological properties in ML and sub-ML phytoplankton assemblages. ....  | 121 |
| Figure 4.7: Parameters from $ETR_{RCII}$ vs E curves. ....  | 122 |
| Figure 4.8: Coupling of $ETR_{RCII}$ and $^{14}C$ -uptake. ....   | 123 |
| Figure 4.9: Relationship between surface water (ML) nitrate ( $NO_3+NO_2$ ) concentrations and the conversion factor ( $K_C/n_{PSII}$ , $mol e^- mol C^{-1} mol chl a mol RCII^{-1}$ ) at light limitation (derived as $\alpha^{RCII} / \alpha^{chl a}$ ) and at light saturation (derived as $P_{max}^{RCII} / P_{max}^{chl a}$ ). ....  | 124 |
| Figure 4.10: Correlation of non-photochemical quenching, $NPQ_{NSV}$ , and the conversion factor between $ETR_{RCII}$ and $^{14}C$ -uptake, $K_C/n_{PSII}$ . ....   | 125 |
| Figure A.1: Spectral distribution of light sources and phytoplankton absorption spectra. ....   | 161 |
| Figure A.2: Phytoplankton assemblage composition. ....  | 163 |
| Figure A.3: Volume normalized rates of $CO_2$ -assimilation. ....   | 164 |
| Figure B.2: Phytoplankton assemblage composition. ....  | 166 |
| Figure B.3: $P$ vs E curves for $^{14}C$ -uptake. ....  | 167 |
| Figure B.4: $P$ vs E curves for $ETR_{RCII}$ . ....   | 168 |

Figure B.5: Phytoplankton absorption spectra.....169  
Figure B.6: Spectral distribution of light and phytoplankton absorption spectra.....170

## List of Symbols

---

|                         |  |
|-------------------------|--|
| A                       | area (particulate retention area of a filter)  |
| V                       | volume   |
| $\Phi$                  | quantum yield  |
| $\Phi_f$                | quantum yield of fluorescence  |
| $\Phi_{e:C}$            | electron requirement for carbon fixation ( $\text{mol } e^- \text{ mol } C^{-1}$ ), note that the more recent symbol for this parameter is $K_C$ |
| $k_f$                   | rate constant of Chla excited state decay due to fluorescence  |
| $k_d$                   | rate constant of Chla excited state decay due to thermal emission  |
| $k_p$                   | rate constant of Chla excited state decay due to photochemistry  |
| $\alpha$                | photosynthetic efficiency under light limitation (derived from PvsE curves)  |
| $\beta$                 | path-length amplification factor (used during QFT)   |
| $a_p(\lambda)$          | spectral absorption coefficient for particles ( $\text{m}^{-1}$ )  |
| $a_{ph}(\lambda)$       | spectral absorption coefficient for phytoplankton ( $\text{m}^{-1}$ )  |
| $a^{chl}_{ph}(\lambda)$ | spectral chla-specific absorption coefficient for phytoplankton ( $\text{m}^2 \text{ mg chla}^{-1}$ )  |
| $\bar{a}^{chl}_{ph}$    | spectrally averaged chla-specific absorption coefficient for phytoplankton ( $\text{m}^2 \text{ mg chla}^{-1}$ )                                 |
| $e^-$                   | electron   |
| $F_o$                   | minimum chla fluorescence yield in the dark-regulated state  |
| $F_m$                   | maximum chla fluorescence yield in the dark-regulated state  |
| $F_v$                   | (= $F_m - F_o$ ), variable chla fluorescence yield in the dark-regulated state   |
| $F_v/F_m$               | maximum quantum yield of PSII photochemistry (but see discussion in chapter 5)   |
| $F_o'$                  | minimum chla fluorescence yield in the light-regulated state   |
| $F'$                    | steady state chla fluorescence yield in the light-regulated state  |
| $F_m'$                  | maximum fluorescence in actinic light  |
| $F_v'$                  | (= $F_m' - F_o'$ ), variable chla fluorescence yield in the light-regulated state  |
| $F_q'$                  | (= $F_m' - F'$ ), 'quenched' variable chla fluorescence yield in the light-regulated state   |
| $1/n_{PSII}$            | mol of chla associated with each RCII ( $\text{mol chla mol RCII}^{-1}$ )  |

|                                  |   |
|----------------------------------|---|
| $K_C$                            | electron requirement for carbon fixation ( $\text{mol e}^- \text{ mol C}^{-1}$ ), note that until recently the symbol for this parameter was $\Phi_{e:C}$ |
| $\sigma_{\text{PSII}}(\lambda)$  | functional PSII absorption cross section ( $\text{A}^2 \text{ RCII}^{-1}$ )   |
| $\sigma_{\text{PSII}}'(\lambda)$ | absorption cross section in ambient light ( $\text{A}^2 \text{ RCII}^{-1}$ )  |
| $\tau_1$                         | time constant for re-oxidation of $Q_A$ (ms)  |
| $\tau_2$                         | time constant for electron transport from PQ pool to PSI (ms)   |
| $\Delta\text{pH}$                | pH gradient (across thylakoid membrane)   |
| $n$                              | sample size   |
| $E_0(\lambda)$                   | surface irradiance  |
| $K_W(\lambda)$                   | absorption of pure water ( $\text{m}^{-1}$ )  |
| $K_{\text{GT}}(\lambda)$         | absorption of dissolved and particulate organic matter ( $\text{m}^{-1}$ )  |
| $K_{\text{PH}}(\lambda)$         | absorption of phytoplankton ( $\text{m}^{-1}$ )   |
| $z$                              | depth (m)   |

## List of Abbreviations

---

|   |   |
|---|---|
| ADP   | adenosine diphosphate                                       |
| ATP   | adenosine triphosphate                                      |
| Allox   | alloxanthin   |
| $\alpha$ carot                                  | $\alpha$ carotene   |
| $\beta$ carot                                   | $\beta$ carotene  |
| BC  | British Columbia  |
| 19'BF   | 19' butanoyloxyfucoxanthin                                  |
| C   | carbon  |
| CCGS  | Canadian coast guard ship                                   |
| CCMP  | culture collection of marine phytoplankton                  |
| Chl   | chlorophyll   |
| ChlF  | chlorophyll <i>a</i> fluorescence                           |
| Chl <i>a</i>                                    | chlorophyll <i>a</i>  |
| Chl <i>b</i>                                    | chlorophyll <i>b</i>  |
| Chl <i>c</i> <sub>3</sub>                       | chlorophyll <i>c</i> <sub>3</sub>                           |
| Chl <i>c</i> <sub>1</sub> <i>c</i> <sub>2</sub> | chlorophyll <i>c</i> <sub>1</sub> <i>c</i> <sub>2</sub>     |
| Chl <i>c</i>                                    | chlorophyll <i>c</i>  |
| CET   | cyclic electron transport                                   |
| CTD   | conductivity, temperature, depth (oceanographic instrument) |
| CO <sub>2</sub>                                 | carbon dioxide  |
| Dd  | diadinoxanthin  |
| DES   | de-epoxidation state  |
| Dt  | diatoxanthin  |
| DPM   | disintegrations per minute                                  |
| DLHC  | disconnected light harvesting complexes                     |
| edLHCs  | energetically decoupled light harvesting complexes          |
| E <sub>0</sub>                                  | surface irradiance  |
| E <sub>insitu</sub>                             | <i>in situ</i> irradiance                                   |
| E <sub>k</sub>                                  | light-saturation parameter (from P <sub>v</sub> sE curves)  |

|   |  |
|---|--|
| ETC   | electron transport chain   |
| ETR   | electron transport rate  |
| ETR <sub>RCII</sub>                         | electron transport rate (RCII-specific rate of charge separation)                |
| Fe  | iron   |
| FRRF  | fast repetition rate fluorometer / fast repetition rate fluorometry              |
| Fuco  | fucoxanthin  |
| GF/F  | glass fibre filter   |
| HNLC  | high nutrient-low chlorophyll  |
| HPLC  | high pressure liquid chromatography / high precision liquid chromatography       |
| 19'HF                                       | 19'hexanoyloxyfucoxanthin  |
| LED   | light emitting diode   |
| LET   | linear electron transfer chain   |
| LHCs  | light harvesting complexes   |
| LT  | local time   |
| NADPH                                       | nicotinamide adenine dinucleotide phosphate (reduced)                            |
| Neo   | 9'cis-neoxanthin   |
| NE Pacific                                  | north east pacific   |
| NEPCC                                       | north east pacific culture collection  |
| NOAA  | national oceanic and atmospheric administration                                  |
| NPQ   | non-photochemical quenching (Stern-Volmer quenching)                             |
| NPQ <sub>NSV</sub>                          | non-photochemical quenching (normalized Stern-Volmer quenching)                  |
| OCS   | ocean climate stations   |
| OSP   | ocean station papa   |
| O <sub>2</sub>                              | oxygen   |
| P680  | chlorophyll molecule in RCII   |
| P <sup>chl<sub>a</sub></sup>                | rate of carbon fixation normalized to chl <sub>a</sub>                           |
| P <sup>chl<sub>a</sub></sup> <sub>max</sub> | maximum (light-saturated) rate of carbon fixation normalized to chl <sub>a</sub> |
| PAM   | pulse amplitude modulated (fluorometer)  |
| PAR   | photosynthetically available radiation   |
| PSC   | photosynthetic carotenoids   |
| PPC   | photo-protective carotenoids   |

|                   |  |
|-------------------|--|
| PSP               | photosynthetic pigments  |
| PSI               | photosystem I  |
| PSII              | photosystem II   |
| PTOX              | plastoquinol oxidase   |
| PQ                | plastoquinone  |
| Prasino           | prasinoxanthin   |
| P <sub>v</sub> sE | productivity / photosynthesis vs light curve   |
| Q <sub>A</sub>    | primary stable electron acceptor after charge separation in RCII   |
| Q <sub>B</sub>    | secondary stable electron acceptor after charge separation in RCII   |
| QFT               | quantitative Filter Technique  |
| qE                | energy dependent quenching, component of NPQ relaxing the fastest, involves but is not limited to the xanthophyll cycle        |
| qT                | state transition quenching, component of NPQ relaxing at medium timescales, assumed to be primarily driven by state transition |
| qI                | very slowly relaxing component of NPQ, including downregulation of PSII and photoinhibition                                    |
| RCI               | reaction center I  |
| RCII              | reaction center II   |
| RMSE              | root mean square error   |
| ROS               | reactive oxygen species  |
| SCF               | spectral correction factor   |
| SD                | standard deviation   |
| ST                | single turnover  |
| SSLC              | steady state light curve   |
| TChl              | total chlorophyll  |
| TSG               | thermosalinograph  |
| TP                | time point   |
| Tpig              | total pigment  |
| Viol              | violaxanthin   |
| XC                | xanthophyll cycle  |
| Zea               | zeaxanthin   |

## Acknowledgements

---

I want to express my sincere gratitude for the guidance provided by my co-supervisors Maite Maldonado and Philippe Tortell. You gave me the freedom to develop my own research, and the support I needed to turn a head full of ideas into science comprehensible to people other than just me. Paul Harrison, Beverley Green and Robert Guy, you were the most knowledgeable committee anybody could ever ask for, and I would like to thank you for all the advice and feedback you provided over the past 5 years.

The captains and crew of the CCGS JP Tully and CCGS Amundsen provided the support which makes oceanographic field work possible, and my times at sea will remain with me as much treasured memories. I would like to thank all the wonderful people I was able to work with at sea and back in the lab at UBC. In particular Dave Semeniuk for the discussions (scientific and not so scientific), Ania Posacka for mental support (often in the form of wine), Anna Hippman for being amazing (and reminding me that I have no idea what working hard means), Maureen Soon (for being the person who can answer every question), Kristina Brown, Lizzy Asher, Rebecca Taylor, Christina Schallenberg, Jade Shiller, Clara Hoppe, Tereza Jarnikova, Natalie Cohen, Carolyn Duckham, Alysia Herr, Dave Capelle, Robert Izette, Mirkko Flecken, Melanie Grenier, Lindsay Fenwick, Chen Zeng, Chris Paine and so many others for sharing knowledge, coffees and beers.

Morning runs with Janine Copp, and dinners provided by my lovely housemates Charlotte Miton, Camille Potey, Caro Kretschler, Martin Möller, Justin Moose and Roberto significantly increased the quality of this thesis.

Andrea Bodnar, Klaas Timmermans and Wafa Abouchami provided me with the opportunity to experience oceanographic research, and encouraged me to apply for a PhD position in a field I did not really know anything about at the time.

I would like to acknowledge the many scientists who took time of their busy schedules to answer my endless questions: Evelyn Lawrence, Sam Laney, Dave Suggett, Greg Mitchel, Charles Dismukes, Martina Doblin, Greg Silsbe, Yannik Huot, Mike Behrenfeld, Richard Geider, Milan Szabo, Robert Strepzek, Adrian Marchetti, Sven Kranz, Jacco Kromkamp and many more. I especially thank Zbigniew Kolber, for all his help, inspiration and humor.

This thesis would not have been possible without Moksha Yoga, cranberry walnut scones from the Boulevard, and the never-ending inspiration I got from Oliver Morton book “Eating the Sun”.

I thank my family, who never once questioned why I had to go to the other side of the world to study some weird green thing floating in the ocean, and Flo for doing this together. I thank the mountains, beaches and forests of British Columbia for their beauty and all the adventures had, and I am grateful for the great privilege to learn.

*“The most important technological contributions to modern science were the photomultiplier and duct tape.”*

William Arnold

# Chapter 1: Introduction

---

Chapter 1 provides a brief unifying context to the experimental work presented in chapters 2-4, discussing the significance and functioning of phytoplankton photosynthesis on both molecular and global scales. This chapter also describes how rates of photosynthesis in the oceans are controlled by interacting environmental variables, and introduces the different measurement approaches and study regions relevant to this thesis. The chapter concludes with a summary of the overall research objectives of this work.

## 1.1 Global significance of aquatic photosynthesis

While terrestrial plants dominate global photoautotrophic biomass (~99 %) on Earth today, aquatic organisms contribute approximately 45 % of global photosynthesis, accounting for 30-50 Tg carbon dioxide (CO<sub>2</sub>) fixed into organic carbon products per year (Falkowski, 1994; Field et al., 1998). In the aquatic environment, free-floating unicellular algae (phytoplankton) are responsible for the majority of this primary production, fueling higher trophic levels of aquatic ecosystems. Setting the upper limit to energy entering aquatic food chains, phytoplankton production is the largest single determinant of fisheries yields (e.g. Chassot et al., 2010). In addition to their role in aquatic ecosystems, phytoplankton can significantly influence global biogeochemical cycles and climate (e.g. Beardall and Raven, 2004; Chavez et al., 2011; Falkowski et al., 1998; Hays et al., 2005). Photosynthetically fixed CO<sub>2</sub> can be sequestered into the deep ocean and thus removed from the atmosphere on geological timescales (Falkowski, 1994), a process known as the biological carbon pump.

Phytoplankton primary production is thus a critical, yet insufficiently characterized, component of aquatic ecosystem and global climate models. There are two indispensable requirements for an improved understanding of marine phytoplankton primary production

- 1) large, accurate datasets in the global oceans
- 2) a better mechanistic understanding of the physiological and environmental controls on photosynthesis

The work presented in this thesis aims to address both of these areas.

## 1.2 Photosynthesis and primary production

In oxygenic photosynthesis, light energy is used to fix inorganic CO<sub>2</sub> into organic carbon products, while water is split and molecular oxygen (O<sub>2</sub>) evolved as a by-product. Thus, the process of photosynthesis results in the production of organic biomass, and the rate of change in the amount of biomass is defined as primary productivity. In order to accurately measure rates of photosynthesis and primary productivity, and mechanistically understand how these rates are controlled by environmental variables, an understanding of processes at the molecular level is necessary. This section will provide a very brief but essential overview of the photosynthetic process, emphasizing aspects which are crucial for the interpretation of data presented in this thesis.

The processes by which photons are absorbed and converted into metabolically useful energy are referred to as the photosynthetic light reactions. The light reactions take place in the thylakoid membrane, which is located in the chloroplast of eukaryotic cells and adjacent to the plasma membranes in cyanobacteria. Two membrane-bound photosystems (PSII and PSI), each consisting of a core complex and energetically linked peripheral light-harvesting complexes (LHCs), are embedded in the thylakoid membrane (Figure 1.1). Light energy is absorbed by the pigments associated with the photosystems and transferred to a pair of chlorophyll molecules in the reaction centers (RCII and RCI). Here, charge separation takes place and excitation energy is converted to electrochemical energy in form of an electron which is moved along the linear electron transfer (LET) chain and replaced by an electron derived from the splitting of water in PSII (Figure 1.1). Ultimately, the electron is used for the regeneration of reductant (NADPH) and a trans-membrane proton gradient associated with electron transport is used for the phosphorylation of ADP into ATP. The products of the light reactions are then available for cell metabolism, primarily the ‘fixation’ of inorganic CO<sub>2</sub> to organic carbon compounds in the Calvin-Benson cycle.

The photosynthetic apparatus evolved over billions of years to maximize efficiency while minimizing photo-damage in a highly variable light environment. To achieve robustness and flexibility, the system therefore developed multiple complex regulation and feedback mechanisms. Importantly, the flow of electrons through the electron transport chain is rarely as

simple and linear as described above. Several alternative cyclic and pseudo-cyclic routes of electron flow and alternative electron sinks can be triggered in response to metabolic demand and environmental cues.

The research presented in this thesis draws from an understanding of how the physicochemical environment affects phytoplankton carbon fixation and photo-physiology on a sub-cellular level, and how these determine rates of marine primary production and their environmental sensitivity.

### **1.3 Environmental controls on marine photosynthesis**

The work presented in this thesis is primarily focused on how environmental factors affect phytoplankton photo-physiology and primary productivity on a physiological level. The experimental approach taken is therefore aimed at broadening our understanding of what controls the efficiency with which sunlight can be converted into chemical energy, and to what extent this energy is used to convert CO<sub>2</sub> into organic carbon products. Clearly, when considering phytoplankton productivity as a component of global biogeochemical cycles and ecosystem functioning, higher level processes like losses (grazing, virus, etc) are crucial to consider. However, the work presented in this thesis is focused on the fundamental process of phytoplankton photosynthesis. Nonetheless, the work presented in this thesis does have direct significance for our understanding of marine photosynthesis at large regional scales.

Similarly, the physicochemical environment dictates the species composition of a phytoplankton assemblage, with implications for rates of productivity. In the realm of this work, I primarily treat the effect of environmental forces on species composition as an extension of physiological changes. In this interpretation a given environment selects for a specific function, and this function can be provided by a physiological adaptation within a species or the selection of a species with given function (Claustre et al., 2005).

In the marine environment, rates of phytoplankton photosynthesis and primary production are always controlled by the interacting effects of multiple environmental parameters (Behrenfeld et al., 2008). Empirically looking at the effect of changes in only one parameter (light, temperature, etc.) is therefore not useful, unless it is done in the context of incorporating the result into a mechanistic understanding of the photosynthetic process and how it adapted to function optimally in its integrated growth environment.

In the context of this thesis, the availability of light is considered the central environmental variable controlling rates of marine phytoplankton primary production and is discussed in section 1.3.1. Other environmental variables (including micro- and macro-nutrients and temperature, section 1.3.2) are considered insofar as they modulate the ability of phytoplankton to use the available light (section 1.4.3).

### ***1.3.1 Light***

Light energy provides the fundamental energy source fueling photosynthesis and all photosynthetic organisms possess sophisticated mechanisms to enhance the capture of light energy when light intensity is low. However, light availability in nature is never constant, and can change from limiting to super-saturating on seasonal, diurnal and sub-second timescales. Under conditions where light absorption exceeds the capacity for energy utilization in downstream processes (e.g. carbon fixation), excess excitation energy can result in the production of reactive oxygen species and consequent damage to the photosynthetic machinery (e.g. Allahverdiyeva and Aro, 2012; Roach and Krieger-Liszkay, 2014). The concept of excess excitation energy is central to the interpretation of data presented in chapters 2-4 and is explained in the form of a conceptual diagram in Figure 2.8.

The work presented in this thesis illustrates the importance of understanding the molecular mechanisms utilized by photosynthetic organisms in order to maximize light use efficiency, while rapidly sensing and preventing excess excitation energy. As I will show, a better understanding of these processes and their drivers are crucial in order to interpret and improve *in situ* measurements and modelling of phytoplankton primary production.

The light environment experienced by marine phytoplankton is highly variable in both the intensity and spectral quality of light over a wide range of time scales (e.g. Harding et al., 1987; Kirk, 2010). Changes are both predictable (e.g. seasons and days) and unpredictable (e.g. vertical displacement of phytoplankton cells within the water-column, short term fluctuations due to cloud cover, and focusing by surface waves). The different time-scales of variability in light availability are reflected in the wide range of physiological approaches photosynthetic organisms evolved in order to maximize absorption under low light conditions and minimize damage under high light conditions. These approaches can be divided into photo-adaptation, photo-acclimation, and photo-regulation. Photo-adaptation involves evolutionarily driven

genomic changes which can be passed on to the next generation. Photo-acclimation is a term used to describe physiological adjustments (e.g. changes in pigment concentration) in response to shorter-term changes (i.e. hours to days) in light availability. The term photo-regulation is used for very short-term responses, which do not involve synthesis or degradation of proteins (e.g. induction of non-photochemical quenching or alternative electron pathways). Such responses are important on times scales of hours or less, associated with (for example) vertical mixing in the upper ocean or short-term meteorological changes in surface irradiance levels.

### **1.3.2 Parameters modulating the response to light**

A multitude of interacting environmental variables modulate the ability of phytoplankton to turn the energy from sunlight into carbon biomass. In vast regions of the oceans, phytoplankton primary productivity is limited by the supply of macro-nutrients. Particularly during the summer months, density stratification separates the upper mixed layer from deeper, nutrient-rich layers, such that phytoplankton growth depletes the upper mixed layer of nutrients. The availability of trace metals, in particular iron (Fe), has also been shown to limit phytoplankton primary production in vast regions of the ocean (e.g. Boyd et al., 2007), including a large area of the Eastern Subarctic Pacific.

Chapter 2 and chapter 3 of this thesis primarily focus on the interacting effects of iron limitation and the availability of light on the functioning of the photosynthetic process, while chapter 4 explores the effects light, low temperature and macro-nutrient limitation on photosynthetic processes in the Arctic Ocean.

## **1.4 Quantifying phytoplankton photosynthesis**

Quantitative estimates of phytoplankton productivity require both appropriate measurement techniques, and the ability to scale measurements across spatial and temporal scales (e.g. from bottle experiments to regional values). In addition, there has been a significant effort put towards the development of numerical models and empirical algorithms to predict productivity from a number of environmental variables, including those assessed by satellite remote sensing. These approaches allow for synoptic observations over regional and even global scales, and predictions of phytoplankton primary productivity into the future. However, the performance and accuracy of all models relies on the availability of *in situ* calibration data at

high temporal and spatial resolution, and a mechanistic understanding of the cell physiological processes which link rates of production to various environmental variables.

This thesis aims to improve spatial and temporal coverage of *in situ* measurements by calibrating ‘traditional’ incubation-based methodologies to bio-optical approaches, which hold promise to provide estimates of phytoplankton primary production at unprecedented resolution. Furthermore, by simultaneously measuring phytoplankton primary production using several approaches, invaluable insight on function and control of this process can be gained.

#### **1.4.1 Incubation based rate measurements**

Phytoplankton primary production has traditionally been measured using a radioactive tracer ( $^{14}\text{C}$ ) (Steenmann-Nielsen, 1952). The technique is sensitive and straightforward; however it involves time-consuming sample handling and incubations *ex situ*. Such incubation-based approaches are known to suffer from a number of potential artifacts, making it difficult to reconcile the measured rate with environmental variables observed at the time of sampling (e.g. Peterson, 1980; Williams et al., 2008). Furthermore, cost and labor intensity make it challenging to accumulate datasets of sufficient resolution for accurate parameterization of primary productivity in modeling approaches.

#### **1.4.2 Active chlorophyll *a* fluorescence**

Approaches based on the induction and detection of chlorophyll *a* fluorescence (ChlF) have been used extensively as a tool to study the molecular mechanisms of photosynthesis, and to assess physiology and productivity of individual plants, plant communities and ecosystems (Baker and Oxborough, 2004; Büchel and Wilhelm, 1993; Govindjee, 1995; Krause and Weis, 1991; Kromkamp and Forster, 2003; Oxborough, 2004; Papageorgiou and Govindjee, 2004; Schreiber et al., 1995; Suggett et al., 2010a). More than two decades ago, this approach was introduced to oceanography as a means to estimate rates of primary production *in situ*, without the need for incubations, and at unprecedented sampling resolution (Kolber and Falkowski, 1993; Suggett et al., 2010b). In the following, a brief overview of the theory used to interpret the kinetics of ChlF yields as measured using fast repetition rate fluorometry (FRRF) is provided. Detailed measurement protocols are given in each of the data chapters, and the potential strengths and limitations of the approach are discussed in chapter 5.

The basic concept relating changes in ChlF yields and photochemistry is based on the fact that energy absorbed by a chlorophyll molecule in the light harvesting antennae must be used for one of three competing pathways: photochemistry, dissipation as heat, or re-emission as fluorescence. Consequently, as long as one can exclude or account for changes in heat dissipation, the ChlF yield is inversely related to photochemistry. More specifically, the ChlF yield is controlled by the redox state of the primary stable electron acceptor of PSII,  $Q_A$ . If  $Q_A$  is reduced ( $Q_A^-$ ) no photochemistry can take place (the RCII is “closed”) and the ChlF yield is high, if  $Q_A$  is oxidized and ready to accept an electron (RCII “open”) the ChlF yield will be lower (Figure 1.2a).

The fast repetition rate fluorometer (FRRF) (Kolber et al., 1998) used in the research presented in this thesis applies a sequence of high intensity, sub-microsecond flashlets with adjustable time interval to a sample of phytoplankton cells. Monitoring the induction and decay of the ChlF induced by these flashlets allows assessment of the reduction and re-oxidation of  $Q_A$ ,  $Q_B$  and the PQ pool. Typically, samples are left at low light conditions prior to measurements in order to relax photo-protective mechanisms active in the pigment antenna, which modulate the amount of absorbed energy which is re-emitted as heat (non-photochemical quenching, NPQ). If no background irradiance is applied during the FRRF measurement all  $Q_A$  are assumed oxidized at the time of the first flashlet. Under these conditions, the vast majority of energy can be used to drive charge separation (i.e. photochemistry) and the ChlF yield is minimal. With a portion of the RCII closed ( $Q_A^-$ ) by the first flashlet, a second flashlet is applied within  $\sim 2 \mu\text{s}$ , well before the reduced  $Q_A$  can re-oxidize (200-300  $\mu\text{s}$ ). Therefore, the ChlF yield observed during the second flashlet will increase by a factor proportional to the fraction of reaction centers closed during the first flashlet. Eventually, all  $Q_A$  will become reduced, the measured ChlF yield saturates, and the maximal ChlF yield,  $F_m$ , is measured (typically after 100 flashlets, collectively providing approximately 5-10 photons per RCII, called a single-turnover excitation protocol) (Figure 1.2b). Extrapolating to the ChlF yield at the zeros flash provides the initial ChlF yield,  $F_o$ . The parameters  $F_o$  and  $F_m$  can be used to calculate the variable fluorescence  $F_v (= F_m - F_o)$ . Normalized to  $F_m$  (to account for changes in biomass) this parameter has been used extensively as an estimate of the maximum quantum efficiency of charge separation at PSII ( $F_v/F_m$ ,  $\Phi_{\text{PSII}}$ ).

If the single-turnover excitation protocol is applied to samples exposed to a known background irradiance, the ChlF yield derived for the zeros flashlet,  $F'$ , will be higher than  $F_o$ ,

because some  $Q_A$  are reduced at the time of measurement and, depending on the intensity of background irradiance, some energy dissipating mechanisms in the pigment antenna (non-photochemical quenching, NPQ) might be activated. The maximum ChlF yield at a given level of background irradiance,  $F_m'$ , is lower than  $F_m$  because of NPQ. The minimum ChlF yield corresponding to a given background light intensity,  $F_o'$ , is difficult to measure experimentally because, by definition, all  $Q_A$  should be oxidized while the NPQ induced by the given background irradiance is still active.  $F_o'$  is therefore lower than  $F_o$ . Throughout the work presented in this thesis,  $F_o'$  is estimated as  $F_o' = F_o / (F_v/F_m + F_o/F_m')$ , assuming that NPQ affects minimum ChlF yields to the same extent as maximum ChlF yields (Oxborough and Baker, 1997). Further, the five ChlF yields,  $F_o$ ,  $F_m$ ,  $F'$ ,  $F_m'$  and  $F_o'$  are used to calculate ChlF parameters related to the efficiency of primary charge separation, following Roháček (2002), and as described in detail in the methods section of the data chapters.

An additional advantage of the FRRF approach is that the rate of rise in ChlF yields during a single-turnover excitation protocol can be used to estimate the functional absorption cross section of PSII ( $\sigma_{PSII}$  and  $\sigma'_{PSII}$ , units of  $\text{\AA}^2 \text{RCII}^{-1}$ ) (Dubinsky et al., 1986; Falkowski et al., 1986a; Kolber et al., 1988) (Figure 1.2b). Probing the kinetics of fluorescence decay after maximal fluorescence ( $F_m$  or  $F'_m$ ) with lower frequency flashlets, provides information on the re-oxidation rate of  $Q_A$ . In this way, electron transport from  $Q_A$  to the PQ pool ( $\tau_1$ , ms) and from the PQ pool to PSI ( $\tau_2$ , ms) can be determined, which, in turn, can be used to estimate the size of the PQ pool (Figure 1.2c).

Non-photochemical quenching (NPQ) of ChlF yields clearly complicates the derivation and interpretation of photochemical quenching. The accurate quantification and elucidation of molecular processes underlying this phenomenon, however, are very active and exciting research fields in their own right (e.g. Derks et al., 2015; Lavaud and Lepetit, 2013; Niyogi and Truong, 2013; Ruban and Mullineaux, 2014; Ruban and Murchie, 2012; 2014; Zaks et al., 2013). Based on characteristic induction and relaxation characteristics, NPQ has been divided into at least three components: rapidly reversible,  $\Delta pH$  dependent  $qE$ ; components related to state transition,  $qT$ ; and slowly reversible, photoinhibition related  $qI$ . Generally, all components of NPQ are collectively quantified as Stern-Volmer quenching,  $NPQ_{SV} = (F_m - F_m')/F_m$  (Bilger and Björkman, 1990). Throughout this thesis however, we estimated NPQ as the normalized Stern-Volmer

quenching coefficient,  $NPQ_{NSV} = (F_m'/F_v') - 1 = F_o'/F_v'$  (McKew et al., 2013), which accounts for NPQ present in the dark-regulated state.

### **1.4.3 Photosynthesis vs light curves**

In the experimental approach taken in the work presented in this thesis, all rates of  $ETR_{RCII}$  and  $^{14}C$ -uptake were measured as a function of light (PvsE curves, see example in Figure 1.3). The relationship between irradiance and photosynthesis is linear at sub-saturating light intensities, and the initial slope,  $\alpha$ , provides a measure of the photosynthetic efficiency at light limitation. Above the saturation irradiance,  $E_k$ , photosynthesis becomes light saturated and the maximum light saturated capacity under given environmental conditions,  $P_{max}$ , is reached. Throughout this thesis I used the simple exponential model by Webb et al. (1974) to derive the parameters  $P_{max}$  and  $\alpha$  from my experimental data.

While all PvsE curves exhibit the same general shape, the derived estimates of efficiency and capacity with respect to light intensity vary extensively as a function of physiological state and environmental constraints (e.g. Cullen et al., 1992; MacIntyre et al., 2002; Sakshaug et al., 1997). Consequently, the approach allows an evaluation of the effects of contrasting growth environments on the efficiency and capacity of phytoplankton cultures or assemblages to utilize available light energy. Importantly, because PvsE derived parameters are essential components of satellite algorithms developed to estimate phytoplankton primary productivity from remotely sensed parameters (Platt and Sathyendranath, 1993), the physiological results presented in this thesis can be linked back to the Earth system scale (see also section 5.3).

## **1.5 Study regions**

This thesis is comprised of studies from two broad oceanographic regions, the North East Subarctic Pacific (Chapters 2 and 3) and the Canadian Arctic Ocean (Chapter 4). This thesis therefore helps to extend FRRF based studies of phytoplankton photo-physiology and primary production into northern high latitude regions, which have been underrepresented in photo-physiological studies. While unique environmental conditions control phytoplankton primary production in each of our study regions, we were able to find interesting similarities in the physiological mechanisms used by phytoplankton assemblages to optimize growth and simultaneously minimize damage to their photosynthetic apparatus. For the work presented in

chapter 2, results from field experiments were supported with laboratory studies on several relevant phytoplankton isolates.

## **1.6 Thesis objective and structure**

My thesis research is based on the simultaneous measurements of FRRF-based  $ETR_{RCII}$  and  $^{14}C$ -uptake rates in field assemblages and lab cultures of marine phytoplankton, exposed to a range of environmental conditions. The data allowed me to investigate the effect of different environmental settings on: (1) magnitude and variability of each rate, (2) the short-term light dependence of each rate ( $P_{vsE}$  curve parameters), and (3) magnitude and variability of the conversion factor linking  $ETR_{RCII}$  and  $^{14}C$ -uptake.

One over-arching goal of this thesis was to assess the applicability of FRRF instruments for the acquisition of high resolution phytoplankton primary productivity estimates in ecologically-relevant carbon units. To this end, I was able to establish that the conversion factor linking  $ETR_{RCII}$  and  $^{14}C$ -uptake varies significantly, but its magnitude appears to be driven by the extent of excitation energy experienced by the photosynthetic apparatus (Figure 2.8). It is therefore likely that a high conversion factor is caused, in part, by the upregulation of alternative electron flow pathways, which alleviate the potentially damaging over-reduction of  $Q_A$ . Overwhelming support for this speculation can be found in recent literature (Bailey et al., 2008; Cardol et al., 2011; Curien et al., 2016; Grossman et al., 2010; Mackey et al., 2008; McDonald et al., 2011; Nawrocki et al., 2015; Zehr and Kudela, 2009). Excess absorbed light energy can also be dissipated before charge separation in RCII, and the extent of this energy dissipation can be estimated from FRRF measurements as NPQ. The work presented in this thesis establishes an empirical correlation between the  $ETR_{RCII} : ^{14}C$ -uptake conversion factor and NPQ. This correlation, which has recently been confirmed by other research groups (Zhu et al., 2016), has potential to improve estimates of phytoplankton primary productivity in carbon units from FRRF measurements alone.

### ***1.6.1 Chapter specific summaries***

Chapter 2 examines the role of iron limitation, and the interacting effects of iron and light availability, on the coupling of  $ETR_{RCII}$  and  $^{14}C$ -uptake in field phytoplankton assemblages in the Subarctic Pacific and single-species cultures grown in the laboratory. Our results show that

excess light conditions cause increased decoupling of carbon fixation and electron transport, particularly under iron limitation. We postulate that the high conversion factor between the two rates is predominantly caused by an upregulation of alternative electron sinks which dissipate excess excitation energy, where excess excitation energy can be caused by high light and / or low iron. Consistent with this idea, we observed a strong correlation between the derived conversion factor and the expression of  $NPQ_{NSV}$  in the pigment antenna. Because estimates of  $NPQ_{NSV}$  can be derived from FRRF data, this correlation can be utilized to estimate carbon-based primary productivity from FRRF data, without the need for any additional measurements.

Chapter 3 is a diurnal study for which rates of  $ETR_{RCII}$  and short-term  $^{14}C$ -uptake, as well as several auxiliary variables, were measured at 3 hour intervals over a 24 hour cycle at Ocean Station Papa (OSP) in the iron-limited NE Pacific. Diurnal variability was present in all measured variables, and was interpreted as a re-balancing of the different components of the photosynthetic process in response to changes in excitation energy, as well as circadian rhythms in cell metabolism. The study provided further support for the applicability of the NPQ-proxy approach to estimate the degree of decoupling of  $ETR_{RCII}$  and  $^{14}C$ -uptake.

Chapter 4 presents a dataset from the Canadian Subarctic and Arctic Ocean collected as part of the Canadian Arctic GEOTRACES expedition during the summer of 2015. A comprehensive set of measurements from a number of stations throughout this region allowed us to gain mechanistic insight into the coordination of the photosynthetic process (light absorption, electron transport and carbon fixation) under the special environmental constraints of the Arctic Ocean (low temperature, strong stratification and macro-nutrient limitation). This knowledge is urgently needed to improve modeling approaches aimed at monitoring the response of phytoplankton primary production in this under-studied and rapidly changing environment. Intriguingly, the correlation between  $NPQ_{NSV}$  and the conversion factor linking  $ETR_{RCII}$  and  $^{14}C$ -uptake, developed in iron limited waters of the NE Pacific, appears to hold very well for phytoplankton assemblages taken from within the shallow summer mixed layer of the Arctic Ocean, suggesting a more general applicability of our approach.

The thesis is concluded with chapter 5. This chapter contains a discussion of general concepts which emerged from the research presented in chapters 2-4 and uses these to propose future research directions in the field.

## 1.7 Figures

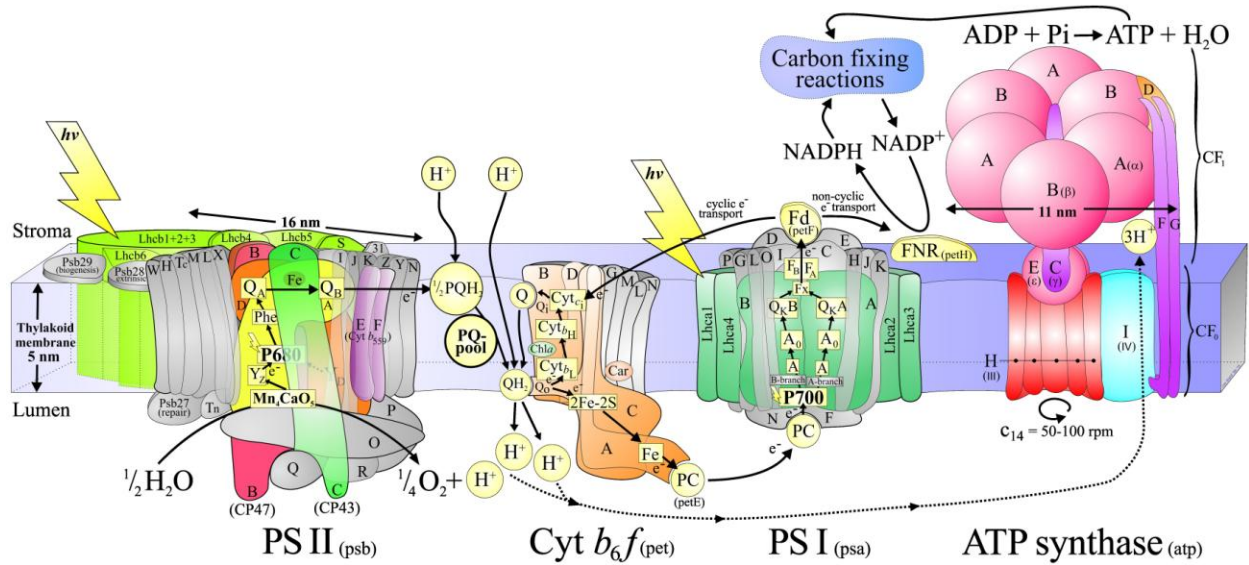


**Figure 1.1: Schematic representation of the photosynthetic light reactions in eukaryotic organisms.** The light reactions of photosynthesis can act as a highly responsive sensory and regulatory system, able to balance the photosynthetic light reactions with downstream metabolism. This tight regulation of the photosynthetic processes upstream from carbon fixation balances light absorption with electron flow and carbon fixation, thus maximizing productivity while minimizing excess absorbed light energy which can lead to the formation of reactive oxygen species (ROS) and oxidative stress. See text for details. Figure used with permission by Dr. Jon Nield, Queen Margaret University, London (<http://macromol.sbcs.qmul.ac.uk/>).

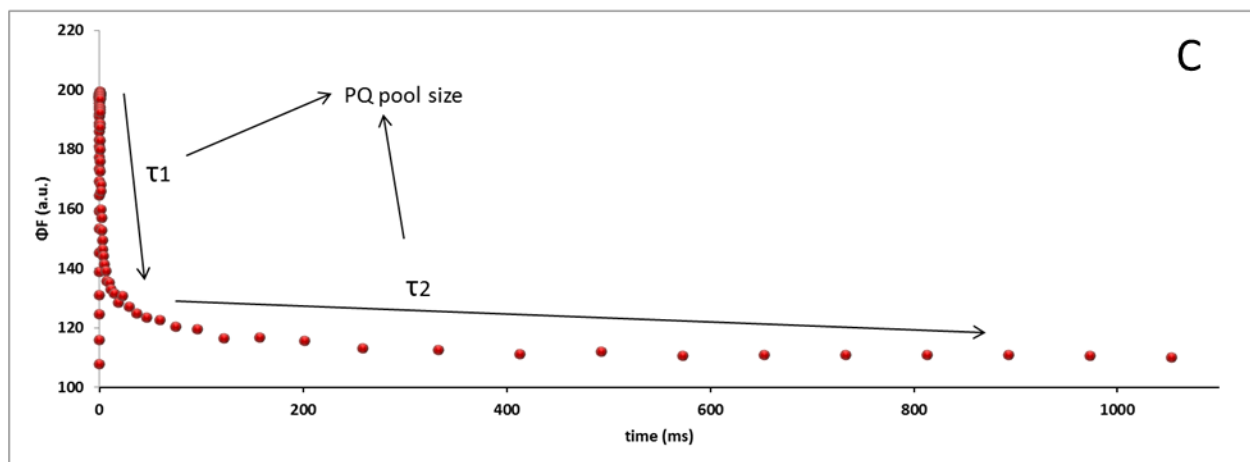
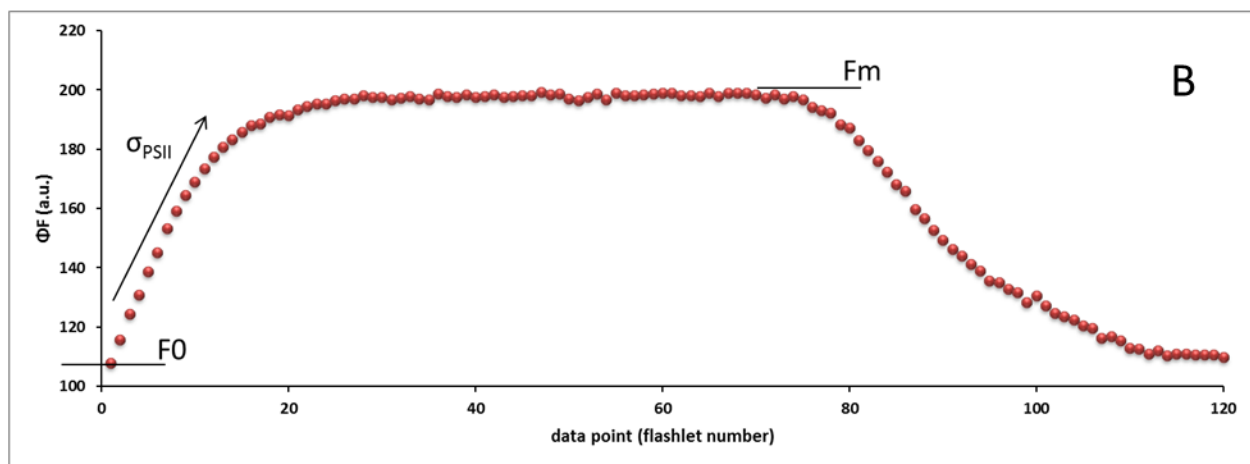
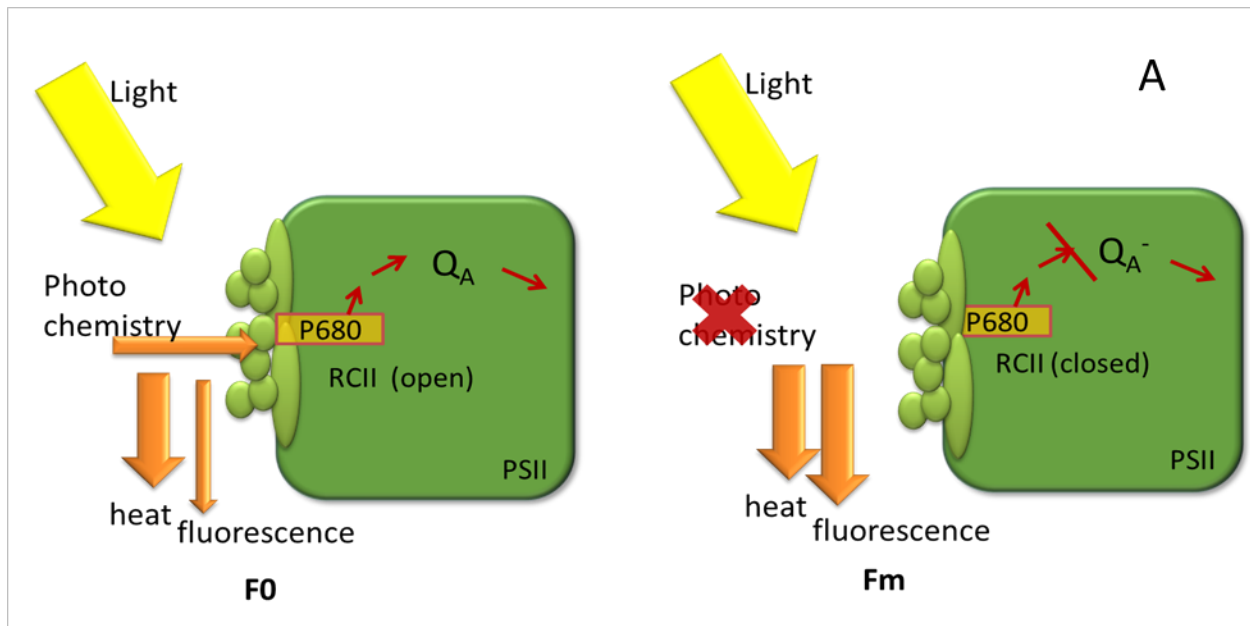


**Figure 1.2: The biophysical model underlying the derivation of ChlF yields and parameters from FRRF measurements.** (A) Variable chlorophyll a fluorescence from PSII. Light absorbed by the light harvesting antennae

of PSII can be dissipated as heat, re-emitted as fluorescence or used for photochemistry, causing a charge separation at RCII and reduction of the primary stable electron acceptor  $Q_A$ . If the sample is in a dark-regulated state, all  $Q_A$  will be oxidized and the fluorescent yield from a pulse of light will be low ( $F_o$ ) because many of the absorbed photons can be used for photochemistry (left panel). If  $Q_A$  is reduced ( $Q_A^-$ ), no further charge separation can take place in RCII, and the fraction of absorbed photons re-emitted as fluorescence will increase. If all  $Q_A$  in a sample are reduced, the fluorescence will reach its maximum level,  $F_m$  (right panel).

(B) Fluorescent transient as derived from a single-turnover FRRF measurement in lab cultures of *Phaeocystis pouchetii* grown in the laboratory. Each point is the fluorescence yield ( $\Phi F$ , a.u.) from one excitation flashlet. A sequence of 70 excitation flashlets with a length of  $0.4 \mu s$  and constant interval of  $1 \mu s$  sequentially close all PSII reaction centers and increase the fluorescence yield from  $F_o$  to  $F_m$ . Because the re-oxidation of the primary electron acceptor  $Q_A$  takes longer than the total sequence of excitation flashlets ( $140 \mu s$ ) the rise in fluorescence reflects the redox state of  $Q_A$  only. Plotting ChlF yield against measurement point, the rate of the increase from  $F_o$  to  $F_m$  can be used to derive the functional absorption cross section ( $\sigma_{PSII}$ ) of PSII.

(C) The decay of the fluorescence yield from  $F_m$  back to  $F_o$  can be followed by 'probing' flashlets and the different time constants of the decay can be used to derive the rate of re-oxidation of downstream components of the ETC and the size of the PQ pool (B). (B) and (C) are the same transient where ChlF yield is plotted against flashlet number and time, respectively.

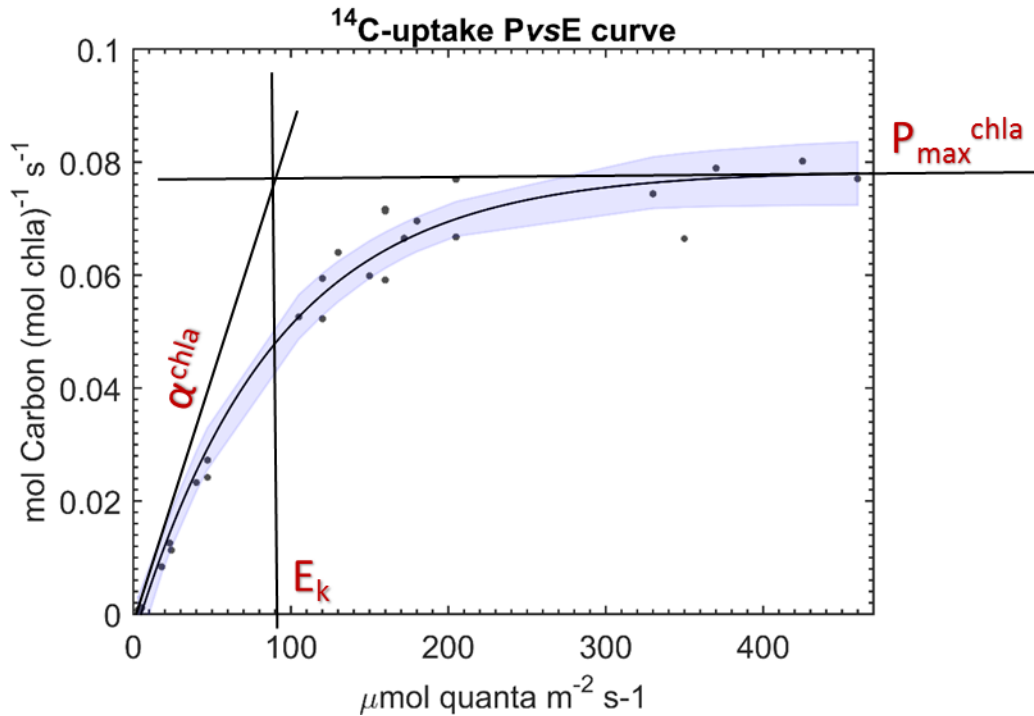


**Figure 1.3: Representative P vs E curve for short term  $^{14}\text{C}$ -uptake rates.** In this example, measured during an Ocean acidification experiment conducted during the Canadian Arctic GEOTRACES expedition 2015, the data was fit to the exponential model of Webb et al., (1974). The derived fit values are  $0.00092 \pm 0.00014 \text{ mol C mol chla}^{-1} (\mu\text{mol quanta m}^{-2} \text{ s}^{-1})$  for the efficiency of carbon fixation under light limitation,  $\alpha^{\text{chla}}$ ,  $0.079 \pm 0.0047 \text{ mol C mol chla}^{-1}$  for the light saturated maximum rate of carbon fixation,  $P_{\text{max}}^{\text{chla}}$ , and  $90.3 \pm 15.1 \mu\text{mol quanta m}^{-2} \text{ s}^{-1}$  for the light saturation parameter  $E_k$ , which is derived as  $P_{\text{max}}^{\text{chla}} / \alpha^{\text{chla}}$ . In this example, and throughout the work presented in this thesis, the error presented with  $\alpha^{\text{chla}}$  and  $P_{\text{max}}^{\text{chla}}$  are the 95 % confidence interval of the derived fit parameter, while the error given for  $E_k$  is the propagated error from  $P_{\text{max}}^{\text{chla}} / \alpha^{\text{chla}}$ . The derivation of fit parameters is emphasized in the figure.

## Chapter 2:

# Interacting effects of light and iron availability on the coupling of photosynthetic electron transport and CO<sub>2</sub>-assimilation in marine phytoplankton

---

### 2.1 Summary

Iron availability directly affects photosynthesis and limits phytoplankton growth over vast oceanic regions. For this reason, the availability of iron is a crucial variable to consider in the development of active *chl a* fluorescence based estimates of phytoplankton primary productivity. These bio-optical approaches require a conversion factor to derive ecologically-relevant rates of CO<sub>2</sub>-assimilation from estimates of electron transport in PSII. The required conversion factor varies significantly across phytoplankton taxa and environmental conditions, but little information is available on its response to iron limitation. In this study, we examine the role of iron limitation, and the interacting effects of iron and light availability, on the coupling of photosynthetic electron transport and CO<sub>2</sub>-assimilation in marine phytoplankton. Our results show that excess irradiance causes increased decoupling of carbon fixation and electron transport, particularly under iron limiting conditions. We observed that RCII specific rates of electron transport ( $ETR_{RCII}$ , mol e<sup>-</sup> mol RCII<sup>-1</sup> s<sup>-1</sup>) increased under iron limitation, and we propose a simple conceptual model for this observation. We also observed a strong correlation between the derived conversion factor and the expression of non-photochemical quenching. Utilizing a dataset from *in situ* phytoplankton assemblages across a coastal – oceanic transect in the Northeast Subarctic Pacific, this relationship was used to predict  $ETR_{RCII} : CO_2$ -assimilation conversion factors and carbon-based primary productivity from FRRF data, without the need for any additional measurements.

## 2.2 Introduction

The photosynthetic assimilation of inorganic CO<sub>2</sub> into organic carbon by marine phytoplankton accounts for almost half of total global primary productivity (Field et al., 1998), and variations in phytoplankton primary productivity can profoundly affect ecosystem dynamics and global climate (e.g. Beardall and Raven, 2004; Chavez et al., 2011; Falkowski et al., 1998; Hays et al., 2005). However, despite its recognized importance, it remains challenging to accurately quantify marine primary production at the temporal and spatial resolution needed to relate its variability back to external environmental conditions. In vast oceanic regions, the availability of iron (Fe) limits marine phytoplankton primary productivity (Moore et al., 2001; Boyd et al., 2007; Behrenfeld et al., 2009). This element plays a fundamental role in the photosynthetic electron transport chain (ETC) and therefore the conversion of light energy to organic carbon products (Briat et al., 2007; Raven et al., 1999; Yruela, 2013).

Approaches currently used to measure phytoplankton primary production quantify rates at different points of the photosynthetic process (evolution of O<sub>2</sub>, assimilation of CO<sub>2</sub>, electron transport in photosystem II). These various rates can be decoupled in response to changes in environmental conditions or phytoplankton taxonomy (Suggett et al., 2009a). For this reason, it is likely that iron limitation will affect the conversion factors between these various productivity metrics. Phytoplankton CO<sub>2</sub>-assimilation can be measured directly using the radioisotope tracer <sup>14</sup>C (Steemann-Nielsen, 1951; Williams et al., 2008). This technique has been widely applied in biological oceanography over the past 60 years, despite a number of well-known limitations (e.g. low spatial and temporal resolution, high cost and labour intensity, bottle artifacts due to exclusion of grazers and contamination, requirement for radio-isotopes, ambiguity of whether net or gross production is measured (Williams et al., 2008; Marra, 2009; Halsey et al., 2010, 2011; Pei and Laws, 2013). In recent years, bio-optical approaches have emerged as an attractive alternative to overcome these limitations. Chlorophyll *a* fluorescence (ChlF) yields, measured by Pump and Probe, FRR, or PAM fluorometry, can be used to estimate rates of linear electron transport (i.e. rates of charge separation) in photosystem II (ETR<sub>RCHII</sub>) (Genty et al., 1989; Huot and Babin, 2010; Kolber and Falkowski, 1993; Kolber et al., 1998; Suggett et al., 2010b), thus providing a measure of gross photosynthesis. Being non-intrusive, instantaneous and relatively inexpensive, these approaches can be used to examine phytoplankton photophysiology at

unmatched spatial and temporal resolution, and improve the coverage of productivity estimates over vast oceanic domains.

Despite significant potential, active ChlF approaches are currently not widely applied to monitor rates of phytoplankton primary productivity. This is due, in part, to uncertainty in the conversion of  $ETR_{RCII}$  to ecologically relevant rates of  $CO_2$ -assimilation (Lawrenz et al., 2013; Suggett et al., 2009a). Numerous studies conducted over the past decades have collectively shown that the conversion factor linking  $ETR_{RCII}$  to  $CO_2$ -assimilation in phytoplankton is not constant, but changes in response to taxonomy and environmental conditions (Barranguet and Kromkamp, 2000; Boyd et al., 1997; Cheah et al., 2011; Corno et al., 2006; Debes et al., 2008; Estévez-Blanco et al., 2006; Fujiki et al., 2007, 2011; Gilbert et al., 2000; Goto et al., 2008; Hancke et al., 2008; Kaiblinger and Dokulil, 2006; Kolber and Falkowski, 1993; Kromkamp et al., 2008, 2011; Lawrenz et al., 2013; Melrose et al., 2006; Moore et al., 2003, 2006; Napoléon and Claquin, 2012; Napoléon et al., 2013; Pemberton et al.; Prieto et al., 2008; Raateoja, 2004; Raateoja et al., 2004; Robinson et al., 2009, 2014; Smyth et al., 2004; Suggett et al., 2001, 2006, 2009a; Tripathy et al., 2010). On the physiological level,  $ETR_{RCII}$  and  $CO_2$ -assimilation can be uncoupled by a number of energy-allocation processes that evolved to maximize photosynthetic efficiency while preventing photo-damage. Marine phytoplankton evolved an exceptional photosynthetic plasticity to achieve this balance under low nutrient and fluctuating light conditions. A number of recent studies have examined this fine-tuning of electron transport and energy allocation within the phytoplankton photosynthetic apparatus, providing mechanistic insight into the processes decoupling  $CO_2$ -assimilation and photosynthetic electron transport (e.g. Bailey et al., 2008; Cardol et al., 2008; Mackey et al., 2008; Zehr and Kudela, 2009; Grossman et al., 2010; Peltier et al., 2010; McDonald et al., 2011; Cardol et al., 2011; Behrenfeld and Milligan, 2013; Halsey and Jones, 2015).

In this study, we examine the interacting effects of iron levels and instantaneous light availability on the coupling of  $ETR_{RCII}$  and  $CO_2$ -assimilation in marine phytoplankton. We derived rates of  $ETR_{RCII}$  normalized to PSII reaction center content ( $\text{mol e}^- \text{mol RCII}^{-1} \text{s}^{-1}$ ), resulting in a conversion factor consisting of two parameters: the amount of chlorophyll *a* (*chl**a*) functionally connected to each RCII ( $1/n_{PSII}$ ,  $\text{mol chl}a^{-1} \text{mol RCII}^{-1}$ ), and the electron requirement for carbon fixation ( $\Phi_{e:C}$ ,  $\text{mol e}^- \text{mol C}$ ). Working with natural phytoplankton assemblages in the Northeast Subarctic Pacific, and mono-specific phytoplankton cultures in the laboratory, we

conducted simultaneous measurements of FRRF-derived  $ETR_{RCII}$  and  $^{14}C$ -based  $CO_2$ -assimilation over a range of irradiances ( $P_{vsE}$  curves) under high and low iron conditions. Our results demonstrate significant and interactive effects of irradiance and iron availability on the coupling of  $ETR_{RCII}$  and  $CO_2$ -assimilation, with an increase in the conversion factor  $\Phi_{e:C}/n_{PSII}$  under excess light and low iron conditions. From a photo-physiological point of view, increased decoupling appeared to be caused by the effects of increased excitation energy on the photosynthetic ETC, resulting in a strong correlation between the derived conversion factor and the expression of non-photochemical quenching (NPQ) in the antennae of PSII. This correlation can, in turn, be used to derive rates of carbon-based productivity from FRRF data, without the need for any additional measurements.

### 2.3 Methods

In this study, we utilized three separate datasets. First, we examined the coupling of  $ETR_{RCII}$  and  $CO_2$ -assimilation in a mixed phytoplankton assemblage during a 6 day ship-board iron addition experiment in iron-limited waters of the Subarctic Pacific (Figure 2.1). Secondly, we conducted experiments with two mono-specific phytoplankton cultures grown under controlled light and iron conditions in the laboratory. These experiments were conducted to examine the physiological effects of iron and light on the conversion factor  $\Phi_{e:C}/n_{PSII}$ , in the absence of potentially confounding taxonomic shifts. Finally, we applied the results obtained from the iron addition experiment to derive a conversion factor predicting rates of  $CO_2$ -assimilation along a coastal to open ocean transect in the NE Subarctic Pacific (Line-P, <https://www.waterproperties.ca/linep/>) (Figure 2.1). All fieldwork for this project was conducted under the authorization and permits of Fisheries and Oceans Canada.

#### 2.3.1 Iron addition experiment

All fieldwork was conducted on board the *CCGS John P. Tully* in August - September 2013. A 6 day iron addition experiment was initiated at P20 (49°34 N, 138°40 W) (Figure 2.1), located in iron-limited HNLC waters. Water was collected before dawn from 7 m depth using a trace metal clean pumping system and an on-deck class 100 laminar flow hood (cf. Johnson et al., 2005). In order to eliminate macro-zooplankton, the water was pre-filtered through acid washed 200  $\mu m$  Nitex mesh. Six trace metal-cleaned 10 L cubitainers were rinsed and filled in

random order. Triplicate iron-addition treatments were amended with 1 nM Fe (ammonium iron (II) sulfate hexahydrate  $((\text{NH}_4)_2\text{Fe}(\text{SO}_4)_2 \cdot 6\text{H}_2\text{O})$ , dissolved in 0.05 M HCl), while triplicate controls were left unamended. Cubitainers were kept in on-deck incubators continuously supplied with seawater pumped from 5 m depth. Light intensity was adjusted to ~ 50 % of full sunlight with neutral density screening and irradiance was continuously logged using a LI-1000 radiation sensor (LI-COR, USA), located 2 m above the incubator. This level of light reduction was chosen to avoid exposing the phytoplankton to irradiances higher than *in situ* values. On days 1, 3 and 5 at exactly 2 hours after local sunrise, 500 mL of water were sub-sampled from each cubitainer using trace metal clean techniques. Sub-samples were analyzed for total chlorophyll *a* concentration ([chl*a*]), photo-physiological parameters and rate measurements as outlined below. On the last day of the experiment, additional samples were collected for pigment analysis by high pressure liquid chromatography (HPLC), and the determination of absorption spectra using the quantitative filter technique (QFT) (Mitchell et al., 2002).

### **2.3.2 Laboratory culturing**

The oceanic centric diatom *Thalassiosira oceanica* (CCMP isolate 1003, Sargasso Sea) and the oceanic prymnesiophyte *Chrysochromulina polylepis* (NEPCC isolate 242, NE Subarctic Pacific) were grown under iron-replete and iron-limiting conditions. We chose these two species as representative eukaryotic open ocean species, common in the region of our field study (Booth, 1988; Chappell et al., 2015). Iron-limited growth conditions were chosen to achieve an approximately 50 % reduction in growth rate. Both species were cultured in 28 mL acid-cleaned polycarbonate tubes using the artificial seawater medium AQUIL (Price et al., 1989), prepared as described by Maldonado et al. (2006). All cultures were kept at 19 °C in continuous, sub-saturating light (ca. 40  $\mu\text{mol quanta m}^{-2} \text{s}^{-1}$ ). Growth was monitored by daily measurements of *in vivo* chl*a* fluorescence using a Turner 10-AU fluorometer, and cultures were kept in exponential growth phase using semi-continuous batch culturing (Brand et al., 1981). Cultures were considered acclimated when growth rates during ca. 40 cell divisions (five successive transfers), varied by <15 % (Brand et al., 1981). Acclimated, exponentially growing cells were used to inoculate triplicate 200 mL cultures. These 200 mL cultures were sub-sampled several times for FRRF measurements (see below), which demonstrated that cells maintained steady-state photo-physiology throughout the sampling phase. During early to mid-exponential phase, each replicate

culture was sampled for duplicate  $\text{ETR}_{\text{RCII}}\text{-PvsE}$  curves, duplicate  $^{14}\text{C}\text{-PvsE}$  curves and triplicate [chl $a$ ] samples. Sterile, trace metal clean techniques were used at all times.

### **2.3.3 Station sampling**

In addition to the iron addition experiment, seawater samples were collected at five hydrographic stations (P4, P12, P16, P20, and P26) spanning a coastal to open ocean transect in the NE Subarctic Pacific (Figure 2.1). Collection of water column hydrographic profiles was performed with a CTD (SeaBird Electronics, model 911 plus) equipped with a dissolved oxygen sensor (SBE 43), fluorometer (Seapoint), and an underwater photosynthetically active radiation (PAR) sensor (Biospherical QSP-400). At each of the stations, water was collected from Niskin bottles at three depths exactly two hours after local sunrise and processed immediately for rate measurements, photo-physiological parameters, and [chl $a$ ] as described below.

### **2.3.4 [chl $a$ ]**

For the 3 sets of experiments outlined above, samples for [chl $a$ ] were filtered onto pre-combusted 25 mm glass fiber filters (GF/F) using low vacuum pressure (<5 mm Hg) and analyzed fluorometrically following the method of Welschmeyer (1994). In the field, triplicate 100-300 mL samples were filtered and stored at -20 °C until analysis within three weeks of collection. In the laboratory, triplicate culture samples (10 mL, 20 mL and 30 mL) were collected and analyzed immediately. Each sample was analyzed in duplicate.

### **2.3.5 Carbon assimilation**

For both laboratory and field work, rates of carbon assimilation were measured as small volume PvsE curves in a custom built photosynthetron (Lewis and Smith, 1983). In the field, 300 mL of water were spiked with 150  $\mu\text{Ci NaH}^{14}\text{CO}_3$  (final concentration 0.5  $\mu\text{Ci mL}^{-1}$ , 52.5 mCi  $\text{mL}^{-1}$  specific activity) (Perkin-Elmer) immediately after sampling. Spiked samples were mixed gently but thoroughly, aliquoted into 20 mL glass scintillation vials and placed into the photosynthetron. Temperature was kept within 1°C of *in situ* temperature by circulating water from a water-bath through an aluminum cooling jacket (the offset from *in situ* temperature was larger for station samples because samples from different depths had to be incubated simultaneously). Light was provided by high power light emitting diodes (LEDs) located under each scintillation vial. Each PvsE curve consisted of 11 light levels spanning intensities from 3 to

600  $\mu\text{mol quanta m}^{-2} \text{ s}^{-1}$ . Actual light intensities were measured before and after each experiment using a  $4\pi$  quantum sensor (QSL-2100, Biospherical Instruments) immersed in water inside a scintillation vial. Incubations lasted for 3-4 hours and were ended by gentle filtration onto 25 mm GF/F filters. Filters were pre-combusted to reduce nominal pore size to approximately 0.4  $\mu\text{m}$ . For each curve, three time-zero samples were taken by filtering 20 mL immediately after spiking. The total  $^{14}\text{C}$  activity added was determined from three 1 mL aliquots of the spiked sample added to 1 mL 1 M NaOH. All work was done under low light and filters were stored in scintillation vials at  $-20\text{ }^{\circ}\text{C}$  until processing within 1 month of the experiment. During laboratory processing, 500  $\mu\text{L}$  of 3 M HCl was added to each filter and vials were left to degas for  $>24$  hours to eliminate any inorganic  $^{14}\text{C}$  remaining in the samples. Ten mL of scintillation cocktail (Scintisafe plus, Fisher) were added to each vial, and vials were then vortexed and left to stand in the dark for  $>12$  hours before analysis on a liquid scintillation counter (Beckman). Disintegrations per minute (DPM) were derived from scintillation counts using a quench curve prepared from commercial  $^{14}\text{C}$  standards (Perkin-Elmer). DPM were converted to units of carbon biomass following Knap et al. (1996).

The  $^{14}\text{C}$  protocol used for laboratory cultures was the same as outlined above with the following exceptions. We spiked 80 mL of exponentially growing culture with 40  $\mu\text{Ci NaH}^{14}\text{CO}_3$  and 3 mL aliquots were incubated in the photosynthetron for 30 minutes. Duplicate curves were measured for each sample. The incubation was terminated by adding 1 mL of 1 M HCl to each vial and samples were dried completely, omitting the filtration step. After drying, salts were re-suspended in 1 mL MilliQ water. Unfortunately, low biomass and logistical constraints (i.e. time available to dry sample) did not allow us to apply this non-filtration approach in the field and consequently initially fixed  $^{14}\text{C}$  excreted as dissolved organic carbon (DOC) was not captured for field samples. For both laboratory and field measurements  $^{14}\text{C}$ -PvsE curves were fit following Webb et al. (1974), as described below.

### **2.3.6 *Chla* fluorescence parameters and $\text{ETR}_{\text{RCII}}$**

A bench-top FRRF instrument (Soliense Inc.) was used for all active ChlF measurements. In the field, opaque bottles were used for sub-sampling from the rosette or iron addition experiment, and light in the laboratory was kept low at all times to allow oxidation of the ETC and relaxation of NPQ. For all measurements, background fluorescence blanks were prepared by

very gently filtering a small amount of sample through a pre-combusted GF/F. Single turnover (ST) flash protocols consisted of 100 flashlets with 1.0  $\mu\text{s}$  length and 2.5  $\mu\text{s}$  interval (46200  $\mu\text{mol quanta m}^{-2} \text{s}^{-1}$  peak power intensity, resulting in a ST flash length of 250  $\mu\text{s}$ , providing ~5-10 quanta per RCII). The excitation power was selected at the beginning of the cruise to saturate the observed fluorescence transients within the first half of the ST excitation protocol. Our experience indicates that this approach offers the best signal-to-noise ratio in the recovered parameters, while accommodating significant variations in the photosynthetic properties of the local phytoplankton populations along the cruise track, without re-adjusting of the excitation protocol. Excitation power was provided by an array of eight LEDs at four wavelengths centered on 445 nm, 470 nm, 505 nm, and 530 nm (equal intensity at each wavelength; see

Figure A1 in the appendix for more information on the spectral distribution). We measured steady state light curves (SSLC), where each sample was exposed to 10 actinic ‘background’ irradiances ranging from 0 to 1000  $\mu\text{mol quanta m}^{-2} \text{s}^{-1}$ , also provided at four wavelengths (

Figure A1 in the appendix). The relatively long duration of the SSLCs in this study could create some potential for the settling of cells which could influence the ChlF yield. However, our sampling region is known to be dominated by small cells (Booth, 1988), which should have a slow settling rate. Equally, the laboratory isolates used during this study stay in suspension for many hours, and it is thus unlikely that rapid settling of cells drastically altered our results.

All ChlF yields and parameters described below were derived by an iterative non-linear fitting procedure, applying the four parameter biophysical model of Kolber et al. (1998) to a mean of 20 consecutive ST flashes using custom software (Z. Kolber). This software accounts for a formation of fluorescence quenching, most likely due to formation of a P680 triplet, which reduces the maximum fluorescence yield attainable during the ST flash by 3-6 %. Throughout the SSLC, ST flashes were applied continuously (at 1 s interval), while the length of each light step was optimized to allow all ChlF yields and derived parameters to reach steady state (i.e. to remain at a constant level after initial strong changes in response to the change in light level, ca. 5 min). ChlF yields and parameters corresponding to each light level were obtained from the mean of the last three acquisitions at each light level. In this way, we derived the fluorescence yields  $F_o$  and  $F_m$  (in dark regulated state) as well as  $F'$  and  $F_m'$  (in the light regulated state for each light level of the SSLC).  $F_o'$  was calculated as  $F_o' = F_o / (F_v/F_m + F_o/F_m')$  (Oxborough and

Baker, 1997). Even though this derivation has become widely accepted in the literature, we caution here that it might not hold for values derived under high background irradiance (see Ruban and Murchie, 2012) and varying stress levels experienced by natural phytoplankton assemblages.

Five fluorescence signals,  $F_o$ ,  $F_m$ ,  $F'$ ,  $F_m'$  and  $F_o'$  were used to calculate ChlF parameters, following Roháček (2002). In the dark-regulated state, we derived the commonly used  $F_v/F_m$  ratio as  $F_v/F_m = (F_m - F_o)/F_m$  (Kitajima and Butler, 1975). For each light level of the SSLC protocol we have calculated the following ChlF parameters: (1) The photochemical quenching of variable fluorescence,  $F_q'/F_v' = (F_m' - F')/(F_m' - F_o')$ , which quantifies the fraction of functional RCII in the open state (i.e. primary quinone acceptor  $Q_A$  in the oxidized state) (Duysens and Sweers, 1963). (2) The maximum quantum yield of PSII photochemistry,  $F_v'/F_m' = (F_m' - F_o')/F_m'$ , which can be used to quantify the extent to which photochemistry in PSII is limited by competition with thermal decay of excitation energy (Oxborough and Baker, 1997). (3) The overall quantum efficiency of photochemical energy conversion in PSII at a given light intensity (note that numerous definitions for this parameter exist in the literature),  $F_q'/F_m' = (F_m' - F')/F_m' = \Phi_{PSII}'$  (the product of  $F_q'/F_v'$  and  $F_v'/F_m'$  (Genty et al., 1989)). Furthermore, the functional absorption cross section of PSII,  $\sigma_{PSII}$  ( $\text{\AA}^2 \text{RCII}^{-1}$ ), was derived from the rate of closure of RCII in the dark-regulated and at each light-regulated state (Kolber and Falkowski, 1993; Kolber et al., 1998). The connectivity parameter,  $\rho$ , was also calculated, but not used in our analysis. Rates of charge separation (i.e.  $ETR_{RCII}$ ) in functional RCII ( $\text{mol e}^- \text{mol RCII}^{-1} \text{s}^{-1}$ ) were estimated as the product of incident irradiance ( $E$ ), the fraction of irradiance absorbed by PSII ( $\sigma_{PSII}$ ) and the efficiency with which charge separation occurs in RCII. We calculated  $ETR_{RCII}$  as

$$ETR_{RCII} = E * \sigma_{PSII}' * \frac{F_q'}{F_v'} * 6.022 * 10^{-3} \quad (2.1)$$

where  $E$  ( $\mu\text{mol quanta m}^{-2} \text{s}^{-1}$ ) is the actinic irradiance at each light level,  $\sigma_{PSII}'$  ( $\text{\AA}^2 \text{RCII}^{-1}$ ) is the functional absorption cross section at  $E$  and  $F_q'/F_v'$  is the photochemical capacity of PSII at  $E$ . The number  $6.022 \times 10^{-3}$  converts  $\mu\text{mol quanta}$  to  $\text{quanta}$  and  $\text{\AA}^2$  to  $\text{m}^2$ . Because of potential systematic errors in the calculation of  $F_o'$ , we also calculated  $ETR_{RCII}$  as

$$ETR_{RCII} = E * \sigma_{PSII} * \frac{(F_q'/F_m')}{(F_v'/F_m')} * 6.022 * 10^{-3} \quad (2.2)$$

which does not require the knowledge of  $F_o'$ . Both calculations are equivalent, assuming that non-photochemical quenching processes affecting ChlF can be adequately accounted for in either the absorption term (Eq. 2.1) and the efficiency term (Eq. 2.2). While Eq. 2.2 does not require  $F_o'$  (which was not measured directly) or  $\sigma_{PSII}'$  (which is difficult to derive at high irradiances), it does rely on parameters measured in the fully dark-regulated state, which can be difficult to achieve in field assemblages. For all  $ETR_{RCII}$  calculated during our iron addition experiment ( $n = 345$ ) the difference between values calculated in both ways ranged from 0.5 to 21 % with a mean coefficient of variance of 5.5 %. Both approaches thus provided similar results in the analysis of our data, and the differences observed were not systematically related to the treatment (high vs low Fe).

Non-photochemical quenching (NPQ) at each light level was estimated as the normalized Stern-Volmer quenching coefficient, defined as  $NPQ_{NSV} = (F_m'/F_v') - 1 = F_o'/F_v'$  (McKew et al., 2013). Quantification of NPQ using  $NPQ_{NSV}$  instead of the more commonly used Stern-Volmer coefficient of quenching, defined as  $NPQ_{SV} = (F_m - F_m')/F_m$  (Bilger and Björkman, 1990), is appropriate for our data-set, as it resolves differences in NPQ present in the dark-regulated state.

### **2.3.7 PvsE curves**

Measurements of  $CO_2$ -assimilation and  $ETR_{RCII}$  were plotted against irradiance, and the exponential model of Webb et al. (Webb et al., 1974) was fit to the data using a non-linear least squares regression procedure in MATLAB. For the  $CO_2$ -assimilation data, an intercept parameter was added to force the regression through the origin and provide a good fit in the linear part of the PvsE curve (Arrigo et al., 2010; Suggett et al., 2001). For both rates of productivity, we derived the light saturated maximum rate  $P_{max}$  and the light utilization efficiency  $\alpha$ . When photoinhibition was observed at high irradiances, the data-points were excluded from the fitting procedure.

### **2.3.8 Derivation of conversion factor**

Because we derived  $ETR_{RCII}$  in units of  $mol e^- mol RCII^{-1} s^{-1}$  and  $CO_2$ -assimilation in units of  $mol C mol chl a^{-1} s^{-1}$ , the conversion factor between the two rates accounts for changes in

chl $a$  functionally associated with each RCII ( $1/n_{PSII}$ , mol chl $a$  mol RCII $^{-1}$ ) and the number of charge separations in RCII needed per CO $_2$ -assimilated into organic carbon products ( $\Phi_{e:C}$ , mol e $^{-}$  mol C $^{-1}$ ).

$$\frac{ETR_{RCII}(\text{mol } e^{-} \text{ mol RCII}^{-1} \text{ s}^{-1})}{CO_2 \text{ assimilation}(\text{mol C mol chl}a^{-1} \text{ s}^{-1})} = \Phi_{e:C} \left( \frac{\text{mol } e^{-}}{\text{mol C}} \right) * \frac{1}{n_{PSII}} \left( \frac{\text{mol chl}a}{\text{mol RCII}} \right) \quad (2.3)$$

In this approach, we attribute the observed decoupling between  $ETR_{RCII}$  and CO $_2$ -assimilation to changes in both  $1/n_{PSII}$  and  $\Phi_{e:C}$ . We recognize that combining  $\Phi_{e:C}$  and  $1/n_{PSII}$  into one conversion factor obscures the mechanistic underlying of the observed decoupling. Nevertheless, as we will show, our approach has the potential to provide FRRF-derived estimates of phytoplankton primary productivity in carbon units without the need for many of the auxiliary measurements and inherent assumptions used in previous studies.

The value of  $1/n_{PSII}$  is known to change significantly as a function of taxonomy (Suggett et al., 2010b), light (Dubinsky et al., 1986; Suggett et al., 2010b), macro-nutrients (Berges et al., 1996), and iron availability (Greene et al., 1991, 1992, 1994; Vassiliev et al., 1995; Allen et al., 2008; Thamatrakoln et al., 2013; Macey et al., 2014). Therefore we could not assume a constant value for  $1/n_{PSII}$ , as has been done in most previous studies (Lawrenz et al., 2013). Although  $1/n_{PSII}$  can be directly measured from oxygen flash yield experiments (e.g. Falkowski et al., 1981; Mauzerall and Greenbaum, 1989; Suggett et al., 2004), the approach is labour-intensive and not practical for routine field sampling. A new approach to derive [RCII] directly from FRRF measurements has been developed (Silsbe, 2015; Oxborough et al., 2012), but not implemented in our study because the inherent assumption that the ratio of rate constants of photochemistry and fluorescence ( $k_p/k_f$ ) is confined to a narrow range, does not hold under varying levels of iron limitation (Behrenfeld and Milligan, 2013; Oxborough et al., 2012; Vassiliev et al., 1995).

Having established a relationship between light intensity and rates of CO $_2$ -assimilation and  $ETR_{RCII}$  for each sample, we were able to model the light dependency of the conversion factor  $\Phi_{e:C}/n_{PSII}$ . This approach allowed us to observe how the coupling of  $ETR_{RCII}$  and CO $_2$ -assimilation is modulated by incident irradiance, and how, in turn, iron limitation influences the light-dependent response. Additionally, we used  $\alpha$  and  $P_{max}$  of each rate to derive the conversion factor under sub-saturating and saturating light conditions, respectively.

## 2.4 Results

### 2.4.1 Effect of iron addition on phytoplankton community composition, photo-physiology, $ETR_{RCII}$ and $CO_2$ -assimilation in the NE Subarctic Pacific

Phytoplankton assemblages at station P20 in the NE Subarctic Pacific (Figure 2.1) responded strongly to iron addition in a ship-board incubation experiment (Figure 2.2). Six days after iron addition, [chl $a$ ] increased by an order of magnitude, whereas the control (i.e. no iron addition) showed only a small increase in [chl $a$ ]. This result confirms that the initial phytoplankton assemblage was iron-limited (Figure 2.2a), and that we were able to carry out the manipulation experiment without significant contamination of the control bottles. The slight increase in [chl $a$ ] in the control treatments is likely attributable to a decrease in grazing pressure and to changes in the light environment (i.e. lower and less fluctuating light). Iron addition also significantly affected phytoplankton photo-physiology, as demonstrated by rapid changes in the parameters  $\sigma_{PSII}$  and  $F_v/F_m$  derived in the dark-regulated state (Figure 2.2b and Figure 2.2c).  $F_v/F_m$  initially increased in both treatments, but then remained low in the control while continuing to increase in the iron addition treatment (Figure 2.2b). While the functional absorption cross-section of PSII,  $\sigma_{PSII}$  ( $\text{\AA}^2 \text{RCII}^{-1}$ ), remained high and relatively constant in the iron-limited control, it declined rapidly after iron addition, and remained ~25 % lower than that of the initial phytoplankton assemblage (Figure 2.2c). The observed changes in  $F_v/F_m$  and  $\sigma_{PSII}$  may have resulted from both photo-physiological responses and from changes in species composition. CHEMTAX analysis of pigments sampled on day 6 of the experiment showed that the addition of iron changed the taxonomic composition of the phytoplankton assemblage (Figure A2 in the appendix). Most prominently, the relative abundance of chlorophytes decreased from 7 % to 1 %, relative abundance of prymnesiophytes decreased from 55 % to 22 %, relative abundance of pelagophytes increased from 17 % to 39 %, and the relative abundance of diatoms increased from 1 % to 16 % in iron amended bottles. A similar response has been observed in previous iron addition experiments conducted in this region (Marchetti et al., 2006).

We measured  $P_{vsE}$  curves of short-term  $CO_2$ -assimilation and  $ETR_{RCII}$  five times during the iron addition experiment (Figure 2.3). Both rates show the expected light dependency, and were affected by iron addition. However, the response to iron addition differed for  $CO_2$ -assimilation and  $ETR_{RCII}$ . Chlorophyll  $a$ -normalized  $CO_2$ -assimilation showed a small, though

not statistically significant, increase after iron addition (Figure 2.3a-e). The observed increase in the *chl*<sub>a</sub>-normalized rate was small, because cellular *chl*<sub>a</sub> content increased in parallel with CO<sub>2</sub>-assimilation (under all nutrient limitations, cellular *chl*<sub>a</sub> in phytoplankton is drastically reduced, a condition referred to as chlorosis, (e.g. Geider and La Roche, 1994). The strong effect of iron addition on CO<sub>2</sub>-assimilation can be seen more clearly when rates are normalized to volume. Indeed, volume-normalized CO<sub>2</sub>-assimilation rates increased more than 8-fold after iron addition in this experiment (Figure A3 in the appendix). In contrast to rates of CO<sub>2</sub>-assimilation, ETR<sub>RCII</sub> decreased significantly after iron addition, when compared to the iron-limited control treatment (Figure 2.3e-j).

The response of CO<sub>2</sub>-assimilation and ETR<sub>RCII</sub> to iron addition is further visualized in Figure 2.4, which shows changes in light-limited slopes ( $\alpha$ ) and light saturated rates ( $P_{\max}$ ), as well as the derived conversion factor  $\Phi_{e:C}/n_{\text{PSII}}$  for  $\alpha$  and  $P_{\max}$ , throughout the experiment. Values for  $\alpha$  and  $P_{\max}$  were derived from the <sup>14</sup>C-based and FRRF-based *P*<sub>v</sub>*s**E* curves shown in Figure 2.3. No statistically significant change in values of  $\alpha$  could be determined for either *chl*<sub>a</sub>-normalized CO<sub>2</sub>-assimilation, ETR<sub>RCII</sub> or  $\Phi_{e:C}/n_{\text{PSII}}$  ( $p > 0.05$ ). Similarly, the  $P_{\max}$  for *chl*<sub>a</sub>-normalized CO<sub>2</sub>-assimilation remained relatively constant in the control, and did not show a statistically significant increase after iron addition ( $p > 0.05$ ) (Figure 2.4d). In contrast, there was a significant ( $p < 0.05$ ) decrease in  $P_{\max}$  for ETR<sub>RCII</sub> following iron-addition, as compared to the control treatments, which exhibited a small increase in this variable over the course of the experiment (Figure 2.4e). The observed changes in the  $P_{\max}$  for CO<sub>2</sub>-assimilation and ETR<sub>RCII</sub>, resulted in a decrease in  $\Phi_{e:C}/n_{\text{PSII}}$  in the iron addition treatment compared to the relatively constant value observed in the iron-limited control (Figure 2.4f). This difference was statistically significant for the last 2 days of the experiment ( $p < 0.05$ ). When compared to the initial value on day 0 of the incubation, the conversion factor  $\Phi_{e:C}/n_{\text{PSII}}$  for  $P_{\max}$  decreased by 66 % after iron addition, and by 16 % in the iron-limited control (Figure 2.4f). These results indicate that the iron-dependent changes in  $\Phi_{e:C}/n_{\text{PSII}}$  are most readily apparent under high irradiance conditions where photosynthesis is light-saturated.

To better explain the iron-dependent decrease in ETR<sub>RCII</sub> and  $\Phi_{e:C}/n_{\text{PSII}}$  observed in our data, we examined changes in additional FRRF-derived ChlF parameters, measured on day 3 after iron addition. We choose day 3 for the in-depth analysis of our data, but trends observed on this day were representative of those observed throughout the experiment. The parameter  $F_q'/F_v'$

represents the efficiency of charge separation in functional RCII (Figure 2.5a). It is an estimate of the fraction of open RCII (i.e.  $Q_A$  oxidized) at any given light level, and therefore always equals one at zero irradiance. On day 3 after iron addition, we observed higher  $F_q'/F_v'$  for the iron-limited control at all irradiance levels (Figure 2.5a), indicating a greater fraction of open reaction centers. The parameter  $F_v'/F_m'$ , the efficiency of excitation energy capture by the fraction of open RCII (Genty et al., 1989), can be used to quantify the extent to which photochemistry in RCII is limited by thermal energy dissipation in the antenna (Oxborough and Baker, 1997). This parameter was significantly reduced in the iron-limited control relative to the iron addition treatment (Figure 2.5b), indicating that the efficiency of excitation energy transfer in the light-harvesting antenna was compromised. The overall efficiency of charge separation per quantum absorbed in PSII ( $F_q'/F_m'$ ) is the product of  $F_q'/F_v'$  and  $F_v'/F_m'$  (Genty et al., 1989; Roháček, 2002). On day 3, at all light levels,  $F_q'/F_m'$  was higher in the iron addition treatment than in the iron-limited control (Figure 2.5c).

We used our PvsE measurements of  $CO_2$ -assimilation and  $ETR_{RCII}$  to examine the light-dependent response of the conversion factor  $\Phi_{e:C}/n_{PSII}$ . Our results (Figure 2.6) show that  $\Phi_{e:C}/n_{PSII}$  increased with increasing irradiance, regardless of iron treatment and day of the experiment (Figure 2.6a-e). However, this light-dependent increase was much more pronounced in the iron-limited control treatment. It is important to note that the magnitude and light-dependency of  $\Phi_{e:C}/n_{PSII}$  in the iron-limited control treatment changed over the course of the experiment relative to the initial sample (Figure 2.6a). This shift in  $\Phi_{e:C}/n_{PSII}$  in the absence of iron addition likely reflects changes in light quality and quantity in the incubation bottles relative to the ambient water column.

Also shown in Figure 2.6 is the light and iron dependency of  $NPQ_{NSV}$ , estimated as  $F_o'/F_v'$ . This parameter showed a light and iron-dependent response that was remarkably similar to  $\Phi_{e:C}/n_{PSII}$ , with values increasing with increasing light, regardless of treatment and day of the experiment, and decreasing in response to iron addition (Figure 2.6f-j). The  $NPQ_{NSV}$  values measured in our initial sample (Figure 2.6f) were higher than those measured in either control or iron addition treatments during the following days. We attribute this effect to a more stable light environment in the incubation bottles, relative to *in situ* irradiance levels.

Given the similar light and iron-dependent responses of  $\Phi_{e:C}/n_{PSII}$  and  $NPQ_{NSV}$ , we sought to examine the relationship between these two variables. In order to do so, however, it was

necessary to derive  $\text{NPQ}_{\text{NSV}}$  and  $\Phi_{\text{e:C/nPSII}}$  values at a standard set of light levels, matching those of the FRRF derived  $\text{ETR}_{\text{RCII-PvsE}}$  curves. For each sample,  $\text{ETR}_{\text{RCII-PvsE}}$  curves consisted of 14 light levels spanning from 0 to  $1000 \mu\text{mol quanta m}^{-2} \text{s}^{-1}$ . These light levels did not exactly match those used for the  $\text{CO}_2$ -assimilation experiments. We thus used the  $\text{PvsE}$  curve fits of our  $^{14}\text{C}$  data to derive the  $\text{CO}_2$ -assimilation values at light levels matching those of the  $\text{ETR}_{\text{RCII-PvsE}}$  curves. In this way, we were able to compile a dataset of 298 paired values for  $\text{NPQ}_{\text{NSV}}$  and  $\Phi_{\text{e:C/nPSII}}$ , derived from 27 sets of  $\text{ETR}_{\text{RCII}}$  and  $^{14}\text{C}$   $\text{PvsE}$  curves during the iron addition experiment. Plotting these  $\Phi_{\text{e:C/nPSII}}$  values against the corresponding  $\text{NPQ}_{\text{NSV}}$  reveals a strong and statistically significant correlation ( $R^2 = 0.70$ ,  $p < 0.0001$ , for quadratic fit) (Figure 2.7).

#### **2.4.2 Effects of iron limitation on photo-physiology and rates of $\text{ETR}_{\text{RCII}}$ and $\text{CO}_2$ -assimilation in mono-specific phytoplankton cultures**

Using methods analogous to those applied to mixed phytoplankton assemblages in the NE Subarctic Pacific; we measured  $\text{PvsE}$  curves of  $\text{CO}_2$ -assimilation and  $\text{ETR}_{\text{RCII}}$  in mono-specific laboratory cultures of two open ocean phytoplankton species. The results, summarized in Table 2.1, show similar trends as observed in our field data. Steady-state growth rates ( $\mu$ ,  $\text{d}^{-1}$ ) in the low iron cultures were 68 % and 49 % of iron-replete growth rates in the diatom *T. oceanica* and the prymnesiophyte *C. polylepis*, respectively (Table 2.1). For both species,  $F_v/F_m$  in iron-limited cultures was reduced (by 32 % and 20 % in *T. oceanica* and *C. polylepis*, respectively). In iron-limited *T. oceanica*,  $\sigma_{\text{PSII}}$  increased by 15 %, while it increased by 5 % in *C. polylepis*. The iron dependent changes in  $\mu$ ,  $F_v/F_m$  and  $\sigma_{\text{PSII}}$  was statistically significant in both species (one tailed  $p < 0.0001$  and  $< 0.01$  for *T. oceanica* and *C. polylepis*, respectively). Chlorophyll *a* - normalized  $\text{CO}_2$ -assimilation at  $P_{\text{max}}$  remained relatively constant in both species ( $p > 0.05$ ). In contrast, we observed a 90 % increase in  $\text{ETR}_{\text{RCII}}$  at  $P_{\text{max}}$  in *T. oceanica* under iron-limited growth conditions. *C. polylepis* also exhibited an increase in  $\text{ETR}_{\text{RCII}}$  at  $P_{\text{max}}$  under iron-limited conditions, but this increase was not statistically significant ( $p > 0.05$ ). Regardless of species-specific differences, both species showed the same trend of increased  $\Phi_{\text{e:C/nPSII}}$  and  $\text{NPQ}_{\text{NSV}}$  under iron limitation (Table 2.1), which is consistent with our field observations. Furthermore, the species-specific differences observed in our laboratory experiments are consistent with changes in phytoplankton assemblage composition observed in our iron addition experiment, where the abundance of diatoms (lower  $\Phi_{\text{e:C/nPSII}}$ ) was increased in the iron addition treatment

and the abundance of prymnesiophytes (higher  $\Phi_{e:C}/n_{PSII}$ ) was decreased (Figure A2 in the appendix).

## 2.5 Discussion

Our results provide new insight into the effects of iron and light availability on the coupling between CO<sub>2</sub>-assimilation and photosynthetic electron transport in natural phytoplankton assemblages and mono-specific laboratory cultures. We show that both of these environmental variables significantly influence  $\Phi_{e:C}/n_{PSII}$ , which has important implications for the use of FRRF measurements to infer rates of CO<sub>2</sub>-assimilation in oceanic waters. Below, we first discuss the observed increase in  $\Phi_{e:C}/n_{PSII}$  under excess light and low iron conditions in the context of previously reported values. We then discuss the effects of iron and light on phytoplankton photo-physiology, and suggest a simple conceptual explanation for the observed increase in ETR<sub>RCII</sub> under iron limitation. We hypothesize, that iron and light-dependent changes in  $\Phi_{e:C}/n_{PSII}$  are driven by the need to dissipate excess excitation energy, caused by either excess light, or the effects of iron limitation on the ETC. In this context, we discuss the correlation between  $\Phi_{e:C}/n_{PSII}$  and NPQ<sub>NSV</sub>, and examine the potential significance of this finding in the context of marine primary productivity studies.

### 2.5.1 Magnitude of the observed conversion factor

The conversion factor  $\Phi_{e:C}/n_{PSII}$ , derived from our measurements of ETR<sub>RCII</sub> and CO<sub>2</sub>-assimilation, varied significantly in response to light and iron availability. In our field experiment, the addition of iron caused the value of  $\Phi_{e:C}/n_{PSII}$  at light saturation ( $P_{max}$ ) to decrease by 66 % within 6 days (Figure 2.4f). Furthermore, short-term changes in light availability had a major effect on the value of  $\Phi_{e:C}/n_{PSII}$ , and this effect was enhanced under iron limitation. A recent meta-analysis of variability in experimentally determined  $\Phi_{e:C}$  from 14 field studies found values ranging from 1.15 to 54.2 with a mean of  $10.9 \pm 6.91 \text{ mol e}^- \text{ mol C}^{-1}$  (Lawrenz et al., 2013). This analysis comprised a wide range of oceanic regions, but did not include observations from the NE Subarctic Pacific or other HNLC regions. Due to our experimental approach, we are unable to derive absolute values for  $\Phi_{e:C}$ . However, if we assume  $1/n_{PSII}$  to be  $500 \text{ mol chl}a \text{ mol RCII}^{-1}$  (Kolber and Falkowski, 1993), as has been done in most previous studies (Lawrenz et al., 2013),  $\Phi_{e:C}$  values on day 3 of the iron-addition experiment

range from 13 to 39 mol e<sup>-</sup> mol C<sup>-1</sup>. Using a constant value of 1/n<sub>PSII</sub> for both treatments is unlikely to be realistic. Even though iron-limited phytoplankton possess less chl<sub>a</sub> per cell, 1/n<sub>PSII</sub>, the ratio of chl<sub>a</sub> to RCII, has frequently been observed to increase under low iron conditions (Allen et al., 2008; Greene et al., 1991, 1992, 1994; Macey et al., 2014). If we thus assume 700 mol chl<sub>a</sub> mol RCII<sup>-1</sup> for the iron-limited control treatment and 500 mol chl<sub>a</sub> mol RCII<sup>-1</sup> for the iron addition treatment (Greene et al., 1992), Φ<sub>e:C</sub> ranges from 13 to 28 mol e<sup>-</sup> mol C<sup>-1</sup>. These Φ<sub>e:C</sub> values represent the range observed across different irradiance levels in our P<sub>v</sub>sE experiments. At the time of sampling, cells in the on board incubator were exposed to ~ 40 μmol quanta m<sup>-2</sup> s<sup>-1</sup>. Assuming 700 and 500 mol chl<sub>a</sub> mol RCII<sup>-1</sup> for the iron-limited and iron-replete treatments, respectively, we derive Φ<sub>e:C</sub> values of ~18 and ~15 mol e<sup>-</sup> mol C<sup>-1</sup>. Values of Φ<sub>e:C</sub> estimated from our data are thus within the range reported in previous field studies (Lawrenz et al., 2013), with no estimate falling below the theoretical minimum of 4 mol e<sup>-</sup> mol C<sup>-1</sup>.

Ideally, measurements of ETR<sub>RCII</sub> and CO<sub>2</sub>-assimilation should be performed simultaneously on the same sample, eliminating differences in incubation time and spectral quality of the light sources used. As discussed in detail in the supplementary material, the differences in spectral distribution of the light sources used for FRRF and <sup>14</sup>C measurements could have led to an underestimation of absolute values of Φ<sub>e:C</sub>/n<sub>PSII</sub> (

Figure A1 in the appendix). However, these differences cannot explain the large iron dependent changes we observed in Φ<sub>e:C</sub>/n<sub>PSII</sub>, since the absorption spectra of iron-limited and iron-enriched treatments did not differ drastically (

Figure A1 in the appendix). Furthermore, differences in incubation times could have influenced the absolute magnitude of the derived conversion factor. Incubation times used for the P<sub>v</sub>sE curves were ca. 5 minutes for FRRF measurements (applied incrementally to the same sample), vs 3-4 hours in the field and 30 minutes in the laboratory for <sup>14</sup>C-assimilation experiments (light levels applied simultaneously to different samples). As has been shown by Halsey et al. (2010, 2011, 2013) and Pei and Laws (2013), the use of fixed incubation times for cells growing at different growth rates could lead to an overestimation of our conversion factor Φ<sub>e:C</sub>/n<sub>PSII</sub> in the iron-limited relative to iron-replete samples. Additionally, the longer incubation time in CO<sub>2</sub>-assimilation experiments might have exacerbated cumulative processes such as photo-damage under excess irradiance. To address this issue, we did not utilize the part of the P<sub>v</sub>sE curves showing photoinhibition. However, we cannot rule out any differential cumulative

effects of photoinhibition on  $ETR_{RCII}$  and  $^{14}C$ -assimilation at  $P_{max}$ . This could potentially decrease  $CO_2$ -assimilation at  $P_{max}$  relative to  $ETR_{RCII}$  at  $P_{max}$  and lead to overestimation of our  $\Phi_{e:C}/n_{PSII}$  values at  $P_{max}$ . Notwithstanding these potential sources of uncertainty in the absolute value of  $\Phi_{e:C}/n_{PSII}$ , the good agreement between our estimated  $\Phi_{e:C}$  (assuming  $\sim 500 - 700 \text{ mol chl}a \text{ mol RCII}^{-1}$ ) and those of previous studies suggests that our observations are robust. More importantly, potential offsets in the absolute values of  $\Phi_{e:C}/n_{PSII}$  do not diminish the significance of the *relative* iron and light-dependent changes we observed in this parameter (discussed below).

### **2.5.2 Interacting effects of iron and light on the conversion factor $\Phi_{e:C}/n_{PSII}$**

Our data show strong and interacting effects of iron and light availability on the conversion factor  $\Phi_{e:C}/n_{PSII}$  in phytoplankton field assemblages and mono-specific laboratory cultures (Figure 2.4c-f, Figure 2.6, Table 2.1). It has been shown that the magnitude of both  $1/n_{PSII}$  and  $\Phi_{e:C}$  vary significantly between phytoplankton taxa (e.g. Suggett et al., 2004, 2010b). Changes in  $\Phi_{e:C}/n_{PSII}$  in field experiments were thus likely influenced by both physiological changes and taxonomic shifts. These two sources of variability are, to a large extent, intrinsically linked, since changes in phytoplankton community composition (Figure A2 in the appendix) reflect the selection of better adapted species under any particular set of environmental conditions (i.e. iron limitation). In the following, we discuss the observed changes in  $\Phi_{e:C}/n_{PSII}$  from a predominantly photo-physiological point of view, since our laboratory results specifically demonstrate such physiological effects.

Numerous metabolic processes, acting between  $ETR_{RCII}$  and  $CO_2$ -assimilation can act to increase  $\Phi_{e:C}$ , and therefore the conversion factor  $\Phi_{e:C}/n_{PSII}$  (e.g. Cardol et al., 2011; Peltier et al., 2010; Rochaix, 2011). In addition to its role in reducing  $CO_2$  to organic carbon products, reductant (NADPH) formed at the end of the ETC can also be used for nitrate and sulphate reduction (Laws, 1991), photorespiration (Beardall, 1989), or respiration via the malate shunt (Scheibe, 2004). These alternative pathways decouple  $ETR_{RCII}$  from  $CO_2$ -assimilation, increasing the value of  $\Phi_{e:C}$ . Similarly, before the formation of NADPH, pseudo-cyclic electron flow can reduce  $O_2$  and create a water-water cycle of electron transport, also increasing  $\Phi_{e:C}$  (e.g. Niyogi, 2000). Pseudo-cyclic electron transport pathways can divert electrons from the ETC before (short water-water cycling, e.g. (Nawrocki et al., 2015)) or after PSI (Mehler-reaction, e.g.

Miyake and Asada, 2003). Cyclic electron transport (CET) around PSII (Falkowski et al., 1986b; Prasil et al., 1996) and charge recombination in PSII (Ivanov et al., 2008; Vass, 2011), act more closely to the initial charge separation in RCII, and can also cause an increase in  $\Phi_{e:C}$ .

We suggest that the higher  $\Phi_{e:C}/n_{PSII}$  observed in response to iron limitation and short-term increases in incident irradiance during the PvsE experiments (Figure 2.6a-e) results predominantly from increases in the alternative electron flow pathways prior to reductant formation. These pathways, which are diagramed conceptually in Figure 2.8, can act as ‘safety valves’ to keep the primary quinone acceptor  $Q_A$  oxidized when excitation energy on the ETC is high, thereby decreasing the potential of damage to RCII (Krause and Jahns, 2003; Bailey et al., 2008; Cardol et al., 2008, 2011; Mackey et al., 2008; Niyogi, 2000; Ort and Baker, 2002; McDonald et al., 2011).

Iron limitation directly affects the photosynthetic ETC and thereby modulates the light-dependent changes in the conversion factor  $\Phi_{e:C}/n_{PSII}$  (Figure 2.6a-e). Importantly, iron limitation has been shown to alter the stoichiometry of ETC components (i.e. expression of iron-rich PSI and cytochrome *b<sub>6</sub>f* complexes is down-regulated to a higher extent than PSII) (e.g. Behrenfeld and Milligan, 2013; Fraser et al., 2013; Greene et al., 1991; Schrader et al., 2011; Strzepek and Harrison, 2004). Low levels of electron acceptors downstream of PSII ultimately restrict the flow of electrons away from PSII during light exposure. This exacerbates the need for short (i.e. acting before PSI) alternative electron flow pathways to dissipate excess excitation energy and prevent over-reduction of RCII (Figure 2.8). A number of recent studies have suggested that re-routing electrons to a midstream plastoquinol oxidase (PTOX) to bypass the electron flow bottleneck of PSI is a common strategy in open ocean phytoplankton (Behrenfeld et al., 2008; Cardol et al., 2008; Bailey et al., 2008; Mackey et al., 2008; Zehr and Kudela, 2009; Grossman et al., 2010; Behrenfeld and Milligan, 2013). Importantly, up-regulation of pseudo-cyclic electron flow under iron limitation not only protects RCII from photo-damage, but also helps to maintain a high  $\Delta pH$  across the thylakoid membrane, providing energy for cell maintenance and growth (Behrenfeld and Milligan, 2013; Laureau et al., 2013). Cyclic electron flow around PSII (Falkowski et al., 1986b; Prasil et al., 1996; Feikema et al., 2006; Cardol et al., 2011; Shinopoulos and Brudvig, 2012) and increases in charge recombination at PSII (Ivanov et al., 2008; Vass, 2011; Vass and Cser, 2009) are two additional mechanisms that can act to prevent over-reduction and damage of RCII when excitation energy is high and the electron flow

bottleneck is prior to PSI. Unlike PTOX-mediated water-water cycling, these processes do not contribute to an increase in  $\Delta\text{pH}$  across the thylakoid membrane. They would, however, contribute to a high  $\text{ETR}_{\text{RCII}}$  and therefore  $\Phi_{\text{e:C/nPSII}}$  (Figure 2.8).

While ambient light intensity has a well-documented effect on values of  $1/n_{\text{PSII}}$ , these changes act on timescales longer than those of short-term PvsE experiments, and are thus unlikely to have caused the light-dependent changes we observed in  $\Phi_{\text{e:C/nPSII}}$  (Figure 2.6). On longer time-scales, however, iron limitation causes a reduction of *chl a* per cell (chlorosis), and an increase in *chl a* per functional RCII ( $1/n_{\text{PSII}}$ ) (Macey et al., 2014; Vassiliev et al., 1995). This well documented response, which has been attributed to preferential down-regulation of RCII (Vassiliev et al., 1995), and up-regulation of iron-stress-induced light harvesting complexes (Behrenfeld and Milligan, 2013; Macey et al., 2014), would act to further increase  $\Phi_{\text{e:C/nPSII}}$  under iron limitation, regardless of light intensity (Figure 2.6a-e).

In summary, we suggest that high excitation energy causes a de-coupling of  $\text{ETR}_{\text{RCII}}$  and  $\text{CO}_2$ -assimilation. This high excitation energy may be a result of short-term exposure to excess irradiance as well as the effect of iron limitation on the ETC. This purely photo-physiological interpretation can be extended to observations made in mixed phytoplankton communities. Here, fluctuating light and low iron conditions will select for species with the best ability to control high excitation energy by adjusting the flow of excitation energy into, and the flow of electrons out of PSII (i.e. diatoms).

### ***2.5.3 Iron limitation increases $\text{ETR}_{\text{RCII}}$***

To our knowledge, this is the first study which shows that  $\text{ETR}_{\text{RCII}}$  decreases after iron addition. This observation may seem counter-intuitive, and it is important to emphasize that our results do not imply an overall increase in photosynthetic electron transport under low iron conditions. Rather, our observations point to an increase in the rate of charge separation at each individual RCII, independent of the reduced total cellular concentration of these RCII. We show that the overall efficiency of PSII photochemistry in the light-regulated state,  $F_q'/F_m'$  ( $= \Phi_{\text{PSII}'}$ ), is reduced under iron limitation (Figure 2.5c), as expected. However, deconvolution of this parameter into its constituents  $F_q'/F_v'$  (Figure 2.5a) and  $F_v'/F_m'$  (Figure 2.5b) shows that  $F_q'/F_v'$ , representing the fraction of open RCII ( $Q_A$  oxidized) at each given light level, increased under iron limitation. We hypothesize that this is likely achieved by increased alternative electron

transport pathways acting to keep RCII open ( $Q_A$  oxidized) and bypassing the electron flow bottleneck at PSI, when excitation energy is high (Figure 2.8). In contrast to  $F_q'/F_v'$ , the parameter  $F_v'/F_m'$  is much lower when iron is limiting (Figure 2.5b), indicating that the excitation energy transfer in the antennae is compromised.

Based on our experimental observations, we suggest a simple mechanistic explanation for the observed increase in  $ETR_{RCII}$  under iron limitation. Cellular iron demand can be significantly decreased by economizing on iron-rich components of the photosynthetic apparatus and ‘funneling’ more electrons down fewer RCII (i.e. increasing  $ETR_{RCII}$ ). In line with this explanation is the observation that values of  $\sigma_{PSII}$  are high under iron limitation, and rapidly decrease after iron addition (Figure 2.2) (Babin et al., 1996; Boyd and Abraham, 2001; Greene et al., 1991, 1992; Hopkinson et al., 2007; Kolber et al., 1994; Petrou et al., 2011; Timmermans et al., 2001; Vassiliev et al., 1995). Strzepek et al. (2011) suggested that increased  $\sigma_{PSII}$  compensates for fewer iron-rich photosynthetic reaction centers in Southern Ocean phytoplankton species. Similarly, Ryan-Keogh et al. (2012) noted that increasing the absorption cross section of RCs by the expression of iron stress induced light harvesting complexes allows cells to reduce the cellular iron requirement while maintaining the same light absorption capacity.

In conclusion, our results and interpretation support a scenario where photosynthetic electron flow has been fine-tuned to maximize energy conversion as well as photo-protection under conditions where ETC component abundance and stoichiometry are compromised by the availability of iron.

#### ***2.5.4 Link to NPQ<sub>NSV</sub>***

Above, we discussed how mechanisms acting downstream of the initial charge separation in RCII are likely to be enhanced under conditions of excess excitation energy, resulting in high  $ETR_{RCII}$  and  $\Phi_{e.c}/n_{PSII}$ . Excess excitation energy can also be dissipated in the pigment antenna, before reaching RCII (Niyogi, 2000). Figure 2.8 shows schematically the ‘safety mechanisms’ used for the dissipation of excess energy at both sides of RCII. Because processes dissipating excess excitation energy in the antenna also quench ChlF yields measured by FRRF, they have collectively been called non-photochemical quenching (NPQ). NPQ, which is present in all oxygenic photosynthetic organisms, encompasses a wide variety of mechanisms acting to

dissipate absorbed light energy as heat before it reaches RCII (Goss and Lepetit; Horton, 2012; Niyogi and Truong, 2013; Ruban et al., 2012; Ruban, 2014; Zaks et al., 2013). Following the approach of McKew et al. (2013), we estimated NPQ from FRRF measurements as so-called normalized Stern-Volmer quenching ( $NPQ_{NSV}$ ). We observed a strong correlation between the conversion factor  $\Phi_{e:C/n_{PSII}}$  and the expression of  $NPQ_{NSV}$  (Figure 2.7). We note that  $\Phi_{e:C/n_{PSII}}$  and  $NPQ_{NSV}$  are not entirely independent parameters, and therefore the strong correlation observed in Figure 2.7 is in part a result of their co-dependence on the ChlF parameter  $F_v'$  (which we used in the derivation of both  $NPQ_{NSV}$  and  $\Phi_{e:C/n_{PSII}}$ ).

At this point, the relationship between  $\Phi_{e:C/n_{PSII}}$  and  $NPQ_{NSV}$  shown in Figure 2.7 is empirical rather than mechanistic. However, while there are a number of processes which will influence  $\Phi_{e:C/n_{PSII}}$  and  $NPQ_{NSV}$  differentially, there are many processes related to the amount of excitation energy experienced by the ETC that would influence both in a consistent manner. Numerous studies have shown that  $\Phi_{e:C}$  increases if light is saturating, i.e. when excitation energy is high (e.g. Corno et al., 2006; Fujiki et al., 2007; Kaiblinger and Dokulil, 2006)). Clearly, excess light would also increase the expression of  $NPQ_{NSV}$ . Indeed, very recent work has pointed to a mechanistic link between alternative electron sinks involving PTOX and the expression of  $NPQ_{NSV}$  (Nawrocki et al., 2015).

### **2.5.5 A possible approach towards improved prediction of CO<sub>2</sub>-assimilation from FRRF data**

While it remains to be seen how strong the correlation between  $\Phi_{e:C/n_{PSII}}$  and  $NPQ_{NSV}$  (Figure 2.7) may be for other datasets, our results provide a potential basis for improved estimates of CO<sub>2</sub>-assimilation from FRRF measurements alone. A number of factors make this approach more desirable than the use of static, regional conversion factors. First, the magnitude of  $\Phi_{e:C/n_{PSII}}$  in phytoplankton assemblages will be determined by a multitude of interacting environmental variables. The use of  $NPQ_{NSV}$  as an integrated physiological measure of environmental effects on electron transport processes will therefore help to constrain the relationship between  $\Phi_{e:C/n_{PSII}}$  and various environmental stressors. Secondly, as our data show, the magnitude of  $\Phi_{e:C/n_{PSII}}$  can vary significantly within the same sample in response to short-term variations in incident light. Such small scale changes would be lost using a static (regional) conversion factor, but are captured with our  $NPQ_{NSV}$ -based approach, as every single  $ETR_{RCII}$

estimate is paired with a corresponding  $\text{NPQ}_{\text{NSV}}$  estimate. Finally, a non-static conversion factor is crucial if the goal is to monitor the effects of environmental change on marine primary productivity, since physiological responses to environmental change will likely affect the conversion factor itself before productivity changes are observed.

As a test of the validity of our approach, we used the  $\Phi_{e,C}/n_{\text{PSII}}$  vs.  $\text{NPQ}_{\text{NSV}}$  correlation determined from our iron addition experiment (Figure 2.7) to predict the  $\text{CO}_2$ -assimilation rates from FRRF-derived  $\text{ETR}_{\text{RCII}}$  and  $\text{NPQ}_{\text{NSV}}$  measured along the Line-P transect. In this case, *in situ* phytoplankton assemblages were collected from within and below the mixed layer, and rate measurements were conducted immediately after collection, without any experimental manipulation (see methods). As shown in Figure 2.9, we obtained a strong correlation between the predicted and measured  $\text{CO}_2$ -assimilation rates (Spearman's  $r = 0.90$ ,  $n = 95$  and two-tailed  $p < 0.0001$  on non-log-transformed data). Our approach consistently underestimates values from the deepest sampling depth, which can likely be attributed to the lack of spectral correction of our data. The RMSE for the values predicted using our approach and measured values is  $48.4 \text{ mol C mol chl}a^{-1} \text{ hr}^{-1}$ . This error represents  $\sim 10\%$  of the total range of values observed along the transect during this study, suggesting that rates of productivity can be predicted with reasonable accuracy. In comparison with our approach, computation of  $\text{CO}_2$ -assimilation from FRRF data assuming a constant  $1/n_{\text{PSII}}$  value of  $500 \text{ mol chl}a \text{ mol RCII}^{-1}$  and  $4 \text{ mol e}^- \text{ mol C}^{-1}$ , significantly under-predicts observed  $\text{CO}_2$ -assimilation rates (RMSE =  $837.3 \text{ mol C mol chl}a^{-1} \text{ hr}^{-1}$ ). Even if we use a constant conversion factor derived from the average of the  $\Phi_{e,C}/n_{\text{PSII}}$  measured during our iron addition experiment, the model error remains larger than that derived using our variable,  $\text{NPQ}_{\text{NSV}}$ -based conversion factor (Figure 2.7). Our data therefore show significant potential in the application of a variable,  $\text{NPQ}_{\text{NSV}}$ -derived conversion factor and associated quantification of carbon uptake rates from FRRF data.

## 2.6 Conclusions

Deriving rates of phytoplankton  $\text{CO}_2$ -assimilation from bio-optical approaches like FRRF has the potential to provide estimates of primary production at unprecedented spatial and temporal resolution. High resolution measurements, covering large oceanic regions, are essential for the monitoring and modelling of marine food webs and global biogeochemical cycles.

Furthermore, such measurements are indispensable for the development and validation of algorithms estimating global marine primary productivity from remote sensing.

Crucial to this approach is a sound characterization of the conversion factor between FRRF-derived  $ETR_{RCII}$  and primary productivity in carbon units. Our data demonstrate that the conversion factor varies significantly in response to iron and light availability in phytoplankton field assemblages and mono-specific laboratory cultures. We interpret the observed variability in the conversion factor  $\Phi_{e:C}/n_{PSII}$  as a manifestation of the extreme photo-physiological flexibility which evolved in phytoplankton to maximize growth under dynamic light and nutrient regimes (Laney, 2006; Mackey, 2010). We hypothesize that, to a large extent, changes in  $\Phi_{e:C}/n_{PSII}$  represent a suite of coordinated photo-physiological adjustments acting to balance light absorption with  $CO_2$ -assimilation under given environmental conditions. These will be manifested on the physiological as well as on the taxonomic level. On the taxonomic level, a low nutrient and / or fluctuating light environment will select for species with the best ability to control high excitation energy by adjusting the flow of excitation energy into, and the flow of electrons out of PSII (manifested in changes of  $NPQ_{NSV}$ ,  $1/n_{PSII}$  and  $\Phi_{e:C}$ ). Future studies will be needed to evaluate the relationship between  $NPQ_{NSV}$  and  $\Phi_{e:C}/n_{PSII}$  in a number of oceanic regions in order to evaluate the potential for improved  $CO_2$ -assimilation estimates from FRRF data.

## 2.7 Tables and figures

**Table 2.1: Effect of iron limitation on photo-physiology in two mono-specific phytoplankton cultures grown in the laboratory.** *Thalassiosira oceanica* (diatom) and *Chrysochromulina polylepis* (prymnesiophyte) were grown in steady state iron-replete and iron-limited conditions. The mean growth rate  $\mu$ , derived from successive measurements in semi-continuous batch cultures, is given in  $d^{-1}$ . The error is the SD of 3 biological replicates, and number of consecutive batch transfers (ca. 4 cell divisions per transfer) used to calculate growth rates are given in brackets.  $F_v/F_m$  and  $\sigma_{PSII}$  are values from cultures in the dark regulated state (10 minutes of  $5 \mu\text{mol quanta m}^{-2} \text{s}^{-1}$  at 730 nm), measured on the day of  $\text{CO}_2$ -assimilation experiments. The error is SD of 3 biological replicates. Changes in these parameters are statistically significant for *T. oceanica* ( $p < 0.0001$ ) and *C. polylepis* ( $p < 0.01$ ).  $P_{\text{max}}$  for  $\text{CO}_2$ -assimilation ( $\text{mol C mol chl}a^{-1} \text{s}^{-1}$ ) and  $\text{ETR}_{\text{RCII}}$  ( $\text{mol e}^- \text{mol RCII}^{-1} \text{s}^{-1}$ ) were derived from  $P_{\text{vsE}}$  curves as described in the methods section. The error is the 95 % confidence interval of the  $P_{\text{max}}$  derived from the fit to data from 6 whole curve measurements (duplicate curves each from 3 biological replicates). The conversion factor  $\Phi_{e:C}/n_{\text{PSII}}$  for  $P_{\text{max}}$  was derived as the quotient of  $P_{\text{max}}$  for  $\text{ETR}_{\text{RCII}}$  and  $P_{\text{max}}$  for  $\text{CO}_2$ -assimilation. The error is the propagated error from numerator and denominator.  $\text{NPQ}_{\text{NSV}}$  was estimated as  $F_o'/F_v'$  from the last ST acquisition during each light level of the  $P_{\text{vsE}}$  curves. The values shown are from the first and last step of the  $P_{\text{vsE}}$  curves (4 and  $800 \mu\text{mol quanta m}^{-2} \text{s}^{-1}$ ). Each  $\text{NPQ}_{\text{NSV}}$  value is the mean of 2 values measured on 3 biological replicates. Changes in response to iron limitation are statistically significant for both species ( $p < 0.0001$ ).

|   | <i>T. oceanica</i>        |                       | <i>C. polylepis</i>      |                       |
|---|---------------------------|-----------------------|--------------------------|-----------------------|
| [Fe]  | 42 nM                     | 0.13 nM               | 42 nM                    | 1.28 nM               |
| $\mu$ ( $d^{-1}$ )                              | $1.27 \pm 0.14$ (n=6) *** | $0.41 \pm 0.09$ (n=5) | $0.53 \pm 0.12$ (n=5) ** | $0.27 \pm 0.05$ (n=4) |
| $F_v/F_m$                                       | $0.63 \pm 0.01$ ***       | $0.43 \pm 0.01$       | $0.51 \pm 0.02$ **       | $0.41 \pm 0.03$       |
| $\sigma_{\text{PSII}}$                          | $643 \pm 3$               | $742 \pm 16$          | $591 \pm 7$              | $621 \pm 3$           |
| $P_{\text{max}}$ $\text{CO}_2$ -assimilation    | $0.030 \pm 0.004$         | $0.035 \pm 0.005$     | $0.032 \pm 0.009$        | $0.028 \pm 0.009$     |
| $P_{\text{max}}$ $\text{ETR}_{\text{PSII}}$     | $174 \pm 9$ *             | $330 \pm 21$          | $370 \pm 26$ *           | $506 \pm 65$          |
| $P_{\text{max}}$ $\Phi_{e:C} / n_{\text{PSII}}$ | $5874 \pm 648$ *          | $9225 \pm 1502$       | $11691 \pm 3730$         | $18145 \pm 6091$      |
| $\text{NPQ}_{\text{NSV}}$                       | $0.37 - 0.47$ ***         | $0.58 - 0.75$         | $0.5 - 0.59$ ***         | $0.72 - 0.79$         |

\*  $p < 0.05$ ; \*\*  $p < 0.01$ ; \*\*\*  $p < 0.0001$

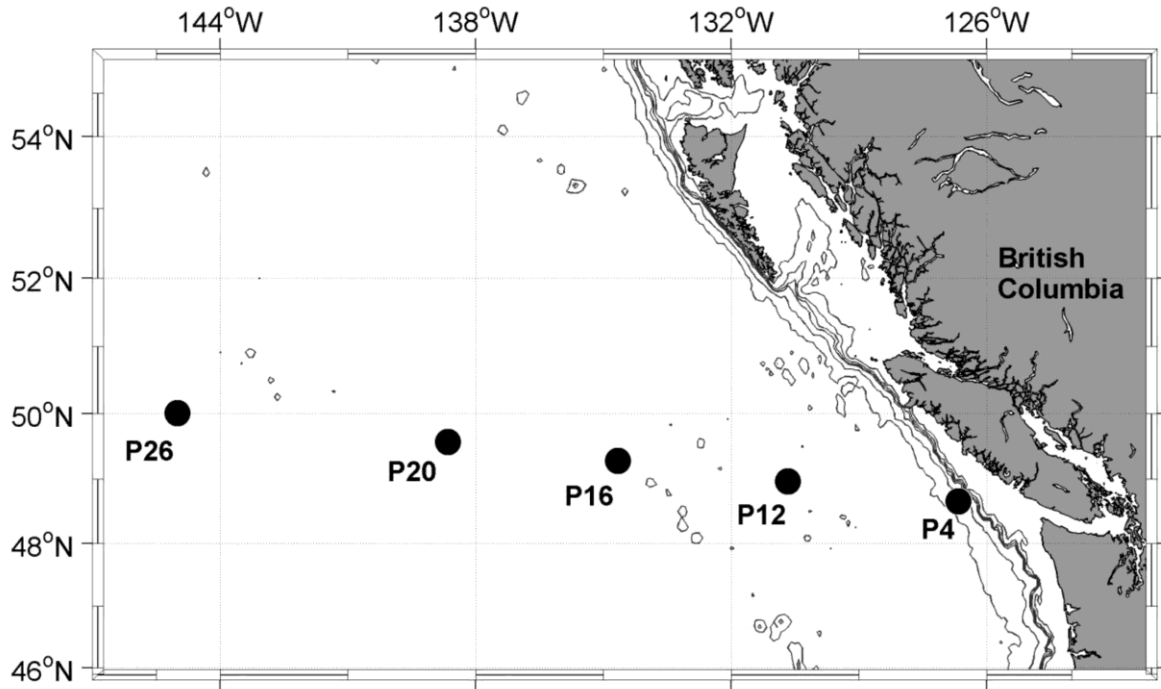


**Figure 2.1: Map of sampling stations along the Line-P transect in the NE Subarctic Pacific.** The iron addition experiment was initiated at station P20, located in iron-limited high nutrient low chlorophyll (HNLC) waters. Sampling depths at other stations along the transect were: 30 m at P4; 5 m, 25 m and 40 m at P12, P16, P20 and P26.

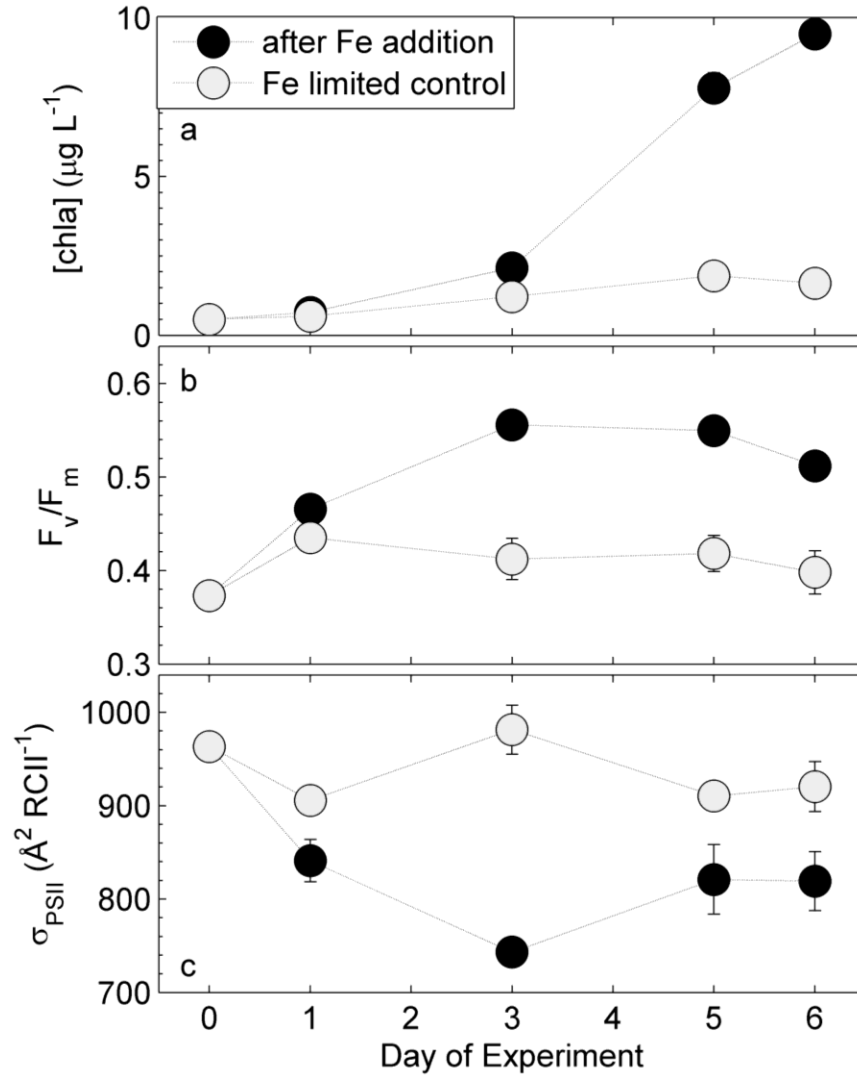


**Figure 2.2: Response of *chl a* biomass and photo-physiology during the on-board iron addition experiment.** The experiment was conducted with a phytoplankton assemblage sampled at station P20. Shown are changes in (a) [*chl a*], (b)  $F_v/F_m$ , and (c)  $\sigma_{PSII}$ . Error bars represent standard errors from three biological replicates and are sometimes smaller than the symbol.

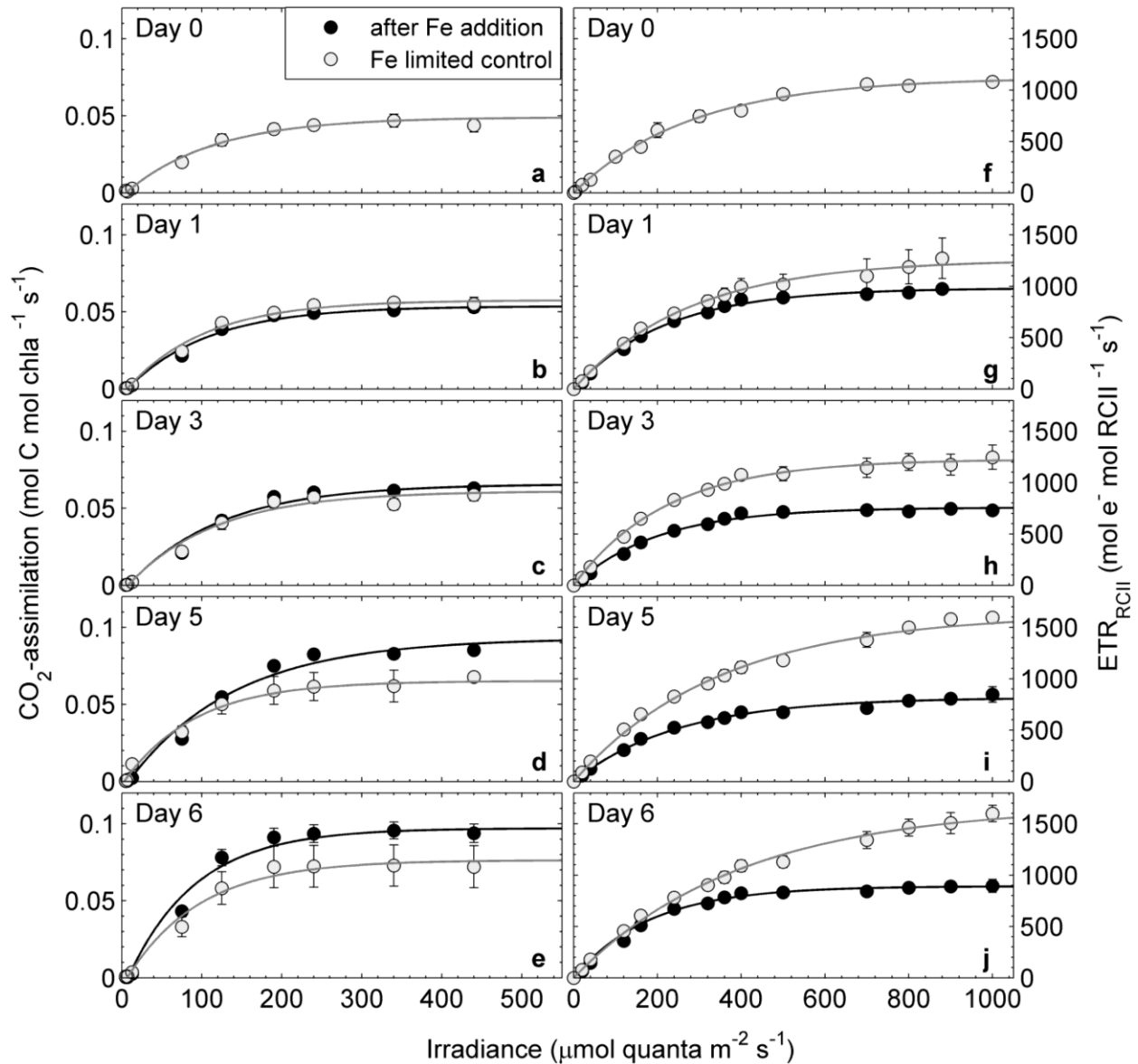


**Figure 2.3: Response of rates of  $\text{CO}_2$ -assimilation ( $\text{mol C mol chl a}^{-1} \text{s}^{-1}$ ) and  $\text{ETR}_{\text{RCII}}$  ( $\text{mol e}^{-} \text{mol RCII}^{-1} \text{s}^{-1}$ ) during the iron addition experiment at station P20.** Both rates were measured as a function of irradiance, and PvsE curves were fit with the exponential model of Webb et al. (1974). Shown are mean values from three biological replicates where error bars represent standard error of mean and are sometimes smaller than symbols.

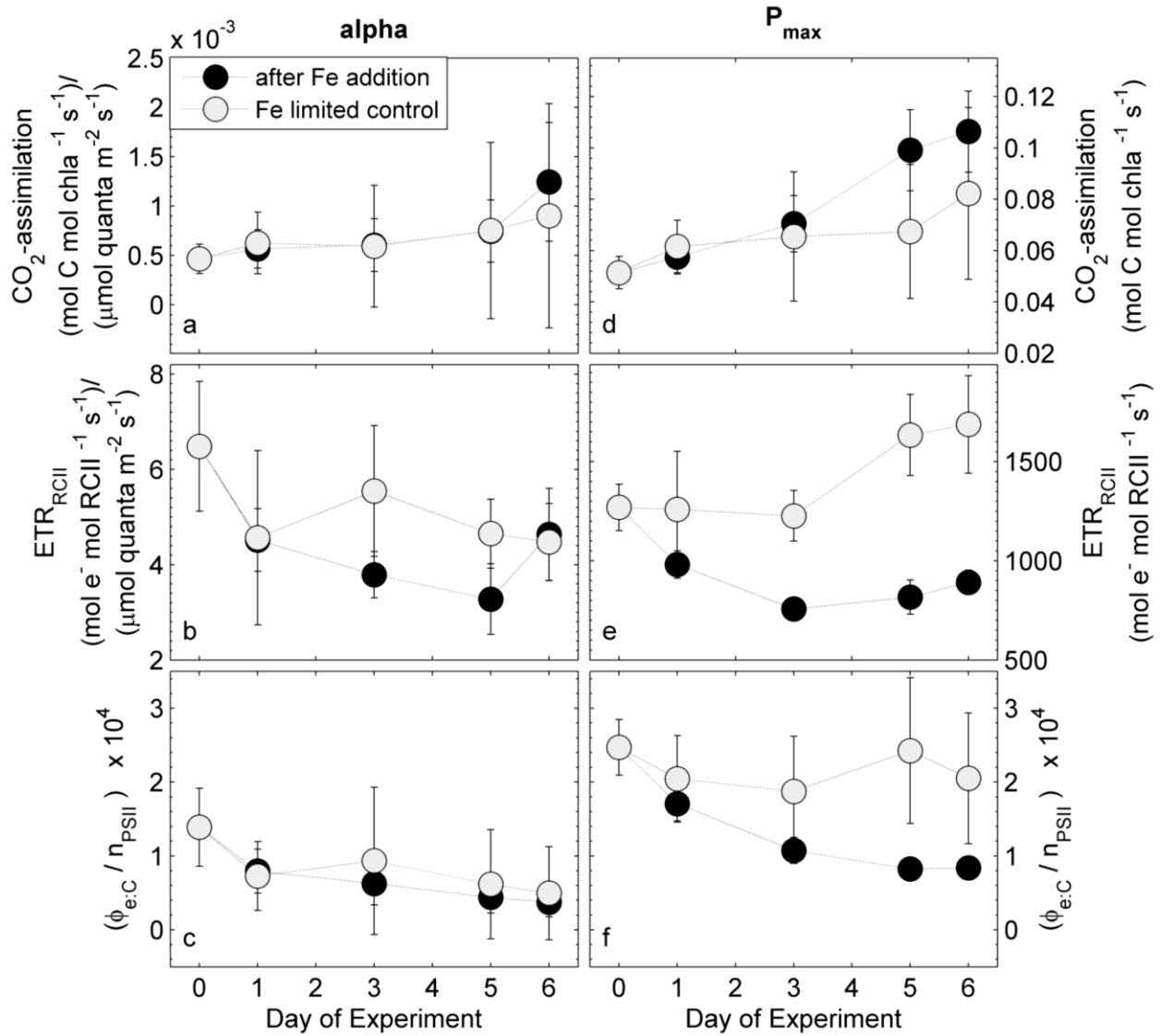


**Figure 2.4: Time-course of  $\alpha$  (a-c) and  $P_{\max}$  (d-f) of  $\text{CO}_2$ -assimilation,  $\text{ETR}_{\text{RCII}}$  and the derived conversion factor  $\Phi_{e:C}/n_{\text{PSII}}$  during the iron addition experiment at station P20.** The conversion factor  $\Phi_{e:C}/n_{\text{PSII}}$  under light limiting conditions is derived from values in (a) and (b). Similarly, the conversion factor  $\Phi_{e:C}/n_{\text{PSII}}$  at light saturation is derived from the values in (d) and (e). The error in (a), (b), (c), and (d) is the 95 % confidence interval of the parameter derived from the fit to data from three biological replicates, and the error in (c) and (f) is the propagated error from (a)/(b) and (d)/(e), respectively.

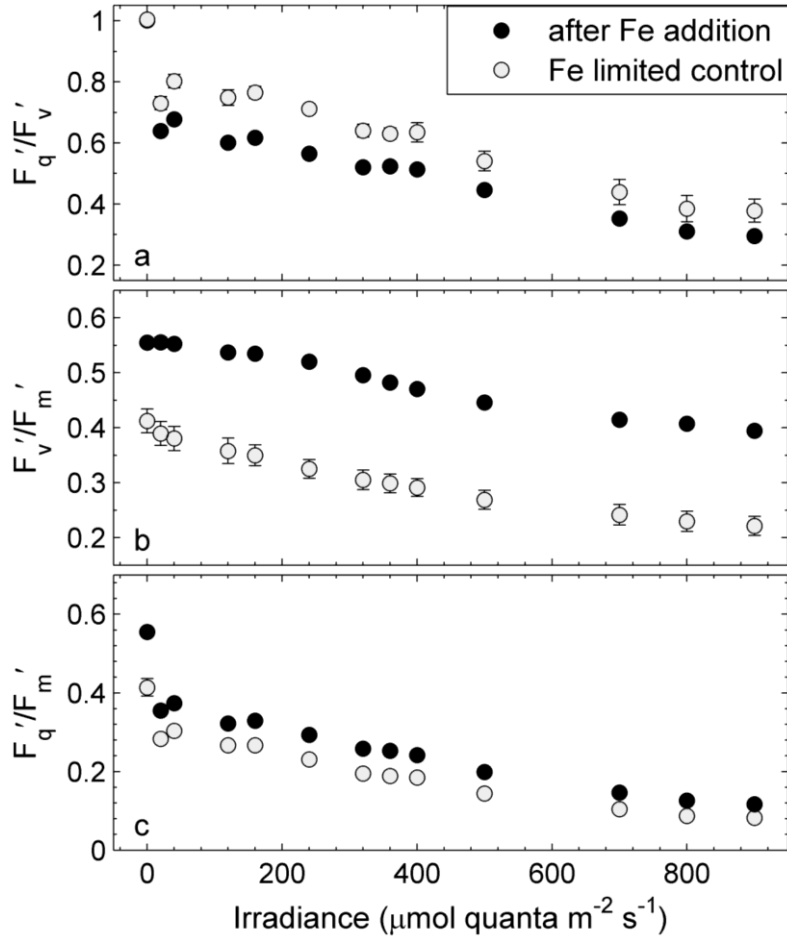


**Figure 2.5: Light dependency of ChlF-derived parameters from FRRF measurements on day three after iron addition and in the iron-limited control treatment.** The parameter  $F'_q/F'_v$  (a) represents the efficiency of charge separation in functional RCII and is an estimate of the fraction of open RCII (i.e.  $Q_A$  oxidized) at any given light level. The parameter  $F'_v/F'_m$  (b) represents the efficiency of excitation energy capture by the fraction of open RCII and can be used to quantify the extent to which non-photochemical quenching in the PSII antenna competes with photochemistry for excitation energy. The parameter  $F'_q/F'_m$  (c) represents the overall quantum efficiency of photochemical energy conversion in PSII ( $\Phi'_{PSII}$ ). See text for a full description of these parameters and their interpretation. Error bars represent standard errors from three biological replicates and are often smaller than symbols.

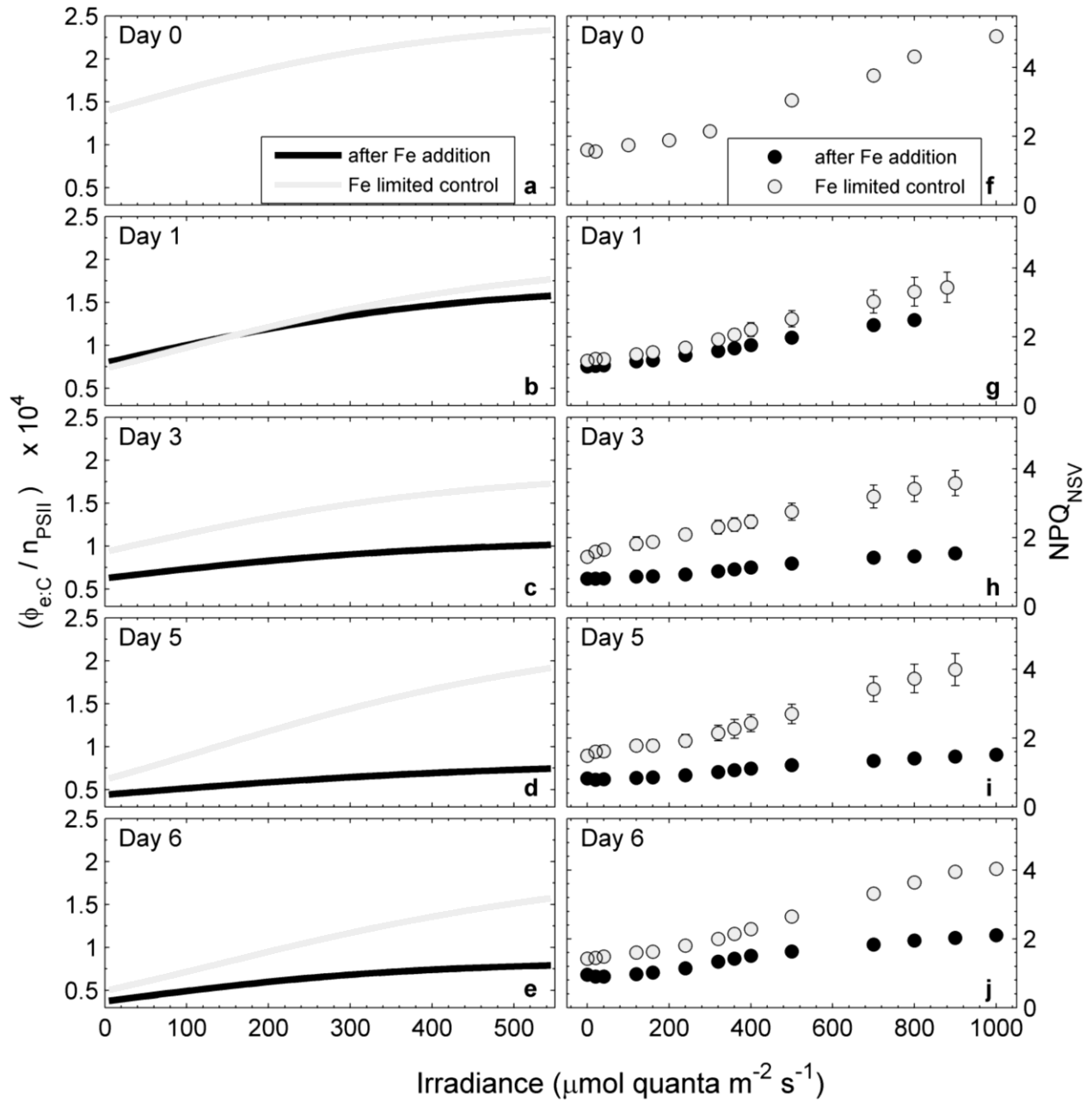


**Figure 2.6. Changes in the light dependency of the conversion factor  $\Phi_{e,C}/n_{PSII}$  (a-e) and  $NPQ_{NSV}$  (f-j) over the course of the iron addition experiment.** Units of  $\Phi_{e,C}/n_{PSII}$  are  $(\text{mol e}^- \text{mol C}) / (\text{mol chl}a \text{mol RCII}^{-1})$ . The curves were derived by dividing corresponding values of  $ETR_{RCII}$  and  $\text{CO}_2$ -assimilation from the PvsE curves presented in Figure 2.3.  $NPQ$  was estimated as the normalized Stern-Volmer quenching coefficient  $NPQ_{NSV} = F_0'/F_v'$  and is unitless. Error bars are the standard error from three biological replicates and often smaller than symbols.

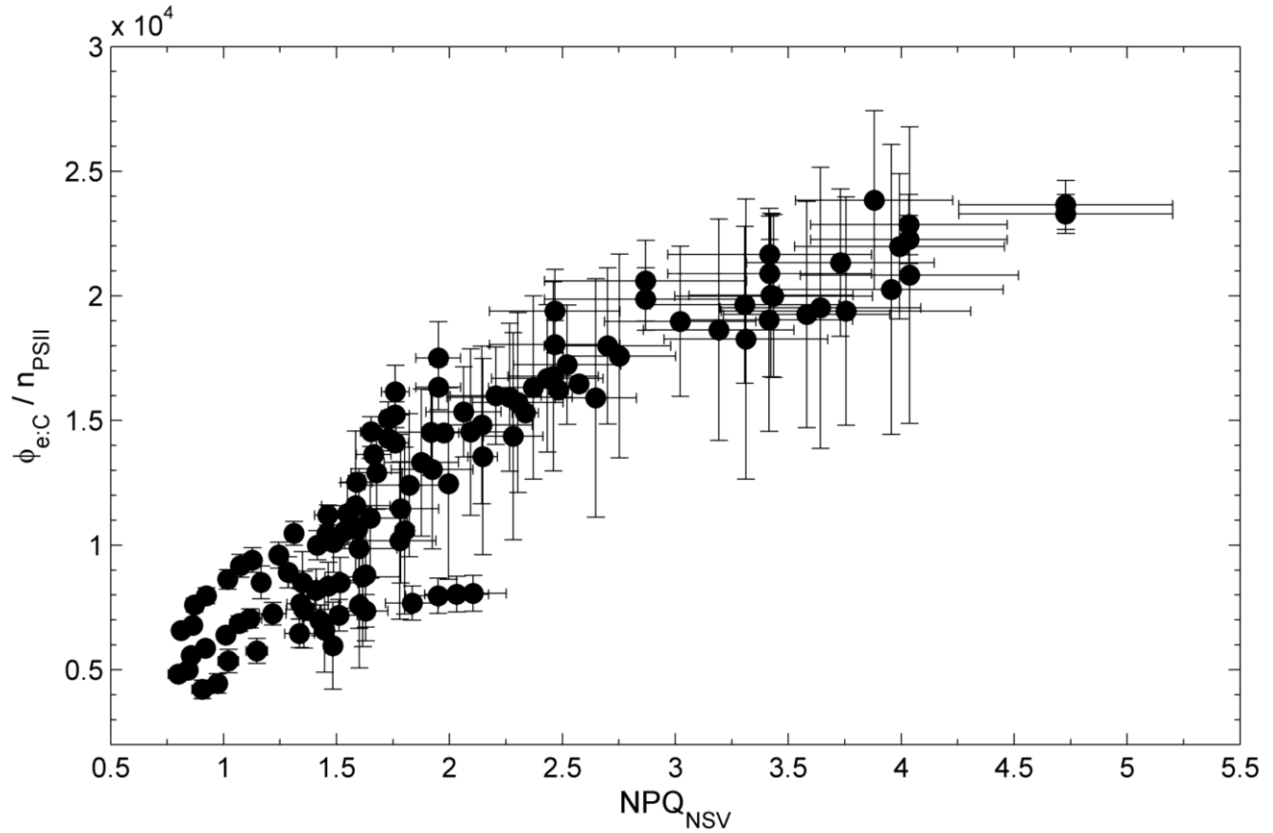


**Figure 2.7: Relationship between the conversion factor  $\Phi_{e:C}/n_{PSII}$  and  $NPQ_{NSV}$  values during the iron addition experiment.** Values of  $\Phi_{e:C}/n_{PSII}$  were derived from PvsE curves of  $CO_2$ -assimilation and  $ETR_{RCII}$  at irradiances corresponding to each  $ETR_{RCII}$ -PvsE curve light level. Units of  $\Phi_{e:C}/n_{PSII}$  are  $(\text{mol } e^- \text{ mol } C^{-1}) / (\text{mol } chl a \text{ mol } RCII^{-1})$ .  $NPQ_{NSV}$  values were derived as  $F_o'/F_v'$  for each light level of the SSLC. Data points represent means and standard errors for parameters derived from three biological replicates. A quadratic fit through all data points ( $\Phi_{e:C}/n_{PSII} = -733.21 NPQ^2 + 8792.4 NPQ - 1477.1$ ) is statistically significant ( $R^2 = 0.70$ ,  $p < 0.0001$ ).

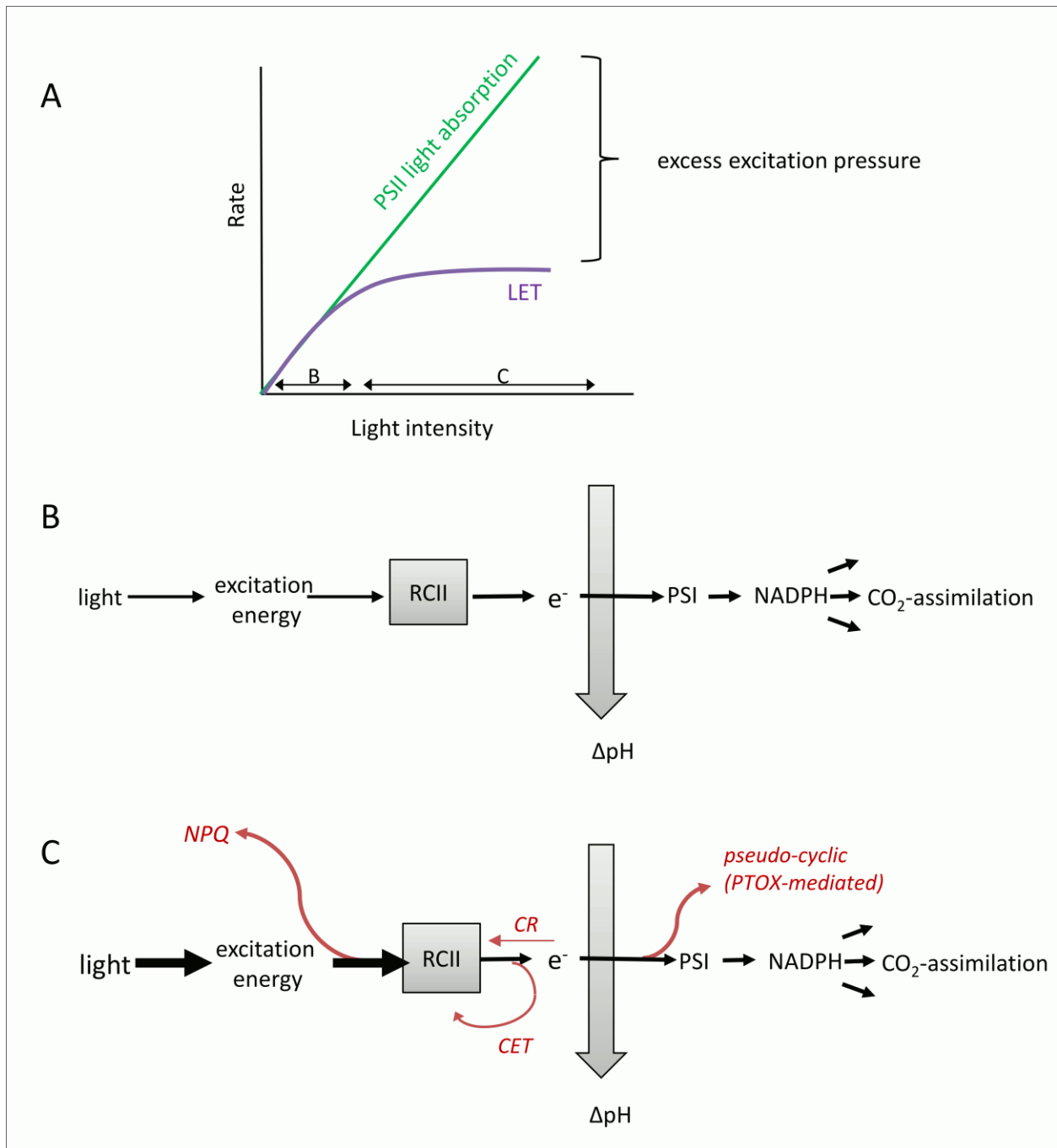


**Figure 2.8: Conceptual diagram visualizing the concept of excess excitation energy and its dissipation before and after charge separation in RCII.** (A) Absorption of light energy by pigments in the light harvesting antenna of PSII cannot be controlled biologically, and rises linearly with incident light intensity. However, rates of linear electron transport (LET) and CO<sub>2</sub>-assimilation saturate at a light intensity determined by the physiological state of the phytoplankton, resulting in a typical PvsE curve. Under optimal growth conditions, it is the resupply of NADP<sup>+</sup> (predominantly from CO<sub>2</sub>-assimilation) which limits LET, while under short-term exposure to excess light and under iron limitation, the ‘bottleneck’ of LET will be located before PSI. Whenever excitonic influx exceeds the

chemical outflux at the level of RCII, excess excitation energy needs to be safely dissipated to prevent photo-damage. (B) Under optimal growth conditions and sub-saturating light, all absorbed photons are used for charge separation in RCII, and the majority of electrons will be used for LET and CO<sub>2</sub>-assimilation, resulting in minimum  $\Phi_{e,C}$ . (C) Conditions of high excitation energy can be caused by short-term exposure to high light, but also by iron limitation, which compromises the functioning of the ETC and has been shown to create a ‘bottle neck’ for LET before PSI. Under these conditions, PTOX-mediated pseudo-cyclic electron flow (e.g. Bailey et al., 2008; Behrenfeld and Milligan, 2013; Behrenfeld et al., 2008; Cardol et al., 2008; Grossman et al., 2010; Mackey et al., 2008; Nawrocki et al., 2015; Zehr and Kudela, 2009), cyclic electron transport around PSII (e.g. Falkowski et al., 1986b; Feikema et al., 2006; Prasil et al., 1996), and charge recombination in RCII (e.g. Ivanov et al., 2008; Vass, 2011; Vass and Cser, 2009), have been suggested to safely dissipate excess excitation energy after RCII (but before PSI). Up-regulation of these alternative electron flow pathways could explain the high  $ETR_{RCII}$  (and  $\Phi_{e,C}/n_{PSII}$ ) observed in our iron-limited samples. Excess excitation energy can also be dissipated in the light harvesting antenna, before charge separation in RCII. Collectively, a number of different molecular processes dissipating excess excitation energy in the PSII antenna can be quantified as  $NPQ_{NSV}$ .

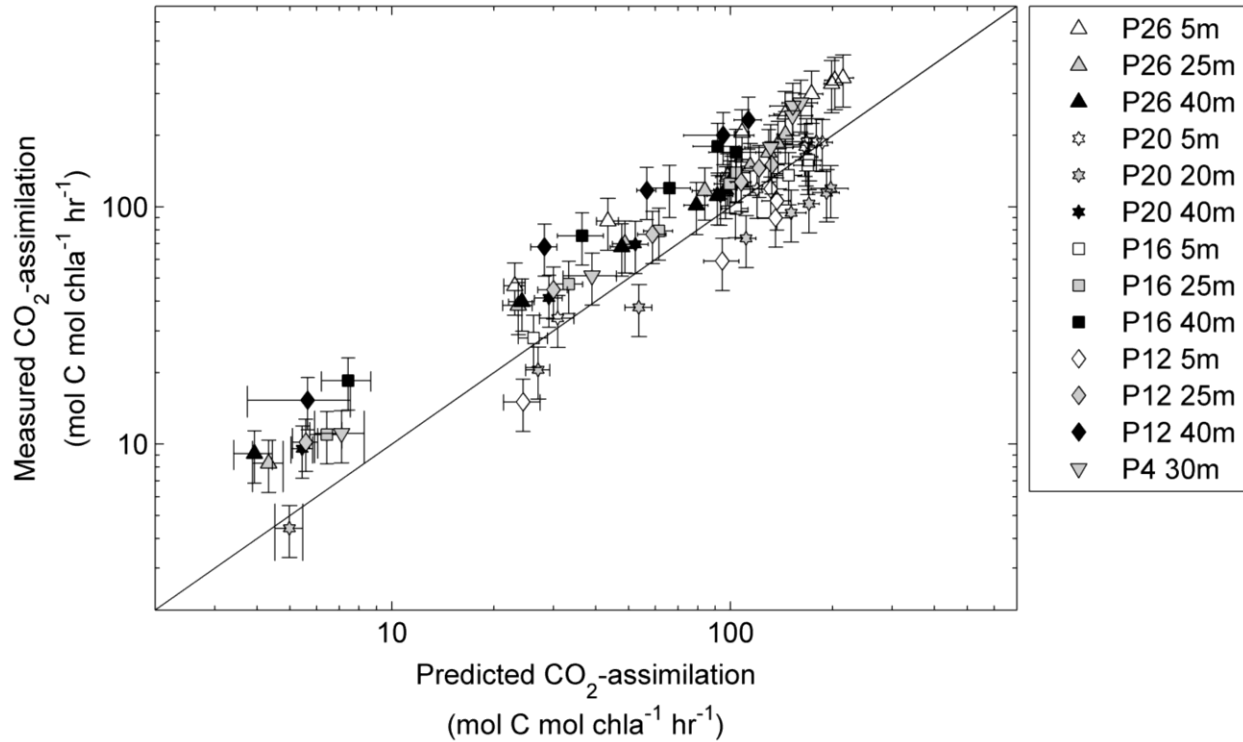


**Figure 2.9: Rates of CO<sub>2</sub>-assimilation (mol C mol chl a<sup>-1</sup> hr<sup>-1</sup>) derived from FRRF measurements plotted against rates measured by <sup>14</sup>C-assimilation experiments.** Samples were taken at one to three depths at five stations along Line-P in the NE Subarctic Pacific (see Figure 2.1). FRRF based P<sub>v</sub>sE curves were used to derive ETR<sub>RCII</sub> and NPQ<sub>NSV</sub> at 8 light levels for each sample, and Φ<sub>e,C</sub>/n<sub>PSII</sub> values were then derived from the relationship presented in Figure 2.7. Φ<sub>e,C</sub>/n<sub>PSII</sub> and ETR<sub>RCII</sub> for each light level were used to calculate CO<sub>2</sub>-assimilation rates. Error bars for predicted CO<sub>2</sub>-assimilation rates represent the propagated error from the ChlF yields of the last three ST acquisitions of each light level during the FRRF P<sub>v</sub>sE curve used to derive NPQ<sub>NSV</sub> and ETR<sub>RCII</sub>. Error bars for measured CO<sub>2</sub>-assimilation rates represent the mean coefficient of variance derived from all duplicate measurements (n=46). The correlation between all predicted and measured data points (n = 95) was statistically significant (Spearman's  $r = 0.90$ , two-tailed  $p < 0.0001$ ). All statistics are for non log-transformed data.

## Chapter 3:

# Diurnal variation in the coupling of photosynthetic electron transport and carbon fixation in iron-limited phytoplankton in the NE Subarctic Pacific

---

### 3.1 Summary

Active chlorophyll *a* fluorescence approaches, including fast repetition rate fluorometry (FRRF), have the potential to provide estimates of phytoplankton primary productivity at unprecedented spatial and temporal resolution. FRRF-derived productivity rates are based on estimates of charge separation at PSII ( $ETR_{RCII}$ ), which must be converted into ecologically relevant units of carbon fixation. Understanding sources of variability in the coupling of  $ETR_{RCII}$  and carbon fixation provides physiological insight into phytoplankton photosynthesis, and is critical for the application of FRRF as a primary productivity measurement tool. In the present study, we simultaneously measured phytoplankton carbon fixation and  $ETR_{RCII}$  in the iron-limited NE Subarctic Pacific, over the course of a diurnal cycle. We show that rates of  $ETR_{RCII}$  are closely tied to the diurnal cycle in light availability, whereas rates of carbon fixation appear to be influenced by endogenous changes in metabolic energy allocation under iron-limited conditions. Unsynchronized diurnal oscillations of the two rates led to 3.5-fold changes in the conversion factor coupling  $ETR_{RCII}$  and carbon fixation ( $K_c/n_{PSII}$ ). Consequently, diurnal variability in phytoplankton carbon fixation cannot be adequately captured with FRRF approaches if a constant conversion factor is applied. Utilizing several auxiliary physiological measurements, we observed that a high conversion factor is associated with conditions of excess light, and correlates with the increased expression of non-photochemical quenching (NPQ) in the pigment antenna, as derived from FRRF measurements. The observed correlation between NPQ and  $K_c/n_{PSII}$ , which requires further validation, has the potential to improve estimates of phytoplankton carbon fixation rates from FRRF measurements alone.

## 3.2 Introduction

Marine phytoplankton account for ~ 50 % of global carbon fixation (Field et al., 1998), and play a key role in Earth's biogeochemical cycles. Understanding the spatial and temporal patterns in marine primary productivity and its response to environmental variability is thus a central oceanographic research question. Traditionally, rates of phytoplankton primary production have been measured using incubation-based assays, tracing the evolution of oxygen or the assimilation of CO<sub>2</sub> (Williams et al., 2008). Over the past two decades, bio-optical approaches based on measurements of active chlorophyll *a* fluorescence (ChlF) yields (Kolber and Falkowski, 1993; Schreiber, 2004) have emerged as an attractive alternative, avoiding artifacts related to bottle containment, and achieving unparalleled spatial and temporal resolution. The method most prominently applied to measure ChlF yields in field assemblages of marine phytoplankton is fast repetition rate fluorometry (FRRF) (Kolber et al., 1998). ChlF yields, as measured by FRRF, can be used to estimate electron transport in photosystem II ( $ETR_{RCII}$ , mol e<sup>-</sup> mol RCII<sup>-1</sup> s<sup>-1</sup>), and these rates can be converted to carbon units based on theoretical calculations. However, empirical comparison of FRRF-derived  $ETR_{RCII}$  and carbon fixation data has shown that the derived conversion factor varies significantly with changes in the physiology and taxonomic composition of phytoplankton assemblages (Suggett et al., 2010b; Lawrenz et al., 2013).

The conversion factor linking  $ETR_{RCII}$  and carbon fixation consists of two parameters, the amount of chlorophyll *a* per number of functional PSII reaction centers ( $1/n_{PSII}$ ; mol chl*a* mol RCII<sup>-1</sup>) and the electron requirement for carbon fixation ( $K_c$ ; mol e<sup>-</sup> mol C<sup>-1</sup>; note that in most previous studies, this latter parameter has been denoted as  $\Phi_{e,C}$ ). Plasticity in both  $1/n_{PSII}$  and  $K_c$  can be observed at the physiological and taxonomic level, and is ultimately a function of given environmental conditions.

In order to optimize growth under fluctuating environmental conditions, phytoplankton photosynthesis and downstream metabolic processes exhibit great plasticity and interconnectivity, allowing rapid responds to changes in fluctuating light and nutrient levels. This physiological regulation influences the coupling between  $ETR_{RCII}$  and carbon fixation. For example, energy (ATP) and reducing power (NADPH) from the photosynthetic light reaction can be used directly for the reduction or assimilation of limiting nutrients, rather than for carbon

fixation (e.g. Laws, 1991; Myers, 1980), resulting in an increased conversion factor  $K_c/n_{PSII}$  (e.g. Napoléon et al., 2013). Furthermore,  $K_c/n_{PSII}$  has been shown to increase under excess light conditions (Babin et al., 1996; Cheah et al., 2011; Corno et al., 2006; Fujiki et al., 2007; Goto et al., 2008; Kaiblinger and Dokulil, 2006; Napoléon and Claquin, 2012; Napoléon et al., 2013; Raateoja, 2004), when the rate of charge separation in RCII can outpace the rate of electron transport along the photosynthetic electron transport chain (ETC). In order to alleviate the ensuing “backpressure”, which can lead to e.g. singlet oxygen formation and photoinhibition, photosynthetic organisms evolved a number of “safety valves” along the ETC (e.g. Niyogi, 2000). Activation of these alternative electron pathways increases the conversion factor  $K_c/n_{PSII}$ . In a previous study, we showed that low iron concentrations enhanced the effect of excess light, further increasing the conversion factor  $K_c/n_{PSII}$  (Schuback et al., 2015).

Given the well-established effect of excess light on the coupling of photosynthetic electron transport and carbon fixation, it is likely that the two rates decouple over the course of a diurnal cycle, if excess irradiance is encountered at noon. However, to our knowledge, there are no direct experimental studies of the diurnal changes in the coupling of  $ETR_{RCII}$  and carbon fixation in marine phytoplankton.

In the present study we simultaneously measured rates of  $^{14}C$ -uptake and  $ETR_{RCII}$  in iron-limited phytoplankton assemblages in the NE Subarctic Pacific over the course of a 24 hour diurnal cycle. Our results show that the conversion factor  $K_c/n_{PSII}$ , derived for *in situ* irradiances at 5 m depth, varied significantly (by a factor of 3.4), with most of the variability attributable to diurnal changes in  $K_c$ . Unless both carbon fixation and  $ETR_{RCII}$  are measured and integrated over a whole diurnal cycle (e.g. Suggett et al., 2006), diurnal variability in  $K_c/n_{PSII}$  should be considered, along with phytoplankton taxonomy and nutrient status (Lawrenz et al., 2013), when deriving regional conversion factors between  $ETR_{RCII}$  and carbon fixation. Building on previously published results (Schuback et al., 2015), we show that the magnitude and variability of  $K_c/n_{PSII}$  can be correlated with FRRF-based measurements of non-photochemical quenching ( $NPQ_{NSV}$ ).

### 3.3 Methods

#### 3.3.1 Study site and water-column hydrography

Field sampling was conducted on board the *CCGS John P. Tully* on June 17<sup>th</sup>/18<sup>th</sup> 2014. During the sampling period, the research vessel stayed within close proximity (10 km) to Ocean Station Papa (OSP), located in iron-limited waters of the NE Subarctic Pacific (50 °N, 145 °W) (<https://www.waterproperties.ca/linep/>). We acknowledge that our sampling approach is not truly Lagrangian, and some variability in nutritional status and taxonomic composition of phytoplankton assemblage could have occurred due to water mass advection. However, we expect that surface hydrography and phytoplankton characteristics are sufficiently homogeneous in this oceanic region, such that minor water mass advection would not have significantly influenced primary productivity or photo-physiological parameters measured over the diurnal cycle.

During our occupation of OSP, we conducted five CTD casts (three casts during the 24 hour diurnal experiment and one each before and after the diurnal sampling) to characterize variability in temperature and salinity depth profiles, from which we derived seawater density using the GSW toolbox in MATLAB (McDougall and Barker, 2011). Mixed layer depth (MLD) was calculated from a density difference criterion ( $\Delta\sigma = 0.05 \text{ kg m}^{-3}$ ). The depth profile of photosynthetically available radiation (PAR, 400-700 nm,  $\mu\text{mol quantam}^{-2} \text{ s}^{-1}$ ) through the upper 100 m of the water column was obtained using a PAR sensor (Biospherical QSP-400) mounted on the rosette during one of the CTD casts (12:30 local time (LT)). The optical extinction coefficient,  $k_d$  ( $\text{m}^{-1}$ ), was calculated as:

$$k_d = (\ln E_0 - \ln E_z)/z \quad (3.1)$$

Where  $E_0$  is surface irradiance and  $E_z$  is irradiance at depth  $z$  (m). Surface PAR ( $E_0^+$ ) was continuously logged (10 minutes intervals) with a LI-1000 down-welling PAR sensor (LI-COR, USA), mounted in a non-shaded position on the ship's superstructure, at a height of ca 7 m above the sea-surface. Unfortunately, 3 hours of PAR data (14:00-17:00 LT) were lost due to an instrument malfunction. To fill the data gap, we utilized shortwave solar radiation data from a nearby moored surface buoy, operated by the Ocean Climate Stations (OCS) group at Pacific

Marine Environmental Laboratory of the National Oceanic and Atmospheric Administration (PMEL-NOAA). All mooring data are available from the NOAA OCS website (<http://www.pmel.noaa.gov/OCS>). We aligned the two sets of irradiance data (ship-based and surface mooring) and extrapolated over the 3 hour gap in order to obtain consistent  $E_0^+$  for the timespan of the diurnal experiment. Surface reflectance was calculated as a function of solar zenith angle following Kirk (2011) using the R package ‘phytotoools’ (Silsbe, 2015). Subtracting surface reflectance provides PAR just under the air-ocean interface ( $E_0^-$ ). PAR at 5 m depth ( $E_{5m}^-$ ) was calculated as  $E_{5m}^- = E_0^- \exp(k_a \times 5m)$ .

Macro-nutrients (P, N, Si) were measured on samples from 2 CTD-rosette casts following the methods outlined in Barwell-Clarke (1996). Additional measurements of surface water (~ 5 m) temperature and salinity were derived from the ship's thermosalinograph (TSG) connected to a continuous seawater supply, and also from the NOAA mooring.

### **3.3.2 Sample collection**

Seawater samples were collected from the seawater intake system (ca 5 m depth) every 3 hours over a 24 hour period and processed immediately for a variety of physiological assays described below. The resulting dataset consists of 8 time-points (TPs). Local sunrise, solar noon and sunset were at 6:30, 14:40 and 22:50, respectively, resulting in 3 night-time TPs (3:00, 21:00, 0:00) and 5 day-time TPs (6:00, 9:00, 12:00, 15:00, 18:00). Samples taken at each TP are summarized in Table 3.1.

### **3.3.3 [chl<sub>a</sub>] and HPLC**

At each TP, duplicate 500 ml samples for [chl<sub>a</sub>] were filtered onto pre-combusted 25 mm glass fiber filters (GF/F) using low vacuum pressure (<5 mm Hg), taking care to keep the filters out of direct light. Filters were stored at -20 °C and analyzed following the method of Welschmeyer (1994) within two weeks of collection. At 4 TPs (3:00, 9:00, 15:00, 21:00) duplicate 2.2 L samples for pigment analysis were filtered onto pre-combusted 25 mm GF/F, as above. Filters were blotted dry with absorbent paper, flash frozen in liquid nitrogen and stored at -80 °C until analysis by reverse-phase high pressure liquid chromatography (HPLC) following the method of Pinckney (2013). The identified pigments were grouped into photosynthetic carotenoids (PSC), photo-protective carotenoids (PPC) and total chlorophyll (TChl) as outlined in Table 3.2. Ratios of these pigment groups were used to assess diurnal changes in the extent of

light stress experienced by the whole phytoplankton assemblage. Xanthophyll cycling (XC) pigments of chromophytes (diatoxanthin (Dt) and diadinoxanthin (Dd)) as well as xanthophyll cycling pigments of prasinophytes and chlorophytes (violaxanthin (Viol) and zeaxanthin (Zea)) were assessed with regard to their relative abundance ( $(Dt+Dd)/chl a$  and  $(Zea+Viol)/chl a$ ), and de-epoxidation state ratios (DES,  $Dt/(Dt+Dd)$  and  $Zea/(Zea+Viol)$ ). Furthermore, pigment data were used to estimate the relative abundance of different phytoplankton taxa at our sampling site. CHEMTAX analysis was performed using the averaged pigment concentrations from each TP. Analysis was performed essentially as described in Taylor et al. (2013). The initial pigment ratio matrix, specific to North Pacific phytoplankton isolates, was taken from Table 5 in Lee et al. (2011).

### 3.3.4 Absorption spectra

Absorption spectra of phytoplankton cellular pigments ( $a_{phy}(\lambda)$ ) were determined following the quantitative filter technique (QFT) as described in (Mitchell et al., 2002). At each TP, duplicate 1.1 L samples were filtered onto pre-combusted 25 mm GF/F under low vacuum pressure and light, taking care to achieve even sample distribution on the filter. Reference filters were prepared by filtering 1.1 L of Milli-Q water. Filters were carefully placed into 25 mm tissue capsules (Fisher), flash frozen in liquid nitrogen and stored at -80 °C until analysis within 1 month of the experiment. Sample filters were analyzed on a Cary BIO-100 dual-beam spectrophotometer (Varian) against reference filters as described in Mitchell et al. (2002). Optical density (OD) was measured from 370-800 nm (1 nm resolution) before and after extraction of pigment with 90 % methanol (Kishino et al., 1985) to determine OD of the whole particulate sample and OD of detritus after pigment extraction, respectively. Each sample and blank was analyzed in triplicate, to minimize error associated with instrument measurements. The wavelength-specific phytoplankton pigment absorption spectrum ( $a_{phy}(\lambda)$ ,  $m^{-1}$ ) was calculated as:

$$a_{phy}(\lambda) = 2.303 \times (OD_{sample}(\lambda) - OD_{detritus}(\lambda)) \times \frac{A}{V} \times \beta^{-1} \quad (3.2)$$

where 2.303 is the conversion of from base-10 to a natural logarithm, A is the particulate retention area of the filter ( $m^2$ ), V is the volume filtered ( $m^3$ ), and  $\beta$  is the path-length amplification coefficient (4.5; Röttgers and Gehrke, (2012)). To determine chl a specific

absorption spectra ( $a^*_{\text{phy}}(\lambda)$ ,  $\text{m}^{-1} \text{mg chl}a^{-1}$ ), values were normalized to corresponding [chl $a$ ] values. Absorption spectra were used for spectral correction of our rate measurements, as described in detail below.

### 3.3.5 FRRF-derived photophysiological parameters and $ETR_{RCII}$

All FRRF measurements were conducted on a bench top FRRF instrument (Soliense Inc.), as described in Schuback et al. (2015). At each TP, background fluorescence blanks were prepared by gently syringe filtering a small amount of sample through a pre-combusted GF/F. We applied a single turnover (ST) protocol consisting of an excitation sequence (100 flashlets with 1.0  $\mu\text{s}$  length and 2.5  $\mu\text{s}$  interval, 46200  $\mu\text{mol quanta m}^{-2} \text{s}^{-1}$  peak power intensity, resulting in a excitation sequence of 250  $\mu\text{s}$ , providing  $\sim 5$ -10 quanta per RCII), followed by a relaxation sequence (50 flashlets with 1.0  $\mu\text{s}$  length and 20  $\mu\text{s}$  interval). Excitation power was provided by an array of eight LEDs at four wavelengths centered on 445 nm, 470 nm, 505 nm, and 530 nm (equal intensity from each wavelength, applied simultaneously). We measured steady state light curves (SSLC), where each sample was exposed to 10 actinic ‘background’ irradiances from 0 to 1000  $\mu\text{mol quanta m}^{-2} \text{s}^{-1}$ , provided at the same four wavelengths. All ChlF yields and parameters described below were derived by an iterative non-linear fitting procedure, applying the four parameter biophysical model of Kolber et al. (1998) to a mean of 20 consecutive ST flashlet sequences using custom software (Z. Kolber). This software accounts for the formation of fluorescence quenching, most likely due to formation of a P680 triplet, which reduces the maximum fluorescence yield attainable during the ST flash by 3-6 %. Throughout the SSLC, ST flashlet sequences were measured continuously (1 s interval) and the length of each light step was optimized to allow all derived parameters to reach steady state (ca 3 min). ChlF yields and parameters corresponding to each light level were obtained from the mean of the last three acquisitions at each light level. In this way, we derived the fluorescence yields  $F_o$  and  $F_m$  (in dark-regulated state) as well as  $F'$  and  $F'_m$  (in the light regulated state for each light level of the SSLC).  $F'_o$  was calculated as  $F'_o = F_o / (F_v / F_m + F_o / F'_m)$  (Oxborough and Baker, 1997). The five fluorescence yields  $F_o$ ,  $F_m$ ,  $F'$ ,  $F'_m$  and  $F'_o$  were used to calculate ChlF parameters, following Roháček (2002) as described in Schuback et al. (2015). Furthermore, the functional absorption cross section of PSII,  $\sigma_{\text{PSII}} (\times 10^{-20} \text{ m}^2 \text{ RCII}^{-1})$ , was derived from the rate of closure of

RCII in the dark-regulated and each light-regulated state (Kolber and Falkowski, 1993; Kolber et al., 1998). We calculated  $ETR_{RCII}$  as:

$$ETR_{RCII} = E \times \sigma'_{PSII} \times \frac{F_q'}{F_v'} \times \Phi_{RC} \times 6.022 \times 10^{-3} \quad (3.3)$$

where  $E$  ( $\mu\text{mol quanta m}^{-2} \text{ s}^{-1}$ ) is the actinic irradiance at each light level,  $\sigma'_{PSII}$  ( $\times 10^{-20} \text{ m}^2 \text{ RCII}^{-1}$ ) is the functional absorption cross section of PSII at each light level, and  $F_q'/F_v'$  is the quantum efficiency of photochemical energy conversion in RCII at a given light intensity. The parameter  $F_q'/F_v'$  can also be interpreted as an estimate of the fraction of RCII in the open state, i.e. the primary stable electron acceptor in the oxidized state (Roháček, 2002). The parameter  $\Phi_{RC}$  ( $\text{mol e}^- \text{ mol photon}^{-1}$ ) has the constant value of 1, given that for each photon absorbed and delivered to RCII, one electron is transferred from  $P_{680}$  to  $Q_A$  (Kolber and Falkowski, 1993). The number  $6.022 \times 10^{-3}$  converts  $\mu\text{mol quanta}$  to  $\text{quanta}$  and  $10^{-20} \text{ m}^2$  to  $\text{m}^2$ .

We additionally calculated  $ETR_{RCII}$  using the alternative approach

$$ETR_{RCII} = E \times \sigma_{PSII} \times \frac{(F_q'/F_m')}{(F_v'/F_m')} \times \Phi_{RC} \times 6.022 \times 10^{-3} \quad (3.4)$$

Both calculations are equivalent, assuming that non-photochemical quenching processes affecting ChlF can be adequately accounted for in either the absorption term (Eq. 3.3) and the efficiency term (Eq. 3.4). The difference between  $ETR_{RCII}$  values calculated in both ways ( $n=71$ ) was negligible, ranging from 1 % to 16 % with a mean coefficient of variance of 6 %.

The parameter  $\tau$  (ms) is the time constant of re-oxidation of the primary stable electron acceptor  $Q_A$  and was estimated from the relaxation sequence of the ST protocol. We used values of  $\tau$ , estimated for the dark-regulated state at each TP, to derive estimates of the rate of  $Q_A$  re-oxidation ( $1/\tau$ ;  $\text{ms}^{-1}$ ). Non-photochemical quenching (NPQ) at each light level was estimated as the so-called normalized Stern-Volmer quenching coefficient,  $NPQ_{NSV} = (F_m'/F_v') - 1 = F_o'/F_v'$  (McKew et al., 2013). This alternative approach to the more common estimate of NPQ ( $(F_m - F_m')/F_m'$ ; Bilger and Björkman, 1990) represents the ratio of total non-photochemical energy dissipation in the light-regulated state to the rate constant of photochemistry (McKew et al., 2013).

### 3.3.6 Carbon fixation

Rates of carbon fixation were measured as small volume PvsE curves in a custom built photosynthetron as described in Schuback et al. (2015). Briefly, 300 mL water samples were spiked with 5.55 MBq NaH<sup>14</sup>CO<sub>3</sub> (final concentration 18.5 kBq mL<sup>-1</sup>, 1.94 GBq mL<sup>-1</sup> specific activity) (Perkin-Elmer). All sample manipulations were conducted under low light. Samples were spiked with tracer within 30 minutes of sampling, mixed gently but thoroughly, and then aliquoted into 20 ml glass scintillation vials and placed into the photosynthetron. The total <sup>14</sup>C activity added was determined from three 1 mL aliquots of the spiked sample added to 1 mL of 1 M NaOH. Additionally, 3 time-zero samples were taken for each curve by filtering 20 mL immediately after adding the spike. During the incubations, temperature was kept within 1 °C of *in situ* temperature by circulating water from a water-bath through an aluminum cooling jacket. Each PvsE curve consisted of 11 light levels spanning intensities from 3 to 600 μmol quanta m<sup>-2</sup> s<sup>-1</sup>. Incubations lasted for 3.5 hours and were ended by gentle filtration onto pre-combusted 25 mm GF/F filters. Given the length of the incubations and the likely slow growth rate of the iron-limited phytoplankton assemblage sampled, our approach likely reflects a rate closer to net rather than gross primary productivity (e.g. Halsey et al., 2011; Pei and Laws, 2013).

Filters were stored in scintillation vials at -20 °C until processing within 1 month of the experiment. During laboratory processing, 500 μL of 3 M HCl was added to each filter and vials were left to degas for >24 hours to eliminate any inorganic <sup>14</sup>C remaining in the samples. Ten mL of scintillation cocktail (Scintisafe plus, Fisher) were added to each vial, and vials were then vortexed and left to stand in the dark for >12 hours before analysis on a liquid scintillation counter (Beckman). Disintegrations per minute (DPM) were derived from scintillation counts using a quench curve prepared from commercial <sup>14</sup>C standards (Perkin-Elmer). DPM were converted to units of carbon biomass following Knap et al. (Knap et al., 1996).

### 3.3.7 Spectral correction and curve-fitting

To account for differences in the spectral distribution of LEDs used in photosynthetron and FRRF instrument, all rates were divided by a spectral correction factor (SCF).

$$SCF = \frac{\sum_{400}^{700} a_{phy}^{chla}(\lambda) E_{in\ situ}(\lambda) \sum_{400}^{700} E_{LED}(\lambda)}{\sum_{400}^{700} a_{phy}^{chla}(\lambda) E_{LED}(\lambda) \sum_{400}^{700} E_{in\ situ}(\lambda)} \quad (3.5)$$

where  $a_{\text{phy}}^{\text{chla}}(\lambda)$  ( $\text{m}^{-1}$ ) is the [chl*a*] specific phytoplankton pigment absorption spectrum determined for each TP as described above,  $E_{\text{LED}}$  is the spectral distribution of the LEDs used in photosynthetron or FRRF, and  $E_{\text{insitu}}$  is the spectral distribution of sunlight at 5 m depth. We estimated the *in situ* spectral distribution of PAR at 5 m depth following Stomp et al., 2007 as

$$E(\lambda, z) = E_0(\lambda) \exp(-[K_w(\lambda) + K_{GT}(\lambda) + K_{PH}(\lambda)]z) \quad (3.6)$$

Here,  $E_0(\lambda)$  is the spectral distribution of incident sunlight and  $K_w(\lambda)$  ( $\text{m}^{-1}$ ) is the absorption by pure water (Pope and Fry, 1997).  $K_{GT}(\lambda)$  ( $\text{m}^{-1}$ ) is the absorption by dissolved and particulate organic matter, estimated as  $K_w(\lambda) = K_{GT}(440) \exp(-S(\lambda - 440))$ , assuming that  $K_{GT}(440) = 0.003 \text{ m}^{-1}$ , a typical value of clear open ocean water (Morel et al., 2007), and  $S = 0.017 \text{ nm}^{-1}$  (Kirk, 2010). Values for  $K_{PH}(\lambda)$  ( $\text{m}^{-1}$ ) were taken from the absorption spectra measured using the filter pad technique as described above.

After spectral correction, carbon fixation and  $\text{ETR}_{\text{RCII}}$  data were plotted against irradiance and fit to the exponential model of Webb et al. (1974) using a non-linear least squares regression procedure in MATLAB. For the carbon fixation data, an intercept parameter was added to force the regression through the origin and provide a good fit in the linear part of the P vs E curve (Arrigo et al., 2010; Suggett et al., 2001). For both rates of productivity, we derived the light saturated maximum rate  $P_{\text{max}}$  ( $P_{\text{max}}\text{-ETR}_{\text{RCII}}$  and  $P_{\text{max}}\text{-C}$ ), the light utilization efficiency  $\alpha$  ( $\alpha\text{-ETR}_{\text{RCII}}$  and  $\alpha\text{-C}$ ), and the light saturation point  $E_k = P_{\text{max}}/\alpha$ . When photoinhibition was observed at high irradiances, the data-points were excluded from the fitting procedure (photoinhibition of  $^{14}\text{C}$ -uptake was only observed at TP1 and TP2 at irradiances  $> 550 \mu\text{mol quanta m}^{-2} \text{ s}^{-1}$ ).

### 3.3.8 Derivation of conversion factor

The conversion factor linking  $\text{ETR}_{\text{RCII}}$  ( $\text{mol e}^- \text{ mol RCII}^{-1} \text{ s}^{-1}$ ) and carbon fixation ( $\text{mol C mol chla}^{-1} \text{ s}^{-1}$ ), was derived as described in Schuback et al. (2015);

$$\frac{\text{ETR}_{\text{RCII}} (\text{mol e}^- \text{ mol RCII}^{-1} \text{ s}^{-1})}{\text{C} - \text{fixation} (\text{mol C mol chla}^{-1} \text{ s}^{-1})} = K_c \left( \frac{\text{mol e}^-}{\text{mol C}} \right) \times 1/n_{\text{PSII}} \left( \frac{\text{mol chla}}{\text{mol RCII}} \right) \quad (3.7)$$

In this approach, the conversion factor between the two rates accounts for changes in chla functionally associated with each RCII ( $1/n_{\text{PSII}}$ ,  $\text{mol chla mol RCII}^{-1}$ ), as well as variability in the number of charge separations in RCII per  $\text{CO}_2$  assimilated ( $K_c$ ,  $\text{mol e}^- \text{ mol C}^{-1}$ ). Reported values for  $K_c$  range from 1.15 – 54.2  $\text{mol e}^- \text{ mol C}^{-1}$  (Lawrenz et al., 2013) and 200 – 950  $\text{mol chla mol}$

RCII<sup>1</sup> for 1/n<sub>PSII</sub> (Suggett et al., 2010). Consequently, values of K<sub>c</sub>/n<sub>PSII</sub> could be expected to range from 230 - 51490 mol e<sup>-</sup> mol C<sup>-1</sup> mol chl<sub>a</sub> mol RCII<sup>-1</sup>.

Based on the measured light dependence of carbon fixation and ETR<sub>RCII</sub> for each sample, we were able to derive the light dependency of the conversion factor K<sub>c</sub>/n<sub>PSII</sub> at each TP. Additionally, we used α and P<sub>max</sub> values from the ETR<sub>RCII</sub> and <sup>14</sup>C PvsE curves to derive the conversion factor under sub-saturating and saturating light conditions, respectively.

### **3.3.9 Relative changes in 1/n<sub>PSII</sub>**

Combining two unknown variables (K<sub>c</sub> and 1/n<sub>PSII</sub>) into one conversion factor, as described above, limits our ability to physiologically interpret observed changes in the coupling of carbon fixation and photosynthetic electron transport. An approach to estimate values of 1/n<sub>PSII</sub> directly from FRRF measurements has been developed by Oxborough et al. (2012). However, this approach relies on the assumption that the ratio of the rate constants of photochemistry (k<sub>p</sub>) and fluorescence (k<sub>f</sub>) stay within a narrow range. This assumption is invalidated under conditions of iron limitation, where k<sub>p</sub> decreases while k<sub>f</sub> increases (e.g. Vassiliev et al., 1995), likely due to the expression of light harvesting complexes that are energetically decoupled from RCII (Behrenfeld and Milligan, 2013; Schrader et al., 2011). Consequently, the approach of Oxborough et al. (2012) should be used with caution when comparing samples over a range of iron limiting conditions.

In the current diurnal study, it is likely that the degree of iron limitation experienced by the phytoplankton assemblage stayed relatively constant during our sampling period, such that k<sub>p</sub>/k<sub>f</sub> values would have remained within a narrow range. Using this rationale, we applied a simplified version of the Oxborough et al. (2012) approach to our data, allowing us to estimate relative diurnal changes in 1/n<sub>PSII</sub>, and, by deduction K<sub>c</sub>. In the original approach by Oxborough et al. (2012), changes in of F<sub>o</sub>/σ<sub>PSII</sub>, measured in the dark-regulated state, are multiplied by an instrument specific calibration factor (K<sub>R</sub>) to derive absolute values of [RCII]. Lacking this instrument specific calibration factor K<sub>R</sub>, we were not able to derive absolute values for [RCII] (and in turn 1/n<sub>PSII</sub>). However, since K<sub>R</sub> is presumed to be constant, we used F<sub>o</sub>/σ<sub>PSII</sub> measured in the dark regulated state at each TP to derive an estimate of relative [RCII] values. These relative [RCII] values were then normalized to [chl<sub>a</sub>] to estimate diurnal changes in 1/n<sub>PSII</sub>, which were, in turn, used to estimate relative diurnal changes in K<sub>c</sub>. from measurements of K<sub>c</sub>/n<sub>PSII</sub>.

## 3.4 Results

### **3.4.1 Physical and chemical characteristics of the water-column during the experiment**

During the sampling period, the upper water-column at OSP was stratified, with a well-defined mixed layer of  $33 \pm 2$  m. As expected for iron-limited waters, excess macronutrients were present in the mixed layer and concentrations did not vary over the course of our sampling (2 casts, 3:30 and 12:30 local time;  $\text{NO}_2 + \text{NO}_3 = 9.1 \pm 0.00 \mu\text{mol L}^{-1}$ ,  $\text{PO}_4 = 0.98 \pm 0.01 \mu\text{mol L}^{-1}$ , and  $\text{Si}(\text{OH})_4 = 14.5 \pm 0.51 \mu\text{mol L}^{-1}$ ). Chlorophyll *a* concentrations were homogeneously distributed throughout the mixed layer ( $0.26 \pm 0.03 \text{ mg m}^{-3}$ ; 8 depths sampled on 1 cast at 12:30 local time), while temperature was nearly invariant ( $10.4 \pm 0.07 \text{ }^\circ\text{C}$ ) during our sampling period. Total daily incident PAR dose over the 24 hour period ( $E_0^+$ ) was  $31.94 \text{ mol quanta m}^{-2}$ , with a noon maximum of  $1,162 \mu\text{mol quanta m}^{-2} \text{ s}^{-1}$ . The water column light extinction coefficient,  $k_d$ , was  $0.07 \text{ m}^{-1}$ , which is a value typical for the open ocean (Kirk, 2010). The photic zone (defined as the 0.1 % light level) extended below the mixed layer depth at all TPs, apart from the nighttime TP (TPs 1, 7 and 8).

### **3.4.2 Phytoplankton community composition**

CHEMTAX analysis of the pigment data suggested that the phytoplankton assemblage at the sampling location was highly diverse. As a contribution to total [chl*a*] biomass the community consisted of approximately 3 % diatoms, 2 % dinoflagellates, 15 % prymnesiophytes, 12 % chlorophytes, 16 % prasinophytes, 14 % cryptophytes, 15 % pelagophytes and 23 % cyanobacteria.

### **3.4.3 Diurnal changes in rates of carbon fixation and $ETR_{RCII}$**

Over the course of the diurnal cycle, we observed significant changes in the PvsE curves for carbon fixation and  $ETR_{RCII}$  (Figure 3.1). However, the two rates, and their light dependency, did not change in parallel (Figure 3.1). As a consequence, we observed significant changes in magnitude and light dependency of the derived conversion factor  $K_c/n_{PSII}$ . At all TP,  $K_c/n_{PSII}$  increased with increasing light (Figure 3.1). The maximum, light-saturated value of  $K_c/n_{PSII}$  as well as the slope of the light dependent increase was highest in the afternoon, with maximum  $K_c/n_{PSII}$  values ( $> 9000 \text{ mol e}^- \text{ mol C}^{-1} \text{ mol chl}a \text{ mol RCII}^{-1}$ ) observed (Figure 3.1).

From the  $P_{vsE}$  curves shown in Figure 3.1 we derived the photosynthetic parameters  $P_{max}$  and  $\alpha$  for both  $ETR_{RCII}$  and carbon fixation (Figure 3.2 c-f). Over the diurnal cycle, the  $P_{max}$ - $ETR_{RCII}$  changed by a factor of 3.2 and closely followed the incident irradiance (Figure 3.2c), with peak values observed around solar noon. In contrast,  $P_{max}$ -C was highest in the early morning and then steadily declined over the course of the day, changing by a factor of 2.5 over the diurnal cycle (Figure 3.2e). The conversion factor  $K_c/n_{PSII}$ , derived for light saturated photosynthesis ( $P_{max}$ - $ETR_{RCII} / P_{max}$ -C), exhibited high values and a pronounced diurnal cycle, varying by a factor of 2.9 (Figure 3.2g). Minimum values of  $K_c/n_{PSII}$  were observed early in the morning, while maximum values were observed during the afternoon.

The light use efficiency per incident quanta under sub-saturating light conditions,  $\alpha$ , showed similar patterns to  $P_{max}$  for both  $ETR_{RCII}$  and carbon fixation (Figure 3.2). Values for  $\alpha$ - $ETR_{RCII}$  peaked during the late morning and then declined during the afternoon and into the evening (Figure 3.2d). In contrast,  $\alpha$ -C was highest before sunrise and steadily decreased throughout the day (Figure 3.2f). Over the course of the diurnal cycle,  $\alpha$ - $ETR_{RCII}$  changed by a factor of 1.9 while  $\alpha$ -C changed by a factor of 3.1. As with  $P_{max}$ , the conversion factor  $K_c/n_{PSII}$  derived for  $\alpha$ , varied strongly (2.4 fold) over the diurnal cycle and showed maximum values during the afternoon, in conjunction with the highest incident PAR levels (Figure 3.2h). At all TP, the conversion factor  $K_c/n_{PSII}$  was higher during light saturated photosynthesis ( $P_{max}$ ) than under conditions of light limitation ( $\alpha$ ) (Figure 3.2g and Figure 3.2h, note different scale of y-axis).

The light saturation point  $E_k$  was higher for  $ETR_{RCII}$  than for carbon fixation at all TPs (Figure 3.3), implying that carbon fixation rates saturated at lower light intensity than  $ETR_{RCII}$ . For both, carbon fixation and  $ETR_{RCII}$ ,  $P_{max}$  and  $\alpha$  changed roughly in parallel (Figure 3.2c, d and Figure 3.2e, f). Consequently, diurnal changes in  $E_k$ , derived as  $P_{max}/\alpha$ , were relatively small (Figure 3.2i). Furthermore, the relatively low values of  $E_k$  ( $\sim 100 - 150 \mu\text{mol quanta m}^{-2} \text{ s}^{-1}$ ) indicate that both,  $ETR_{RCII}$  and carbon fixation, were saturated at *in situ* irradiance levels for most of the day (Figure 3.2i).

Using the  $P_{vsE}$  curves measured for both  $ETR_{RCII}$  and carbon fixation (Figure 3.1), we derived rates corresponding to the 5 m irradiance levels at each TP (Figure 3.3b and Figure 3.3c). Over the diurnal cycle, these derived *in situ* rates of  $ETR_{RCII}$  changed by a factor of 5.1 (Figure 3.3b), closely following changes in ambient irradiance levels (Figure 3.3a), with peak values

around noon. By comparison, carbon fixation derived for *in situ* light levels at 5 m depth changed by a factor of 1.7 over the period of our sampling (Figure 3.3c). The maximum rate of realized carbon fixation at 5 m depth ( $0.0433 \pm 0.0112 \text{ mol C mol chl}a^{-1} \text{ s}^{-1}$ ) was reached in the morning, well before the daily irradiance maximum (Figure 3.3a and Figure 3.3c). The derived *in situ* conversion factor  $K_c/n_{PSII}$  varied by a factor of 3.4. Lowest derived values of *in situ*  $K_c/n_{PSII}$  were observed early in the morning after which values increased until reaching a maximum in the afternoon (Figure 3.3d).

#### **3.4.4 Relative changes in $1/n_{PSII}$**

Relative values of  $1/n_{PSII}$ , shown in Figure 3.4a, were highest in the early morning, and then declined by 37 % through the afternoon, with lowest values observed at midnight (Figure 3.4). The magnitude of diurnal change in  $1/n_{PSII}$  was significantly less than the diurnal changes observed in  $K_c/n_{PSII}$ , which were 245 % at *in situ* irradiances (Figure 3.4b), 185 % at light saturation ( $P_{max}$ ; Figure 3.4c) and 138 % at light limitation ( $\alpha$ , Figure 3.4d). We examined  $K_c$ -specific variability by normalizing  $K_c/n_{PSII}$  estimates to the relative changes in  $1/n_{PSII}$ . As shown in Figure 3.4, the derived relative changes in  $K_c$  showed a diel pattern very similar to that observed for  $K_c/n_{PSII}$  at *in situ* irradiances (Figure 3.4b), at light saturation ( $P_{max}$ , Figure 3.4c), and under light limitation ( $\alpha$ , Figure 3.4d). This result indicates that changes in  $K_c$  were the primary drivers of observed variability in  $K_c/n_{PSII}$ .

#### **3.4.5 Photo-regulatory changes**

In addition to the apparent diurnal changes in carbon fixation and  $ETR_{RCII}$ , we observed strong diurnal oscillations in a number of photo-physiological parameters, as well as changes in pigment composition of the phytoplankton assemblage. While higher resolution pigment data would have been desirable, the changes in pigment ratios shown in Figure 3.5 indicate that the phytoplankton assemblage sampled from 5 m depth experienced super-saturating light conditions for a substantial part of the day.

The ratio of photo-protective carotenoids (PPC) to total pigment (TPig), changed by a factor of 1.4 over the diurnal cycle, with lowest values observed at the pre-dawn TP (3:00) and highest in the afternoon (15:00) (Figure 3.5a). Similarly, the proportion of xanthophyll cycling (XC) pigments to total *chl*a increased from pre-dawn (3:00) to mid-afternoon (15:00). This increase was observed in XC pigments specific to chromophytes (42 % increase in  $(Dd+Dt)/chl_a$ ,

Figure 3.5b) as well as chlorophyte and prasinophyte-specific XC pigments (17 % increase in (Zea+Viol)/chl<sub>a</sub>, Figure 3.5c). Changes in relative abundance of XC pigments indicate that a higher proportion of the pigment pool is dedicated to photoprotection.

In addition to changes in XC pigments, we also observed a 2.4-fold increase in the DES ratio ( $Dt/(Dd+Dt)$ ) of chromophyte algae between 3:00 and 15:00 (Figure 3.5b), and a 1.8-fold increase in the DES ratio of chlorophytes and prasinophytes ( $Zea/(Zea+Viol)$ , Figure 3.5c). The changes in the DES ratio are an indicator of the activation of the photo-protective XC process (Brunet et al., 2011). Our results should be considered as conservative estimates of the DES ratios, given the potential for reversal of the high light induced de-epoxidation during sample processing (samples were exposed to low light for approximately 30 – 60 minutes during sample collection and filtration). Notwithstanding the relatively low temporal resolution of our pigment samples, the observed changes in pigment ratios indicate that the phytoplankton assemblage sampled from 5 m depth experienced super-saturating light conditions for a substantial part of the day. Further evidence for super-saturating light conditions in the mixed layer comes from observations of diurnal changes in PSII-specific photo-physiological parameters derived from FRRF measurements (Figure 3.6). Values of  $F_v/F_m$ , measured in the dark-regulated state, varied from 0.12 to 0.32 and showed an inverse relationship to irradiance (Figure 3.6a), likely indicating down-regulation or damage of PSII during high irradiance conditions. The parameter  $1/\tau$  ( $ms^{-1}$ ) is an estimate of the rate of electron transfer from the first stable electron acceptor  $Q_A$  to the second stable electron acceptor  $Q_B$ . Values of  $1/\tau$  varied in parallel with available irradiance over the diurnal cycle, changing approximately 3-fold, and indicating faster electron transport downstream of charge separation in RCII during daylight hours (Figure 3.6b). Estimates of the expression of non-photochemical quenching,  $NPQ_{NSV}$ , at *in situ* (5 m depth) irradiance levels changed 7.6-fold over the diurnal cycle, with maximum values near the peak of solar irradiance (Figure 3.6c). Spectrally corrected values of the functional absorption cross section of PSII,  $\sigma'_{PSII}$ , also derived for *in situ* irradiance levels, correlated inversely with irradiance (Figure 3.6d). This decrease further confirms the induction of photo-protective mechanisms within the pigment antenna, preventing excess energy from reaching RCII. Photochemical quenching, estimated as  $F_q'/F_v'$ , indicates the fraction of RCII in the 'open state', with the primary stable electron acceptor  $Q_A$  in the oxidized state (Roháček, 2002). Values of  $F_q'/F_v'$ , derived for a reference irradiance value of  $500 \mu mol \text{ quanta } m^{-2} s^{-1}$  at all TP ( $F_q'/F_v'$

(500)), show significant change over the diurnal cycle, with mid-day values twice as high as those observed during the night (Figure 3.6e).

### 3.5 Discussion

The experimental approach and results presented in this study confirm the hypothesized diurnal variation in the coupling of  $ETR_{RCII}$  and carbon fixation under iron-limited conditions. Building on the work of others (Behrenfeld et al., 2004, 2008; Halsey and Jones, 2015) we interpret our results in the context of environmentally driven shifts in cellular energy allocation, which decouple photosynthesis from net growth on diurnal timescales. We speculate that the observed patterns are caused by photo-physiological plasticity on a molecular level, which enables phytoplankton to maximize growth while minimizing photo-damage under iron-limited conditions.

In the following, we first discuss diurnal variation at the level of carbon fixation and put our observations in context with the rich information available from the literature. We then consider the diurnal changes in  $ETR_{RCII}$  and the derived conversion factor  $K_c/n_{PSII}$ , and discuss the relevance of our results to the development of FRRF-based phytoplankton primary productivity measurements.

#### 3.5.1 Diurnal changes in carbon fixation

Diurnal variations in the capacity ( $P_{max-C}$ ), efficiency ( $\alpha-C$ ) and realized rates of carbon fixation are characteristic of phytoplankton assemblages in the natural environment, and in laboratory cultures (Bryant et al., 2005; Doblin et al., 2011; Doty and Oguri, 1957; Erga and Skjoldal, 1990; Harding et al., 1981, 1982, 1987; John et al., 2012; MacCaull and Platt, 1977; Prézelin, 1992; Stross et al., 1973; Zhao and Quigg, 2015). The general consensus is that carbon fixation is not passively regulated by the availability of light, but by complex metabolic feedbacks and endogenous circadian rhythms.

For example, it has been shown that expression of genes involved in carbon fixation peaks before dawn (Ashworth et al., 2013; Granum et al., 2009), ‘priming’ cells to achieve maximum rates early in the day. High carbon fixation capacities ( $P_{max-C}$ ) before sunrise, as observed in our data (Figure 3.2e), further confirm endogenous circadian control of this pathway.

In our data,  $P_{\max}\text{-C}$  and  $\alpha\text{-C}$  peaked early in the morning and co-varied over the diurnal cycle (Figure 3.2e and Figure 3.2f). As a result,  $E_k$  (which is derived from the ratio of these parameters) remained relatively constant (Figure 3.2i). This ‘ $E_k$ -independent’ variability in the photosynthetic parameters  $P_{\max}\text{-C}$  and  $\alpha\text{-C}$  has long been considered somewhat enigmatic, but is now accepted to be driven by shifts in cellular energy allocation (Behrenfeld et al., 2004, 2008; Bruyant et al., 2005; Halsey and Jones, 2015). In phytoplankton, the fraction of photosynthetically-derived reductant (NADPH) and energy equivalent (ATP) allocated to carbon fixation and net growth as well as the ratio of NADPH:ATP produced are finely tuned to match metabolic demand. Metabolic demand, in turn, is a function of evolved endogenous rhythms and external environmental forcing. As discussed below, the decline in  $P_{\max}\text{-C}$  (Figure 3.2e),  $\alpha\text{-C}$  (Figure 3.2f), and realized rates of carbon fixation (Figure 3.3c) after a peak in the early morning, are likely due to such shifts in energy allocation, and to the damaging effects of excess light, which accumulate throughout the light-period.

### **3.5.2 Diurnal changes in $ETR_{RCII}$ and the conversion factor $K_c/n_{PSII}$**

In contrast to the diurnal cycles of  $P_{\max}\text{-C}$  and  $\alpha\text{-C}$ , changes in  $P_{\max}\text{-ETR}_{RCII}$  and  $\alpha\text{-ETR}_{RCII}$  followed availability of light more closely, peaking around noon (Figure 3.2c,d). Similarly, realized  $ETR_{RCII}$ , derived for *in situ* irradiances at each TP, correlated more closely with light availability than realized rates of carbon fixation (Figure 3.3b). While it has been demonstrated that virtually all stages of photosynthesis exhibit circadian control (Suzuki and Johnson, 2001), our results suggests that  $ETR_{RCII}$  responds more directly to changes in light availability than the subsequent conversion of light energy into cellular organic carbon. It is important to note that the accumulation of photo-damage and inhibition over the course of the light-period is likely to impart some level of hysteresis to diurnal changes in  $ETR_{RCII}$ . Relative to carbon fixation, however, our results show that  $ETR_{RCII}$  is much more closely tied to instantaneous changes in light availability. The resulting decoupling of carbon fixation and photosynthetic electron transport is reflected in the diurnal variability in  $K_c/n_{PSII}$  (Figure 3.2g, Figure 3.2h, Figure 3.3d). Based on our estimates of relative changes in  $1/n_{PSII}$  over the diel cycle (Figure 3.4), we conclude that the majority of diurnal variability in  $K_c/n_{PSII}$  results from changes in  $K_c$ .

In our dataset, in situ values for  $K_c/n_{PSII}$  ranged from 2700 to 9200 mol e<sup>-</sup> mol C<sup>-1</sup> mol chl*a* mol RCII<sup>-1</sup>. Assuming a constant  $1/n_{PSII}$  of 500 mol chl*a* mol RCII<sup>-1</sup> (Kolber and Falkowski, 1993), the derived  $K_c$  ranges from 5-18 mol e<sup>-</sup> mol C, which is within the range of previously reported values (Lawrenz et al., 2013) and above the theoretical minimum of 4 mol e<sup>-</sup> mol C.

The large diurnal variability in  $ETR_{RCII}$  and carbon fixation and the highly variable  $K_c/n_{PSII}$ , reflect the integrated growth environment experienced by the sampled phytoplankton assemblage. The lowest values of  $K_c/n_{PSII}$  were observed early in the morning (Figure 3.3d), indicating that much of the energy harvested from sunlight and converted into chemical energy was used directly for carbon fixation. Thereafter, the conversion factor  $K_c/n_{PSII}$  increased rapidly, reaching a maximum in the afternoon (Figure 3.3d).

Diurnal variation in  $K_c/n_{PSII}$  can result from a number of interconnected cell physiological mechanisms aimed at re-balancing of energy and/or reductant. Firstly, it is possible that diurnal oscillations in cell metabolism result in changes in organic carbon respiration and/or excretion. In our 3.5 hours <sup>14</sup>C-uptake experiments, transient organic carbon pools destined for respiration or excretion could have been captured to different extents, affecting the derived conversion factor  $K_c/n_{PSII}$ . Changes in cellular energy allocation, controlled in part by endogenous circadian rhythms, could also have affected the conversion factor  $K_c/n_{PSII}$ , by re-routing NADPH and ATP generated by the photosynthetic light reaction to processes other than carbon fixation, thus increasing  $K_c/n_{PSII}$ . Processes decoupling  $ETR_{RCII}$  from carbon fixation include nutrient assimilation (Laws, 1991), carbon concentrating mechanisms (Giordano et al., 2005), photorespiration (Foyer et al., 2009), and malate formation (Halsey and Jones, 2015). Pseudo-cyclic electron transport through the Mehler-ascorbate peroxidase pathway also has the ability to increase the conversion factor  $K_c/n_{PSII}$  by allowing  $ETR_{RCII}$  to increase without affecting carbon fixation (Miyake and Asada, 2003; Niyogi, 2000). Moreover, processes acting before PSI can decouple  $ETR_{RCII}$  and carbon fixation by ‘siphoning’ electrons out of the ETC to alleviate over-reduction under super-saturating light condition. Pseudo-cyclic electron transport through midstream terminal oxidases (Bailey et al., 2008; Mackey et al., 2008), cyclic electron transport around PSII (Feikema et al., 2006; Prasil et al., 1996), and charge recombination in RCII (Vass, 2011) could all be important under high mid-day irradiances, increasing  $ETR_{RCII}$  without affecting CO<sub>2</sub>-assimilation, and thus leading to a higher conversion factor  $K_c/n_{PSII}$ .

Iron limitation, as experienced by the phytoplankton assemblage we sampled, directly affects the functioning of the ETC, which is rich in iron containing redox-chain components (Raven et al., 1999; Yruela, 2013). It is thus likely that the need for safe dissipation of excess excitation energy after charge separation in RCII is enhanced under iron limitation (Behrenfeld and Milligan, 2013; Schuback et al., 2015), leading to a greater decoupling of  $ETR_{RCII}$  and carbon fixation (Schuback et al., 2015). Pseudo-cyclic electron flow could alleviate over-reduction of the ETC under iron limiting conditions, while also contributing to ATP production (Behrenfeld and Milligan, 2013). The resulting increase in the cellular ATP:NADPH ratio would match the shift in energy demand from growth (higher NADPH requirement) to maintenance (higher ATP requirement), which takes place under nutrient limited growth conditions.

While the exact nature and extent of operation of these various pathways and their actual influence on the coupling of  $ETR_{RCII}$  and carbon fixation remains to be verified, we suggest that the observed changes in the conversion factor  $K_c/n_{PSII}$  over the diurnal cycle reflect the interactions of external phasing of photosynthetic metabolism by the availability of light and internal metabolic rhythms in cell metabolism, which optimize energy allocation and growth under iron-limited conditions.

### **3.5.3 Diurnal changes in photo-physiology at the level of PSII**

In our data, several lines of evidence demonstrate that the phytoplankton assemblage we sampled from 5 m depth experienced super-saturating irradiance during part of the day. A suite of mechanisms was activated to dissipate the excess excitation energy in the pigment antenna, before it could reach RCII. This was indicated by changes in pigment ratios (Figure 3.5) and FRRF-derived photo-physiological parameters (Figure 3.6). The light harvesting antennae of phytoplankton are comprised of both photosynthetic and photo-protective pigments, the relative abundance of which can change in response to irradiance. The ratio  $[PPC]/[TPig]$ , provides information on the degree of high light acclimation of a mixed phytoplankton assemblage (Brunet et al., 2011). In our data,  $[PPC]/[TPig]$  increased during the day (Figure 3.5a), indicating that the phytoplankton assemblage experienced and responded to super-saturating irradiance levels. Furthermore, significant changes in the DES ratio of chromophytes ( $Dt/(Dt+Dd)$ , Figure 3.5b), as well as chlorophytes and prasinophytes ( $Zea/(Zea+Viol)$ , Figure 3.5c) illustrate rapid

activation of photo-protective energy dissipation in the pigment antenna in response to diurnal changes in irradiance (Brunet et al., 2011).

Figure 3.6 shows pronounced diurnal variability in a number of FRRF derived parameters. Both  $F_v/F_m$  (Figure 3.6a) and  $1/\tau$  (Figure 3.6d) were derived for the dark-regulated state at each TP. To reach this dark-regulated state, samples were kept under very low light for a minimum of 30 minutes prior to the measurement. In theory, such low-light incubation allows for oxidation of the ETC and relaxation of all NPQ processes, enabling the measurement of maximum ChlF yields. In practice, however, a fully dark-regulated state cannot be achieved in natural phytoplankton assemblages, where optimal dark-acclimation times can be on the order of hours long (From et al., 2014), and would depend on recent light history and taxonomic composition. Consequently, the interpretation of ChlF yields and parameters in field phytoplankton assemblages should be treated with caution. Notwithstanding these caveats, the FRRF-derived ChlF yields and parameters shown in Figure 3.6 show clearly that, at the level of PSII, the sampled phytoplankton assemblage experienced and reacted to excess irradiance.

While it is known that nutritional state and taxonomy both strongly influence values of  $F_v/F_m$  (Suggett et al., 2009b), it is very unlikely that changes in either are responsible for pronounced diurnal cycle of  $F_v/F_m$  observed in our data (Figure 3.6a). We therefore attribute the mid-day decrease in  $F_v/F_m$  to persistent photo-protective changes and photoinhibition in PSII (Öquist et al., 1992).

Processes including the light-induced changes in pigment composition shown in Figure 3.5, act to dissipate excess excitation energy in the pigment antenna, before reaching RCII. These processes also quench ChlF yields, as measured by FRRF. Consequently, so-called non-photochemical quenching (NPQ), as estimated from FRRF measurements, has been widely used as an estimate for photo-protective energy dissipation (Derks et al., 2015; Demming-Adams et al., 2014). NPQ encompasses a wide variety of mechanisms, all acting to dissipate absorbed light energy as heat before it reaches RCII (e.g. Derks et al., 2015). Following the approach of McKew et al. (2013) we estimated NPQ from FRRF measurements as so-called normalized Stern-Volmer quenching ( $NPQ_{NSV}$ ). The 7.6-fold change in  $NPQ_{NSV}$ , estimated for *in situ* light availability at 5 m depth (Figure 3.6b), confirms that the phytoplankton assemblage sampled experienced, and rapidly reacted to, super-saturating light conditions. The inverse light dependence of the functional absorption cross-section of PSII,  $\sigma'_{PSII}$ , derived for *in situ*

irradiance at each TP (Figure 3.6c), provides a further illustration of rapid changes taking place in the pigment antenna to prevent excess excitation energy from reaching RCII.

In addition to the protective mechanisms acting in the pigment antenna to prevent charge separation in RCII, photo-protective mechanisms also act after charge separation in RCII (Section 3.5.2). These mechanisms alleviate over-reduction by allowing rapid re-oxidation of the primary stable electron acceptor  $Q_A$ . Our data show evidence of the up-regulation of such alternative electron sinks during mid-day (Figure 3.6). Figure 3.6d shows a light-dependent increase in  $1/\tau$ , which provides an estimate of the rate of re-oxidation of the first stable electron acceptor  $Q_A$ . Increased  $1/\tau$  thus suggests faster electron flow downstream from  $Q_A$ , which is consistent with the up-regulation of alternative electron sinks. Further support for this idea comes from diel changes in the estimated fraction of  $Q_A$  in the oxidized state ( $F_q'/F_v'$ ), derived for a reference irradiance of  $500 \mu\text{mol quanta m}^{-2} \text{s}^{-1}$  (Figure 3.6e). The mid-day increase in the oxidized fraction of  $Q_A$  at a constant saturating irradiance of  $500 \mu\text{mol quanta m}^{-2} \text{s}^{-1}$  strongly suggests the up-regulation of alternative electron sinks, which most likely serve a photo-protective function (Mackey et al., 2008). Up-regulation of these photo-protective mechanisms, influences the coupling between electron transport and carbon fixation, and thus directly affects the conversion factor  $K_c/n_{\text{PSII}}$ .

#### **3.5.4 Linking $K_c/n_{\text{PSII}}$ and $\text{NPQ}_{\text{NSV}}$**

Excess excitation energy leads to the induction of processes preventing energy transfer to RCII, and to processes acting to prevent over-reduction of the ETC after charge separation.  $\text{NPQ}_{\text{NSV}}$  provides an estimate of thermal energy dissipation upstream of RCII, which acts to prevent excess electron transport and over-reduction of the ETC. Downstream changes in electron flow after charge separation at RCII are reflected in changes in  $K_c/n_{\text{PSII}}$ , through the induction of various mechanisms, as discussed in the previous section. Following the approach and interpretation suggested by Schuback et al. (2015), we examined the correlation between the derived conversion factor  $K_c/n_{\text{PSII}}$  and estimates of  $\text{NPQ}_{\text{NSV}}$ . For this analysis, we used estimates of  $\text{NPQ}_{\text{NSV}}$  for each light level and TP of the FRRF light curves and derived values of  $K_c/n_{\text{PSII}}$  by extrapolation along the carbon fixation and  $\text{ETR}_{\text{RCII}}$  based  $P_{\text{vs}}E$  curves. As shown in Figure 3.7, we found a strong linear correlation between these two variables ( $R^2 = 0.81$ ,  $p < 0.0001$ ,  $n = 64$ ).

As described in detail in Schuback et al. (2015), the observed empirical correlation between  $K_c/n_{PSII}$  and  $NPQ_{NSV}$  can be rationalized in terms of photo-physiological mechanisms, acting to dissipate excess excitation energy both upstream and downstream of charge separation in RCII. The dissipation of excess excitation energy as thermal energy before reaching RCII, estimated as  $NPQ_{NSV}$ , prevents excess electron transport and over-reduction of the ETC. After the initial charge separation in RCII, excess electron transport and over-reduction of the ETC can be alleviated by a number of alternative electron pathways; the up-regulation of which will increase  $K_c/n_{PSII}$  (e.g. Bailey et al., 2008; Cardol et al., 2011; Laureau et al., 2013; Mackey et al., 2008; McDonald et al., 2011; Niyogi, 2000; Streb et al., 2005; Vass, 2011; Zehr and Kudela, 2009). Thus, both  $NPQ_{NSV}$  and  $K_c/n_{PSII}$  respond strongly to excess excitation energy, providing a possible mechanistic interpretation for their correlation. In fact, a positive feedback loop exists between energy dissipation in the antenna and photosynthetic control in the ETC, because alternative electron pathways enhance the trans-membrane  $\Delta pH$ , which triggers several components of NPQ (Nawrocki et al., 2015). The correlation between  $NPQ_{NSV}$  and  $K_c/n_{PSII}$  is likely to be especially strong under iron limiting conditions, due to the enhancement of energy dissipation mechanisms when the functioning of the ETC is compromised by the availability of iron.

While a correlation between  $NPQ_{NSV}$  and  $K_c/n_{PSII}$  has important implications for the derivation of carbon-based primary productivity rates from FRRF measurements, the correlation can be confounded by ambiguity and inherent biases in the derivation of all involved parameters. For example, while the correlations between  $NPQ_{NSV}$  and  $K_c/n_{PSII}$  in the present, as well as our previously published dataset (Schuback et al., 2015), are strong, their regression slopes differ. The observed discrepancy could be explained in several ways. Firstly, data in our previous study was not corrected for spectral differences between the FRRF instrument, the  $^{14}C$ -uptake experiments and *in situ* light. As a consequence, absolute values of the derived conversion factor were likely over-estimated (for example, in data from the Arctic dataset presented in chapter 4, the application of spectral correction to both rates reduced the derived conversion factor at least two-fold). Furthermore, data presented in Schuback et al. (2015) included phytoplankton assemblages sampled over a range of iron-limited and iron-replete conditions. The resulting variability in phytoplankton growth rates influence the balance between net and gross carbon

fixation captured in 3 hour  $^{14}\text{C}$ -uptake experiments (Halsey et al., 2011; Milligan et al., 2015; Pei and Laws, 2013), and affect the derived conversion factor  $K_c/n_{\text{PSII}}$ .

More generally, significant uncertainty remains in the estimation of  $\text{ETR}_{\text{RCII}}$  from ChlF yields, particularly if the theoretical biophysical models are applied to mixed phytoplankton assemblages containing species with contrasting photosynthetic architectures and photo-physiological characteristics. Inherent biases and potential systematic errors in the derivation of  $\text{ETR}_{\text{RCII}}$  will inevitably affect the derived conversion factor  $K_c/n_{\text{PSII}}$ . Similarly, it remains unclear if the quenching of ChlF yields, used to derive NPQ, correlate linearly with increases in thermal energy dissipation in the pigment antenna (Derks et al., 2015). Ultimately, larger datasets, spanning multiple oceanic regions and phytoplankton assemblages of contrasting taxonomic composition and physiological state are needed to further investigate the correlation between  $\text{NPQ}_{\text{NSV}}$  and  $K_c/n_{\text{PSII}}$ .

### 3.6 Conclusion

The lure of FRRF instruments lies in their potential for autonomous, instantaneous data acquisition at high temporal and spatial resolution. However, uncertainty in the conversion factor needed to convert rates of  $\text{ETR}_{\text{RCII}}$  into ecologically relevant rates of carbon fixation remains a significant challenge. Through a suite of photo-physiological data and ancillary measurements, our results provide some insight into the potential mechanistic causes leading to an uncoupling of  $\text{ETR}_{\text{RCII}}$  and carbon fixation over diurnal cycles in iron-limited phytoplankton assemblages. Beyond providing improved methods to estimate phytoplankton carbon fixation rates, information on magnitude and variability of the conversion factor linking  $\text{ETR}_{\text{RCII}}$  and carbon fixation allows a better mechanistic understanding of how phytoplankton harvest and allocate light energy in response to environmental conditions. Our mechanistic understanding of these processes is crucial for the modeling and prediction of patterns in marine primary productivity in the face of climate-dependent changes in oceanic ecosystems.

More generally, it is important to consider that the dynamics of marine productivity over long time-scales are ultimately controlled by interactions among biological and physical processes that have strong diurnal components. Several recent studies suggest a previously under-appreciated importance of closely coupled diurnal oscillations as the underlying mechanisms of ecosystem stability in open ocean food webs (Ottesen et al., 2014; Ribalet et al.,

2015). Our results show strong diurnal variability in photo-physiology and cell metabolism of mixed phytoplankton assemblages. These physiological processes likely influence the phasing and periodicity of higher trophic level processes, and may ultimately contribute to conveying stability to the system.

### 3.7 Tables and figures

**Table 3.1: Parameters measured at each time-point during the diurnal experiment.**

| <b>Time Point</b>          | <b>1</b> | <b>2</b> | <b>3</b> | <b>4</b> | <b>5</b> | <b>6</b> | <b>7</b> | <b>8</b> |
|----------------------------|----------|----------|----------|----------|----------|----------|----------|----------|
| <b>Local time</b>          | 3:00     | 6:00     | 9:00     | 12:00    | 15:00    | 18:00    | 21:00    | 0:00     |
| <b>[chl<math>a</math>]</b> | x        | x        | x        | x        | x        | x        | x        | x        |
| <b>HPLC</b>                | x        |          | x        |          | x        |          | x        |          |
| <b>Absorption Spectra</b>  | x        | x        | x        | x        | x        | x        | x        | x        |
| <b>FRRF measurements</b>   | x        | x        | x        | x        | x        | x        | x        | x        |
| <b>C-fixation</b>          | x        | x        | x        | x        | x        | x        | x        | x        |

**Table 3.2 :Phytoplankton pigments used for the derivation of diagnostic pigment ratios.** Pigments identified from HPLC analysis were chlorophyll  $c_3$  (Chl  $c_3$ ), chlorophyll  $c_1c_2$  (Chl  $c_1c_2$ ), 19'butanoyloxyfucoxanthin (19'BF), fucoxanthin (Fuco), 19'hexanoyloxyfucoxanthin (19'HF), 9'cis-neoxanthin (Neo), prasinoxanthin (Prasino), violaxanthin (Viola), diadinoxanthin (Dd), alloxanthin (Allox), diatoxanthin (Dt), lutein, zeaxanthin (Zea), chlorophyll b (Chl  $b$ ), chlorophyll  $a$  allomer (Chl  $a$  allomer), chlorophyll  $a$  + divinyl chlorophyll  $a$  (Chl  $a$ ), chlorophyll  $a'$  (Chl  $a$  prime),  $\alpha$  carotene ( $\alpha$  carot),  $\beta$  carotene ( $\beta$  carot).

| <b>Pigment group</b>                      | <b>Pigments</b>  |
|---|--|
| <b>Photo-protective carotenoids (PPC)</b> | Neo + Viola + Dd + Allox + Dt + Lutein + Zea + $\beta$ carot                   |
| <b>Photosynthetic carotenoids (PSC)</b>   | 19'BF + Fuco + 19'HF + Prasino + $\alpha$ carot                                |
| <b>Total chlorophyll (Tchl)</b>           | Chl $c_3$ + Chl $c_1c_2$ + Chl $b$ + Chl $a$ allomer + Chl $a$ + Chl $a$ prime |
| <b>Total pigment (TPig)</b>               | PPC + PSC + Tchl   |

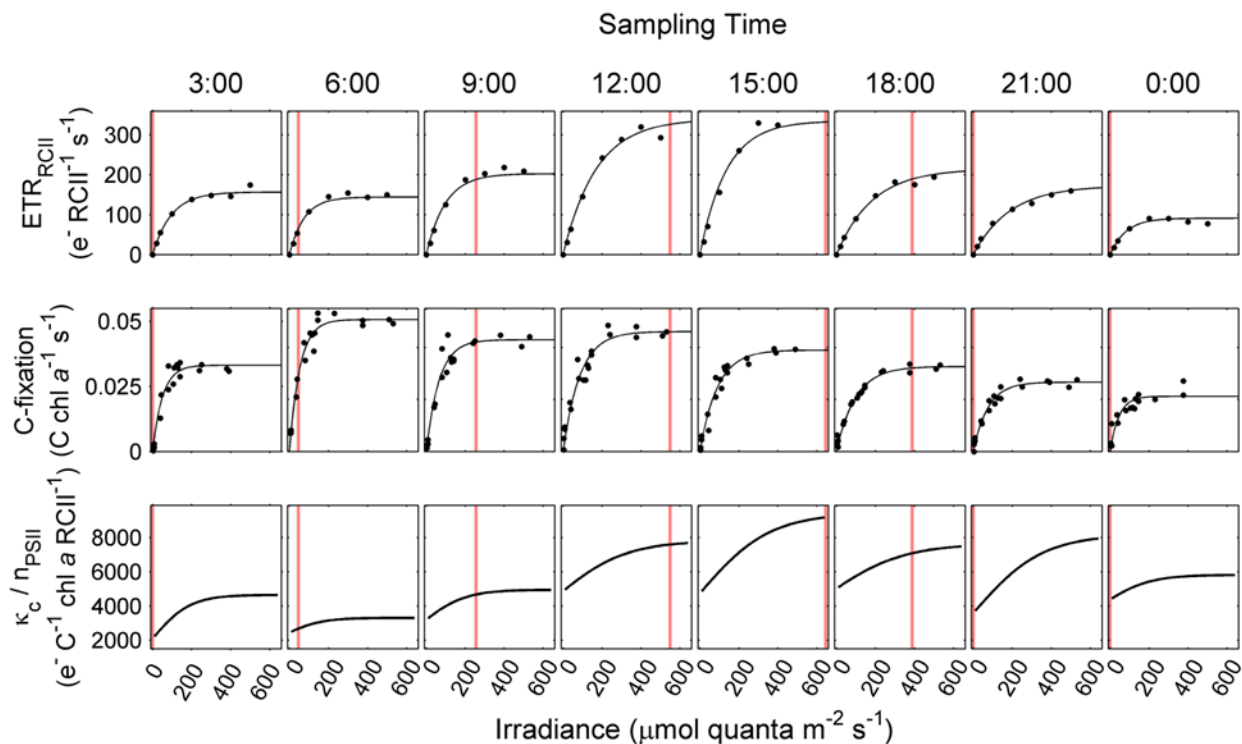


**Figure 3.1: Diurnal variation in rates and light dependency of  $ETR_{RCII}$ , carbon fixation and the derived conversion factor  $K_c/n_{PSII}$ .** PvsE curves of  $ETR_{RCII}$  ( $\text{mol e}^- \text{mol RCII}^{-1} \text{s}^{-1}$ ) and carbon fixation ( $\text{mol C mol chl a}^{-1} \text{s}^{-1}$ ) were measured at 3 hour intervals over a 24 hour diurnal cycle. Data were fit to the exponential model of Webb et al. (1974). The conversion factor  $K_c/n_{PSII}$  ( $\text{mol e}^- \text{mol C}^{-1} \text{mol chl a mol RCII}^{-1}$ ), and its light dependency, were derived as the quotient of corresponding values of  $ETR_{RCII}$  and carbon fixation. The vertical line on plots corresponds to *in situ* PAR values at 5 m depth during sampling for each time-point.

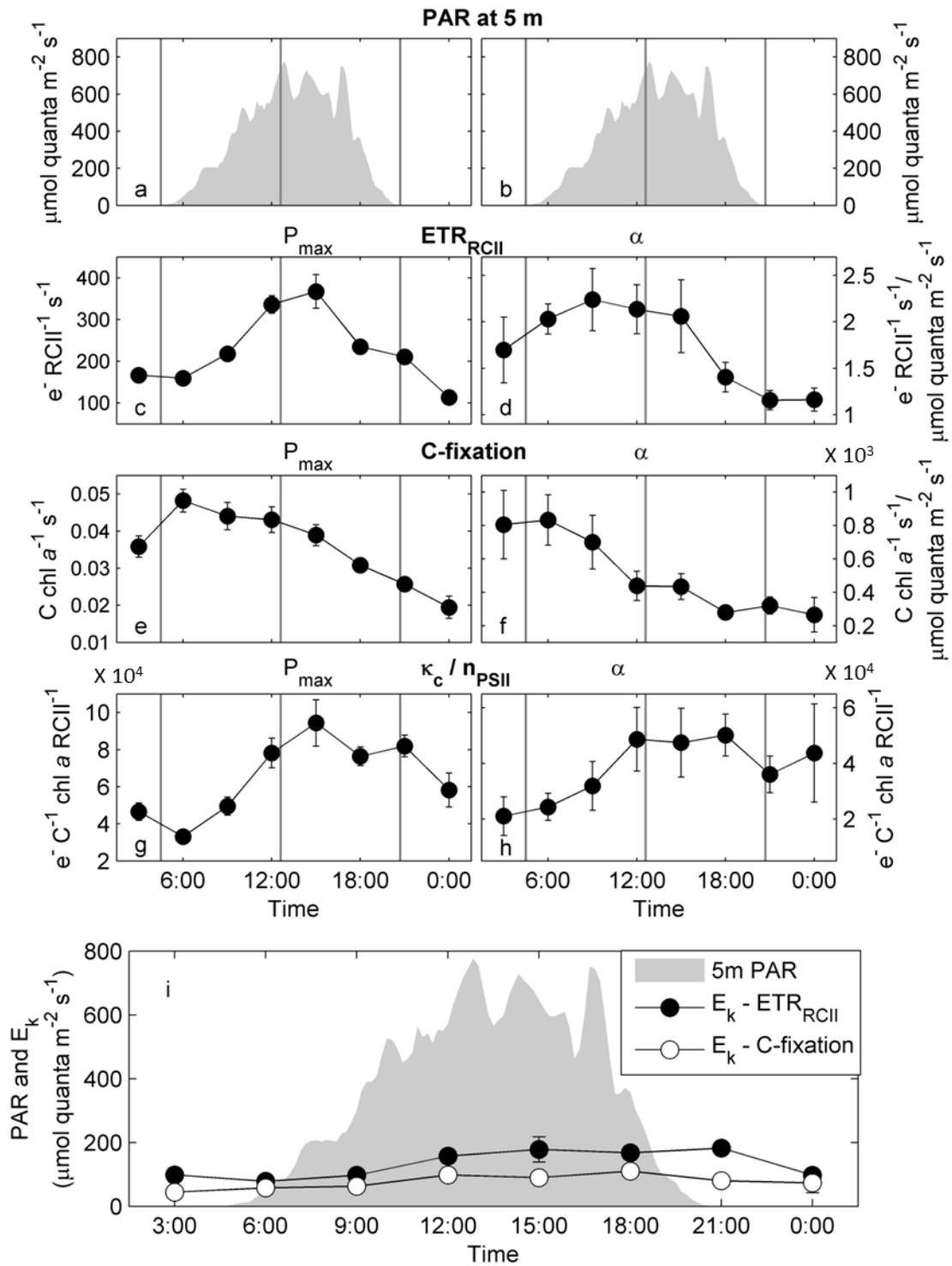


**Figure 3.2: Diurnal changes in capacities and efficiencies of  $E_{TR_{RCII}}$  and carbon fixation and the derived conversion factor  $K_c/n_{PSII}$ . The conversion factor  $K_c/n_{PSII}$  at light saturation (g) is derived from the values in (c) and**

(e). Similarly, the conversion factor  $K_c/n_{PSII}$  under light limiting conditions (h) is derived from values in (d) and (f). The error in (b), (c), (e), and (f) is the 95 % confidence interval of the parameter derived from the fit to data shown in Figure 3.1 , and the error in (d) and (g) is the propagated error for (b)/(c) and (e)/(f), respectively. PAR at 5 m depth is shown in (a) and (b). The vertical gray lines in panel (a-h) mark sunrise, solar noon and sunset. Panel (i) shows the light saturation parameter  $E_k$  for  $ETR_{RCII}$  and carbon fixation in relation to *in situ* light availability.

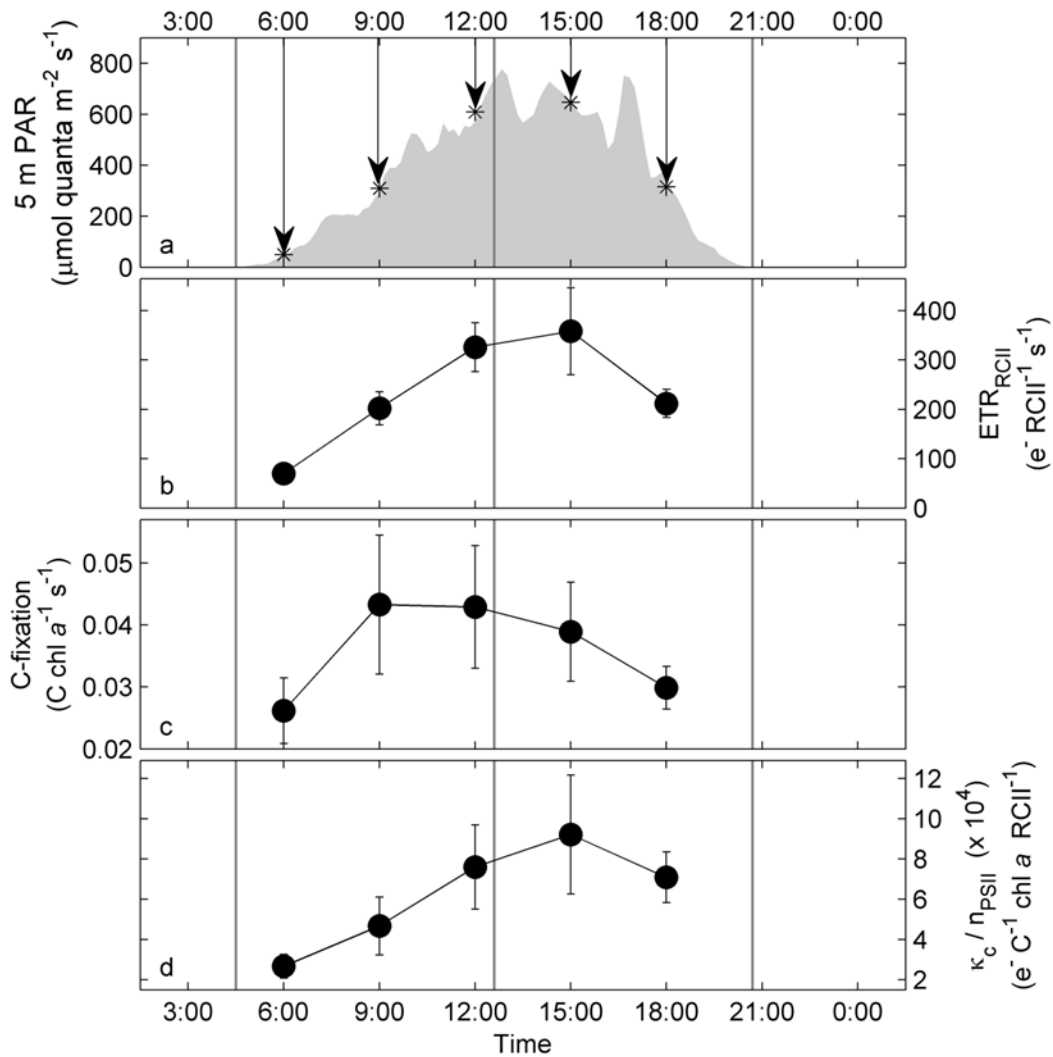


**Figure 3.3: Diurnal changes in  $\text{ETR}_{\text{RCII}}$ , carbon fixation and  $\kappa_c/n_{\text{PSII}}$  derived for *in situ* light intensities at 5 m depth.** Diurnal changes in irradiance at 5 m depth (a), with arrows indicating the PAR value used to derive rates in (b) and (c). Realized rates of  $\text{ETR}_{\text{RCII}}$  (b) and carbon fixation (c) at each time-point were derived from the PvsE relationship established in Figure 3.1. The error in (b) and (c) is the propagated 95 % confidence interval of the parameter PvsE fit parameters, and the error in (d) is the propagated error from (b)/(c). The vertical gray lines in all plots mark sunrise, solar noon and sunset.

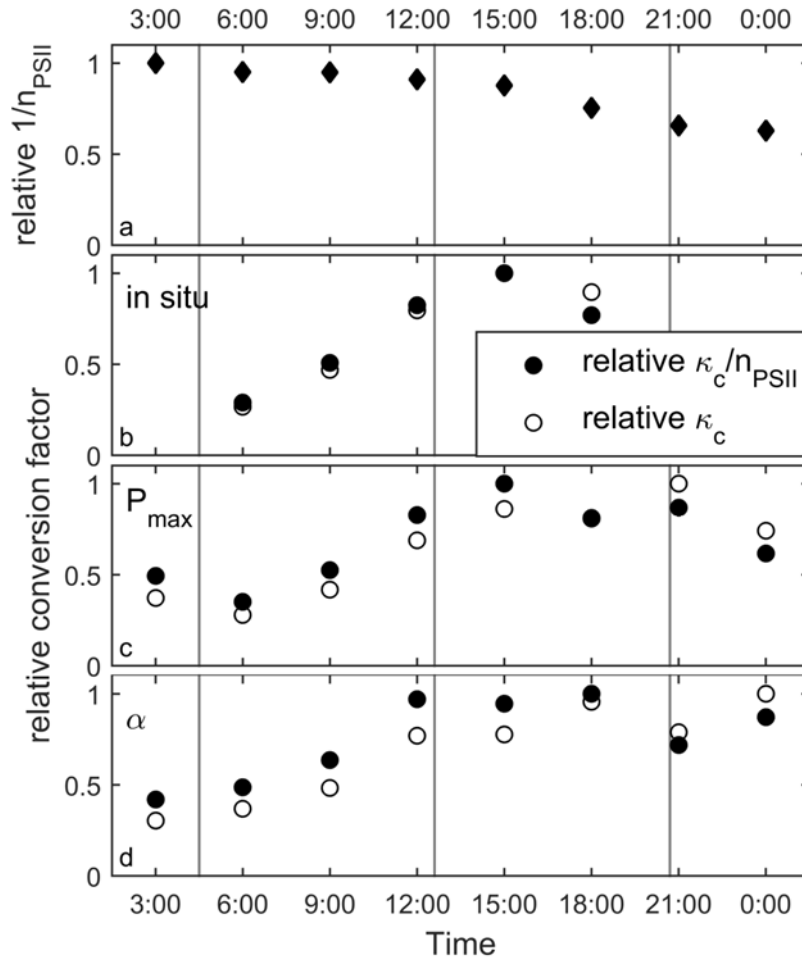


**Figure 3.4: Relative changes in the components of our conversion factor  $K_c/n_{PSII}$  over the diurnal cycle.** Panel (a) shows diurnal changes in  $1/n_{PSII}$  ( $\text{mol chl}a \text{ mol RCII}^{-1}$ ), estimated as  $(F_o/\sigma_{PSII})/[chl a]$ . These relative values of  $1/n_{PSII}$  were then used to derive relative values of  $K_c$  ( $\text{mol e}^- \text{ mol C}^{-1}$ ) from values of  $K_c/n_{PSII}$ . This was done for the conversion factor derived for *in situ* irradiances at 5 m depth (b), the conversion factor derived for light saturated rates (c) and the conversion factor for light limited rates (d). All values are scaled to 1 for clarity.

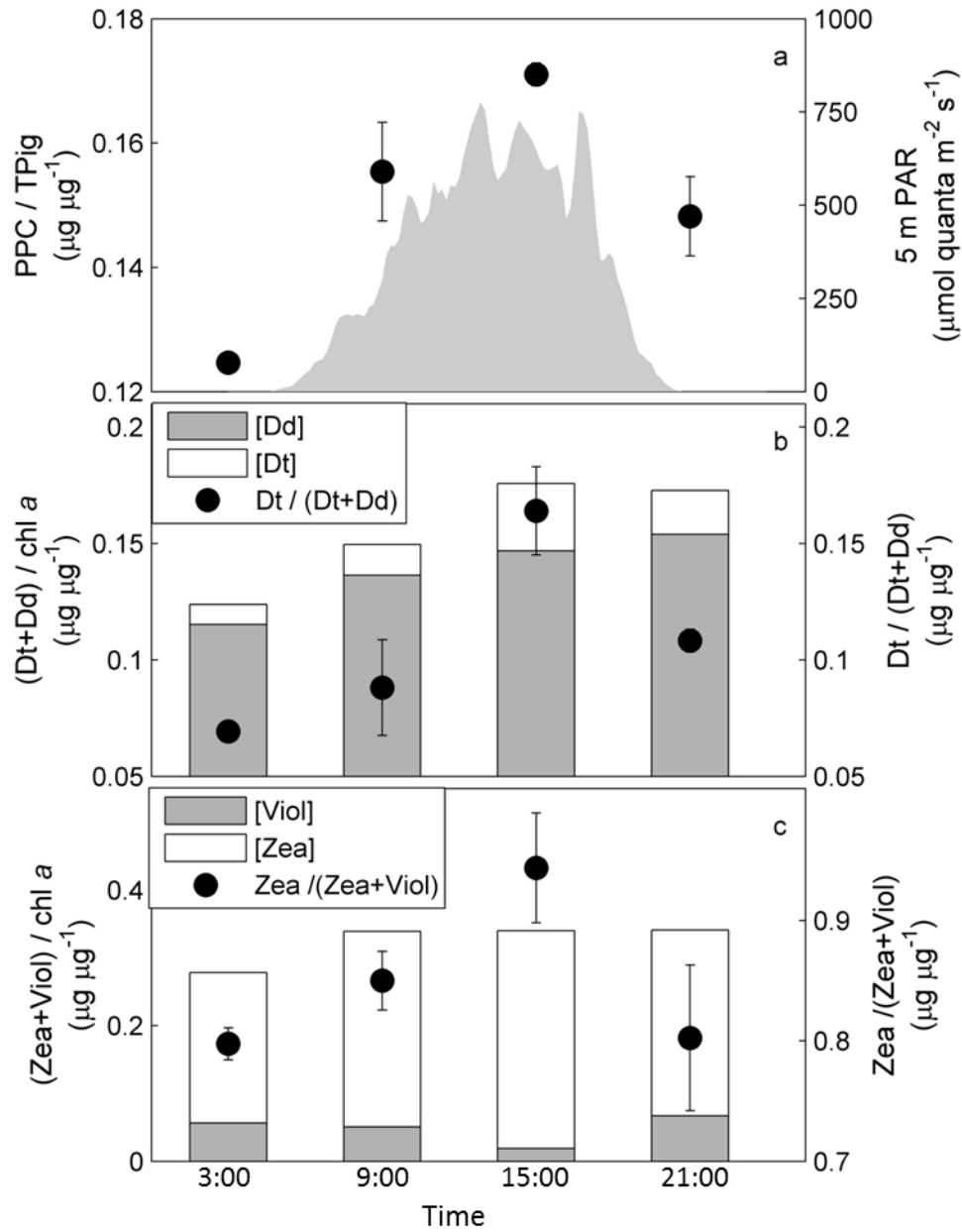


**Figure 3.5: Diurnal changes in pigment ratios.** Panel (a) shows changes in the abundance of all photo-protective pigment (PPC), relative to the total pigment present (TPig) at each time-point. See Table 3.2 for a definition of pigment groups used to derive these ratios. Panel (b) shows relative changes in the abundance of the chromophyte xanthophyll cycling pigments Dd and Dt, normalized to [chl *a*]. Changes in the de-epoxidation state ration (DES ratio = Dt/(Dt+Dd)), also shown in (b), indicate the extent of active photo-protective energy dissipation through xanthophyll cycling in the pigment antenna. Similarly, panel (c) shows xanthophyll cycling pigments Viol and Zea, specific to prasinophytes and chlorophytes. Error bars are the range of values from two replicate samples taken at each time-point.

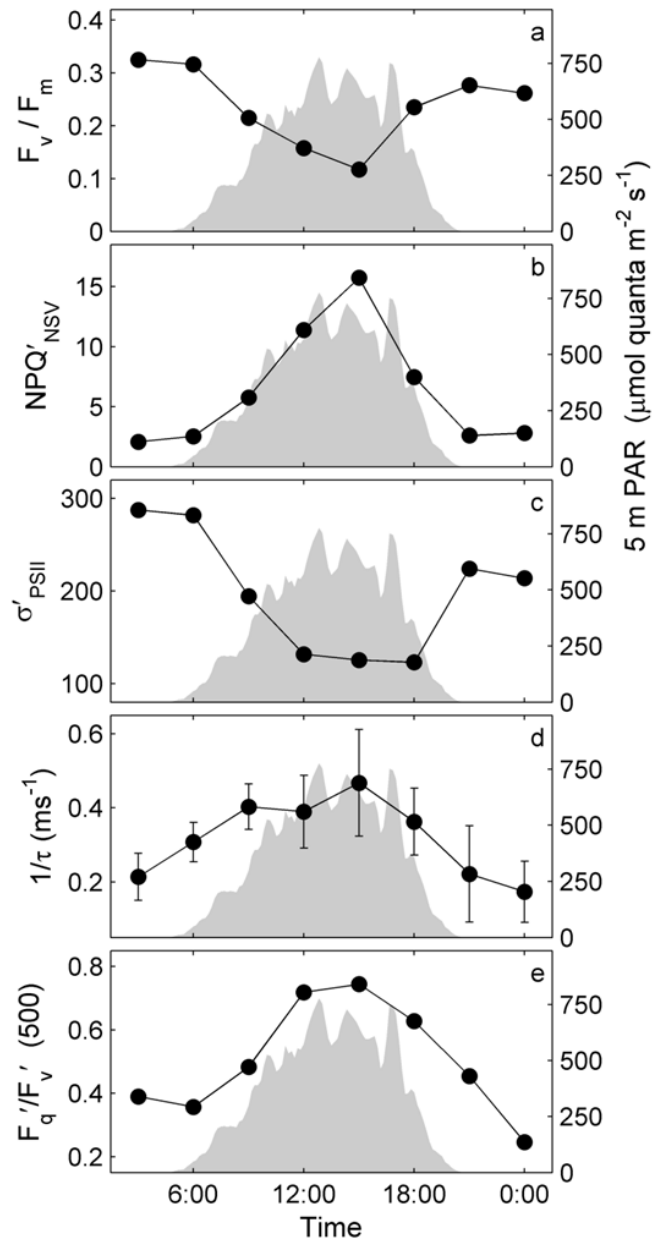


**Figure 3.6: Diurnal changes in PSII photo-physiological parameters derived from FRRF measurements.** Panel (a)  $F_v/F_m$  in the dark-regulated state at each TP. Panel (b) and (c) show the normalized Stern-Volmer quenching,  $NPQ'_{NSV}$ , derived as  $F_o'/F_v'$  (McKew et al., 2013) and the functional absorption cross section,  $\sigma'_{PSII}$ , both estimated for *in situ* light availability at each TP. Values in (b) and (c) were calculated by extrapolating between values derived for each light step of the FRRF steady state light curves. Panel (d) shows estimates of the rate of re-oxidation of  $Q_A$ . Panel (e) shows estimates of photochemical quenching ( $F_q'/F_v'$ ), indicating the fraction of open RCII (primary stable electron acceptor  $Q_A$  oxidized) at a reference irradiance level of  $500 \mu\text{mol quanta m}^{-2}\text{s}^{-1}$ .

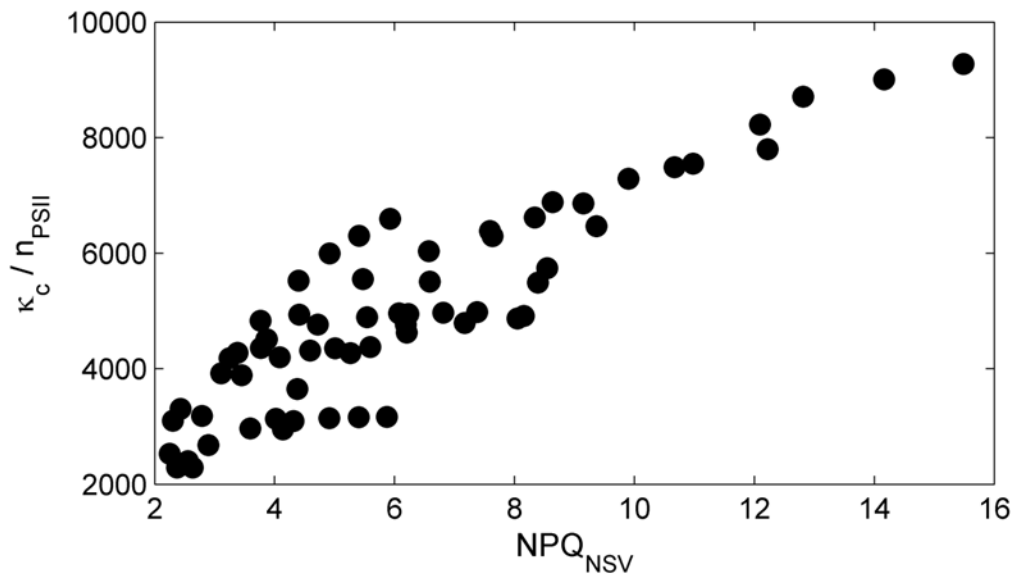


**Figure 3.7: Correlation between the conversion factor  $K_c/n_{PSII}$  and the expression of  $NPQ_{NSV}$ .**  $NPQ_{NSV}$  was derived as  $F_o'/F_v'$  (McKew et al., 2013), for each step of the FRRF light curve at each TP. Values of  $K_c/n_{PSII}$  corresponding to the same light intensities were derived by extrapolation along the carbon fixation and  $ETR_{RCH}$  based  $PvsE$  curves.

## Chapter 4: Primary productivity and the coupling of photosynthetic electron transport and carbon fixation in the Arctic Ocean

---

### 4.1 Summary

We examined the light absorption properties and light-dependent rates of photosynthetic electron transport and  $^{14}\text{C}$ -uptake in phytoplankton of the Canadian Subarctic and Arctic Ocean. Our results reveal high variability in the light-saturated, chlorophyll *a*-specific rate of  $^{14}\text{C}$ -uptake ( $P_{\text{max}}^{\text{chla}}$ ; 0.7 to 8.0 mg C mg chl $a^{-1}$  h $^{-1}$ ), and the light-dependant efficiency of  $^{14}\text{C}$ -uptake ( $\alpha^{\text{chla}}$ ; 0.01 to 0.09 mg C mg chl $a^{-1}$  h $^{-1}$  [ $\mu\text{mol quanta m}^{-2} \text{ s}^{-1}$ ] $^{-1}$ ). Variability in  $P_{\text{max}}^{\text{chla}}$  was tied to light availability in the stratified water-column, while both  $P_{\text{max}}^{\text{chla}}$  and  $\alpha^{\text{chla}}$  were correlated to the degree of nitrate depletion in the mixed layer. For all samples, we observed that  $^{14}\text{C}$ -uptake rates reached light saturation at lower irradiances than  $\text{ETR}_{\text{RCII}}$ , leading to significant, light-dependent de-coupling of the two rates. For samples taken from within the mixed layer, we found that the conversion factor from photochemistry to carbon fixation was strongly correlated with the magnitude of non-photochemical quenching, as derived from FRRF measurements. This correlation, which supports recent findings from the Subarctic Pacific Ocean, has the potential to greatly improve the quantification of carbon-based primary productivity from FRRF measurements alone. Our observations reveal distinct photo-physiological strategies for optimizing productivity within and below the shallow summer Arctic mixed layer, and provide mechanistic understanding of the environmental regulation of light absorption, electron transport and carbon fixation. Such mechanistic insight is important for more robust prediction of future primary production in a rapidly changing Arctic Ocean.

### 4.2 Introduction

The Arctic Ocean represents one of the most rapidly changing and least studied regions of the world's oceans (e.g. Wassmann, 2015; Wassmann et al., 2011). Anticipated changes in ice cover, light penetration, mixed layer stratification, and nutrient supply will inevitably affect phytoplankton primary productivity (i.e. photosynthetic conversion of  $\text{CO}_2$  into organic carbon), and this will, in turn, influence ecosystem carrying capacity and  $\text{CO}_2$  sequestration potential (e.g.

Tremblay et al., 2015). In recent years, there has been increased focus on quantifying Arctic Ocean primary productivity, based on new *in situ* measurements (Coupel et al., 2015a; Fernández-Méndez et al., 2015; Huot et al., 2013a; Martin et al., 2012; Palmer et al., 2011, 2013; Varela et al., 2013), compilations of historical data (Codispoti et al., 2013; Hill et al., 2013; Matrai et al., 2013), regional tuning of remote sensing algorithms (Ardyna et al., 2014; Arrigo and van Dijken, 2011; Browning et al., 2014a; Lewis et al.; Pabi et al., 2008; Petrenko et al., 2013) and numerical modeling approaches (Dupont, 2012; Hu et al., 2016; Popova et al., 2012; Vancoppenolle et al., 2013). Collectively, these studies have demonstrated strong heterogeneity of phytoplankton primary productivity in Subarctic and Arctic regions, driven primarily by the availability of light and macro-nutrients. High rates of productivity are associated with ice edge (Perrette et al., 2011) and under-ice blooms (Arrigo et al., 2012), while strong density stratification and the development of deep chlorophyll maxima (DCM) are important later during the growing season (Martin et al., 2013; Tremblay et al., 2015). To further improve our understanding of phytoplankton productivity in the Arctic Ocean, it is critical to increase the spatial and temporal coverage of *in situ* measurements, and improve the mechanistic understanding of how the photosynthetic process is adapted to, and controlled by, the unique environmental constraints of the Arctic Ocean environment. The experimental approach taken in the present study aims to address both of these issues.

The principal objective of the present study was to quantify Arctic Ocean primary productivity from simultaneous measurements of different components of the photosynthetic process (light absorption, photosynthetic electron transport, and carbon fixation), and to examine how these processes respond to dominant environmental gradients, including light and nutrient levels. Our approach allowed us to gain insight into the coupling of different components of the photosynthetic process leading to primary production. This, in turn, provides mechanistic insight into the environmental controls on phytoplankton productivity, and the physiological processes used by Arctic phytoplankton assemblages to tune photosynthetic processes to specific environmental conditions.

Our approach also allowed us to directly compare rates of phytoplankton primary production as estimated from standard  $^{14}\text{C}$ -uptake experiments with estimates of initial charge separation in photosystem II ( $\text{ETR}_{\text{RCII}}$ ) as estimated from measurements of chlorophyll a ( $\text{chl}a$ ) fluorescence yields by fast repetition rate fluorometry (FRRF). The FRRF technique was

developed for oceanographic research over 20 years ago (Kolber et al. 1998), and many authors have sought to apply this method to obtain high resolution productivity estimates without the need for sample containment (e.g. Suggestt et al., 2010). Because FRRF instruments can be deployed *in situ* for autonomous data collection at unprecedented spatial and temporal resolution, they could play a significant role in expanding the coverage of primary productivity data in the Arctic Ocean (Hancke et al., 2015). However, the conversion of FRRF-derived  $ETR_{RCH}$  into ecologically-relevant rates of carbon fixation requires a sound understanding of the coupling between the two processes, in relation to various metabolic processes which reflect environmental constraints (Lawrenz et al., 2013; Suggestt et al., 2009a). Such mechanistic insight is presently lacking for Arctic Ocean phytoplankton assemblages.

We report significant variability in the conversion factor between  $ETR_{RCH}$  and  $^{14}C$ -uptake, and demonstrate that this variability can be related to the extent of excitation energy experienced at the photo-physiological level, which acts as an integrated expression of environmental constraints. We further show that, for samples taken from within the upper mixed layer, the conversion factor can be empirically related to FRRF-based estimates of non-photochemical quenching (NPQ), supporting recent findings (Schuback et al., 2015, 2016; Zhu et al., 2016) and providing additional support for the applicability of this proxy approach.

Our results provide new measurements of Arctic primary productivity, and insight into the unique environmental controls of phytoplankton photo-physiology and carbon fixation. The mechanistic insights derived from our observations will be helpful in the continued development of regional Arctic Ocean productivity models and satellite algorithms, ultimately leading to more robust predictions of future changes in primary productivity in the Arctic Ocean (Babin et al., 2015; Lee et al., 2015).

## 4.3 Methods

### 4.3.1 Sample collection

Samples were collected onboard the *CCGS Amundsen* between July 14<sup>th</sup> and August 18<sup>th</sup> 2015, on a transect from Quebec City, Qc, to Kugluktuk, Nunavut, Canada (Figure 4.1). At 9 out of 12 stations, samples were collected from two depths; within the mixed layer at approximately 50 % surface irradiance, and below the mixed layer, targeting the deep chlorophyll maximum

(DCM), if present. Samples were collected using a Niskin bottles on a rosette equipped with a Conductivity-Temperature-Depth (CTD) sensor (Seabird). At 3 stations we only sampled at one depth within the mixed layer, using the ship's underway water supply (nominal sampling depth 7 m). Mixed layer depth (MLD) was calculated from temperature and salinity-derived density profiles, using a density difference criterion ( $\Delta\sigma = 0.125 \text{ kg m}^{-3}$ ). We aimed to collect all samples between approximately 2 and 4 hours after local sunrise (Table 4.1). A depth profile of photosynthetically available radiation (PAR, 400-700 nm,  $\mu\text{mol quanta m}^{-2} \text{ s}^{-1}$ ) was obtained using a PNF-300 radiometer (Biospherical Instruments) deployed before the rosette cast and used to calculate the optical extinction coefficient,  $k_d$  ( $\text{m}^{-1}$ ), as

$$k_d = (\ln E_0 - \ln E_z) / z \quad (4.1)$$

Where  $E_0$  and  $E_z$  (400-700 nm,  $\mu\text{mol quanta m}^{-2} \text{ s}^{-1}$ ) are the irradiance at surface and at depth  $z$  (m), respectively. Additionally, surface PAR was continuously logged (10 minute intervals) with a down-welling PAR sensor (Li-COR), mounted in a non-shaded position on the ship's superstructure. Surface irradiance ( $E_0$ ) at the time of sampling was calculated as the average PAR measured during the time of the cast and used to estimate instantaneous *in situ* PAR ( $E_z$ ) as

$$E_z = E_0 \times \exp(-k_d \times z) \quad (4.2)$$

Furthermore, we calculated optical depth (OD) at each sampling depth as

$$OD = z \times k_d \quad (4.3)$$

Filtered (0.2  $\mu\text{m}$ ) seawater samples for nitrate ( $\text{NO}_3$ ), nitrite ( $\text{NO}_2$ ), phosphate ( $\text{PO}_4$ ) and silicate ( $\text{Si}[\text{OH}]_4$ ) analyses were stored at  $-20 \text{ }^\circ\text{C}$  until analysis using an automated nutrient analyzer (Bran and Luebbe Autoanalyzer III) within a few days. Ammonium ( $\text{NH}_4^+$ ) was determined by fluorometry following the method of Holmes et al., (1999). A summary of all measured variables is provided in Table 4.1 and Table 4.2.

#### 4.3.2 [chl<sub>a</sub>] and HPLC

For each station and depth, duplicate samples (250-500 mL) for total [chl<sub>a</sub>] analysis were filtered onto 25 mm glass fiber filters (GF/F, Whatman, 0.7  $\mu\text{m}$  nominal pore size) using low vacuum pressure (<100 mm Hg). For size fractionated [chl<sub>a</sub>], separate water samples (200-500

mL) were filtered onto polycarbonate membrane filters (5  $\mu\text{m}$  pore size). Filters were stored at -20 °C and [chl $a$ ] was determined fluorometrically in 90 % acetone extracts following the method of Welschmeyer (1994) within a few days of sample collection. Additionally, duplicate 1-2 L samples were filtered onto 25 mm GF/F for pigment analysis by reverse-phase high-performance liquid chromatography (HPLC). Filters were blotted dry with absorbent paper, flash frozen in liquid nitrogen and stored at -80 °C until analysis following the method of Pinckney (2013). Pigment data were used to estimate the relative abundance of different phytoplankton taxa at each sampling point using CHEMTAX V1.9 analysis (Wright and Jeffreys 2006), essentially as described in Taylor et al. (2013). Pigment ratio matrices for ML (high light) and sub-ML (low light) samples were taken from Higgins et al. (2011) and Coupel et al. (2015b). These preliminary pigment ratios were optimized for function in our dataset by running them on ML and sub-ML samples from station K1. The output matrices from this optimization step were subsequently used as initial matrices for all samples. The average final matrices for both ML and sub-ML samples differed from the optimized initial matrices by less than 30 %. Final pigment ratio matrices are given Table B2 in the appendix.

Identified pigments were grouped into photosynthetic carotenoids (PSC), photo-protective carotenoids (PPC) and total chlorophyll (TChl). Following Roy et al. (2011) we defined PSC as 19'butanoyloxyfucoxanthin + fucoxanthin + 19'hexanoyloxyfucoxanthin + prasinoxanthin +  $\alpha$ -carotene; while the PPC include 9'cis-neoxanthin + violaxanthin + diadinoxanthin + alloxanthin + diatoxanthin + lutein + zeaxanthin +  $\beta$ -carotene. Total chlorophyll was defined as chl  $c_3$  + chl  $c_1c_2$  + chl  $b$  + chl $a$  allomer + chl $a$  + divinyl chl $a$  + chl $a'$  + chlorophyllide  $a$ . Ratios of these pigment groups were used to assess the extent of light stress experienced by the phytoplankton assemblages sampled.

We also used the HPLC pigment dataset to estimate size distribution of phytoplankton cells within the assemblages sampled using the method developed by Uitz et al. (2006) as applied to Arctic Ocean phytoplankton assemblages by Huot et al. (2013).

### **4.3.3 Absorption spectra**

Absorption spectra of phytoplankton cellular pigments ( $a_{\text{phy}}(\lambda)$ ) were determined following the quantitative filter technique (Mitchell et al., 2002). For each sampling point, duplicate 0.5 – 1.5 mL samples were filtered onto pre-combusted 25 mm GF/F under low

vacuum pressure and light, taking care to achieve even sample distribution on the filter. Reference filters were prepared by filtering 1.1 L of Milli-Q water. Filters were carefully placed into 25 mm tissue capsules (Fisher Scientific), flash frozen in liquid nitrogen and stored at -80 °C until analysis. Sample filters were analyzed on a Cary BIO-100 dual-beam spectrophotometer (Varian) against reference filters as described in Mitchell et al. (2002). Optical density (OD) was measured from 370-750 nm (1 nm resolution) before and after extraction of pigment with 90 % methanol (Kishino et al., 1985) to determine OD of the whole particulate sample and OD of detritus after pigment extraction, respectively. Each sample and blank was analyzed in duplicate, to minimize error associated with instrument measurements. Following Bricaud and Stramski (1990), an empirical path length amplification factor ( $\beta$ ) was used to correct for the differential scattering of cells on the filter and cells in suspension.

The wavelength-specific phytoplankton pigment absorption ( $a_{phy}(\lambda)$ ,  $m^{-1}$ ) was calculated as:

$$a_{phy}(\lambda) = 2.303 \times OD_{sample} \times A/V \quad (4.4)$$

where 2.303 is the conversion of from base-10 to a natural logarithm, A is the particulate retention area of the filter ( $m^2$ ), and V is the volume filtered ( $m^3$ ). To determine *chl a* specific absorption spectra ( $a_{chl a}^{phy}(\lambda)$ ,  $m^2 \text{ mg chl a}^{-1}$ ), values were normalized to corresponding [*chl a*] values. Furthermore, we derived the spectrally averaged (400-700 nm) *chl a* specific phytoplankton absorption coefficient ( $\bar{a}_{phy}^{chl a}$ ,  $m^2 \text{ mg chl a}^{-1}$ ) weighted for the spectrum of available light as

$$\bar{a}_{phy}^{chl a} = \frac{\sum_{400}^{700} a_{phy}^{chl a}(\lambda) E_{insitu}(\lambda)}{\sum_{400}^{700} E_{insitu}(\lambda)} \quad (4.5)$$

#### 4.3.4 $^{14}\text{C}$ – uptake

Rates of carbon fixation were measured as duplicate small volume light-response curves in a custom built photosynthetron as described in Schuback et al. (2015). All sample manipulations were conducted under low light and temperature conditions. Samples (470 mL) were spiked with  $\text{NaH}^{14}\text{CO}_3$  (final concentration  $22 \text{ kBq mL}^{-1}$ ,  $2.109 \text{ MBq mol}^{-1}$  specific activity, Perkin-Elmer) within 30 minutes of sampling, mixed gently but thoroughly, and then aliquoted into 20 ml glass scintillation vials and placed into the photosynthetron. Temperature in

the photosynthesizer was kept within 1°C of sea surface temperature by circulating water from a water-bath through an aluminum cooling jacket. The total  $^{14}\text{C}$  activity added was determined from three 0.5 mL aliquots of the spiked sample added to 0.5 mL of 1 M NaOH. Additionally, two time-zero samples were taken for each duplicate curve by filtering 20 mL immediately after adding the spike. Each  $^{14}\text{C}$ -uptake vs E curve consisted of 10 light levels spanning intensities from 3 to 500  $\mu\text{mol quanta m}^{-2} \text{ s}^{-1}$ . Incubations lasted for 2 hours and were ended by gentle filtration onto pre-combusted 25 mm GF/F filters. Filters were returned to the scintillation vials, acidified with 0.5 mL of 1 M HCl and left to degas for > 24 hours to eliminate any inorganic  $^{14}\text{C}$  remaining in the samples. Ten mL of scintillation cocktail (ECOLUM<sup>TM</sup>, MP Biomedicals) were added to each vial, and vials were then vortexed and left to stand in the dark for >12 hours before analysis on a liquid scintillation counter (Beckman). Disintegrations per minute (DPM) were derived from scintillation counts using a quench curve prepared from commercial  $^{14}\text{C}$  standards. DPM were converted to units of carbon biomass following Knap et al. (1996), and all calculations were adjusted for the dissolved inorganic carbon (DIC) concentration measured at each station and depth.

After spectral correction (see below), [chl $a$ ]-normalized rates of  $^{14}\text{C}$ -uptake were plotted against irradiance and fit to the exponential model of Webb et al. (1974), including an intercept parameter (Arrigo et al., 2010; Suggett et al., 2001). Using a non-linear least squares regression procedure in MATLAB, we derived the light saturated maximum rate  $P_{\text{max}}^{\text{chl}a}$  ( $\text{mg C mg chl}a^{-1} \text{ h}^{-1}$ ), the light utilization efficiency  $\alpha^{\text{chl}a}$  ( $\text{mol C mol chl}a^{-1} \text{ s}^{-1} [\mu\text{mol quanta m}^{-2} \text{ s}^{-1}]^{-1}$ ), and the light saturation point  $E_k$  ( $=P_{\text{max}}/\alpha$ ,  $\mu\text{mol quanta m}^{-2} \text{ s}^{-1}$ ).

#### **4.3.5 FRRF photo-physiology and ETR<sub>RCII</sub>**

Measurements chl $a$  fluorescence (ChlF) yields were conducted on a bench-top FRRF instrument (Soliense Inc.). For each sample, background fluorescence blanks were prepared by gently syringe filtering a small amount of water through a pre-combusted GF/F. We applied a single turnover (ST) protocol consisting of an excitation sequence (70 flashlets with 0.7  $\mu\text{s}$  length and 2.5  $\mu\text{s}$  interval, 87800  $\mu\text{mol quanta m}^{-2} \text{ s}^{-1}$  peak power intensity, resulting in a excitation sequence of 225  $\mu\text{s}$ , providing ~7-12 quanta per RCII) and a relaxation sequence (50 flashlets with 0.7  $\mu\text{s}$  length and 20  $\mu\text{s}$  initial interval, where the interval between flashlets was set to increase exponentially, resulting in a gradual decrease of the average excitation power).

Excitation power was provided by at four wavelengths centered on 445, 470, 505, and 530 nm (equal intensity from each wavelength, applied simultaneously). We measured steady state light response curves, where each sample was exposed to 9 actinic ‘background’ irradiances from 0 to 1000  $\mu\text{mol quanta m}^{-2} \text{s}^{-1}$ , provided at the same four wavelengths. All ChlF yields and parameters described below were derived by an iterative non-linear fitting procedure, applying the four parameter biophysical model of Kolber et al. (1998) to a mean of 10 consecutive ST flashlet sequences using custom software (Z. Kolber). Throughout the light curve, ST flashlet sequences were measured continuously (1 s interval) and the length of each light step was optimized to allow all derived parameters to reach steady state (20 acquisitions pre light level). ChlF yields and parameters corresponding to each light level were obtained from the mean of the last two acquisitions at each light level. In this way, we derived the ChlF yields  $F_o$  and  $F_m$  (in dark-regulated state) as well as  $F'$  and  $F_m'$  (in the light regulated state for each light level of the light curve).  $F_o'$  was calculated as  $F_o' = F_o / (F_v / F_m + F_o / F_m')$  (Oxborough and Baker, 1997).

The five fluorescence yields  $F_o$ ,  $F_m$ ,  $F'$ ,  $F_m'$  and  $F_o'$  were used to calculate ChlF parameters, following Roháček (2002) as described in Schuback et al. (2015). Furthermore, the functional absorption cross section of PSII,  $\sigma_{\text{PSII}}$  ( $\text{\AA}^2 \text{RCII}^{-1}$ ), was derived from the rate of closure of RCII in the dark-regulated and each light-regulated state (Kolber and Falkowski, 1993; Kolber et al., 1998). The parameter  $\sigma_{\text{PSII}}$  was spectrally corrected, as described below.

We calculated  $\text{ETR}_{\text{RCII}}$  as:

$$\text{ETR}_{\text{RCII}} = E \times \sigma'_{\text{PSII}} \times q_P \times \Phi_{\text{RC}} \times 6.022 \times 10^{-3} \quad (4.6)$$

where  $E$  ( $\mu\text{mol quanta m}^{-2} \text{s}^{-1}$ ) is the actinic irradiance at each light level,  $\sigma'_{\text{PSII}}$  ( $\text{\AA}^2 \text{RCII}^{-1}$ ) is the functional absorption cross section of PSII at each light level, and  $q_P$  ( $= F_q' / F_v'$ ) is the quantum efficiency of photochemical energy conversion in RCII at a given light intensity. The parameter  $\Phi_{\text{RC}}$  ( $\text{mol e}^- \text{mol photon}^{-1}$ ) has the constant value of 1, given that for each photon absorbed and delivered to RCII, one electron is transferred from  $\text{P}_{680}$  to  $\text{Q}_A$  (Kolber and Falkowski, 1993). The number  $6.022 \times 10^{-3}$  converts  $\mu\text{mol quanta}$  to quanta and  $\text{\AA}^2$  to  $\text{m}^2$ .

We followed the approach of Silsbe and Kromkamp (2012) to derive the curve fit parameters  $\text{P}_{\text{max}}^{\text{RCII}}$  ( $\text{mol e}^- \text{mol RCII}^{-1} \text{s}^{-1}$ ),  $\alpha^{\text{RCII}}$  ( $\text{mol e}^- \text{mol RCII}^{-1} \text{s}^{-1} [\mu\text{mol quanta m}^2 \text{s}^{-1}]^{-1}$ ) and  $E_k$  ( $= \text{P}_{\text{max}} / \alpha$ ,  $\mu\text{mol quanta m}^2 \text{s}^{-1}$ ) of  $\text{ETR}_{\text{RCII}}$ . This approach avoids the explicit dependence of  $\text{ETR}_{\text{RCII}}$  on the predictor variable ( $E$ ), when fitting  $\text{ETR}_{\text{RCII}}$  vs  $E$  curves. In order to fit the data,

we used a modified version of the exponential model of Webb et al (1974) to relate ( $\sigma'_{PSII} \times q_P$ ) to the background irradiance during the FRRF measurements (E):

$$(\sigma'_{PSII} \times q_P) = [P_{max}(1 - \exp(-\alpha \times E/P_{max}))] \times E^{-1} \quad (4.7)$$

The conversion factor between rates of  $ETR_{RCII}$  and  $^{14}C$ -uptake ( $K/n_{PSII}$ ;  $\text{mol e}^- \text{mol C}^{-1} \text{mol chl}a \text{mol RCII}^{-1}$ ) was derived as described in detail in Schuback et al. (2016).

The rate constants of a series of electron transport processes after charge separation in RCII were estimated from fitting three exponential decay components to ChlF decay kinetics during the relaxation sequence of the ST protocol. In this way, we estimated the rate constants for  $1/\tau_1$  (re-oxidation of  $Q_A$ , i.e. electron transfer from  $Q_A$  to  $Q_B$ ,  $\text{ms}^{-1}$ ), and the size of the PQ pool ( $\text{mol PQ mol } Q_B^{-1}$ ).

Non-photochemical quenching (NPQ) at each light level was estimated as the so-called normalized Stern-Volmer quenching coefficient,  $NPQ_{NSV} = (F_m'/F_v') - 1 = F_o'/F_v'$  (McKew et al., 2013). This alternative approach to the more common estimate of  $NPQ = (F_m - F_m')/F_m'$  (Bilger and Björkman, 1990) represents the ratio of total non-photochemical energy dissipation in the light-regulated state to the rate constant of photochemistry (McKew et al., 2013).

#### 4.3.6 Spectral correction

To account for differences in the spectral distribution of LEDs used in the photosynthetron and FRRF instruments, and to estimate rates which are appropriate for the spectral distribution of light at the sampling depth in relation to the spectral absorption capacity of the phytoplankton assemblage, we calculated a spectral correction factor (SCF), specific to each station and depth.

$$SCF = \frac{\sum_{400}^{700} a_{phy}^{chl}a(\lambda) E_{in\ situ}(\lambda) \sum_{400}^{700} E_{LED}(\lambda)}{\sum_{400}^{700} a_{phy}^{chl}a(\lambda) E_{LED}(\lambda) \sum_{400}^{700} E_{in\ situ}(\lambda)} \quad (4.8)$$

Here,  $a_{phy}(\lambda)$  ( $\text{m}^{-1}$ ) is the phytoplankton pigment absorption spectrum determined as described above,  $E_{LED}$  is the spectral distribution of the LEDs used in photosynthetron or FRRF, and  $E_{in\ situ}$  is the spectral distribution of sunlight at the sampling depth. We measured  $E_{LED}$  using a micro-spectrometer equipped with a fibre-optic probe (STS-VIS, Ocean Optics) and estimated  $E_{in\ situ}$  following Stomp et al. (2007) as

$$E(\lambda, z) = E_0(\lambda) \exp(-[K_w(\lambda) + K_{GT}(\lambda) + K_{PH}(\lambda)]z) \quad (4.9)$$

Here,  $E_0(\lambda)$  is the spectral distribution of incident sunlight and  $K_w(\lambda)$  ( $\text{m}^{-1}$ ) is the absorption by pure water (Pope and Fry, 1997).  $K_{GT}(\lambda)$  ( $\text{m}^{-1}$ ) is the absorption by dissolved and particulate organic matter, estimated as  $K_{GT}(\lambda) = K_{GT}(440)\exp(-S(\lambda - 440))$ . Values for  $K_{GT}(440)$  were measured in a 10 cm cuvette on a spectrometer (Ultrospec II, LKB Biochrom) referenced to a MilliQ water blank. Samples were taken at each station and prepared by sequential filtration through a GF/F and 0.2  $\mu\text{m}$  pore size syringe filter (acrodisc<sup>TM</sup>, Pall Corporation). The parameter  $S$  was assumed to be 0.017  $\text{nm}^{-1}$  (Kirk, 2010). Values for  $K_{PH}(\lambda)$  ( $\text{m}^{-1}$ ) were taken from the absorption spectra measured using the filter pad technique as described above. We acknowledge that this approach is not specifically designed for the optically complex waters of the Arctic Ocean, and values are only approximations of the actual spectral distribution of light at a specific depth.

#### 4.4 Results and Discussion

In the following, we first present observed rates of primary production derived from  $^{14}\text{C}$ -uptake experiments. We compare the magnitude and variability of the derived parameters  $\alpha^{\text{chla}}$  and  $P_{\text{max}}^{\text{chla}}$  with previous  $^{14}\text{C}$ -uptake datasets from the Arctic Ocean, and discuss the correlation of these parameters with environmental variables in the context of model development. We then examine photo-physiological processes at the level of light absorption and electron transport in PSII. Finally, we assess the stoichiometric relationships between photosynthetic electron transport and carbon fixation, examining variability in the coupling of these two processes in response to dominant environmental constraints. While our dataset is too small to draw general conclusions, our experimental approach allows us to gain some insight into how phytoplankton assemblages achieve optimal balance of the different components of the photosynthetic process, under the special environmental constraints of the Arctic Ocean. We also use our new observations to expand on recent work (Schuback et al., 2015, 2016) exploring the feasibility of predicting the conversion factor between  $\text{ETR}_{\text{RCII}}$  and  $^{14}\text{C}$ -uptake rates from FRRF derived estimates of non-photochemical quenching ( $\text{NPQ}_{\text{NSV}}$ ) in the pigment antenna.

#### **4.4.1 Hydrographic properties and phytoplankton community composition**

Our sampling stations spanned a wide geographic area, encompassing the Subarctic (Labrador Sea and Hudson Bay) and Arctic Ocean (Baffin Bay and Canadian Arctic Archipelago) (Figure 4.1), and exhibited significant chemical, physical and biological variability. The hydrographic characteristics of our 12 sampling stations are summarized in Table 4.1, while depth-specific physical and chemical data, and total chlorophyll *a* concentrations are given in Table 4.2. At all sampling stations, the upper mixed layer (defined as  $\Delta\sigma = 0.125 \text{ kg m}^{-3}$ ) was well defined and shallower than the euphotic zone (defined as 0.1 % surface light level). Chlorophyll *a* concentrations were consistently higher in samples collected below the mixed layer (sub-ML) relative to mixed layer samples (ML), with well-defined sub-ML chlorophyll maxima present at 4 stations. Size fractionated chl*a* data revealed that a significant portion of phytoplankton biomass in both the sub-ML samples (41-93 %) and in ML samples (14-90 %) was  $> 5 \mu\text{m}$  (Table 4.2). The light attenuation coefficient,  $k_d$ , ranged from 0.07 to  $0.14 \text{ m}^{-1}$  (Table 4.1). Water temperature at the sampling depth ranged from  $-1.4$  to  $6.5 \text{ }^\circ\text{C}$  (Table 4.2), and was consistently lower at the sub-ML depth. As expected, macronutrient concentrations were lower in the ML samples (Table 4.2), particularly for  $\text{NO}_2+\text{NO}_3$ , whose concentrations were often more than an order of magnitude lower in the ML samples, relative to corresponding sub-ML samples (Table 4.2). With nitrate concentrations  $< 0.25 \mu\text{mol L}^{-1}$  (well below the half-saturation constant of nitrate uptake measured by Eppley et al., (1969)), and ratios of dissolved N:P significantly less than the 16:1 Redfield ratio (Table 2.4), we presume that nitrate availability was the limiting macro-nutrient controlling ML primary productivity, as has been previously demonstrated for this region (Tremblay and Gagnon, 2009a).

CHEMTAX analysis of pigments suggests that diatoms dominated phytoplankton assemblages at almost all stations (Table 4.3, appendix Figure B1). Dinoflagellates also appeared to be an important component of many ML assemblages, while the Prasino-3 group (including *Micromonas pusilla*, a species identified as very abundant in the Arctic Ocean, (Lovejoy et al., 2007) ) was present in many sub-ML samples. Hapto-7, a group including *Chrysochromulina* spp. was only abundant ( $>20 \%$  of total chl*a*) in the sub-ML samples in Baffin Bay (stations BB2 and BB3, Table 4.3, appendix Figure B1).

#### 4.4.2 Variability in $^{14}\text{C}$ -uptake rates

All  $^{14}\text{C}$ -uptake vs E curves are shown in Figure B2 in the appendix, while the derived fit parameters are summarized in Table 4.4. The maximum light-saturated  $^{14}\text{C}$ -uptake rates ( $P_{\text{max}}^{\text{chla}}$ ) varied greatly, ranging by more than an order of magnitude from 0.7 to 8.0 mg C mg chl $a^{-1}$  h $^{-1}$  (1.0 to 7.6 mg C mg chl $a^{-1}$  h $^{-1}$  when excluding samples from the Subarctic). These values are higher than what has been reported previously for the Arctic Ocean (Fernández-Méndez et al., 2015; Gallegos et al., 1983; Huot et al., 2013a; Palmer et al., 2011, 2013; Rao and Platt, 1984; Smith Jr and Sakshaug, 2013). One important explanation for the high values observed during the present study is the approach we used to account for differences in the spectral distribution of light available *in situ* compared to that that provided artificially in the photosyntheticron (see methods). The phytoplankton absorption spectrum matched the spectral distribution of *in situ* light more closely than the light provided by the LEDs used in the photosyntheticron, and spectral correction thus increased the derived  $^{14}\text{C}$ -uptake rates significantly (Figure B5 in the appendix). The average spectral correction factor was  $1.6 \pm 0.7$  for all samples,  $1.4 \pm 0.8$  for all ML and  $1.8 \pm 0.2$  for all sub-ML samples. Prior to spectral correction,  $P_{\text{max}}^{\text{chla}}$  values ranged from 0.39 to 5.16 mg C mg chl $a^{-1}$  h $^{-1}$ . These values are relatively high, but within the range previously observed in the Arctic Ocean (e.g. Babin et al., 2015; Coupel et al., 2015). We suggest that future studies employ spectral correction to derive the most ecologically-relevant and comparable rates of primary productivity from *in vitro* methods.

The high variability of  $P_{\text{max}}^{\text{chla}}$  values has important implications for the development of primary productivity algorithms. Many current productivity models for the Arctic Ocean assume a constant value for this parameter (see reviews by Babin et al., 2015; Lee et al., 2015). In contrast, our dataset, which includes observations from one season only, contains  $P_{\text{max}}^{\text{chla}}$  values that vary by a factor of 11 (7 when excluding Subarctic stations), suggesting that the assumption of constant  $P_{\text{max}}^{\text{chla}}$  is unrealistic. The maximum carbon fixation capacity of phytoplankton ( $P_{\text{max}}^{\text{chla}}$ ) is always controlled by multiple, interacting environmental variables. In our dataset, the two primary extrinsic drivers of variability in  $P_{\text{max}}^{\text{chla}}$  appeared to be light and nutrient levels. In support of previous observations (e.g. Huot et al., 2013), we found that  $P_{\text{max}}^{\text{chla}}$  decreased with depth, and was consistently lower and less variable for samples taken from under the mixed layer (Figure 4.2a and Figure 4.2d). The observed pattern can be attributed to photo-acclimation, where the phytoplankton community isolated below the upper mixed layer is well acclimated to

low and less variable light conditions, resulting in an increase in [chl $a$ ] per cell. For samples taken from within the mixed layer, we found that variability in  $P_{\max}^{\text{chl}a}$  was significantly correlated with nitrate concentration ( $R^2 = 0.93$ ,  $p < 0.005$ , Figure 4.3a), underscoring the role of macro-nutrient limitation as a constraint on carbon fixation capacity.

Values of  $\alpha^{\text{chl}a}$  (i.e. slope of the light-dependent increase in  $^{14}\text{C}$ -uptake) ranged from 0.01 to 0.09 mg C mg chl $a^{-1}$  h $^{-1}$  ( $\mu\text{mol quanta m}^{-2} \text{ s}^{-1}$ ) $^{-1}$  but did not show a consistent trend with depth (Figure 4.2b and Figure 4.2e). While some previous studies from the Arctic Ocean have reported increasing  $\alpha^{\text{chl}a}$  with depth (Martin et al., 2012; Palmer et al., 2011), this pattern is only expected for phytoplankton assemblages that include groups with primary light-harvesting pigments other than chl $a$  (i.e. cyanobacteria) (MacIntyre et al., 2002). Across our sampling stations, we did not find any evidence of cyanobacteria-rich phytoplankton assemblages, supporting previous observations at a range of locations across the Arctic Ocean (Li et al., 2009; Pedrós-Alió et al., 2015). The lack of depth dependence of  $\alpha^{\text{chl}a}$ , also observed by Huot et al. (2013), should thus, a priori, be expected for the Arctic Ocean. As observed for  $P_{\max}^{\text{chl}a}$ , values of  $\alpha^{\text{chl}a}$  within the ML samples were correlated with nitrate concentration ( $R^2 = 0.65$ ,  $p = 0.08$ , Figure 4.3b).

The light saturation parameter of  $^{14}\text{C}$ -uptake,  $E_k$ , was relatively low (consistently under 100  $\mu\text{mol quanta m}^{-2} \text{ s}^{-1}$ ), and strikingly invariable for samples taken from both within and under the mixed layer ( $78 \pm 10$  and  $39 \pm 7$   $\mu\text{mol quanta m}^{-2} \text{ s}^{-1}$ , respectively; Figure 4.2c and Figure 4.2f). The derived values of  $E_k$  for  $^{14}\text{C}$ -uptake are in good agreement with values reported previously for the Arctic Ocean (e.g. Huot et al., 2013). The low variability in  $E_k$  can be further visualized by plotting values of  $P_{\max}^{\text{chl}a}$  against the corresponding  $\alpha^{\text{chl}a}$  values (Figure 4.4). Presentation of the data in this way highlights the parallel changes in  $P_{\max}^{\text{chl}a}$  and  $\alpha^{\text{chl}a}$  within each growth regime (ML and sub-ML), which resulted in a relatively constant  $E_k$  (derived from the slope of the regression).

The observed changes in the maximum capacity ( $P_{\max}^{\text{chl}a}$ ) and efficiency ( $\alpha^{\text{chl}a}$ ) of  $^{14}\text{C}$ -uptake can be explained mechanistically as variability in the metabolic use of photosynthetically generated reductant (Behrenfeld et al., 2004, 2008). Specifically, the parallel changes in  $P_{\max}^{\text{chl}a}$  and  $\alpha^{\text{chl}a}$  imply a decoupling of photosynthesis at the level of PSII and  $^{14}\text{C}$ -fixation, as reductant is increasingly used for functions other than carbon fixation (Behrenfeld et al., 2004, 2008). An increase in the fraction of reductant allocated to functions other than carbon fixation would be expected when growth rate is slow (due to e.g. limitation by nutrients). Indeed we observed that

the parallel changes in  $P_{\max}^{\text{chla}}$  and  $\alpha^{\text{chla}}$  in ML samples correlate strongly with the extent of nitrate depletion (Figure 4.3a and Figure 4.3b). This result further demonstrates the influence of nitrate availability on primary productivity within the shallow summer mixed layer of the Subarctic and Arctic Ocean (Figure 4.3) (Tremblay and Gagnon, 2009b). Based on  $^{14}\text{C}$ -uptake data alone we can thus hypothesize a decoupling of photosynthetic electron transport and  $^{14}\text{C}$ -uptake under low nutrient conditions within the mixed layer. Below, we present direct observations supporting this hypothesis, and show how a mechanistic understanding of the coupling of electron transport and carbon fixation could lead to improved carbon-based estimates of phytoplankton primary productivity from FRRF measurements.

#### **4.4.3 Light absorption and photo-physiology in PSII**

In order to gain additional insight into the coordination of light absorption, electron transport and carbon fixation under the special environmental constraints of the Arctic Ocean, we utilized a suite of measurements to track the process of light absorption, charge separation in PSII and photosynthetic electron transport kinetics. The tight regulation of the photosynthetic processes upstream from carbon fixation allows phytoplankton to balance light absorption with electron flow and carbon fixation, thus maximizing productivity while minimizing excess absorbed light energy which can lead to the formation of reactive oxygen species (ROS) and oxidative stress (Murata et al., 2007; Vass, 2012). As discussed below, such physiological regulation is clearly evident in our dataset.

#### **4.4.4 Absorption spectra**

Mean absorption spectra for ML and sub-ML samples are shown in Figure B2 in the appendix, while derived diagnostic absorption parameters are summarized in Table 4.5. Our data clearly show a reduction in *chl a*-normalized light absorption for sub-ML assemblages relative to ML assemblages (Figure B4 in the appendix). Reduced absorption per *chl a* results from the so called package effect, associated with the self-shading of pigment molecules. This effect is higher in larger cells and low light acclimated phytoplankton assemblages (Duysens, 1956; Kirk, 2010; Morel and Bricaud, 1981). We can approximate the extent of pigment packaging as a reduction in the spectrally weighted values of  $\bar{a}_{\text{phy}}^{\text{chla}}$  in sub-ML relative to ML samples (Table 4.4, Figure 4.5a). Mean values for  $\bar{a}_{\text{phy}}^{\text{chla}}$  were  $0.01 \pm 0.004 \text{ m}^2 (\text{mg chl a})^{-1}$  for all ML samples, as compared to  $0.007 \pm 0.001 \text{ m}^2 (\text{mg chl a})^{-1}$  for all sub-ML samples (a mean reduction of 25

%). These values are in good agreement with those reported by (Palmer et al., 2013) in the Beaufort and Chukchi Seas. An increase in pigment packaging is also commonly assessed as a decrease in the  $a_{\text{phy}}^{\text{chl}a}(675)$ , a wavelength at which the absorption of accessory pigments is negligible. The values of  $a_{\text{phy}}^{\text{chl}a}(675)$  in our dataset (Table 4.5) are within the range of values observed in the Beaufort and Chukchi Seas (Wang et al., 2005) and the Labrador Sea (Cota et al., 2003), and indicate a relatively high degree of pigment packaging, particularly for the sub-ML samples.

The consistently higher degree of pigment packaging in our sub-ML relative to ML samples can predominantly be attributed to an increase in cellular pigment as a response to low light conditions (Kirk, 2010). The generally high levels of pigment packaging found in our entire dataset, however, are likely also an effect of cell size. Irrespective of light levels, large cells are known to exhibit more pigment packaging than small cells (e.g. Bricaud et al., 1995; Ciotti et al., 2002; Fujiki and Taguchi, 2002; Lohrenz et al., 2003). The degree of pigment packaging characteristic of large cells is consistent with the results from pigment analysis by CHEMTAX (Table 4.3, appendix Figure B1), which indicated a high relative abundance of diatoms at our sampling stations, and the large fraction (up to 90 %) of total chl $a$  in the > 5  $\mu\text{m}$  size class (Table 4.2). Indirect estimates of phytoplankton size distribution using pigment ratios following Uitz et al. (2008) (data not shown) or the ratio of  $a_{\text{phy}}^{\text{chl}a}(445)/a_{\text{phy}}^{\text{chl}a}(675)$  (Table 4.5) provided additional evidence that the phytoplankton assemblages were dominated by larger cells. We note that a high percentage of large cells are somewhat unexpected given the very low nutrient conditions measured in surface waters. Such low nutrient conditions are typically associated with a high abundance of small cells, with high surface area to volume ratios to facilitate uptake of nutrients at low concentrations.

#### **4.4.5 Diagnostic pigment ratios**

In support of our light absorption measurements, diagnostic pigment ratios showed that the phytoplankton communities sampled from within and below the mixed layer were acclimated to different growth environments. On average, the fraction of the total pigment pool allocated to photo-protection (PPC/TPig) was more than two-fold higher for the ML ( $0.044 \pm 0.02$ ) relative to the sub-ML ( $0.017 \pm 0.01$ ) samples (Table 4.5, Figure 4.5b). Similarly, the ratio of the xanthophyll cycling proteins Dd and Dt to total pigment ( $[\text{Dd} + \text{Dt}]/\text{TPig}$ ) was significantly

greater in the ML than the sub-ML samples ( $0.017 \pm 0.01$  vs.  $0.007 \pm 0.003$ , Table 4.5, Figure 4.5c). Furthermore, the de-epoxidation state (DES,  $Dt/[Dd + Dt]$ , Brunet et al., 2011), was higher in the ML than in the sub-ML samples ( $0.138 \pm 0.13$  vs.  $0.034 \pm 0.024$ ; Table 4.5, Figure 4.5d). The DES represents an indicator of the activation of the photo-protective xanthophyll cycling, and the difference we observed between ML and sub-ML samples is particularly significant given that samples were collected relatively early in the day prior to peak solar irradiance levels. An even greater difference in DES between ML and sub-ML samples might be expected later in the day. Our results thus show that photo-protective mechanisms within the light-harvesting antennae were activated in the ML assemblages. The pigment ratios for the ML samples in our dataset indicate a substantial degree of light stress experienced by phytoplankton within the shallow and nitrate depleted summer mixed layer.

#### ***4.4.6 FRRF derived photo-physiology***

In addition to our light absorption data, we utilized FRRF measurements for an in-depth analysis of the photo-physiological state and electron transport characteristics of phytoplankton assemblages. In presenting our results, it is important to note that the biophysical model used to interpret FRRF measurements of ChlF yields was developed based on a functional model of the photosynthetic apparatus, which is not necessarily equally representative for all phytoplankton species present in our samples. Furthermore, taxonomic variability exists in all derived parameters (e.g. Suggett et al., 2009b). Notwithstanding these limitations, we believe that our data provide valid information on the effect of key environmental parameters on the mean photo-physiological state, and photosynthetic capacity, of *in situ* phytoplankton assemblages.

The tuning of the photosynthetic process to the different growth environments within and below the mixed layer is clearly visible in FRRF-derived photo-physiological parameters (Table 4.6). Figure 4.6 summarizes these results, showing the ratio of photo-physiological parameters in ML and sub-ML samples for each station. Spectrally corrected values of the functional absorption-cross section,  $\sigma_{PSII}$  ( $\text{\AA}^2 \text{RCII}^{-1}$ ), were consistently lower in ML samples. A lower  $\sigma_{PSII}$ , as observed for ML compared to sub-ML assemblages, protects against damage by absorption of excess light near the surface (Moore et al., 2006). Conversely, a higher  $\sigma_{PSII}$  in sub-ML assemblages allows for more light absorption per RCII, which is advantageous at the consistently low irradiance levels characteristic for this growth environment. The parameter 1-qP has been

used as an approximation of excitation energy experienced by the photosynthetic apparatus (Anderson et al., 1995; Kramer et al., 2004). The values shown in Table 4.6 were derived for a reference background irradiance of  $60 \mu\text{mol quanta m}^{-2} \text{s}^{-1}$ . The data show that given the same incident irradiance, the ML samples experience considerably less (25-180 %) excitation energy than the corresponding sub-ML samples (Figure 4.6). The same trend is observed when the extent of excitation energy is estimated as 1-qL following Kramer et al. 2004 (Table 4.6). This lower realized excitation energy at the level of charge separation in RCII (1-qP) can be explained mechanistically by a decrease in absorption ( $\sigma_{\text{PSII}}$ ). The statistical correlation between values of 1-qP and  $\sigma_{\text{PSII}}$  in our data is strong (Pearson linear correlation coefficient  $r = 0.65$ ,  $p < 0.05$ ). Lower 1-qP can also result from an increased ability to drain electrons out of PSII, which can be achieved by an increased PQ pool size. Indeed, we observed a larger PQ pool in the ML samples (Table 4.6, Figure 4.6) and values of PQ pool size were negatively correlated to  $\sigma_{\text{PSII}}$  (Pearson linear correlation coefficient  $r = -0.77$ ,  $p < 0.05$ ) and 1-qP (Pearson linear correlation coefficient  $r = -0.68$ ,  $p < 0.05$ ). A larger PQ pool allows for more buffering capacity, preventing the ‘backpressure’ of electrons along the electron transport chain and over-reduction of  $Q_A$  during short periods of super-saturating light intensity. Similarly, the larger PQ pool likely also contributes to the observed increase in the rate constant of  $Q_A^-$  re-oxidation,  $1/\tau$  ( $\text{ms}^{-1}$ ), in ML compared to corresponding sub-ML samples ( $0.95 \pm 0.16 \text{ ms}^{-1}$  vs.  $0.83 \pm 0.13 \text{ ms}^{-1}$ , Table 4.6, Figure 4.6). Collectively, these data indicate that phytoplankton assemblages within the nitrate deprived, shallow mixed layer are acclimated to frequent conditions of excess excitation energy (i.e. excess light absorption relative to energy utilization downstream of charge separation in RCII).

#### **4.4.7 Light-dependent rates of charge separation in RCII**

Light-response curves of  $\text{ETR}_{\text{RCII}}$  are shown in Figure B3 in the appendix, while the derived fit parameters ( $\alpha^{\text{RCII}}$  and  $\text{ETR}_{\text{max}}^{\text{RCII}}$ ) are summarized in Table 4.4. Maximum rates of initial charge separation in RCII ( $\text{ETR}_{\text{max}}^{\text{RCII}}$ ) ranged from 117 to 446  $\text{mol e}^- \text{mol RCII}^{-1} \text{s}^{-1}$ , and were consistently higher in ML samples relative to sub-ML samples ( $352 \pm 62$  vs  $213 \pm 75$ , Table 4.4, Figure 4.7a and Figure 4.7d). Values of  $\alpha^{\text{RCII}}$  ranged from 2.1 to 4.8  $\text{mol e}^- \text{mol RCII}^{-1} \text{s}^{-1}$  ( $\mu\text{mol quanta m}^{-2} \text{s}^{-1}$ ) $^{-1}$  and were consistently higher in sub-ML samples ( $3.7 \pm 0.8$  vs.  $2.3 \pm 0.3$ , for ML and sub-ML samples respectively; Table 4.4, Figure 4.7b and Figure 4.7e). The

magnitude of observed  $ETR_{\max}^{\text{RCII}}$  and  $\alpha^{\text{RCII}}$  are in good agreement with values derived using PAM fluorometry in a recent study in an Arctic Fjord by Hancke et al. (2015).

The higher  $ETR_{\max}^{\text{RCII}}$  we observed in ML samples are consistent with the depth-dependent patterns in FRRF-derived photo-physiological parameters described above (Table 4.6, Figure 4.6). Phytoplankton assemblages acclimated to the high and variable light climate of the upper mixed layer have the ability to alleviate excess excitation energy through faster re-oxidation of  $Q_A^-$  ( $1/\tau$ ) and a larger PQ pool (Table 4.6, Figure 4.6). This, in turn, enables higher maximum rates of photosynthetic electron transport, as reflected in the increased  $ETR_{\max}^{\text{RCII}}$  we observed. A higher  $\alpha^{\text{RCII}}$  in samples taken from the low and less variable light climate under the mixed layer indicates higher light absorption per RCII, which is consistent with the observed increase in  $\sigma_{\text{PSII}}$ . The higher  $\sigma_{\text{PSII}}$  results in a faster increase in absorbed irradiance per RCII per unit increase in incident light, which yields an increase in  $\alpha^{\text{RCII}}$ .

As observed for the  $^{14}\text{C}$ -uptake rates, the  $E_k$  of  $ETR_{\text{RCII}}$  was consistently higher in ML ( $152 \pm 28 \mu\text{mol quanta m}^{-2} \text{s}^{-1}$ ) relative to sub-ML assemblages ( $59 \pm 24 \mu\text{mol quanta m}^{-2} \text{s}^{-1}$ ), reflecting acclimation of the phytoplankton communities to the two different growth environments (Table 4.4, Figure 4.7c and Figure 4.7f).

#### **4.4.8 Coupling of $ETR_{\text{RCII}}$ and $^{14}\text{C}$ -uptake**

Our suite of measurements provides us with the opportunity to examine the relative changes in carbon fixation and photosynthetic electron transport across a range of environmental conditions. Figure 4.8 shows that the rates of  $ETR_{\text{RCII}}$  consistently saturated at higher irradiances than the corresponding  $^{14}\text{C}$ -uptake ( $46 \pm 12$  % higher irradiance for ML samples and  $28 \pm 17$  % for sub-ML samples). Under conditions where  $ETR_{\text{RCII}}$  exhibits a light-dependent increase while  $^{14}\text{C}$ -uptake is light-saturated (i.e. at light intensities greater than the  $E_k$  of  $^{14}\text{C}$ -uptake but less than the  $E_k$  of  $ETR_{\text{RCII}}$ ), electrons must be dissipated through alternative pathways to avoid over-reduction of  $Q_A$ . Under these conditions, FRRF and  $^{14}\text{C}$ -based measurements of productivity will become de-coupled (i.e. the derived conversion factor will increase). Indeed, a deviation from a linear correlation between  $ETR_{\text{RCII}}$  and carbon fixation at super-saturating irradiances has commonly been reported in the literature (Cheah et al., 2011; Corno et al., 2006; Fujiki et al., 2007; Goto et al., 2008; Hancke et al., 2015; Kaiblinger and Dokulil, 2006; Raateoja, 2004; Zhu et al., 2016).

The larger difference in  $E_k$  between  $ETR_{RCII}$  and  $^{14}C$ -in the ML relative to the sub-ML samples (Table 4.4, Figure 4.8a) can be reconciled with metabolic acclimation processes in the contrasting growth environments. Within the shallow, nitrate deprived summer mixed layer of the Arctic and Subarctic Oceans, short term exposure to super-saturating irradiances and over-reduction of  $Q_A$  are more likely to occur than under conditions prevailing in sub-surface waters below the mixed layer (lower irradiance and higher nutrient levels). The low temperature conditions present in this region hinders the ability of cells to buffer these light fluctuations, and thus compromise photochemical responses to excess irradiance (e.g. Gray et al., 1997; Huner et al., 1998; Öquist et al., 1993). This higher susceptibility to excess excitation energy at low temperatures reflects the need to balance temperature-insensitive photochemical reactions (light absorption and charge separation) against downstream, temperature-dependent metabolism (such as carbon fixation (Morgan-Kiss et al., 2006)). Under ML conditions of low temperature, high and fluctuating light and low growth rate (due to nutrient-limitation), the capacity to dissipate short term excess excitation energy clearly provides a selective advantage.

We can gain further insight into the coupling between photosynthetic electron transport and carbon fixation by comparing the derived the conversion factor between  $ETR_{RCII}$  and  $^{14}C$ -uptake ( $K_C/n_{PSII}$ ) at light limitation (i.e.  $\alpha^{RCII} / \alpha^{chla}$ ) and at light saturation (i.e.  $P_{max}^{RCII} / P_{max}^{chla}$ ) (Table 4.4). As discussed in previous work (Schuback et al., 2015, 2016), this conversion factor is complex, and consists of two parameters: the electron requirement for carbon fixation,  $K_C$  ( $\text{mol } e^- \text{ mol } C^{-1}$ ), and the amount of *chl a* functionally associated with each RCII,  $1/n_{PSII}$  ( $\text{mol } chl a \text{ mol } RCII^{-1}$ ). Figure 4.8b shows that the conversion factor,  $K_C/n_{PSII}$ , for each sample is higher under conditions of light saturation (derived as  $P_{max}^{RCII} / P_{max}^{chla}$  for each sample), when compared to the conversion factor for light limited rates (derived as  $\alpha^{RCII} / \alpha^{cha}$  for each sample). This result is expected based on the higher  $E_k$  observed for  $ETR_{RCII}$  compared to that for  $^{14}C$ -uptake (Figure 4.8a). Somewhat counter-intuitively, however, Figure 4.8b also shows that generally high conversion factors were observed in sub-ML, when compared to ML samples. Our data thus show evidence of increased conversation factors within individual phytoplankton assemblages when exposed to super-saturating light, but also increased values in low light acclimated as compared to high light acclimated assemblages. We suggest that the elevated values of  $K_C/n_{PSII}$  in sub-ML when compared to ML assemblages result from an increase in  $1/n_{PSII}$  ( $\text{mol } chl a \text{ mol } RCII^{-1}$ ), which is a well-documented photo-acclimation response to low

light conditions (e.g. Dubinsky et al., 1986). In contrast, the rapid increase in  $K_C/n_{PSII}$  observed within assemblages exposed to short-term super-saturating irradiances (comparing conversion factors at  $P_{max}$  to conversion factors at  $\alpha$ ) is likely due to a photo-regulatory increase in  $K_C$  ( $\text{mol e}^- \text{mol C}^{-1}$ ). This could be achieved by an up-regulation of alternative electron pathways that alleviate ‘backpressure’ of electrons along the electron transport chain (e.g. Curien et al., 2016; Niyogi, 2000). Indeed, numerous studies conclude that plastid terminal oxidase (PTOX) mediated alternative electron pathways, may play a critical role in balancing photosynthetic electron flows when the acceptor side of PSI is limited by low temperature (Ivanov et al., 2012; Laureau et al., 2013; McDonald et al., 2011; Peltier et al., 2010; Streb and Cornic, 2012; Streb et al., 2005).

For the samples taken from within the upper mixed layer, we observed that the conversion factor  $K_C/n_{PSII}$ , at both light limitation and light saturation was correlated with the extent of nitrate depletion, with highest conversion factors under the lowest nitrate conditions (Figure 4.9). This result implies an increased decoupling of  $ETR_{RCII}$  and  $^{14}\text{C}$ -uptake under nitrate limitation, and can be explained by a greater allocation of photosynthetically produced reductant to processes other than carbon fixation (i.e. growth) (Figure 4.3). Indeed, recent laboratory studies provides direct evidence that nitrate starvation causes an up-regulation of alternative photosynthetic electron flow pathways, including PTOX mediated oxygen reduction (Saroussi et al., 2016), likely as a safety mechanism to prevent over-reduction of  $Q_A$  under conditions when carbon fixation capacity is comprised (Li et al., 2016; Saroussi et al., 2016).

#### **4.4.9 Using NPO estimates to improve carbon based primary production from FRRF measurements in the Arctic Ocean**

Mechanisms dissipating excess excitation energy can take place before and after charge separation in RCII. As discussed above, energy dissipation mechanisms that occur downstream of light absorption, though the induction of alternative electron flow pathways, are likely the cause of the increased decoupling of electron transport and carbon fixation under conditions of excess excitation energy. Absorbed light energy can also be dissipated as heat before charge separation in RCII. This process can be approximated from FRRF measurements as NPQ (Demming-Adams et al., 2014). Given that increased NPQ and the induction of alternative electron flow pathways are both driven by excess excitation energy, it is reasonable to postulate

that the magnitude of these ‘upstream’ and ‘downstream’ energy dissipation processes is correlated. Moreover, there is a mechanistic link between the two processes, since the induction of alternative electron pathways increases the thylakoid membrane pH gradient, which triggers the induction of NPQ in the pigment antenna (Nawroki 2015, Saroussi 2016).

Extending on previous work in the Subarctic Pacific (Schuback et al., 2015, 2016), we sought to assess the correlation between the derived conversion factor  $K_C/n_{PSII}$  and the expression of  $NPQ_{NSV}$ . As shown in Figure 4.10, the previously observed correlation from the Subarctic Pacific holds well for all samples taken from within the mixed layer. Both the Arctic phytoplankton assemblages we sampled here, and the iron-limited phytoplankton assemblages examined by Schuback et al., (2016) showed a very similar slope in the highly significant regression between the conversion factor and NPQ ( $K_C/n_{PSII} = 486NPQ_{NSV} + 1854$ ;  $R^2 = 0.75$ ,  $p < 0.01$ ). Moreover, the y-intercept of this regression, 1854, is strikingly close to the theoretical minimum value of  $K/n_{PSII}$ , which is approximately  $1600 e^- C^{-1} chl a RCII^{-1}$  (assuming  $4 mol e^- mol C^{-1}$  and  $400 chl a mol RCII^{-1}$ ). The good coherence of these two data sets and their accordance with theoretical expectations suggests that the proposed relationship is robust. Furthermore, a recent study by Zhu et al. (2016) found a strong correlation between the ETR to carbon fixation conversion factor and NPQ in an extensive dataset from the eutrophic Ariake Bay, Japan.

Based on our observations, we speculate that the integrated growth environments of phytoplankton assemblages from the upper mixed layers of the Arctic Ocean and Subarctic Pacific may be similar in a photo-physiological sense. In the dataset from the iron-limited Subarctic Pacific (Schuback et al. 2016), the combined effects of diurnal changes in ocean surface irradiance and iron limitation of photosynthetic electron transport created conditions of excess excitation energy. In the Arctic phytoplankton assemblages, similar photo-physiological conditions may result from growth in low temperature, macro-nutrient limited waters.

In their comprehensive study, Zhu et al. (2016) observed a correlation between the derived conversion factor and daily PAR, which was even stronger than the correlation between the conversion factor and NPQ. This strong correlation with PAR is not unexpected, given the eutrophic, temperate conditions of their study site. Under these conditions, variations in incident irradiance are likely the only appreciable cause for excess excitation energy, suggested to be responsible for the decoupling of ETR and carbon fixation. Importantly though, in the systems

studied by Schuback et al. (2015, 2016) and in the present study, excess excitation energy is not just a function of incident light, but enhanced by metabolic limitations downstream of charge separation in RCII (e.g. effects of iron limitation on the electron transport chain, low temperature on enzymatic reactions, and nutrient limitation on cellular energy allocation). The NPQ-proxy effectively provides an integrator of the interacting effects of all these variables, and can be derived directly from FRRF measurements, at high resolution and without the need for any additional instruments or sample manipulation.

Whereas we observed a strong empirical relationship between the derived conversion factor  $K_C/n_{PSII}$  and  $NPQ_{NSV}$  in all samples taken from within the mixed layer; samples taken from below the mixed layer showed significant variability in  $K_C/n_{PSII}$  with little variability in  $NPQ_{NSV}$  (Figure 4.10). In this context, it is important to note that values of  $K_C/n_{PSII}$  and  $NPQ_{NSV}$  shown in Figure 4.10 were derived from light-response curve measurements with irradiances ranging from 0 – 500  $\mu\text{mol quanta m}^{-2} \text{s}^{-1}$  for each sample. The upper range of these applied irradiances is somewhat unrealistic for the sub-ML samples, which were taken from depth where *in situ* irradiances are unlikely to exceed 50  $\mu\text{mol quanta m}^{-2} \text{s}^{-1}$ . If we consider only values of  $K_C/n_{PSII}$  and  $NPQ_{NSV}$  for the low irradiances relevant for sub-ML samples,  $NPQ_{NSV}$  is essentially constant. Variability in  $K_C/n_{PSII}$  remains across stations, however no significant light-dependent variability of  $K_C/n_{PSII}$  within samples was observed under these conditions. As discussed above, we speculate that the observed high  $K_C/n_{PSII}$  in our sub-ML samples is primarily caused by a photo-acclimatory increase in  $1/n_{PSII}$  ( $\text{mol chl}a \text{ mol RCII}^{-1}$ ). The consistently low excitation energy, as experienced by the sub-ML assemblages, triggers the increase of chl*a* per RCII, which maximizes light absorption. The ability to dissipate excess excitation energy by rapid photo-regulatory mechanisms like  $NPQ_{NSV}$  and alternative electron pathways (which, in turn, would affect  $K_C$ ) however, appears to be essentially absent in sub-ML assemblages. Consequently, our NPQ-proxy approach, which holds significant potential in improving carbon-based estimates of phytoplankton primary production from FRRF measurements, only performs well within the shallow nitrate limited summer mixed layer. The empirical approach may not be well suited for phytoplankton assemblages below the mixed layer, including deep chlorophyll maxima. Given the importance of sub-ML contributions to total water column productivity in the Arctic Ocean (e.g. Martin et al., 2013; Tremblay et al., 2015), this result presents a significant limitation of our approach. However, the result also underscores the physiologically distinct characteristics of

sub-ML phytoplankton assemblages, which optimize growth under the unusual conditions of consistently low excitation energy. Going forward, it will likely be necessary to employ distinct modelling approaches to better represent the environmental controls on primary productivity in surface and sub-surface Arctic Ocean environments.

#### **4.5 Conclusion**

Our results provide new information on phytoplankton primary productivity in the Subarctic and Arctic Ocean and provide mechanistic insight into the tight regulation of various components of the photosynthetic process in response to environmental gradients in light and nutrient availability. Our results provide further support for the use of NPQ as a convenient proxy for the magnitude and variability of the conversion factor needed to derive carbon-based rates of phytoplankton primary productivity from FRRF-derived ETR, in regions where excess excitation energy is frequently encountered by phytoplankton assemblages. However, the approach may not be suitable for conditions of consistently low excitation energy, present in the Arctic Ocean sub-ML chlorophyll maximum. This result highlights the importance of vertical stratification as a key factor partitioning marine ecosystems of the Arctic Ocean into contrasting domains (e.g. Carmack and McLaughlin, 2011; Carmack and Wassmann, 2006; Tremblay et al., 2015). Phytoplankton primary productivity within these two domains is likely to react differently to the rapid effects of climate change, anticipated in this region. Several recent modelling studies have suggested future increases in Arctic Ocean primary productivity, mainly due to a decrease in the extent of the icepack, and increased light availability (e.g. Arrigo and van Dijken, 2011, 2015; Pabi et al., 2008). Based on our observations, an increase in surface irradiance would, indeed, have the potential to increase productivity in light limited sub-ML assemblages, while ML assemblages would show lower light-dependent stimulation, due to the constraints of low temperature and nitrate depletion.

The experimental approach taken in the present study highlights the importance and applicability of a mechanistic understanding of the photosynthetic process and its environmental determinants to improve estimates of phytoplankton primary productivity in the rapidly changing Arctic marine ecosystem.

## 4.6 Tables and figures

**Table 4.1: Physical and hydrological characteristics of sampling stations.** Mixed layer depth (MLD, m), extinction coefficient ( $k_d$ ,  $m^{-1}$ ), surface PAR at time of sampling ( $E_0$ ,  $\mu\text{mol quanta } m^{-2} s^{-1}$ ) during July and August 2015.

| Sta.  | Date                  | Hours<br>after<br>sunrise | Latitude    | Longitude   | MLD | $k_d$    | $E_0$                                 |
|-------|-----------------------|---------------------------|-------------|-------------|-----|----------|---------------------------------------|
|       |                       |                           | $^{\circ}N$ | $^{\circ}E$ | $m$ | $m^{-1}$ | $\mu\text{mol quanta } m^{-2} s^{-1}$ |
| K1    | 14 <sup>th</sup> July | 1                         | 56.12       | -53.37      | 18  | 0.10     | 20                                    |
| LS2   | 17 <sup>th</sup> July | 0.5                       | 60.45       | -56.55      | 41  | 0.08     | 7                                     |
| HB1   | 22 <sup>nd</sup> July | 2                         | 60.30       | -78.48      |     |          |                                       |
| HB2   | 24 <sup>th</sup> July | 2                         | 59.70       | -78.70      |     |          |                                       |
| BB1.5 | 4 <sup>th</sup> Aug   | 2.5                       | 67.99       | -58.39      |     |          |                                       |
| BB3   | 6 <sup>th</sup> Aug   | 4                         | 71.41       | -68.59      | 8   | 0.10     | 382                                   |
| BB2   | 8 <sup>th</sup> Aug   | 4                         | 72.75       | -67.00      | 13  | 0.09     | 35                                    |
| CAA1  | 10 <sup>th</sup> Aug  | 4                         | 74.52       | -80.56      | 32  | 0.14     | 94                                    |
| CAA5  | 13 <sup>th</sup> Aug  | 4                         | 74.53       | -90.80      | 5   | 0.07     | 457                                   |
| CAA6  | 15 <sup>th</sup> Aug  | 4                         | 74.75       | -97.46      | 6   | 0.13     | 460                                   |
| CAA7  | 16 <sup>th</sup> Aug  | 2                         | 73.66       | -96.53      | 2   | 0.09     | 18                                    |
| VS    | 17 <sup>th</sup> Aug  | 4                         | 69.87       | -99.5       | 8   | 0.13     | 224                                   |

**Table 4.2: Depth-specific hydrological variables for ML and sub-ML samples for each station.** The table is divided into ML and sub-ML sampling depths for each station. Samples at station HB1, HB2 and BB1.5 were taken from the ships underway sampling system (7 m depth).  $E_z$  represents the PAR at depth of sampling at time of sampling. %E is the percent surface PAR. OD is optical depth, and DIC is dissolved inorganic carbon.

| Sta.   | depth    | $E_z$                        | % $E_0$ | OD  | Temp        | Sal        | DIC  | $NO_2+NO_3$ | $NH_4$            | Si(OH) <sub>4</sub> | PO <sub>4</sub> | [chl $a$ ]      |              |
|--------|----------|------------------------------|---------|-----|-------------|------------|------|-------------|-------------------|---------------------|-----------------|-----------------|--------------|
|        | <i>m</i> | $\mu mol\ q\ m^{-2}\ s^{-1}$ |         |     | $^{\circ}C$ | <i>psu</i> |      |             | $\mu mol\ L^{-1}$ |                     |                 | $\mu g\ L^{-1}$ | % >5 $\mu m$ |
| ML     |          |                              |         |     |             |            |      |             |                   |                     |                 |                 |              |
| K1     | 7.5      | 9.8                          | 48      | 0.7 | 6.5         | 33.3       | 2037 | 0.21        | 0.03              | 0.11                | 0.01            | 0.57            | 14           |
| LS2    | 7        | 4.0                          | 57      | 0.6 | 4.5         | 33.8       | 2071 | 0.13        | 0                 | 0.03                | 0.14            | 0.88            | 29           |
| HB1    | 7        |                              |         |     | 2.8         | 16.3       |      |             |                   |                     |                 | 0.36            |              |
| HB2    | 7        |                              |         |     | 1.0         | 14.9       |      |             |                   |                     |                 | 0.09            |              |
| BB1.5  | 7        |                              |         |     | 2.5         | 29.9       |      |             |                   |                     |                 | 0.41            |              |
| BB3    | 5.5      | 226                          | 59      | 0.5 | 3.9         | 30.8       | 2024 | 0.21        | 0                 | 0.55                | 4.07            | 0.18            | 44           |
| BB2    | 6        | 20.6                         | 60      | 0.5 | 5.3         | 30.9       | 2008 | 0.05        | 0.06              | 0.52                | 4.51            | 0.15            | 25           |
| CAA1   | 5        | 46.5                         | 49      | 0.7 | 3.1         | 32.3       | 2013 | 0.06        | 0                 | 0.38                | 1.22            | 0.69            | 42           |
| CAA5   | 7        | 287                          | 63      | 0.5 | 0.4         | 27.9       | 2012 | 0.09        |                   | 0.48                | 1.58            | 0.35            | 54           |
| CAA6   | 5        | 244                          | 53      | 0.6 | 0.1         | 29.6       | 1872 | 0.05        |                   | 0.41                | 1.88            | 0.37            | 90           |
| CAA7   | 6        | 10.6                         | 58      | 0.5 | -0.3        | 30.0       | 2014 | 0.04        |                   | 0.56                | 3.53            | 0.35            | 58           |
| VS     | 8        | 82.2                         | 37      | 1.0 | 0.1         | 25.4       | 1822 |             |                   |                     |                 | 0.20            | 61           |
| sub-ML |          |                              |         |     |             |            |      |             |                   |                     |                 |                 |              |
| K1     | 38       | 0.5                          | 2.4     | 3.7 | 4.6         | 34.6       | 2066 | 1.92        | n/a               | 0.28                | 1.00            | 4.69            | 75           |
| LS2    | 38       | 0.3                          | 4.7     | 3.0 | 3.7         | 33.9       | 2072 | 2.22        | 0.34              | 0.27                | 1.13            | 1.24            | 41           |
| HB1    |          |                              |         |     |             |            |      |             |                   |                     |                 |                 |              |
| HB2    |          |                              |         |     |             |            |      |             |                   |                     |                 |                 |              |
| BB1.5  |          |                              |         |     |             |            |      |             |                   |                     |                 |                 |              |
| BB3    | 27       | 28.9                         | 7.6     | 2.6 | -1.2        | 32.5       | 2081 | 1.08        | 0                 | 0.73                | 5.92            | 5.10            | 81           |
| BB2    | 33       | 2.8                          | 8.0     | 2.9 | -1.4        | 32.8       | 2107 | 3.90        | 0.93              | 0.84                | 8.85            | 1.70            | 63           |
| CAA1   | 35       | 0.7                          | 0.7     | 5.0 | 0.9         | 32.5       | 2057 | 2.08        | 0.25              | 0.63                | 4.09            | 2.07            | 93           |
| CAA5   | 20       | 16.5                         | 3.6     | 3.3 | -1.4        | 31.9       | 2112 | 4.32        |                   | 0.82                | 8.83            | 0.61            | 64           |
| CAA6   | 24       | 22.0                         | 4.8     | 3.0 | -1.1        | 31.4       | 2030 | 0.42        |                   |                     | 1.76            | 3.07            | 86           |
| CAA7   | 36       | 0.7                          | 3.7     | 3.3 | -1.3        | 31.9       | 2130 | 6.57        |                   | 1.18                | 15.08           | 0.34            | 60           |
| VS     | 39       | 1.7                          | 0.8     | 4.9 | -1.2        | 29.3       | 1993 |             |                   |                     |                 | 4.80            | 85           |

**Table 4.3: Relative taxonomic composition of the phytoplankton assemblage as inferred from**

**CHEMTAX analysis of HPLC pigments.** The table is divided into ML and sub-ML sampling depth at each station. Values present the percent contribution of each group to total chl*a* biomass. Chemotaxonomic groups were defined following Higgins et al. (2011) as recently adapted for Arctic phytoplankton by (Coupel et al., 2015b). Diatoms include all diatoms including the abundant *Chaetoceros* spp. Dino are dinoflagellates containing peridinin (e.g. *Heterocapsa rotundata*). Chloro are chlorophytes (e.g. *Dunalella tertiolecta*). Pras3 stands for the prasinophytes type-3 group, who containing prasinoxanthin (e.g. *Micromonas* sp.). Pras2 stands for the prasinophytes type-2 group, who do not contain prasinoxanthin (e.g. *Pyramimomas* sp.). Crypto stands for chryptophytes. Chryso stands for the chryso-pelago group which includes chrysophytes and pelagophytes. Hapto-7 refers to the haptophytes type-7 group, which are prymnesiophytes including *Chrysochromulina* spp. c3-flag are the c3-flagellate group including non-peridinin containing dinoflagellates as defined in Coupel et al. (2015b).

| Sta.   | depth | Diatom | Dino | Chloro | Pras3 | Pras2 | Crypto | Chrys | c3-flag | Hap-7 |
|--------|-------|--------|------|--------|-------|-------|--------|-------|---------|-------|
| ML     |       |        |      |        |       |       |        |       |         |       |
| K1     | 7.5   | 37     | 14   | 0      | 11    | 6     | 4      | 9     | 1       | 16    |
| LS2    | 7     | 39     | 19   | 0      | 17    | 6     | 1      | 3     | 7       | 8     |
| HB1    | 7     | 77     | 0    | 0      | 7     | 5     | 3      | 0     | 8       | 0     |
| HB2    | 7     | 58     | 7    | 24     | 5     | 1     | 4      | 0     | 0       | 0     |
| BB1.5  | 7     | 25     | 10   | 0      | 16    | 10    | 3      | 0     | 32      | 3     |
| BB3    | 5.5   | 48     | 15   | 4      | 7     | 7     | 8      | 1     | 5       | 5     |
| BB2    | 6     | 44     | 16   | 11     | 9     | 5     | 4      | 2     | 1       | 8     |
| CAA1   | 5     | 47     | 4    | 0      | 24    | 15    | 2      | 2     | 4       | 2     |
| CAA5   | 7     | 50     | 19   | 1      | 7     | 3     | 3      | 2     | 14      | 1     |
| CAA6   | 5     | 52     | 16   | 1      | 7     | 1     | 3      | 2     | 17      | 1     |
| CAA7   | 6     | 46     | 11   | 4      | 11    | 6     | 8      | 8     | 0       | 5     |
| VS     | 8     | 67     | 8    | 0      | 9     | 2     | 3      | 3     | 6       | 3     |
| sub-ML |       |        |      |        |       |       |        |       |         |       |
| K1     | 38    | 83     | 6    | 0      | 0     | 1     | 1      | 3     | 6       | 0     |
| LS2    | 38    | 35     | 5    | 0      | 28    | 14    | 2      | 1     | 12      | 3     |
| HB1    |       |        |      |        |       |       |        |       |         |       |
| HB2    |       |        |      |        |       |       |        |       |         |       |
| BB1.5  |       |        |      |        |       |       |        |       |         |       |
| BB3    | 27    | 42     | 2    | 1      | 15    | 2     | 11     | 2     | 3       | 24    |
| BB2    | 23    | 36     | 3    | 1      | 22    | 8     | 3      | 3     | 3       | 21    |
| CAA1   | 35    | 49     | 3    | 1      | 24    | 7     | 2      | 1     | 11      | 2     |
| CAA5   | 20    | 60     | 4    | 2      | 17    | 2     | 3      | 3     | 9       | 2     |
| CAA6   | 24    | 84     | 5    | 0      | 1     | 1     | 1      | 2     | 3       | 1     |
| CAA7   | 36    | 64     | 4    | 1      | 13    | 0     | 2      | 3     | 9       | 3     |
| VS     | 39    | 87     | 0    | 2      | 0     | 0     | 2      | 0     | 0       | 8     |

**Table 4.4: PvsE curve fit parameters for  $ETR_{RCII}$  and  $^{14}C$ -uptake, and the derived conversion factor between these rates. See next page for full legend.**

|        |       | $ETR_{RCII}$     |                 |          | $^{14}C$ -uptake |                 |         | Conversion factor |             |
|--------|-------|------------------|-----------------|----------|------------------|-----------------|---------|-------------------|-------------|
| Sta.   | depth | $P_{max}^{RCII}$ | $\alpha^{RCII}$ | $E_k$    | $P_{max}^{chla}$ | $\alpha^{chla}$ | $E_k$   | CF $P_{max}$      | CF alpha    |
| ML     |       |                  |                 |          |                  |                 |         |                   |             |
| K1     | 7.5   | 259 ± 19         | 2.1 ± 0.1       | 124 ± 11 | 8.0 ± 0.3        | 0.08 ± 0.02     | 72 ± 8  | 1573 ± 126        | 1334 ± 294  |
| LS2    | 7     | 296 ± 13         | 2.9 ± 0.1       | 102 ± 6  | 7.0 ± 0.4        | 0.09 ± 0.01     | 75 ± 13 | 2043 ± 139        | 1505 ± 246  |
| HB1    | 7     | 419 ± 35         | 2.7 ± 0.2       | 155 ± 16 | 4.1 ± 0.4        | 0.07 ± 0.02     | 61 ± 22 | 4914 ± 661        | 1966 ± 699  |
| HB2    | 7     | 446 ± 78         | 2.5 ± 0.3       | 178 ± 36 | 3.2 ± 0.4        | 0.04 ± 0.02     | 80 ± 34 | 6708 ± 1457       | 3021 ± 1259 |
| BB1.5  | 7     | 404 ± 35         | 2.2 ± 0.1       | 181 ± 18 | 1.8 ± 0.1        | 0.02 ± 0.01     | 83 ± 22 | 11073 ± 1333      | 5062 ± 1282 |
| BB3    | 5.5   | 312 ± 29         | 2.1 ± 0.1       | 147 ± 17 | 7.6 ± 0.9        | 0.08 ± 0.02     | 66 ± 26 | 1991 ± 299        | 1256 ± 343  |
| BB2    | 6     | 380 ± 51         | 2.1 ± 0.2       | 184 ± 29 |                  |                 |         |                   |             |
| CAA1   | 5     | 364 ± 18         | 2.1 ± 0.1       | 177 ± 10 | 4.3 ± 0.3        | 0.05 ± 0.01     | 92 ± 17 | 4099 ± 325        | 2139 ± 377  |
| CAA5   | 7     |                  |                 |          |                  |                 |         |                   |             |
| CAA6   | 5     | 348 ± 17         | 2.3 ± 0.1       | 148 ± 9  | 3.4 ± 0.4        | 0.04 ± 0.01     | 92 ± 29 | 4903 ± 559        | 3021 ± 917  |
| CAA7   | 6     | 289 ± 39         | 2.3 ± 0.2       | 124 ± 21 | 3.9 ± 0.6        | 0.05 ± 0.02     | 84 ± 42 | 3550 ± 735        | 2413 ± 1168 |
| VS     | 8     |                  |                 |          | 4.0 ± 0.8        | 0.05 ± 0.03     | 74 ± 42 |                   |             |
| Sub-ML |       |                  |                 |          |                  |                 |         |                   |             |
| K1     | 38    | 223 ± 84         | 2.3 ± 0.8       | 98 ± 50  | 0.7 ± 0.03       | 0.01 ± 0.00     | 50 ± 7  | 14750 ± 563       | 7747 ± 2813 |
| LS2    | 38    | 242 ± 11         | 3.5 ± 0.3       | 53 ± 5   | 4.1 ± 0.25       | 0.07 ± 0.02     | 45 ± 13 | 2834 ± 216        | 2355 ± 562  |
| HB1    |       |                  |                 |          |                  |                 |         |                   |             |
| HB2    |       |                  |                 |          |                  |                 |         |                   |             |
| BB1.5  |       |                  |                 |          |                  |                 |         |                   |             |
| BB3    | 27    | 174 ± 20         | 3.6 ± 0.7       | 48 ± 11  | 1.8 ± 0.09       | 0.08 ± 0.01     | 29 ± 5  | 4713 ± 579        | 2141 ± 528  |
| BB2    | 23    | 222 ± 21         | 4.5 ± 0.8       | 49 ± 10  | 1.2 ± 0.04       | 0.03 ± 0.00     | 39 ± 4  | 9051 ± 912        | 7173 ± 1419 |
| CAA1   | 35    |                  |                 |          | 1.3 ± 0.09       | 0.03 ± 0.01     | 36 ± 9  |                   |             |
| CAA5   | 20    | 371 ± 26         | 3.9 ± 0.3       | 95 ± 9   | 1.6 ± 0.13       | 0.04 ± 0.01     | 46 ± 13 | 11158 ± 1176      | 5417 ± 1496 |
| CAA6   | 24    | 184 ± 17         | 3.6 ± 0.5       | 52 ± 9   | 2.0 ± 0.19       | 0.05 ± 0.02     | 38 ± 11 | 4357 ± 558        | 3206 ± 1032 |
| CAA7   | 36    | 173 ± 9          | 4.8 ± 1.2       | 40 ± 6   | 1.4 ± 0.28       | 0.04 ± 0.03     | 30 ± 19 | 6094 ± 1244       | 5555 ± 3546 |
| VS     | 39    | 117 ± 23         | 3.3 ± 1.7       | 36 ± 20  | 1.0 ± 0.2        | 0.03 ± 0.02     | 36 ± 23 | 5434 ± 1486       | 5352 ± 4377 |

**Table 4.4: P vs E curve fit parameters for  $ETR_{RCII}$  and  $^{14}C$ -uptake, and the derived conversion factor between these rates.** The table is divided into ML and sub-ML sampling depth at each station. Fit parameters for  $ETR_{RCII}$  and  $^{14}C$ -uptake are derived from  $^{14}C$ -uptake vs E curves shown in Figure S2. The error presented with  $P_{max}$  and  $\alpha$  is the 95 % confidence interval of the curve fit, while the error presented with  $E_k$  is the propagated error of  $P_{max}/\alpha$ .  $P_{max}^{RCII}$  is the light saturated maximum rate of charge separation in RCII ( $\text{mol e}^- \text{mol RCII}^{-1} \text{s}^{-1}$ ).  $\alpha^{RCII}$  is the light-dependent increase in the rate of charge separation in RCII before light saturation ( $\text{mol e}^- \text{mol RCII}^{-1} \text{s}^{-1} [\mu\text{mol quanta m}^{-2} \text{s}^{-1}]^{-1}$ ).  $E_k$  is the light saturation parameter of charge separation in RCII ( $\mu\text{mol quanta m}^{-2} \text{s}^{-1}$ ).  $P_{max}^{chla}$  is the light saturated maximum rate of  $^{14}C$ -uptake ( $\text{g C g chl a}^{-1} \text{h}^{-1}$ ).  $\alpha^{chla}$  is the light-dependent increase in the rate of  $^{14}C$ -uptake before light saturation ( $\text{g C g chl a}^{-1} \text{h}^{-1} [\mu\text{mol quanta m}^{-2} \text{s}^{-1}]^{-1}$ ).  $E_k$  is the light saturation parameter of  $^{14}C$ -uptake ( $\mu\text{mol quanta m}^{-2} \text{s}^{-1}$ ). The conversion factor  $K_C/n_{PSII}$  between rates of  $ETR^{RCII}$  and  $^{14}C$ -uptake ( $\text{mol e}^- \text{mol C}^{-1} \text{mol chl a mol RCII}^{-1}$ ) was derived for light saturated rates at  $P_{max}$  and light limited rates  $\alpha$ . The error presented with each conversion factor represents the propagated error from  $P_{max}^{RCII} / P_{max}^{chla}$  and  $\alpha^{RCII} / \alpha^{chla}$ .

**Table 4.5: Diagnostic light absorption parameters and pigment ratios.** See next page for full legend.

| <b>Sta.</b> | <b>depth</b> | $\bar{a}_{\text{phy}}^{\text{cha}}$ | $a_{\text{phy}}^{\text{cha}}(675)$ | $a_{\text{phy}}^{\text{cha}}(440)/(675)$ | <b>PPC/Tpig</b> | <b>D+D/Tpig</b> | <b>Dt/D+D</b> |
|-------------|--------------|-------------------------------------|------------------------------------|--|-----------------|-----------------|---------------|
|             | <i>m</i>     | $m^2 \text{ mg chl}a^{-1}$          | $m^2 \text{ mg chl}a^{-1}$         |  |                 |                 |               |
| ML          |              |                                     |                                    |  |                 |                 |               |
| K1          | 7.5          | 0.009                               | 0.008                              | 2.4                                      | 0.038 ± 0.007   | 0.018 ± 0.003   | 0.052 ± 0.003 |
| LS2         | 7            | 0.007 ± 0.001                       | 0.006 ± 0.003                      | 2.1 ± 1.2                                | 0.025 ± 0.002   | 0.007 ± 0.002   | 0.036 ± 0.050 |
| HB1         | 7            |                                     | 0.003                              |  | 0.024 ± 0.001   | 0.011 ± 0.003   | 0.108 ± 0.031 |
| HB2         | 7            | 0.004 ± 0.002                       | 0.002 ± 0.001                      | 2.2 ± 1.1                                | 0.057 ± 0.006   | 0.011 ± 0.001   | 0.000 ± 0.000 |
| BB1.5       | 7            | 0.009 ± 0.000                       | 0.009 ± 0.001                      | 1.6 ± 0.2                                | 0.028 ± 0.001   | 0.009 ± 0.001   | 0.471 ± 0.006 |
| BB3         | 5.5          | 0.010 ± 0.000                       | 0.009 ± 0.001                      | 2.0 ± 0.3                                | 0.079 ± 0.013   | 0.035 ± 0.005   | 0.230 ± 0.010 |
| BB2         | 6            | 0.012 ± 0.001                       | 0.011 ± 0.002                      | 2.1 ± 0.4                                | 0.057 ± 0.014   | 0.024 ± 0.007   | 0.197 ± 0.035 |
| CAA1        | 5            | 0.014 ± 0.000                       | 0.014 ± 0.000                      | 2.0 ± 0.1                                | 0.044 ± 0.005   | 0.014 ± 0.001   | 0.171 ± 0.016 |
| CAA5        | 7            | 0.014 ± 0.001                       | 0.014 ± 0.001                      | 1.7 ± 0.1                                | 0.036 ± 0.001   | 0.015 ± 0.000   | 0.072 ± 0.007 |
| CAA6        | 5            | 0.006 ± 0.002                       | 0.006 ± 0.001                      | 1.9 ± 0.8                                | 0.033 ± 0.009   | 0.016 ± 0.007   | 0.061 ± 0.026 |
| CAA7        | 6            | 0.013 ± 0.003                       | 0.011 ± 0.001                      | 1.9 ± 0.2                                | 0.072 ± 0.034   | 0.033 ± 0.006   | 0.240 ± 0.009 |
| VS          | 8            | 0.014 ± 0.001                       | 0.010 ± 0.004                      | 2.4 ± 0.9                                | 0.031 ± 0.019   | 0.015 ± 0.012   | 0.022 ± 0.031 |
| Sub-ML      |              |                                     |                                    |  |                 |                 |               |
| K1          | 38           | 0.007 ± 0.000                       | 0.006 ± 0.000                      | 1.6 ± 0.1                                | 0.006 ± 0.000   | 0.005 ± 0.001   | 0.022 ± 0.007 |
| LS2         | 38           | 0.005 ± 0.001                       | 0.005 ± 0.002                      | 1.6 ± 0.8                                | 0.016 ± 0.000   | 0.002 ± 0.000   | 0.000 ± 0.000 |
| HB1         |              |                                     |                                    |  |                 |                 |               |
| HB2         |              |                                     |                                    |  |                 |                 |               |
| BB1.5       |              |                                     |                                    |  |                 |                 |               |
| BB3         | 27           | 0.008 ± 0.000                       | 0.010 ± 0.001                      | 1.5 ± 0.3                                | 0.022 ± 0.005   | 0.011 ± 0.007   | 0.051 ± 0.028 |
| BB2         | 33           | 0.011 ± 0.000                       | 0.011 ± 0.001                      | 1.7 ± 0.1                                | 0.022 ± 0.006   | 0.008 ± 0.002   | 0.065 ± 0.004 |
| CAA1        | 35           | 0.005 ± 0.002                       | 0.005 ± 0.001                      | 1.4 ± 0.7                                | 0.021 ± 0.009   | 0.007 ± 0.000   | 0.063 ± 0.001 |
| CAA5        | 20           | 0.012 ± 0.000                       | 0.011 ± 0.001                      | 1.6 ± 0.2                                | 0.021 ± 0.010   | 0.010 ± 0.005   | 0.042 ± 0.012 |
| CAA6        | 24           | 0.003 ± 0.000                       | 0.003 ± 0.000                      | 1.3 ± 0.3                                | 0.016           | 0.007           | 0.024         |
| CAA7        | 36           | 0.011 ± 0.001                       | 0.011 ± 0.001                      | 1.7 ± 0.3                                | 0.022 ± 0.012   | 0.012 ± 0.006   | 0.035 ± 0.001 |
| VS          | 39           | 0.004 ± 0.000                       | 0.004 ± 0.000                      | 1.3 ± 0.1                                | 0.008           | 0.005           | 0.000         |

**Table 4.5: Diagnostic light absorption parameters and pigment ratios.** The table is divided into ML and sub-ML sampling depth at each station. All values are presented as the mean and range of duplicate measurements. The parameter  $\bar{a}_{\text{phy}}^{\text{chl}a}$  ( $\text{m}^2 \text{mg chl}a^{-1}$ ) is the spectrally integrated (400-700 nm) chl $a$  specific phytoplankton absorption coefficient. This parameter, as well as  $a_{\text{phy}}^{\text{chl}a}(675)$ , are used as indicators of the extent of pigment packaging, where a high degree of packaging are indicative of low light acclimation and large cell size. The ration of  $a_{\text{phy}}^{\text{chl}a}(440)/(675)$  in particular has been used as an indicator of cell size. The ratio of photo-protective carotenoids to total pigment (PPC/TPig) indicates light acclimation state of a phytoplankton assemblage. The ratio of diadinoxanthin and diatoxanthin to total pigment ( $[D + D]/\text{Tpig}$ ) shows the proportion of pigment allocated to the xanthophyll cycle of chromophytes, while the ratio of diatoxanthin to the sum of diatoxanthin and diadinoxanthin represents the activation state of the chromophyte xanthophyll cycle. See methods for definitions of pigment groups.

**Table 4.6: Photo-physiological parameters derived from FRRF measurements.** The table is divided into ML and sub-ML sampling depth at each station. All parameters are presented as the mean and standard deviation of three consecutive measurements on the same sample (see methods for details). Values for the functional absorption cross-section  $\sigma_{PSII}$  have been spectrally corrected to account for differences in the spectral quality of LEDs in the FRRF instrument and the *in situ* light at sampling depth. Values shown are from the dark-regulated state. The parameter  $1/\tau$  ( $\text{ms}^{-1}$ ) is an estimate of the rate constant of re-oxidation of the primary stable electron acceptor  $Q_A$  (i.e. electron transport from  $Q_A$  to  $Q_B$ ). The parameter (1-qP) is an estimate of the extent of excitation energy (the fraction of  $Q_A$  reduced) and the value presented is derived for a background irradiance of  $60 \mu\text{mol quanta m}^{-2} \text{s}^{-1}$ . While (1-qP) assumes no connectivity between photosynthetic units ('puddle' model), (1-qL) assumes that if a RCII is closed ( $Q_A$  reduced) the exciton is still able to cause a charge separation in another RCII ('lake' model) (Kramer et al., 2004).

| Sta.          | depth    | $\sigma_{PSII}$                 | $1/\tau$         | PQ pool                       | 1-qP (60)       | 1-qL (60)       |
|---------------|----------|---------------------------------|------------------|-------------------------------|-----------------|-----------------|
|               | <i>m</i> | $\text{\AA}^2 \text{RCII}^{-1}$ | $\text{ms}^{-1}$ | $\text{mol PQ mol } Q_B^{-1}$ |                 |                 |
| <b>ML</b>     |          |                                 |                  |                               |                 |                 |
| K1            | 7.5      | $333 \pm 6$                     | $0.96 \pm 0.05$  | $7.3 \pm 1.2$                 | $0.45 \pm 0.04$ | $0.67 \pm 0.04$ |
| LS2           | 7        | $414 \pm 5$                     | $0.96 \pm 0.02$  | $5.9 \pm 0.4$                 | $0.36 \pm 0.07$ | $0.58 \pm 0.08$ |
| HB1           | 7        | $391 \pm 6$                     | $0.81 \pm 0.02$  | $8.7 \pm 0.6$                 | $0.15 \pm 0.06$ | $0.24 \pm 0.08$ |
| HB2           | 7        | $374 \pm 75$                    | $0.95 \pm 0.58$  | $6.2 \pm 1.1$                 | $0.19 \pm 0.21$ | $0.24 \pm 0.25$ |
| BB1.5         | 7        | $359 \pm 22$                    | $0.55 \pm 0.13$  | $7.8 \pm 1.5$                 | $0.40 \pm 0.06$ | $0.45 \pm 0.06$ |
| BB3           | 5.5      | $296 \pm 29$                    | $1.14 \pm 0.23$  | $7.0 \pm 2.7$                 | $0.22 \pm 0.05$ | $0.37 \pm 0.07$ |
| BB2           | 6        | $352 \pm 30$                    | $1.09 \pm 0.21$  | $5.4 \pm 3.4$                 | $0.32 \pm 0.07$ | $0.55 \pm 0.07$ |
| CAA1          | 5        | $342 \pm 5$                     | $0.92 \pm 0.05$  | $8.1 \pm 0.8$                 | $0.42 \pm 0.03$ | $0.48 \pm 0.03$ |
| CAA5          | 7        | $376 \pm 13$                    | $1.13 \pm 0.08$  | $7.8 \pm 3.6$                 | $0.24 \pm 0.12$ | $0.37 \pm 0.14$ |
| CAA6          | 5        | $353 \pm 6$                     | $0.92 \pm 0.05$  | $8.1 \pm 0.8$                 | $0.20 \pm 0.04$ | $0.37 \pm 0.06$ |
| CAA7          | 6        | $337 \pm 12$                    | $1.01 \pm 0.22$  | $6.5 \pm 3.4$                 | $0.23 \pm 0.09$ | $0.35 \pm 0.11$ |
| VS            | 8        | $390 \pm 14$                    | $0.91 \pm 0.06$  | $4.8 \pm 0.7$                 | $0.30 \pm 0.11$ | $0.44 \pm 0.14$ |
| <b>Sub-ML</b> |          |                                 |                  |                               |                 |                 |
| K1            | 38       | $562 \pm 2$                     | $0.91 \pm 0.03$  | $1.7 \pm 0.0$                 | $0.69 \pm 0.04$ | $0.83 \pm 0.03$ |
| LS2           | 38       | $515 \pm 5$                     | $0.92 \pm 0.04$  | $4.8 \pm 0.1$                 | $0.46 \pm 0.10$ | $0.67 \pm 0.10$ |
| HB1           |          |                                 |                  |                               |                 |                 |
| HB2           |          |                                 |                  |                               |                 |                 |
| BB1.5         |          |                                 |                  |                               |                 |                 |
| BB3           | 27       | $400 \pm 1$                     | $0.83 \pm 0.02$  | $5.4 \pm 0.1$                 | $0.58 \pm 0.15$ | $0.73 \pm 0.13$ |
| BB2           | 23       | $485 \pm 3$                     | $0.81 \pm 0.03$  | $5.4 \pm 0.2$                 | $0.49 \pm 0.14$ | $0.69 \pm 0.13$ |
| CAA1          | 35       |                                 |                  |                               |                 |                 |
| CAA5          | 20       | $486 \pm 12$                    | $1.04 \pm 0.16$  | $6.0 \pm 2.2$                 | $0.30 \pm 0.11$ | $0.81 \pm 0.13$ |
| CAA6          | 24       | $428 \pm 6$                     | $0.78 \pm 0.04$  | $5.8 \pm 0.3$                 | $0.56 \pm 0.13$ | $0.73 \pm 0.12$ |
| CAA7          | 36       | $508 \pm 24$                    | $0.75 \pm 0.40$  | $3.3 \pm 0.7$                 | $0.55 \pm 0.08$ | $0.77 \pm 0.06$ |
| VS            | 39       | $390 \pm 4$                     | $0.62 \pm 0.05$  | $4.7 \pm 0.5$                 | $0.65 \pm 0.04$ | $0.82 \pm 0.03$ |

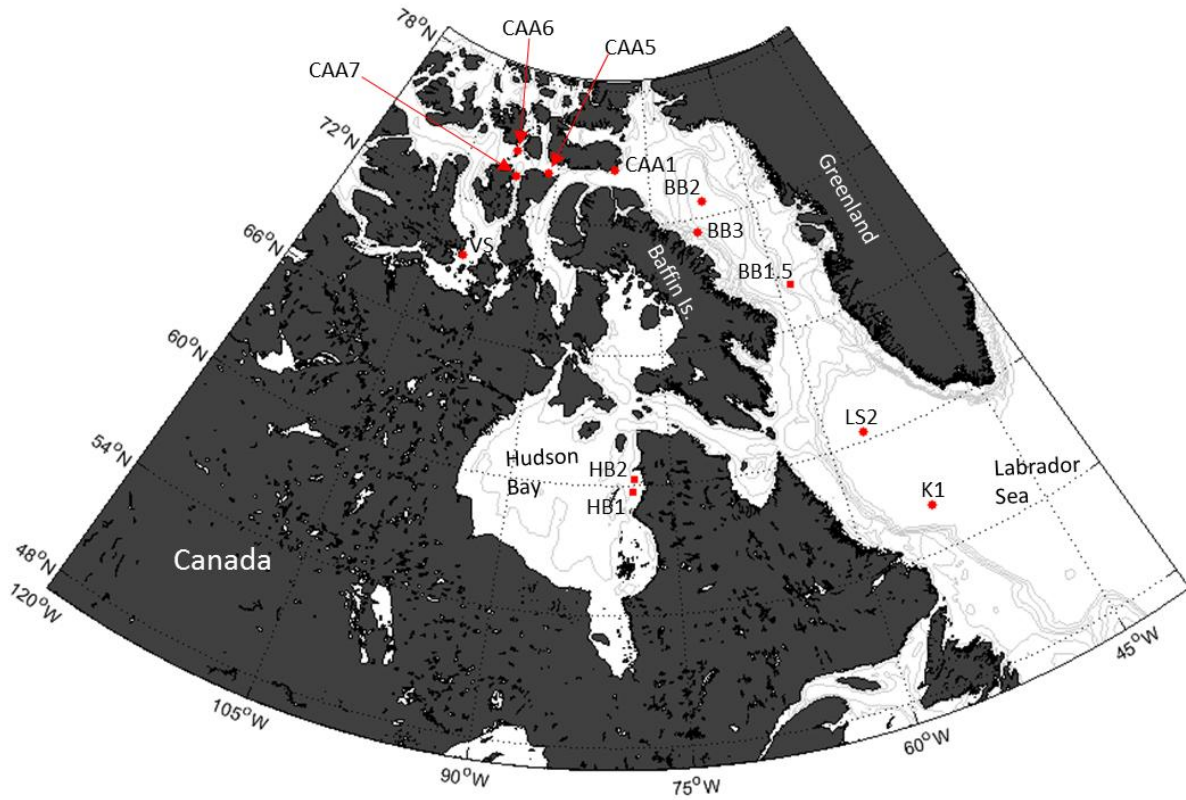


**Figure 4.1: Map of stations sampled.** See Table 4.1 and 4.2 for hydrological characteristics of the stations at the time of sampling. At stations HB1, HB2 and BB1.5 water was sampled from within the mixed layer only, using the ships underway water supply (7 m depth). At all other stations two samples were taken from the rosette of which one was within the mixed layer (50 % surface PAR) and one under the mixed layer (targeting the deep chl*a* maximum, if present).

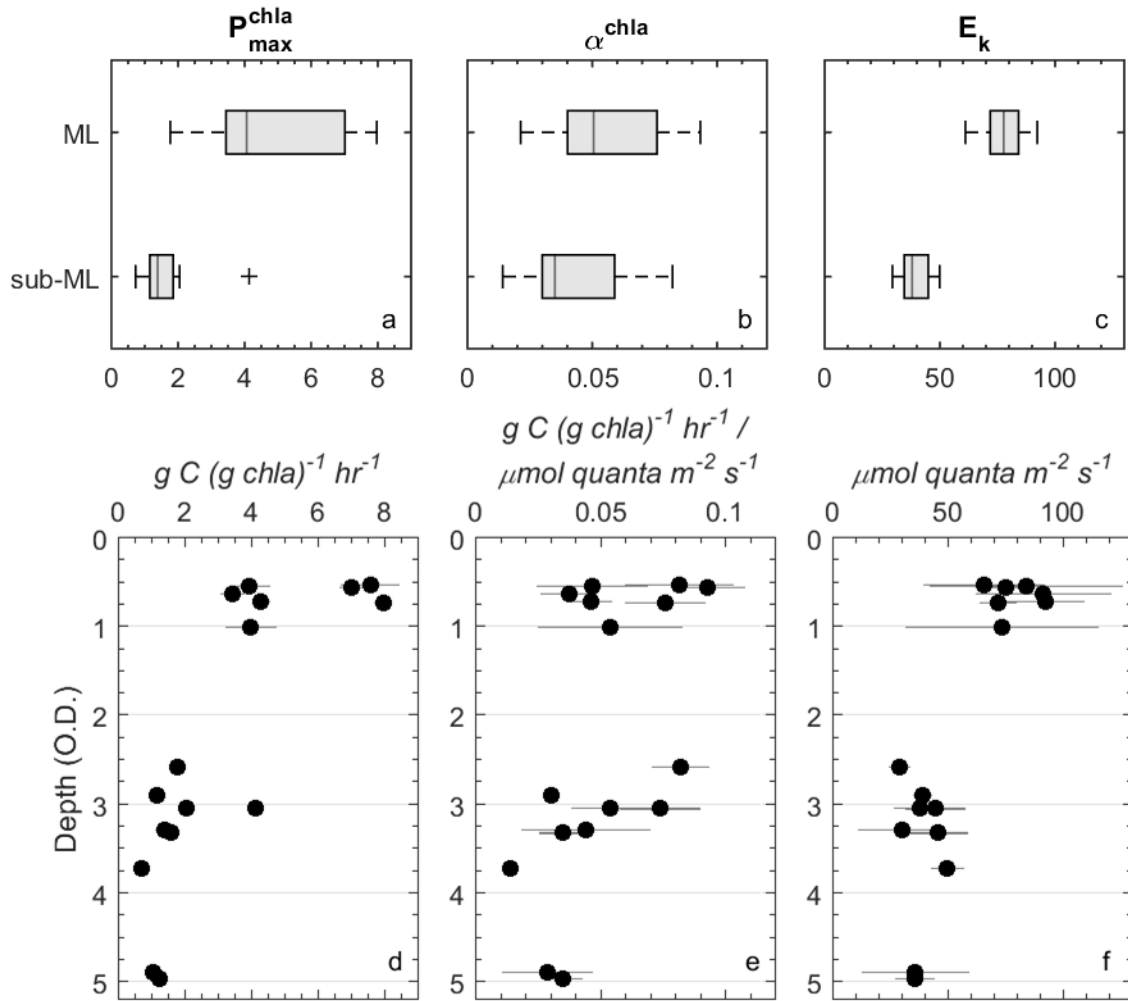


**Figure 4.2: Parameter derived from  $^{14}\text{C}$ -uptake vs E curves.** Comparison of ML vs sub-ML values of (a)  $P_{\text{max}}^{\text{chla}}$ , (b)  $\alpha^{\text{chla}}$  and (c)  $E_k$  of  $^{14}\text{C}$ -uptake. On each boxplot, the central mark indicates the median, and the box extends to the 25th and 75th percentiles, respectively. The whiskers extend over the range of values observed, excluding outlier values (shown as '+'). The difference in values for ML and CM samples was statistically significant for  $P_{\text{max}}^{\text{chla}}$  and  $E_k$ , but not  $\alpha^{\text{chla}}$  ( $p < 0.05$ , two tailed t-test assuming unequal variance). Panes d-f show the depth-dependence of  $P_{\text{max}}^{\text{chla}}$ ,  $\alpha^{\text{chla}}$  and  $E_k$  of  $^{14}\text{C}$ -uptake. The error in (d) and (e) is the 95 % confidence interval of the fit parameters derived from a fit to duplicate curves, while the error in (f) is the propagated error from the fit parameters ( $E_k = P_{\text{max}}^{\text{chla}} / \alpha^{\text{chla}}$ ). Note that all PvsE curves used to derive fit parameters are shown in Figure S2 in the appendix. Depth in panel d-f is given as optical depth (O.D.).

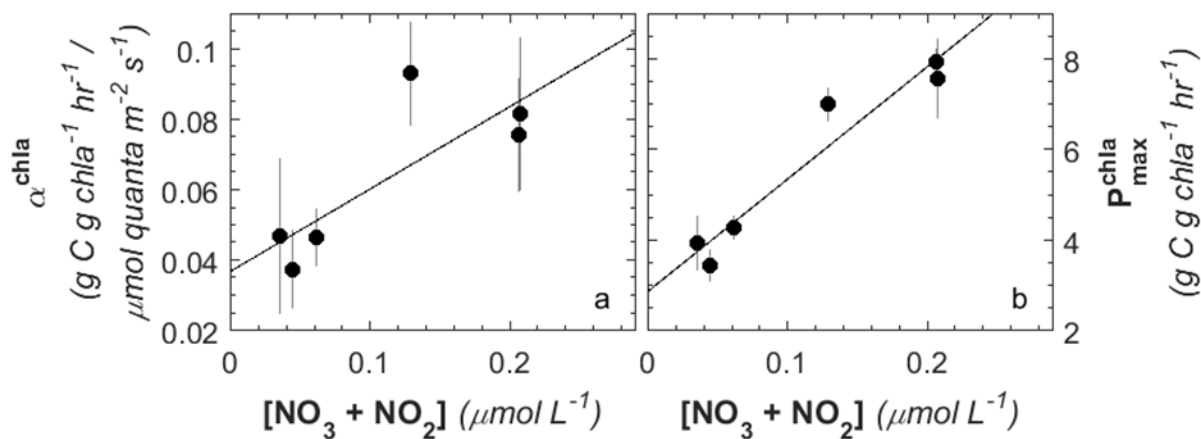


**Figure 4.3: Relationship between surface water (ML) nitrate ( $\text{NO}_3+\text{NO}_2$ ) concentrations and  $^{14}\text{C}$ -uptake  $P_{\text{max}}^{\text{chla}}$  and  $\alpha^{\text{chla}}$ . Lines represent the least square regression, which is statistically strong for both parameter and statistically significant for  $P_{\text{max}}^{\text{chla}}$  ( $R^2=0.65$ ,  $p=0.08$  and  $R^2=0.93$ ,  $p<0.005$  for (a) and (b), respectively).**

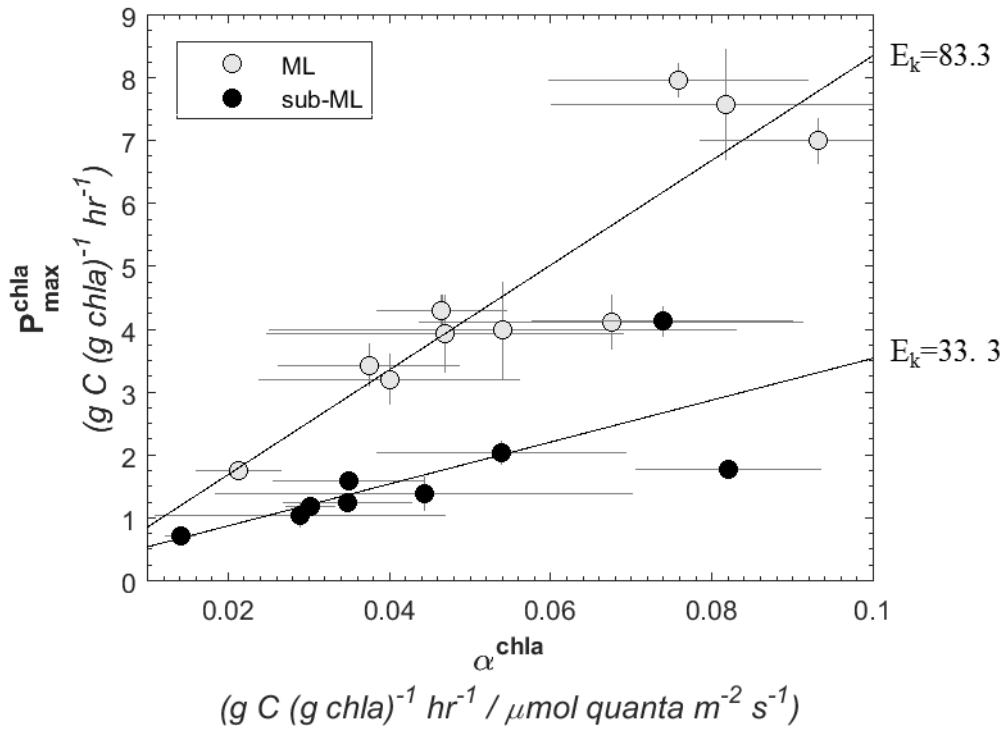


**Figure 4.4: Co-variation of  $\alpha^{chla}$  and  $P_{max}^{chla}$ .** The curve fit parameters  $\alpha^{chla}$  (g C g chla<sup>-1</sup> h<sup>-1</sup> [μmol quanta m<sup>-2</sup> s<sup>-1</sup>]<sup>-1</sup>) and  $P_{max}^{chla}$  (g C g chla<sup>-1</sup> h<sup>-1</sup>) change in parallel for ML (light symbols) and sub-ML samples (dark symbols). The slope of the regression corresponds to the mean light-saturation parameter  $E_k$  (μmol quanta m<sup>-2</sup> s<sup>-1</sup>) of <sup>14</sup>C-uptake within these growth environments.

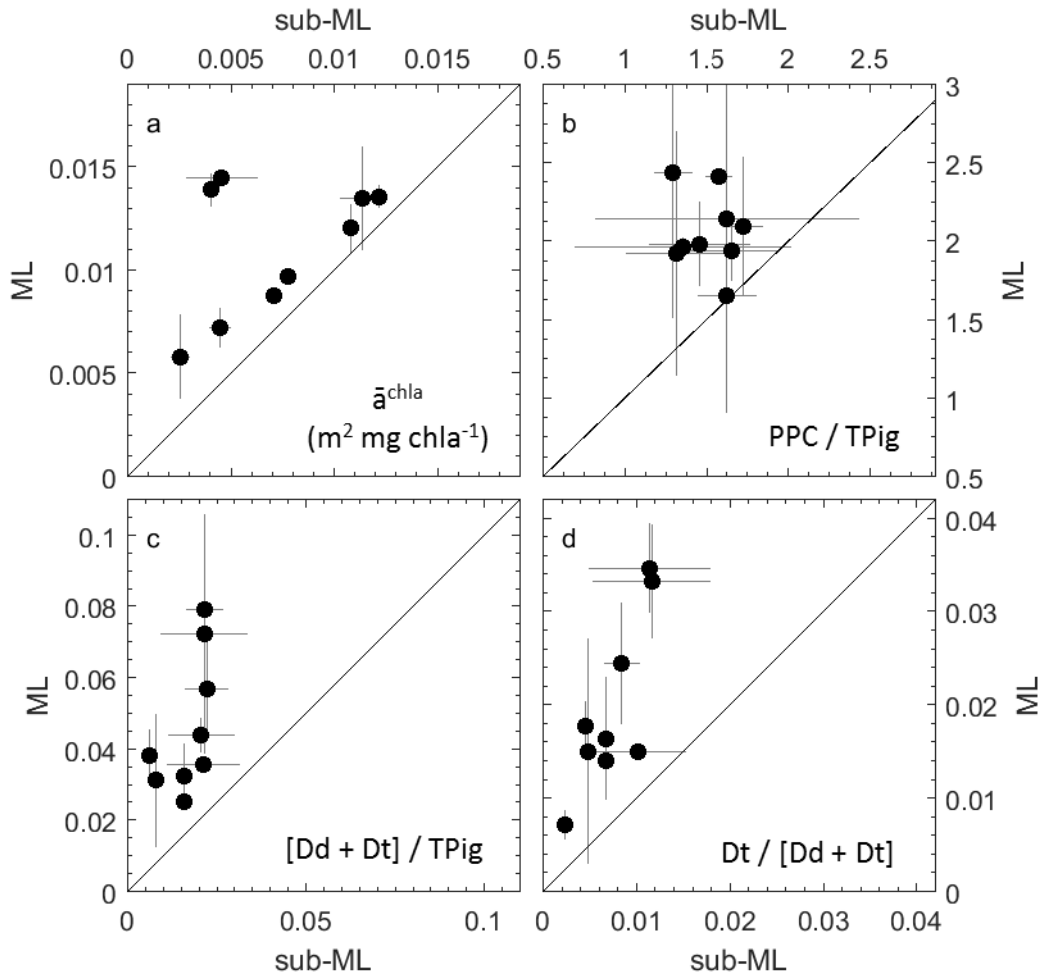


**Figure 4.5: Diagnostic absorption parameters and pigment ratios.** Comparison of ML and corresponding sub-ML samples of (a)  $\bar{a}_{\text{phy}}^{\text{chla}}$  (b) PPC/TPig (c) (Dt+Dd)/Tpig (d) Dt/(Dt+Dd). Shown are mean values and the range of duplicate measurements for each station and depth, with the 1:1 line shown in each sub-plot. See text for details of the different pigments included in the analysis.

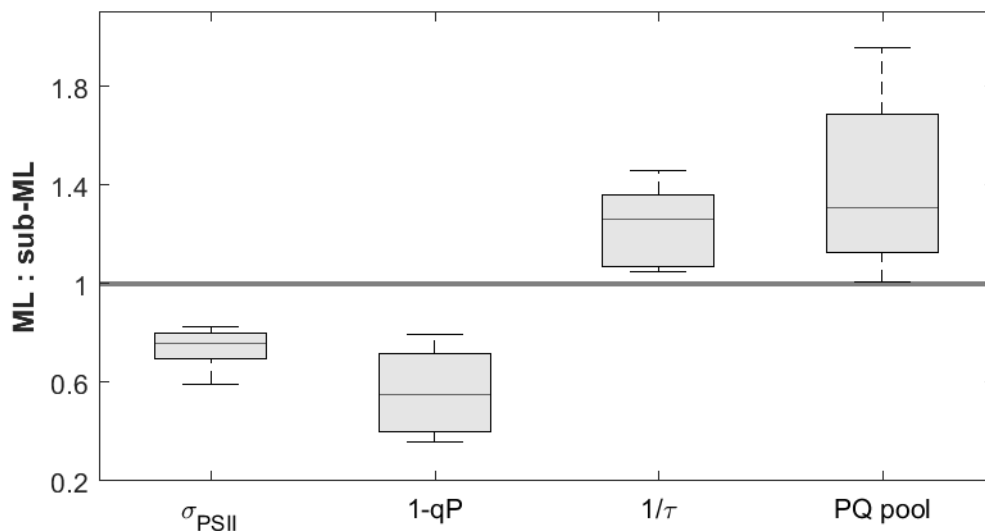


**Figure 4.6: Comparison of FRRF-derived photo-physiological properties in ML and sub-ML phytoplankton assemblages.** Values shown in the boxplots represent the ratio between ML and corresponding sub-ML samples of spectrally corrected  $\sigma_{\text{PSII}}$ , (1-qP),  $1/\tau$ , and PQ pool size. Parameters were derived in the dark-regulated state, apart from (1-qP), which was derived at a background irradiance of  $60 \mu\text{mol quanta m}^{-2} \text{s}^{-1}$ . See text for a description of the various parameters shown in the figure. The central mark on each plot indicates the median, the edge of the box represents the 25th and 75th percentiles, and the whiskers extend over the range of values observed.

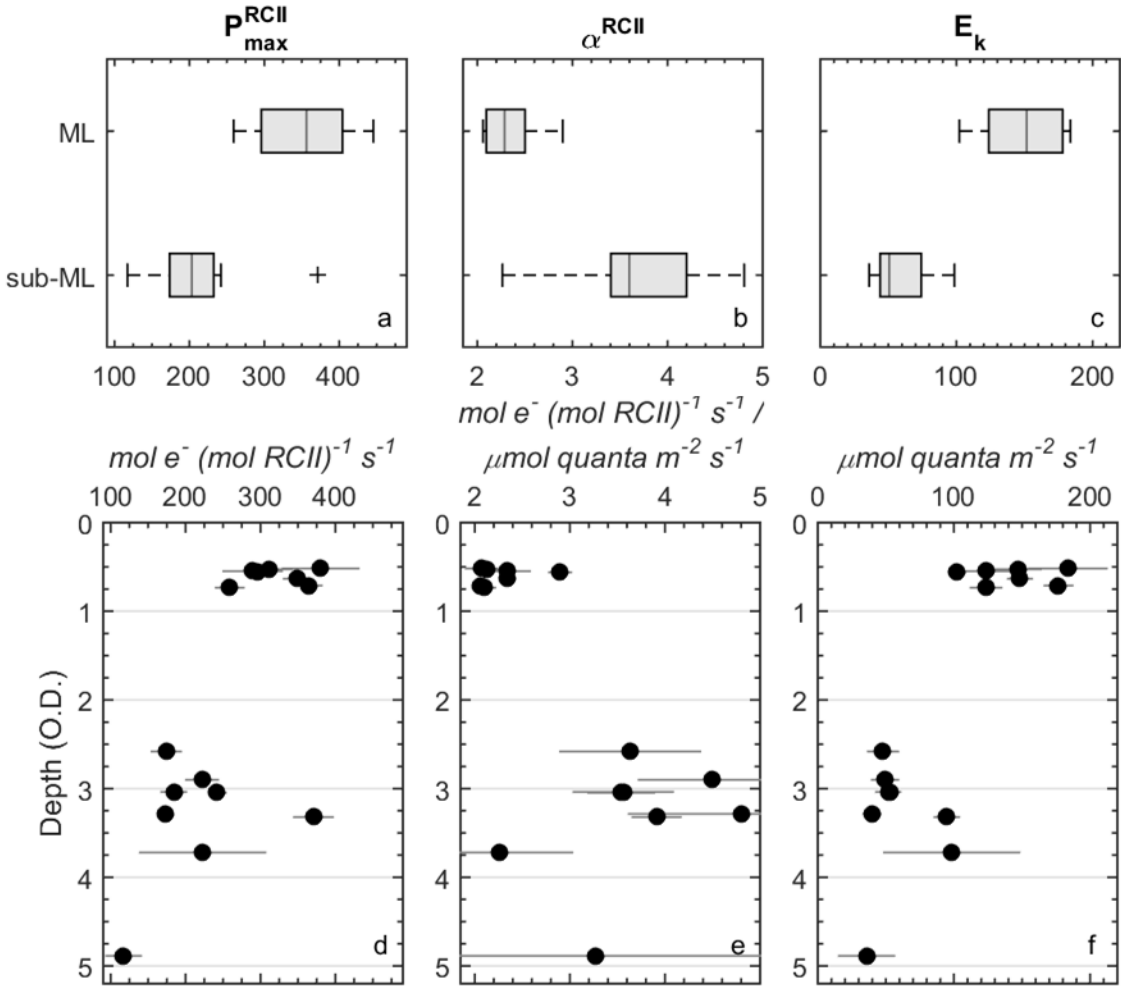


**Figure 4.7: Parameters from  $ETR_{RCII}$  vs  $E$  curves.** Comparison of ML vs sub-ML samples for (a)  $P_{max}^{RCII}$ , (b)  $\alpha^{RCII}$  and (c)  $E_k$  of  $ETR_{RCII}$ . On each box, the central mark indicates the median, and the box extends to the 25th and 75th percentiles, respectively. The whiskers extend over the range of values observed, excluding outlier values (shown as '+'). Panels d-f show the depth dependence of  $P_{max}^{RCII}$ ,  $\alpha^{RCII}$  and  $E_k$  of  $ETR_{RCII}$ . The error in (d) and (e) is the 95 % confidence interval of the fit parameters, while the error in (f) is the propagated error from the fit parameters ( $E_k = P_{max}^{chla} / \alpha^{chla}$ ). Depth in panel d-f is given as optical depth (O.D.).

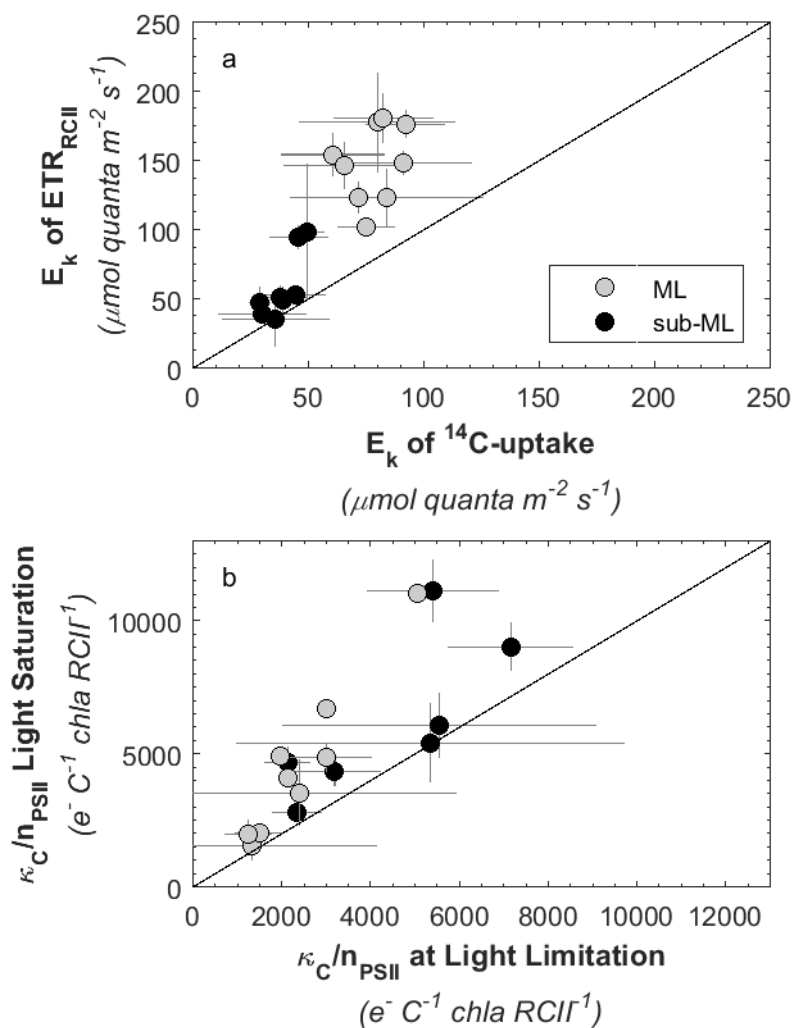


**Figure 4.8: Coupling of  $ETR_{RCII}$  and  $^{14}\text{C-uptake}$ .** (a) Comparison of the light saturation parameter  $E_k$ , of  $ETR_{RCII}$  and  $^{14}\text{C-uptake}$  measured within the same samples for ML (light symbols) and sub-ML samples (dark symbols); (b) comparison of the conversion factor ( $\kappa_C/n_{PSII}$ ,  $\text{mol } e^- \text{ mol } C^{-1} \text{ mol chla mol } RCII^{-1}$ ) at light limitation (derived as  $\alpha^{RCII}/\alpha^{chla}$ ) and at light saturation (derived as  $P_{max}^{RCII}/P_{max}^{chla}$ ). The 1:1 line is shown in each sub-plot.

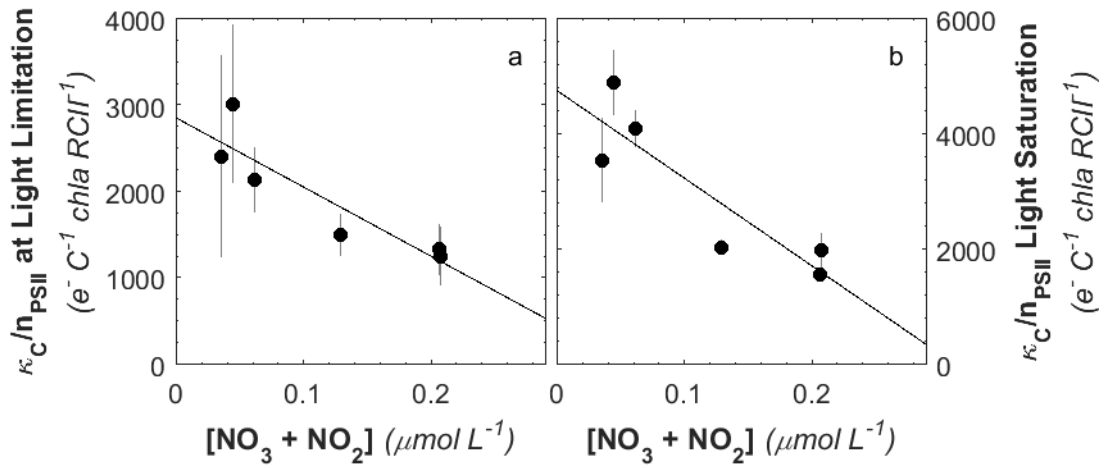


**Figure 4.9: Relationship between surface water (ML) nitrate ( $\text{NO}_3+\text{NO}_2$ ) concentrations and the conversion factor ( $K_C/n_{\text{PSII}}$ ,  $\text{mol e}^- \text{mol C}^{-1} \text{mol chla mol RCII}^{-1}$ ) at light limitation (derived as  $\alpha^{\text{RCII}}/\alpha^{\text{chla}}$ ) and at light saturation (derived as  $P_{\text{max}}^{\text{RCII}}/P_{\text{max}}^{\text{chla}}$ ). Lines represent the least square regression, which is statistically significant in both cases ( $R^2 = 0.81$ ,  $p < 0.05$  and  $R^2 = 0.79$ ,  $p < 0.05$  for (a) and (b), respectively).**

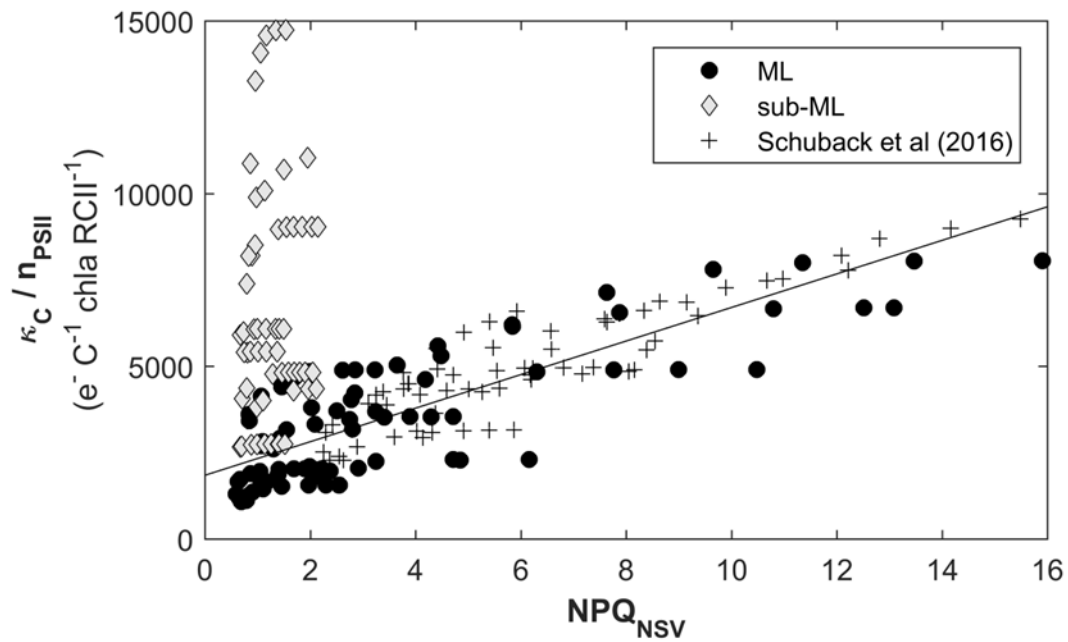


**Figure 4.10: Correlation of non-photochemical quenching,  $NPQ_{NSV}$ , and the conversion factor between  $ETR_{RCII}$  and  $^{14}C$ -uptake,  $K_C/n_{PSII}$ .** Values of  $NPQ_{NSV}$  and  $K_C/n_{PSII}$  were derived from light response curves of  $^{14}C$ -uptake and ChlF yields measured by FRRF. The linear regression through data-points from Schuback et al. (2016) and the ML samples from the present study,  $K/n_{PSII} = 486 NPQ_{NSV} + 1854$ , is significant ( $R^2 = 0.75$ ,  $p < 0.01$ ).

## Chapter 5: General discussion

---

As with any sustained research effort, the work presented in this thesis raises as many new questions as it answers. In this chapter, I present a number of concepts and ideas emerging from the experimental work presented in the previous chapters, and discuss the broader significance and applicability of key findings, drawing general conclusions and suggesting future research directions.

### 5.1 Evolutionary considerations

The work presented in this thesis illustrates how understanding of the photosynthetic process at the molecular and photo-physiological level can be used to improve estimates of phytoplankton primary productivity. While understanding *how* photosynthesis functions on a sub-cellular level provides important information, considering *why* it does so can be even more insightful. In other words, one needs to consider the evolutionary forces that have shaped the photosynthetic process, in order to understand its response to current day environmental variability. Evolutionary pressure to develop mechanisms for rapid sensing and effective dissipation of excess excitation energy, and balance electron flow and carbon fixation has shaped the sophisticated plasticity of phytoplankton photosynthesis. An appreciation of these evolutionary pressures provides an important context for the interpretation of data presented in chapters 2-4.

The first photosynthetic organisms evolved 3.2-2.4 billion years ago, well before the oxygen produced as a by-product of water splitting in oxygenic photosynthesis significantly changed the oxygenation state of the atmosphere (e.g. Falkowski, 2006). Thus, the photosynthetic process itself contributed to drastically changing the environment in which it evolved, with important consequences for the functioning of the photosynthetic light reactions of marine phytoplankton. As I will explain in the following, the damaging effects of excess excitation energy and consequently the requirement for safe dissipation processes are a direct consequence of the oxygenation of the atmosphere.

Under conditions of excess excitation energy, absorbed energy in the pigment antenna cannot be used for charge separation and electron transport, resulting in the formation of a 'triplet

state' in the reaction center chlorophyll molecule P680. In a reducing environment this 'triplet state' would be harmless and rapidly decay back to its ground state. In an oxidizing environment, however, the P680 triplet readily reacts with molecular oxygen (Allahverdiyeva and Aro, 2012; Vass, 2011). The singlet oxygen produced in this way can destroy surrounding molecules, a process known as acceptor-side photoinhibition (Aro et al., 1993). Preventing conditions of excess excitation energy (and the resulting acceptor-side photoinhibition) during the photosynthetic process is not trivial, given that this process couples photochemical and biochemical processes with vastly different rate constants and significantly different temperature sensitivities (e.g. Huner et al., 1998). The scarcity of iron in vast marine regions (chapters 2 and 3), itself a direct consequence of the oxygenation of the ocean, further enhances the likelihood of excess excitation energy to occur. Iron was readily available in the ancient anaerobic and highly reducing ocean, and hence incorporated into many cellular processes, including the photosynthetic electron transport chain (e.g. Raven et al., 1999). However, the solubility of iron in aqueous solution was drastically reduced in an oxygenated environment, compromising the optimal functioning of the photosynthetic electron transport chain and enhancing susceptibility to excess excitation energy.

The above considerations help explain why present day phytoplankton possess numerous processes to dissipate excess energy before (NPQ) and after (alternative electron sinks) charge separation in PSII. The correlation of processes acting before and after charge separation in PSII represents a key finding of this thesis and its significance is discussed in detail in the next section.

## **5.2 NPQ as an integrator for physiological state**

One emerging concept of this thesis is the role of excess excitation energy as a central expression of physiological stress caused by interacting environmental variables and metabolic states. Excitation energy can be defined as the relative redox state of the primary stable electron acceptor  $Q_A$  (e.g. Hünner et al., 2012), which is, in turn, controlled by the balance between the rate of excitation energy reaching RCII and downstream metabolic processes affecting re-oxidation of  $Q_A$ . Consequently, the redox state of  $Q_A$  is not only sensitive to changes in light availability, but also to changes in the ability of downstream processes to utilize electrons from charge separation in PSII. In order to dissipate excess excitation energy, cascades of interacting

and self-regulating photo-physiological mechanisms are triggered by a highly reduced electron transport chain and/or the concomitant steep pH gradient across the thylakoid membrane. This thesis exploits the correlation between the 'up-stream' processes of NPQ in the pigment antenna with 'downstream' mechanisms acting to alleviate the over-reduction of the electron transport chain after charge separation in RCII (see Figure 2.8). The downstream energy dissipation mechanisms are reflected in changes in the conversion factor between FRRF-derived ETR and  $^{14}\text{C}$ -uptake. Thus, the correlation between NPQ (which can be easily estimated from FRRF measurements) and the conversion factor has the potential to significantly improve FRRF-based productivity estimates. A number of factors make this approach more desirable than the static, regional conversion factors, proposed by e.g. Lawrenz et al. (2013).

While it is clear that some key environmental variables will have a disproportionate effect on the conversion factor, the magnitude and variability of the conversion factor ultimately reflect the expression of a multitude of interacting environmental variables. The use of NPQ as an integrated physiological measure of environmental effects on electron transport processes therefore offers a unique opportunity to simultaneously assess various environmental stressors. Moreover, as is clearly visible from the PvsE curve approach taken in this thesis, the magnitude of the conversion factor can vary significantly within a given sample in response to short-term variations in incident light. Such small scale changes would be lost using a static (regional) conversion factor, but are captured with the NPQ-proxy approach. Here, every single  $\text{ETR}_{\text{RCII}}$  estimate is paired with a corresponding NPQ estimate, without the need for any additional sampling or instrumentation. Finally, a non-static conversion factor is crucial if the goal is to utilize FRRF instruments to monitor the effects of environmental change on marine primary productivity. The variable conversion factor between  $\text{ETR}_{\text{RCII}}$  and carbon fixation represents the expression of the photo-physiological plasticity needed to balance different components of the photosynthetic process and prevent damage (section 5.1), thus 'buffering' environmental fluctuations. Therefore, the conversion factor is likely to change first in response to environmental change, which could lead to misinterpretation of data. For example, a shallower upper mixed layer, anticipated as a response to global warming, will increase light availability and consequently ETR as derived from FRRF measurements. If a static conversion factor was to be used, an increase in ETR would be interpreted as an increase in carbon-based productivity. However, it is likely that in many instances low nutrient concentrations in the mixed layer would

prevent the utilization of increased electron flow for increased carbon fixation. Under such conditions, the conversion factor, not carbon fixation, would increase.

### 5.3 Linking the molecular to the global scale

Synoptic monitoring of phytoplankton primary productivity is needed to understand ecosystem dynamics and global biogeochemical cycles, over large temporal and spatial scales. One of the overarching goals of this thesis is to improve the quantification of marine phytoplankton primary productivity over large scales without the need for time-consuming *in situ* measurements. Traditional oceanographic measurements of primary productivity have relied on discrete bottle assays, which may introduce artifacts of sample containment, and cannot fully capture the synoptic scales needed to understand regional and global-scale biogeochemical processes. Likely, the most effective approach to synoptically assess entire ocean basins is remote sensing by satellites. Remotely sensed water-leaving irradiance provides information on the light available for photosynthesis, as well as estimates of chl $a$  biomass. The greatest uncertainty in current satellite primary productivity algorithms lies in how to parameterize the variability in biomass-specific photosynthetic rates (e.g. Westberry and Behrenfeld, 2014); and numerous approaches have been developed to relate biomass-specific rates to independent variables such as temperature, nutrient concentrations, phytoplankton community structure, growth irradiance, or combinations thereof (e.g. Behrenfeld and Falkowski, 1997; Behrenfeld et al., 2002; Huot et al., 2007; Uitz et al., 2008). As explained in the introduction of this thesis, two important requirements for the improvement of satellite algorithms are higher resolution data and a better mechanistic understanding of the environmental controls on the photosynthetic process. The experimental approach taken in this thesis provides mechanistic insight into how physicochemical variables affect cell physiology and metabolism, while presenting field-based observations that help constrain the parameterization of remote sensing algorithms. Particularly useful for empirical parameterization of productivity algorithms are  $^{14}\text{C}$ -uptake PvsE derived fit parameters (e.g. Behrenfeld 2002). To this end, the work presented in chapters 2-4 demonstrates strong diurnal periodicity under iron limitation (Chapter 3), and unexpected variability in Arctic waters (Chapter 4). For Arctic phytoplankton assemblages, the results presented in chapter 4 also suggest an empirical correlation between productivity and the extent of nitrate depletion within

the upper mixed layer, and highlight the distinction between the mixed layer and sub-surface populations.

More empirical data on marine phytoplankton primary productivity and key controlling environmental variables are needed for a better parameterization of satellite algorithms and numerical modelling approaches. To this end, this thesis shows that an appreciation of molecular scale photosynthetic regulation is indispensable if FRRF approaches are to be developed as a tool for high resolution acquisition of *in situ* phytoplankton primary productivity estimates. Moreover, this thesis emphasizes the importance of a mechanistic, photo-physiological understanding of the photosynthetic process to maximize the ability of satellite algorithms and numerical models to predict future changes in marine primary productivity in response to environmental perturbations.

#### **5.4 Potentials and limitations of induced ChlF approaches in oceanography**

Induced ChlF approaches, including FRRF, provide a sensitive, non-invasive tool to specifically probe the activity and functioning of the photosynthetic apparatus. While the approach is likely the most widely applied technique in photosynthesis research (Govindjee, 1995; Papageorgiou and Govindjee, 2004), where it has been used for almost a century, its introduction to oceanographic research is comparatively recent (Falkowski and Kiefer, 1985; Falkowski and Kolber, 1995; Kolber and Falkowski, 1993; Suggett et al., 2010a).

Optical instruments, providing autonomous, instantaneous, and high-resolution measurements of fluorescence, absorption or scattering properties of *in situ* phytoplankton assemblages are ideally suited for oceanographic research (e.g. Dickey, 1991). Such approaches are increasingly supplementing and replacing more traditional methods relying on the collection of water samples and laboratory analyses (Cullen et al., 1997; Schofield et al., 1999). At present however, it remains challenging to accurately infer ecologically-relevant properties such as phytoplankton biomass, physiology, taxonomy or primary productivity from these optical measurements. In the case of induced ChlF approaches in oceanography, the ability to rapidly acquire large amounts of data has somewhat surpassed the ability to accurately interpret the signal.

Predominantly, it is a misunderstanding of the basic principles and not the method *per se*, which has hampered its promise of providing low cost, high-resolution, non-intrusive data on phytoplankton primary productivity and nutritional status. In the following sections I discuss potentials and limitations of FRRF approaches for primary productivity estimates (section 5.4.1) and as an indicator of iron limitation (section 5.4.2) in marine phytoplankton.

#### ***5.4.1 FRRF and productivity***

The derivation and interpretation of FRRF derived ChlF yields and parameters rely on the application of conceptual, biophysical models. These models were developed primarily in the context of basic photosynthesis research in eukaryotic, single-species cultures. Consequently, application of such concepts and theories to mixed phytoplankton assemblages in the ocean is bound to be problematic. Moreover, even for single-species cultures of phytoplankton, the ChlF yield measured is the expression of numerous processes related to the adjustment of the photosynthetic apparatus to dominant environmental constraints and metabolic needs. In the laboratory, well controlled reference conditions can be achieved to minimize this problem. For autonomous field sampling of mixed phytoplankton assemblages, however, identifying the relative contribution of light-history, taxonomic composition and other sources of variability influencing FRRF measurements requires great care. One example of this predicament is that electron transport rate calculations require ChlF yields measured in the fully dark-regulated state (i.e. the electron transport chain is oxidized and all NPQ processes are relaxed). In practice, this is impossible to achieve in mixed field assemblages, introducing some uncertainty into the derived rates.

Throughout this thesis I applied the four parameter biophysical model by Kolber and Falkowski (1993) to derive rates of electron transport from ChlF yields. Since its introduction, many different variations of this model have been used in the literature, and alternative modeling approaches have recently been introduced (Oxborough et al., 2012). The most noticeable refinement in the calculation of rates of electron transport from ChlF yields over that past two decades is the realization of variability in parameters that were previously assumed to be constant. For example, a great amount of research has been dedicated to constrain the variability in the electron requirement for carbon fixation,  $K_c$  ( $\text{mol e}^- \text{mol C}^{-1}$ ). A constant value of  $4 \text{ mol e}^- \text{mol C}^{-1}$ , which is the theoretical minimum, was originally applied to directly derive rates of

productivity in carbon units from FRRF measurements (Kolber and Falkowski, 1993). More recently, research has focused on deriving rates of electron transport ( $ETR_{PSII}$ ,  $\text{mol e}^- \text{mol chl}a^{-1} \text{s}^{-1}$ ) from FRRF measurements and predicting the appropriate value of  $K_c$  from controlling environmental conditions (e.g. Lawrenz et al., 2013). In this thesis, I take this approach a step further, treating the parameter  $1/n_{PSII}$  ( $\text{mol chl}a \text{mol RCII}^{-1}$ ) as another critical unknown whose variability (in response to taxonomy, physiological status etc.) could contribute significantly to the observed discrepancy between FRRF-derived ETR and carbon fixation. Clearly, the derived conversion factor  $K_c/n_{PSII}$  ( $\text{mol e}^- \text{mol C}^{-1} \text{mol chl}a \text{mol RCII}^{-1}$ ) is complex, and prevents a full mechanistic understanding of the processes decoupling carbon fixation and electron transport. Arguably though, it is a more ‘honest’ approach, where variability in  $1/n_{PSII}$  cannot be incorrectly attributed to variability in  $K_c$ . Furthermore, RCII-specific rates of electron transport ( $ETR_{RCII}$ ,  $\text{mol e}^- \text{mol RCII}^{-1} \text{s}^{-1}$ ) are derived with more confidence than chl*a* specific rates ( $ETR_{PSII}$ ,  $\text{mol e}^- \text{mol chl}a^{-1} \text{s}^{-1}$ ) and give important insight into photo-physiological optimization strategies (e.g. the unexpected increase in  $ETR_{RCII}$  in iron limited phytoplankton, Chapter 2).

In summary, research efforts in the past 20 years have clearly shown that the conversion factor required to estimate carbon-based rates of phytoplankton primary productivity from FRRF-derived estimates of electron transport is far too variable to be assumed constant. Recent work has subsequently focused on determining appropriate regional conversion factors (e.g. Lawrenz et al. 2013). The work presented in this thesis adds a new dimension, by introducing estimates of NPQ as a proxy for the magnitude and variability of the conversion factor. This approach is a major contribution of this thesis, and one, which due to its simplicity, holds significant promise to improve carbon-based estimates of phytoplankton primary productivity from FRRF measurements (section 5.2).

While it is true that the presence of a variable conversion factor between rates of electron transport and carbon fixation complicates the applicability of FRRF instruments to assess phytoplankton productivity, this variability also provides insight into the regulation of the photosynthetic process leading to carbon fixation. Research efforts aimed at constraining the conversion factor and developing FRRF-based productivity estimates often seem to overlook the opportunity to study photosynthetic carbon fixation simultaneously at different points along the process. Many recent studies have demonstrated that the coupling of initial photochemical reactions and realized rates of carbon fixation is particularly variable in phytoplankton (e.g.

Bailey et al., 2008; Curien et al., 2016; Grossman et al., 2010; Rochaix, 2011). If the ultimate goal is to understand how photosynthetic carbon fixation is controlled by interacting environmental variables and to predict the response of marine primary productivity to climate change, mechanistic understanding of this variability is crucial. Consequently, while it is important to further refine and improve approaches to derive carbon-based productivity estimates from FRRF measurements, the potential of this method to assess other aspects of phytoplankton physiology should not be overlooked.

#### **5.4.2 FRRF and iron limitation**

The parameter  $F_v/F_m$ , derived from FRRF measurements, is often referred to as the efficiency of charge separation in PSII or simply the photochemical efficiency of PSII. In biological oceanography, this derived parameter has become widely used as a physiological indicator of iron limitation in phytoplankton, with low  $F_v/F_m$  values used as a diagnostic for iron stress (e.g. Greene et al., 1994; Kolber et al., 1994; Ryan-Keogh et al., 2013). This interpretation of  $F_v/F_m$  implies that iron limitation reduces the efficiency of charge separation in PSII, and should, therefore, reduce the rate of  $ETR_{RCII}$  ( $\text{mol e}^- \text{mol RCII}^{-1} \text{s}^{-1}$ ). However, results from field and laboratory experiments presented in chapter 2 show that this is not the case (Table 2.1, Figure 2.3 and Figure 2.4). Rather, the decrease in  $F_v/F_m$  under iron limitation is caused by an increase in  $F_o/F_m$ , likely due to fluorescent chl $a$ -containing complexes, which fluoresce (increase  $F_o$ ) but do not exhibit variable fluorescence (no increase of  $F_m$ ). As suggested by previous authors (e.g. Behrenfeld et al., 2006b; Schrader et al., 2011; Behrenfeld and Milligan, 2013; Macey, 2014), this could be due to the presence of chl $a$  containing light harvesting complexes (LHCs) associated with damaged and dysfunctional RCII, and/or LHCs which are energetically decoupled from functional RCII (edLHCs or DLHCs). Therefore, the diagnostic decrease of  $F_v/F_m$  under iron limitation should not be interpreted as a decrease in the photochemical efficiency of charge separation in RCII. Rather, the entire process of photosynthesis, from energy capture to carbon fixation, is fine-tuned to maximize efficiency, and it is this fine-tuning that is manifested in changes of variable fluorescence properties. Results from this thesis underscore this interpretation.

The specific biological function of such edLHCs associated with iron-dependent decreases in  $F_v/F_m$  remains unresolved. Based on the experimental results presented in chapter 2,

it is possible to support and expand on the ideas of others (Behrenfeld and Milligan, 2013; Berera et al., 2009; Cadoret et al., 2004; Ihalainen et al., 2005; Kojima et al., 2006; Wilson et al., 2006; Yeremenko et al., 2004) who suggest that edLHCs represent an evolutionary adaptation for enhanced non-photochemical quenching potential in the antennae. Interestingly, Belgio et al. (2014) recently demonstrated that non-photochemical quenching in the antennae complexes of vascular plants only dissipate excess energy when RCII are closed, and does not act as quencher when RCII are open. Assuming that the edLHCs of marine phytoplankton express similar quenching characteristics, these edLHCs could then be responsible for the characteristic decrease in  $F_v/F_m$ , having a function which is energetically and evolutionarily justified.

The fact that adaptation to iron limitation resulted in molecular scale adjustments with characteristic changes in ChlF yields provides a further example of how an understanding and appreciation of sub-cellular processes can be extrapolated to signals detectable from space. Recent work has suggested that diagnostic changes in sun-induced chlorophyll fluorescence yields can be used to quantify areas in the global oceans where primary productivity is affected by iron limitation (Behrenfeld et al., 2009), after accounting for the effect of NPQ (Browning et al., 2014b). Satellite detected sun-induced chlorophyll fluorescence holds tremendous promise to synoptically assess numerous aspects of phytoplankton physiology in the world's oceans. However, at present, the interpretation of the signal requires a much better mechanistic understanding of photo-physiological processes and their regulation (Huot et al., 2005, 2013b; Morrison and Goodwin, 2010). FRRF-derived *in situ* measurements of numerous aspects of phytoplankton photo-physiology have great potential to aid in the development and validation of such approaches.

## **5.5 Future directions**

The following section provides a number of specific recommendations for future studies building on the results presented in chapters 2-4.

### **5.5.1 Spectral correction**

Spectral correction of phytoplankton primary productivity measured *ex situ* is essential to produce ecologically-relevant and inter-comparable data. Clearly, if satellite algorithms or numerical models are developed and validated using uncorrected data, their ability to accurately

estimate phytoplankton primary productivity *in situ* will be compromised. In many FRRF instruments, excitation as well as background light is supplied at a narrow bandwidth of blue wavelength. Because phytoplankton will absorb light most efficiently at this wavelength, the resulting ChlF yields and the signal to noise ratio will be maximal. However, if FRRF-derived  $ETR_{RCII}$  is to be compared to  $^{14}C$ -uptake rates, the difference in spectral distribution of light sources for these two measurements needs to be accounted for, relative to the spectral light absorption characteristics of the phytoplankton. Moreover, derivation of ecologically-relevant rates for any given region requires *ex situ* measurements to be scaled to the spectral distribution of *in situ* light at the depth of sampling. In the case of  $^{14}C$ -uptake PvsE curve experiments, the spectral distribution of light in the photosyntheticron is often not reported (or even measured), so that spectral correction of derived rates and fit parameters are not consistently applied. Given the increasing availability of highly portable and relatively low cost spectrally-resolved PAR sensors, characterizing light sources *ex situ* should become a more routine measurement. Preferably, spectral distribution of light sources in FRRF instruments and in photosyntheticrons should be identical, and well-tuned to the spectral distribution of *in situ* light. To this end, it would be desirable to increase the application of *in situ* multi-wavelength radiometers to validate and improve approaches to model the spectral quality of *in situ* light, like the one utilized in this thesis.

The ultimate goal to develop FRRF as a routine approach for accurate estimates of *in situ* productivity requires the deployment of instruments *in situ*, thus avoiding the need for spectral correction entirely. This is theoretically possible with current technology. Such *in situ* FRRF deployments would require a multi-wavelength excitation source connected to a multi-wavelength radiometer, allowing instantaneous adjustment of the relative intensity of each wavelength in the FRRF instrument to match the spectral distribution of *in situ* light at the depth of measurement.

### **5.5.2 Uncertainties in $^{14}C$ -uptake experiments**

For more than 5 decades,  $^{14}C$ -uptake experiments have remained the standard method in biological oceanography against which most other primary productivity methods are compared or calibrated. However, this methodological approach has its own limitations, including the need for *ex situ* incubations (e.g. Bender et al., 1987; Fitzwater et al., 1982; Quay et al., 2010; Ryther,

1956), and uncertainty about whether gross or net primary productivity is being measured (Halsey et al., 2010, 2011; Marra, 2009; Milligan et al., 2015; Pei and Laws, 2013). Traditionally, it has been assumed that long incubation times (>12 hours) approximate net productivity (initially fixed carbon minus carbon lost by autotrophic respiration), while short incubation times (<2 hours) approximate gross productivity. Recent research has shown, however, that this is not the case, with incubation times of less than an hour yielding estimated rates closer to net than to gross productivity under nutrient limiting conditions (Halsey et al., 2011). This result is important in the context of the work presented in this thesis because the ETR to  $^{14}\text{C}$ -uptake conversion factor will be lower if net rather than gross  $^{14}\text{C}$ -uptake is measured. In order to better constrain the above uncertainty, the experimental approach taken throughout this thesis (i.e. the comparison of  $^{14}\text{C}$ -based and  $\text{ETR}_{\text{RCII}}$ -based  $P_{\text{vsE}}$  curves) should be extended to include time-course measurements of  $^{14}\text{C}$ -uptake  $P_{\text{vsE}}$  curves (e.g. 0.5, 1, 2, 4 hour incubation times). This approach will likely reveal a reduction in the derived conversion factor with increasing incubation time, with the rate of reduction in conversion factor likely being faster under conditions of nutrient limitation.

### **5.5.3 Confirmation of alternative electron flow pathways**

The three data chapters included in this thesis suggest that the increased decoupling of  $\text{ETR}_{\text{RCII}}$  and  $^{14}\text{C}$ -uptake, observed under conditions of excess excitation energy, is due to an upregulation of alternative electron flow pathways which act as ‘safety valves’ to alleviate potentially harmful over-reduction of  $Q_A$ . In particular, the involvement of short water-water cycling of electrons through plastid terminal oxidase (PTOX) is suggested as an adaptation to low iron (chapters 2 and 3) and low temperature (chapter 4) under conditions of excess light. While there is strong support for this idea in the recent literature (e.g. Bailey et al., 2008; Curien et al., 2016; Grossman et al., 2010; Halsey and Jones, 2015; Laureau et al., 2013; Mackey et al., 2008; McDonald et al., 2011; Ort and Baker, 2002; Rochaix, 2011; Zehr and Kudela, 2009), additional measurements could help to further clarify the nature of the underlying mechanism. For instance, use of the PTOX inhibitor octy gallate (Hohmann-Marriott 2010, Ivanov 2012) would provide a reasonably straightforward approach to further confirm the importance of PTOX mediated water-water cycling in the decoupling of  $\text{ETR}_{\text{RCII}}$  and  $^{14}\text{C}$ -uptake under excess excitation energy.

## References

---

- Allahverdiyeva, Y., and Aro, E.M. (2012). Photosynthetic Responses of Plants to Excess Light: Mechanisms and Conditions for Photoinhibition, Excess Energy Dissipation and Repair. *Photosynthesis* 275–297.
- Allen, A.E., LaRoche, J., Maheswari, U., Lommer, M., Schauer, N., Lopez, P.J., Finazzi, G., Fernie, A.R., and Bowler, C. (2008). Whole-cell response of the pennate diatom *Phaeodactylum tricornutum* to iron starvation. *Proc. Natl. Acad. Sci.* 105, 10438–10443.
- Anderson, J.M., Chow, W.S., and Park, Y.-I. (1995). The grand design of photosynthesis: Acclimation of the photosynthetic apparatus to environmental cues. *Photosynth. Res.* 46, 129–139.
- Ardyna, M., Babin, M., Gosselin, M., Devred, E., Rainville, L., and Tremblay, J.-É. (2014). Recent Arctic Ocean sea ice loss triggers novel fall phytoplankton blooms. *Geophys. Res. Lett.* 41, 6207–6212.
- Aro, E.-M., Virgin, I., and Andersson, B. (1993). Photoinhibition of Photosystem II. Inactivation, protein damage and turnover. *Biochim. Biophys. Acta BBA - Bioenerg.* 1143, 113–134.
- Arrigo, K.R., and van Dijken, G.L. (2011). Secular trends in Arctic Ocean net primary production. *J. Geophys. Res. Oceans* 116, C09011.
- Arrigo, K.R., and van Dijken, G.L. (2015). Continued increases in Arctic Ocean primary production. *Prog. Oceanogr.* 136, 60–70.
- Arrigo, K.R., Mills, M.M., Kropuenske, L.R., Dijken, G.L. van, Alderkamp, A.-C., and Robinson, D.H. (2010). Photophysiology in Two Major Southern Ocean Phytoplankton Taxa: Photosynthesis and Growth of *Phaeocystis antarctica* and *Fragilariopsis cylindrus* under Different Irradiance Levels. *Integr. Comp. Biol.* 50, 950–966.
- Arrigo, K.R., Perovich, D.K., Pickart, R.S., Brown, Z.W., van Dijken, G.L., Lowry, K.E., Mills, M.M., Palmer, M.A., Balch, W.M., Bahr, F., et al. (2012). Massive phytoplankton blooms under Arctic sea ice. *Science* 336, 1408–1408.
- Ashworth, J., Coesel, S., Lee, A., Armbrust, E.V., Orellana, M.V., and Baliga, N.S. (2013). Genome-wide diel growth state transitions in the diatom *Thalassiosira pseudonana*. *Proc. Natl. Acad. Sci.* 110, 7518–7523.
- Babin, M., Morel, A., Claustre, H., Bricaud, A., Kolber, Z., and Falkowski, P.G. (1996). Nitrogen- and irradiance-dependent variations of the maximum quantum yield of carbon fixation in eutrophic, mesotrophic and oligotrophic marine systems. *Deep Sea Res. Part Oceanogr. Res. Pap.* 43, 1241–1272.

- Babin, M., Bélanger, S., Ellingsen, I., Forest, A., Le Fouest, V., Lacour, T., Ardyna, M., and Slagstad, D. (2015). Estimation of primary production in the Arctic Ocean using ocean colour remote sensing and coupled physical–biological models: Strengths, limitations and how they compare. *Prog. Oceanogr.* 139, 197–220.
- Bailey, S., Melis, A., Mackey, K.R.M., Cardol, P., Finazzi, G., van Dijken, G., Berg, G.M., Arrigo, K., Shrager, J., and Grossman, A. (2008). Alternative photosynthetic electron flow to oxygen in marine *Synechococcus*. *Biochim. Biophys. Acta BBA - Bioenerg.* 1777, 269–276.
- Baker, N.R., and Oxborough, K. (2004). Chlorophyll fluorescence as a probe of photosynthetic productivity. *Chlorophyll Fluoresc.* 65–82.
- Barranguet, C., and Kromkamp, J. (2000). Estimating primary production rates from photosynthetic electron transport in estuarine microphytobenthos. *Mar. Ecol.-Prog. Ser.* 204, 39–52.
- Barwell-Clarke, J.F.W. (1996). Institute of Ocean Sciences Nutrient Methods and Analysis. Can. Tech. Rep. Hydrogr. Ocean Sci. 43, 1-14.
- Beardall, J. (1989). Photosynthesis and photorespiration in marine phytoplankton. *Aquat. Bot.* 34, 105–130.
- Beardall, J., and Raven, J.A. (2004). The potential effects of global climate change on microalgal photosynthesis, growth and ecology. *Phycologia* 43, 26–40.
- Behrenfeld, M.J., and Falkowski, P.G. (1997). Photosynthetic rates derived from satellite-based chlorophyll concentration. *Limnol. Oceanogr.* 42(1), 1–20.
- Behrenfeld, M.J., and Milligan, A.J. (2013). Photophysiological Expressions of Iron Stress in Phytoplankton. *Annu. Rev. Mar. Sci.* 5, 217-246.
- Behrenfeld, M., Westberry, T., Boss, E., O'Malley, R., Siegel, D., Wiggert, J., Franz, B., McClain, C., Feldman, G., Doney, S., et al. (2009). Satellite-Detected Fluorescence Reveals Global Physiology of Ocean Phytoplankton. *Biogeosciences* 6, 779–794.
- Behrenfeld, M.J., Marañón, E., Siegel, D.A., and Hooker, S.B. (2002). Photoacclimation and nutrient-based model of light-saturated photosynthesis for quantifying oceanic primary production. *Mar. Ecol. Prog. Ser.* 228, 103-117.
- Behrenfeld, M.J., Prasil, O., Babin, M., and Bruyant, F. (2004). In search of a physiological basis for covariations in light-limited and light-saturated photosynthesis. *J. Phycol.* 40, 4–25.
- Behrenfeld, M.J., Worthington, K., Sherrell, R.M., Chavez, F.P., Strutton, P., McPhaden, M., and Shea, D.M. (2006). Controls on tropical Pacific Ocean productivity revealed through nutrient stress diagnostics. *Nature* 442, 1025–1028.

- Behrenfeld, M.J., Halsey, K.H., and Milligan, A.J. (2008). Evolved physiological responses of phytoplankton to their integrated growth environment. *Philos. Trans. R. Soc. B Biol. Sci.* *363*, 2687–2703.
- Belgio, E., Kapitonova, E., Chmeliov, J., Duffy, C.D.P., Ungerer, P., Valkunas, L., and Ruban, A.V. (2014). Economic photoprotection in photosystem II that retains a complete light-harvesting system with slow energy traps. *Nat. Commun.* *5* (4433).
- Bender, M., Grande, K., Johnson, K., Marra, J., Williams, P.J.L., Sieburth, J., Pilson, M., Langdon, C., Hitchcock, G., and Orchardo, J. (1987). A comparison of four methods for determining planktonic community production. *Limnol Ocean.* *32*, 1085–1098.
- Berera, R., van Stokkum, I.H.M., d’Haene, S., Kennis, J.T.M., van Grondelle, R., and Dekker, J.P. (2009). A Mechanism of Energy Dissipation in Cyanobacteria. *Biophys. J.* *96*, 2261–2267.
- Berges, J.A., Charlebois, D.O., Mauzerall, D.C., and Falkowski, P.G. (1996). Differential Effects of Nitrogen Limitation on Photosynthetic Efficiency of Photosystems I and II in Microalgae. *Plant Physiol.* *110*, 689–696.
- Bilger, W., and Björkman, O. (1990). Role of the xanthophyll cycle in photoprotection elucidated by measurements of light-induced absorbance changes, fluorescence and photosynthesis in leaves of *Hedera canariensis*. *Photosynth. Res.* *25*, 173–185.
- Booth, B.C. (1988). Size classes and major taxonomic groups of phytoplankton at two locations in the Subarctic pacific ocean in May and August, 1984. *Mar. Biol.* *97*, 275–286.
- Boyd, P.W., and Abraham, E.R. (2001). Iron-mediated changes in phytoplankton photosynthetic competence during SOIREE. *Deep Sea Res. Part II Top. Stud. Oceanogr.* *48*, 2529–2550.
- Boyd, P.W., Aiken, J., and Kolber, Z. (1997). Comparison of radiocarbon and fluorescence based (pump and probe) measurements of phytoplankton photosynthetic characteristics in the northeast Atlantic Ocean. *Oceanogr. Lit. Rev.* *44*.
- Boyd, P.W., Jickells, T., Law, C.S., Blain, S., Boyle, E.A., Buesseler, K.O., Coale, K.H., Cullen, J.J., De Baar, H.J.W., Follows, M., et al. (2007). Mesoscale iron enrichment experiments 1993–2005: Synthesis and future directions. *Science* *315*, 612–617.
- Brand, L.E., Guillard, R.R.L., and Murphy, L.S. (1981). A method for the rapid and precise determination of acclimated phytoplankton reproduction rates. *J. Plankton Res.* *3*, 193–201.
- Briat, J.-F., Curie, C., and Gaymard, F. (2007). Iron utilization and metabolism in plants. *Curr. Opin. Plant Biol.* *10*, 276–282.
- Bricaud, A., and Stramski, D. (1990). Spectral absorption coefficients of living phytoplankton and nonalgal biogenous matter: A comparison between the Peru upwelling area and the Sargasso Sea. *Limnol. Oceanogr.* *35*, 562–582.

- Bricaud, A., Babin, M., Morel, A., and Claustre, H. (1995). Variability in the chlorophyll-specific absorption coefficients of natural phytoplankton: Analysis and parameterization. *J. Geophys. Res. Oceans* *100*, 13321–13332.
- Browning, T.J., Bouman, H.A., and Moore, C.M. (2014b). Satellite-detected fluorescence: Decoupling nonphotochemical quenching from iron stress signals in the South Atlantic and Southern Ocean: Deconvolving satellite fluorescence. *Glob. Biogeochem. Cycles* *28*, 510–524.
- Brunet, C., Johnsen, G., Lavaud, J., and Roy, S. (2011). Pigments and photoacclimation processes. In *Phytoplankton Pigments*, S. Roy, C. Llewellyn, E.S. Egeland, and G. Johnsen, eds. (Cambridge University Press), pp. 445-471.
- Bruyant, F., Babin, M., Genty, B., Prasil, O., Behrenfeld, M.J., Claustre, H., Bricaud, A., Garczarek, L., Holtzendorff, J., and Koblizek, M. (2005). Diel variations in the photosynthetic parameters of *Prochlorococcus* strain PCC 9511: Combined effects of light and cell cycle. *Limnol. Oceanogr.* 850–863.
- Büchel, C., and Wilhelm, C. (1993). In vivo analysis of slow chlorophyll fluorescence kinetics in algae: progress, problems and perspectives. *Photochem. Photobiol.* *58*, 137–148.
- Cadoret, J.-C., Demoulière, R., Lavaud, J., van Gorkom, H.J., Houmard, J., and Etienne, A.-L. (2004). Dissipation of excess energy triggered by blue light in cyanobacteria with CP43' (isiA). *Biochim. Biophys. Acta BBA - Bioenerg.* *1659*, 100–104.
- Cardol, P., Bailleul, B., Rappaport, F., Derelle, E., Béal, D., Breyton, C., Bailey, S., Wollman, F.A., Grossman, A., Moreau, H., et al. (2008). An original adaptation of photosynthesis in the marine green alga *Ostreococcus*. *Proc. Natl. Acad. Sci.* *105*, 7881–7886.
- Cardol, P., Forti, G., and Finazzi, G. (2011). Regulation of electron transport in microalgae. *Biochim. Biophys. Acta BBA-Bioenerg.* *1807*, 912–918.
- Carmack, E., and McLaughlin, F. (2011). Towards recognition of physical and geochemical change in Subarctic and Arctic Seas. *Prog. Oceanogr.* *90*, 90–104.
- Carmack, E., and Wassmann, P. (2006). Food webs and physical–biological coupling on pan-Arctic shelves: Unifying concepts and comprehensive perspectives. *Prog. Oceanogr.* *71*, 446–477.
- Chappell, P.D., Whitney, L.P., Wallace, J.R., Darer, A.I., Jean-Charles, S., and Jenkins, B.D. (2015). Genetic indicators of iron limitation in wild populations of *Thalassiosira oceanica* from the northeast Pacific Ocean. *ISME J.* *9*, 592–602.
- Chassot, E., Bonhommeau, S., Dulvy, N.K., Mélin, F., Watson, R., Gascuel, D., and Le Pape, O. (2010). Global marine primary production constrains fisheries catches. *Ecol. Lett.* *13*, 495–505.
- Chavez, F.P., Messié, M., and Pennington, J.T. (2011). Marine Primary Production in Relation to Climate Variability and Change. *Annu. Rev. Mar. Sci.* *3*, 227–260.

- Cheah, W., McMinn, A., Griffiths, F.B., Westwood, K.J., Wright, S.W., Molina, E., Webb, J.P., and van den Enden, R. (2011). Assessing Sub-Antarctic Zone primary productivity from fast repetition rate fluorometry. *Deep Sea Res. Part II Top. Stud. Oceanogr.* 58, 2179–2188.
- Ciotti, A.M., Lewis, M.R., and Cullen, J.J. (2002). Assessment of the relationships between dominant cell size in natural phytoplankton communities and the spectral shape of the absorption coefficient. *Limnol. Oceanogr.* 47, 404–417.
- Claustre, H., Babin, M., Merien, D., Ras, J., Prieur, L., Dallot, S., Prasil, O., Dousova, H., and Moutin, T. (2005). Toward a taxon-specific parameterization of bio-optical models of primary production: A case study in the North Atlantic. *J. Geophys. Res. Oceans* 110(C7).
- Codispoti, L.A., Kelly, V., Thessen, A., Matrai, P., Suttles, S., Hill, V., Steele, M., and Light, B. (2013). Synthesis of primary production in the Arctic Ocean: III. Nitrate and phosphate based estimates of net community production. *Prog. Oceanogr.* 110, 126–150.
- Corno, G., Letelier, R.M., Abbott, M.R., and Karl, D.M. (2006). Assessing Primary Production Variability in the North Pacific Subtropical Gyre: a Comparison of Fast Repetition Rate Fluorometry and  $^{14}\text{C}$  Measurements. *J. Phycol.* 42, 51–60.
- Cota, G.F., Harrison, W.G., Platt, T., Sathyendranath, S., and Stuart, V. (2003). Bio-optical properties of the Labrador Sea. *J. Geophys. Res. Oceans* 108, 3228.
- Coupel, P., Ruiz-Pino, D., Sicre, M.A., Chen, J.F., Lee, S.H., Schiffrine, N., Li, H.L., and Gascard, J.C. (2015a). The impact of freshening on phytoplankton production in the Pacific Arctic Ocean. *Prog. Oceanogr.* 131, 113–125.
- Coupel, P., Matsuoka, A., Ruiz-Pino, D., Gosselin, M., Marie, D., Tremblay, J.-É., and Babin, M. (2015b). Pigment signatures of phytoplankton communities in the Beaufort Sea. *Biogeosciences* 12, 991–1006.
- Cullen, J.J., Yang, X., and MacIntyre, H.L. (1992). Nutrient limitation of marine photosynthesis. In *Primary Productivity and Biogeochemical Cycles in the Sea*, (Springer US), pp. 69–88.
- Cullen, J.J., Ciotti, A.M., Davis, R.F., and Lewis, M.R. (1997). Emerging technologies and modeling. Optical detection and assessment of algal blooms. *Limnol. Oceanogr.* 42(5), 1223–1239.
- Curien, G., Flori, S., Villanova, V., Magneschi, L., Giustini, C., Forti, G., Matringe, M., Petroustos, D., Kuntz, M., and Finazzi, G. (2016). The Water to Water Cycles in Microalgae. *Plant Cell Physiol.* pcw048.
- Debes, H., Gaard, E., and Hansen, B. (2008). Primary production on the Faroe shelf: Temporal variability and environmental influences. *J. Mar. Syst.* 74, 686–697.
- Demming-Adams B., Garab, G, Adams W., Govindjee (2014). *Non-Photochemical Quenching and Energy Dissipation in Plants, Algae and Cyanobacteria* (Springer Netherlands).

- Derks, A., Schaven, K., and Bruce, D. (2015). Diverse mechanisms for photoprotection in photosynthesis. Dynamic regulation of photosystem II excitation in response to rapid environmental change. *Biochim. Biophys. Acta BBA - Bioenerg.* *1847*, 468–485.
- Dickey, T.D. (1991). The emergence of concurrent high-resolution physical and bio-optical measurements in the upper ocean and their applications. *Rev. Geophys.* *29*, 383–413.
- Doblin, M.A., Petrou, K.L., Shelly, K., Westwood, K., van den Enden, R., Wright, S., Griffiths, B., and Ralph, P.J. (2011). Diel variation of chlorophyll-a fluorescence, phytoplankton pigments and productivity in the Sub-Antarctic and Polar Front Zones south of Tasmania, Australia. *Deep Sea Res. Part II Top. Stud. Oceanogr.* *58*, 2189–2199.
- Doty, M.S., and Oguri, M. (1957). Evidence for a Photosynthetic Daily Periodicity. *Limnol. Oceanogr.* *2*, 37–40.
- Dubinsky, Z., Falkowski, P.G., and Wyman, K. (1986). Light Harvesting and Utilization by Phytoplankton. *Plant Cell Physiol.* *27*, 1335–1349.
- Dupont, F. (2012). Impact of sea-ice biology on overall primary production in a biophysical model of the pan-Arctic Ocean. *J. Geophys. Res. Oceans* *117*, C8.
- Duysens, L.N. (1956). The flattening of the absorption spectrum of suspensions, as compared to that of solutions. *Biochim. Biophys. Acta* *19*, 1–12.
- Duysens, L.N.M., and Sweers, H.E. (1963). Studies on microalgae and photosynthetic bacteria. *Jpn. Soc. Plant Physiol. Univ. Tokyo* , 353.
- Eppley, R.W., Rogers, J.N., and McCarthy, J.J. (1969). Half-Saturation Constants for Uptake of Nitrate and Ammonium by Marine Phytoplankton. *Limnol. Oceanogr.* *14*, 912–920.
- Erga, S.R., and Skjoldal, H.R. (1990). Diel variations in photosynthetic activity of summer phytoplankton in Lindåspollene, western Norway. *Mar.Ecol. Prog. Ser.* *65*, 73-85.
- Estévez-Blanco, P., Cermeño, P., Espiñeira, M., and Fernández, E. (2006). Phytoplankton photosynthetic efficiency and primary production rates estimated from fast repetition rate fluorometry at coastal embayments affected by upwelling (Rías Baixas, NW of Spain). *J. Plankton Res.* *28*, 1153–1165.
- Falkowski, P.G. (1994). The role of phytoplankton photosynthesis in global biogeochemical cycles. *Photosynth. Res.* *39*, 235–258.
- Falkowski, P.G. (2006). Tracing oxygen's imprint on Earth's metabolic evolution. *Science* *311*, 1724–1725.
- Falkowski, P., and Kiefer, D.A. (1985). Chlorophyll a fluorescence in phytoplankton: relationship to photosynthesis and biomass. *J. Plankton Res.* *7*, 715–731.

- Falkowski, P.G., and Kolber, Z. (1995). Variations in chlorophyll fluorescence yields in phytoplankton in the world oceans. *Funct. Plant Biol.* 22, 341–355.
- Falkowski, P.G., Owens, T.G., Ley, A.C., and Mauzerall, D.C. (1981). Effects of Growth Irradiance Levels on the Ratio of Reaction Centers in Two Species of Marine Phytoplankton. *Plant Physiol.* 68, 969–973.
- Falkowski, P.G., Wyman, K., Ley, A.C., and Mauzerall, D.C. (1986a). Relationship of steady-state photosynthesis to fluorescence in eucaryotic algae. *Biochim. Biophys. Acta BBA - Bioenerg.* 849, 183–192.
- Falkowski, P.G., Fujita, Y., Ley, A., and Mauzerall, D. (1986b). Evidence for Cyclic Electron Flow around Photosystem II in *Chlorella pyrenoidosa*. *Plant Physiol.* 81, 310–312.
- Falkowski, P.G., Barber, R.T., and Smetacek, V. (1998). Biogeochemical controls and feedbacks on ocean primary production. *Science* 281, 200–206.
- Feikema, O.W., Marosvölgyi, M.A., Lavaud, J., and van Gorkom, H.J. (2006). Cyclic electron transfer in photosystem II in the marine diatom *Phaeodactylum tricorutum*. *Biochim. Biophys. Acta BBA - Bioenerg.* 1757, 829–834.
- Fernández-Méndez, M., Katlein, C., Rabe, B., Nicolaus, M., Peeken, I., Bakker, K., Flores, H., and Boetius, A. (2015). Photosynthetic production in the central Arctic Ocean during the record sea-ice minimum in 2012. *Biogeosciences* 12, 3525–3549.
- Field, C.B., Behrenfeld, M.J., Randerson, J.T., and Falkowski, P. (1998). Primary production of the biosphere: integrating terrestrial and oceanic components. *Science* 281, 237–240.
- Fitzwater, S.E., Knauer, G.A., and Martin, J.H. (1982). Metal contamination and its effect on primary production measurements. *Limnol. Oceanogr.* 27, 544–551.
- Foyer, C.H., Bloom, A.J., Queval, G., and Noctor, G. (2009). Photorespiratory Metabolism: Genes, Mutants, Energetics, and Redox Signaling. *Annu. Rev. Plant Biol.* 60, 455–484.
- Fraser, J.M., Tulk, S.E., Jeans, J.A., Campbell, D.A., Bibby, T.S., and Cockshutt, A.M. (2013). Photophysiological and Photosynthetic Complex Changes during Iron Starvation in *Synechocystis* sp. PCC 6803 and *Synechococcus elongatus* PCC 7942. *PLoS ONE* 8, e59861.
- From, N., Richardson, K., Mousing, E.A., and Jensen, P.E. (2014). Removing the light history signal from normalized variable fluorescence ( $F_v/F_m$ ) measurements on marine phytoplankton. *Limnol. Oceanogr. Methods* 12, 776–783.
- Fujiki, T., and Taguchi, S. (2002). Variability in chlorophyll a specific absorption coefficient in marine phytoplankton as a function of cell size and irradiance. *J. Plankton Res.* 24, 859–874.
- Fujiki, T., Suzue, T., Kimoto, H., and Saino, T. (2007). Photosynthetic electron transport in *Dunaliella tertiolecta* (Chlorophyceae) measured by fast repetition rate fluorometry: relation to carbon assimilation. *J. Plankton Res.* 29, 199–208.

- Fujiki, T., Matsumoto, K., Watanabe, S., Hosaka, T., and Saino, T. (2011). Phytoplankton productivity in the western Subarctic gyre of the North Pacific in early summer 2006. *J. Oceanogr.* 67, 295–303.
- Gallegos, C.L., Platt, T., Harrison, W.G., and Irwin, B. (1983). Photosynthetic parameters of arctic marine phytoplankton: vertical variations and time scales of adaptation. *Limnol Ocean.* 28, 698–708.
- Geider, R.J., and La Roche, J. (1994). The role of iron in phytoplankton photosynthesis, and the potential for iron-limitation of primary productivity in the sea. *Photosynth. Res.* 39, 275–301.
- Genty, B., Briantais, J.-M., and Baker, N.R. (1989). The relationship between the quantum yield of photosynthetic electron transport and quenching of chlorophyll fluorescence. *Biochim. Biophys. Acta BBA - Gen. Subj.* 990, 87–92.
- Gilbert, M., Domin, A., Becker, A., and Wilhelm, C. (2000). Estimation of Primary Productivity by Chlorophyll a in vivo Fluorescence in Freshwater Phytoplankton. *Photosynthetica* 38, 111–126.
- Giordano, M., Beardall, J., and Raven, J.A. (2005). CO<sub>2</sub> Concentrating Mechanisms in Algae: Mechanisms, Environmental Modulation, and Evolution. *Annu. Rev. Plant Biol.* 56, 99–131.
- Goss, R., and Lepetit, B. (2015). Biodiversity of NPQ. *J. Plant Physiol.* 172, 13–32.
- Goto, N., Miyazaki, H., Nakamura, N., Terai, H., Ishida, N., and Mitamura, O. (2008). Relationships between electron transport rates determined by pulse amplitude modulated (PAM) chlorophyll fluorescence and photosynthetic rates by traditional and common methods in natural freshwater phytoplankton. *Fundam. Appl. Limnol. Arch. Fr Hydrobiol.* 172, 121–134.
- Govindjee (1995). Sixty-three years since Kautsky: Chlorophyll a fluorescence. *Aust J Plant Physiol* 22, 131–160.
- Granum, E., Roberts, K., Raven, J.A., and Leegood, R.C. (2009). Primary Carbon and Nitrogen Metabolic Gene Expression in the Diatom *Thalassiosira pseudonana* (bacillariophyceae): Diel Periodicity and Effects of Inorganic Carbon and Nitrogen1. *J. Phycol.* 45, 1083–1092.
- Gray, G.R., Chauvin, L.-P., Sarhan, F., and Huner, N.P. (1997). Cold acclimation and freezing tolerance (a complex interaction of light and temperature). *Plant Physiol.* 114, 467–474.
- Greene, R.M., Geider, R.J., and Falkowski, P.G. (1991). Effect of iron limitation on photosynthesis in a marine diatom. *Limnol. Oceanogr.* 36, 1772–1782.
- Greene, R.M., Geider, R.J., Kolber, Z., and Falkowski, P.G. (1992). Iron-induced changes in light harvesting and photochemical energy conversion processes in eukaryotic marine algae. *Plant Physiol.* 100, 565–575.
- Greene, R.M., Kolber, Z.S., Swift, D.G., Tindale, N.W., and Falkowski, P.G. (1994). Physiological Limitation of Phytoplankton Photosynthesis in the Eastern Equatorial Pacific

- Determined from Variability in the Quantum Yield of Fluorescence. *Limnol. Oceanogr.* *39*, 1061–1074.
- Grossman, A.R., Mackey, K.R.M., and Bailey, S. (2010). A Perspective on Photosynthesis in the Oligotrophic Oceans: Hypotheses Concerning Alternate Routes of Electron Flow<sup>1</sup>. *J. Phycol.* *46*, 629–634.
- Halsey, K.H., and Jones, B.M. (2015). Phytoplankton Strategies for Photosynthetic Energy Allocation. *Annu. Rev. Mar. Sci.* *7*, 265–297.
- Halsey, K.H., Milligan, A.J., and Behrenfeld, M.J. (2010). Physiological optimization underlies growth rate-independent chlorophyll-specific gross and net primary production. *Photosynth. Res.* *103*, 125–137.
- Halsey, K.H., Milligan, A.J., and Behrenfeld, M.J. (2011). Linking Time-Dependent Carbon-Fixation Efficiencies in *Dunaliella Tertiolecta* (chlorophyceae) to Underlying Metabolic Pathways<sup>1</sup>. *J. Phycol.* *47*, 66–76.
- Halsey, K.H., O'Malley, R.T., Graff, J.R., Milligan, A.J., and Behrenfeld, M.J. (2013). A common partitioning strategy for photosynthetic products in evolutionarily distinct phytoplankton species. *New Phytol.* *198*, 1030–1038.
- Hancke, K., Hancke, T.B., Olsen, L.M., Johnsen, G., and Glud, R.N. (2008). Temperature Effects on Microalgal Photosynthesis-Light Responses Measured by O<sub>2</sub> Production, Pulse-Amplitude-Modulated Fluorescence, and <sup>14</sup>C Assimilation<sup>1</sup>. *J. Phycol.* *44*, 501–514.
- Hancke, K., Dalsgaard, T., Sejr, M.K., Markager, S., and Glud, R.N. (2015). Phytoplankton Productivity in an Arctic Fjord (West Greenland): Estimating Electron Requirements for Carbon Fixation and Oxygen Production. *PLOS ONE* *10*, e0133275.
- Harding, L.W., Meeson, B.W., Prézelin, B.B., and Sweeney, B.M. (1981). Diel periodicity of photosynthesis in marine phytoplankton. *Mar. Biol.* *61*, 95–105.
- Harding, L.W., Prézelin, B.B., Sweeney, B.M., and Cox, J.L. (1982). Primary production as influenced by diel periodicity of phytoplankton photosynthesis. *Mar. Biol.* *67*, 179–186.
- Harding, L.W., Fisher, T.R., and Tyler, M.A. (1987). Adaptive Responses of Photosynthesis in Phytoplankton: Specificity to Time-Scale of Change in Light. *Biol. Oceanogr.* *4*, 403–437.
- Hays, G.C., Richardson, A.J., and Robinson, C. (2005). Climate change and marine plankton. *Trends Ecol. Evol.* *20*, 337–344.
- Higgins, H.W., Wright, S.W., and Schlüter, L. (2011). Quantitative interpretation of chemotaxonomic pigment data. In *Phytoplankton Pigments*, S. Roy, C. Llewellyn, E.S. Egeland, and G. Johnsen, eds. (Cambridge University Press), pp. 257–313.

- Hill, V.J., Matrai, P.A., Olson, E., Suttles, S., Steele, M., Codispoti, L.A., and Zimmerman, R.C. (2013). Synthesis of integrated primary production in the Arctic Ocean: II. In situ and remotely sensed estimates. *Prog. Oceanogr.* *110*, 107–125.
- Hohmann-Marriott, M.F., Takizawa, K., Eaton-Rye, J.J., Mets, L., and Minagawa, J. (2010). The redox state of the plastoquinone pool directly modulates minimum chlorophyll fluorescence yield in *Chlamydomonas reinhardtii*. *FEBS Lett.* *584*, 1021–1026.
- Holmes, R.M., Aminot, A., K erouel, R., Hooker, B.A., and Peterson, B.J. (1999). A simple and precise method for measuring ammonium in marine and freshwater ecosystems. *Can. J. Fish. Aquat. Sci.* *56*, 1801–1808.
- Hopkinson, B.M., Mitchell, B.G., Reynolds, R.A., Wang, H., Selph, K.E., Measures, C.I., Hewes, C.D., Holm-Hansen, O., and Barbeau, K.A. (2007). Iron limitation across chlorophyll gradients in the southern Drake Passage: Phytoplankton responses to iron addition and photosynthetic indicators of iron stress. *Limnol. Oceanogr.* *52*, 2540–2554.
- Horton, P. (2012). Optimization of light harvesting and photoprotection: molecular mechanisms and physiological consequences. *Philos. Trans. R. Soc. B Biol. Sci.* *367*, 3455–3465.
- Hu, H., Wang, J., Liu, H., and Goes, J. (2016). Simulation of phytoplankton distribution and variation in the Bering-Chukchi Sea using a 3-D physical-biological model. *J. Geophys. Res. Oceans*
- Huner, N.P.,  quist, G., and Sarhan, F. (1998). Energy balance and acclimation to light and cold. *Trends Plant Sci.* *3*, 224–230.
- H ner, N.P.A., Bode, R., Dahal, K., Hollis, L., Rosso, D., Krol, M., and Ivanov, A.G. (2012). Chloroplast redox imbalance governs phenotypic plasticity: the “grand design of photosynthesis” revisited. *Front. Plant Sci.* *3*, 255.
- Huot, Y., and Babin, M. (2010). Overview of Fluorescence Protocols: Theory, Basic Concepts, and Practice. In *Chlorophyll a Fluorescence in Aquatic Sciences: Methods and Applications*, D.J. Suggett, O. Pr sil, and M.A. Borowitzka, eds. (Springer Netherlands), pp. 31–74.
- Huot, Y., Brown, C.A., and Cullen, J.J. (2005). New algorithms for MODIS sun-induced chlorophyll fluorescence and a comparison with present data products: MODIS fluorescence algorithms. *Limnol. Oceanogr. Methods* *3*, 108–130.
- Huot, Y., Babin, M., Bruyant, F., Grob, C., Twardowski, M.S., and Claustre, H. (2007). Relationship between photosynthetic parameters and different proxies of phytoplankton biomass in the subtropical ocean. *Biogeosciences* *4*, 853–868.
- Huot, Y., Babin, M., and Bruyant, F. (2013a). Photosynthetic parameters in the Beaufort Sea in relation to the phytoplankton community structure. *Biogeosciences* *10*, 3445–3454.

- Huot, Y., Franz, B.A., and Fradette, M. (2013b). Estimating variability in the quantum yield of Sun-induced chlorophyll fluorescence: A global analysis of oceanic waters. *Remote Sens. Environ.* *132*, 238–253.
- Ihalainen, J.A., D’Haene, S., Yeremenko, N., van Roon, H., Arteni, A.A., Boekema, E.J., van Grondelle, R., Matthijs, H.C.P., and Dekker, J.P. (2005). Aggregates of the Chlorophyll-Binding Protein IsiA (CP43’) Dissipate Energy in Cyanobacteria. *Biochemistry (Mosc.)* *44*, 10846–10853.
- Ivanov, A.G., Sane, P.V., Hurry, V., Oquist, G., and Huner, N.P.A. (2008). Photosystem II reaction centre quenching: mechanisms and physiological role. *Photosynth. Res.* *98*, 565–574.
- Ivanov, A.G., Rosso, D., Savitch, L.V., Stachula, P., Rosembert, M., Oquist, G., Hurry, V., and Hüner, N.P.A. (2012). Implications of alternative electron sinks in increased resistance of PSII and PSI photochemistry to high light stress in cold-acclimated *Arabidopsis thaliana*. *Photosynth. Res.* *113*, 191–206.
- John, D.E., López-Díaz, J.M., Cabrera, A., Santiago, N.A., Corredor, J.E., Bronk, D.A., and Paul, J.H. (2012). A day in the life in the dynamic marine environment: how nutrients shape diel patterns of phytoplankton photosynthesis and carbon fixation gene expression in the Mississippi and Orinoco River plumes. *Hydrobiologia* *679*, 155–173.
- Johnson, K.S., Miller, L.A., Sutherland, N.E., and Wong, C.S. (2005). Iron transport by mesoscale Haida eddies in the Gulf of Alaska. *Deep Sea Res. Part II Top. Stud. Oceanogr.* *52*, 933–953.
- Kaiblinger, C., and Dokulil, M.T. (2006). Application of fast repetition rate fluorometry to phytoplankton photosynthetic parameters in freshwaters. *Photosynth. Res.* *88*, 19–30.
- Kirk, J.T.O. (2010). *Light and Photosynthesis in Aquatic Ecosystems* (Cambridge University Press).
- Kishino, M., Takahashi, M., Okami, N., and Ichimura, S. (1985). Estimation of the spectral absorption coefficients of phytoplankton in the sea. *Bull. Mar. Sci.* *37*, 634–642.
- Kitajima, M., and Butler, W.L. (1975). Quenching of chlorophyll fluorescence and primary photochemistry in chloroplasts by dibromothymoquinone. *Biochim. Biophys. Acta BBA - Bioenerg.* *376*, 105–115.
- Knap, A.H., Michaels, A., Close, A.R., Ducklow, H., and Dickson, A.G. (1996). Protocols for the joint global ocean flux study (JGOFS) core measurements. *JGOFS Repr. IOC Man. Guid. No 29 UNESCO 1994* *19*.
- Kojima, K., Suzuki-Maenaka, T., Kikuchi, T., and Nakamoto, H. (2006). Roles of the cyanobacterial isiABC operon in protection from oxidative and heat stresses. *Physiol. Plant.* *128*, 507–519.

- Kolber, Z., and Falkowski, P.G. (1993). Use of Active Fluorescence to Estimate Phytoplankton Photosynthesis in Situ. *Limnol. Oceanogr.* 38, 1646–1665.
- Kolber, Z., Zehr, J., and Falkowski, P. (1988). Effects of growth irradiance and nitrogen limitation on photosynthetic energy conversion in photosystem II. *Plant Physiol.* 88, 923–929.
- Kolber, Z.S., Barber, R.T., Coale, K.H., Fitzwateri, S.E., Greene, R.M., Johnson, K.S., Lindley, S., and Falkowski, P.G. (1994). Iron limitation of phytoplankton photosynthesis in the equatorial Pacific Ocean. *Nature* 371, 145–149.
- Kolber, Z.S., Prášil, O., and Falkowski, P.G. (1998). Measurements of variable chlorophyll fluorescence using fast repetition rate techniques: defining methodology and experimental protocols. *Biochim. Biophys. Acta BBA - Bioenerg.* 1367, 88–106.
- Kramer, D.M., Johnson, G., Kiirats, O., and Edwards, G.E. (2004). New Fluorescence Parameters for the Determination of  $Q_A$  Redox State and Excitation Energy Fluxes. *Photosynth. Res.* 79, 209–218.
- Krause, G.H., and Jahns, P. (2003). Pulse Amplitude Modulated Chlorophyll Fluorometry and its Application in Plant Science. In *Light-Harvesting Antennas in Photosynthesis*, B.R. Green, and W.W. Parson, eds. (Springer Netherlands), pp. 373–399.
- Krause, G.H., and Weis, E. (1991). Chlorophyll Fluorescence and Photosynthesis: The Basics. *Annu. Rev. Plant Physiol. Plant Mol. Biol.* 42, 313–349.
- Kromkamp, J.C., and Forster, R.M. (2003). The use of variable fluorescence measurements in aquatic ecosystems: differences between multiple and single turnover measuring protocols and suggested terminology. *Eur. J. Phycol.* 38, 103–112.
- Kromkamp, J.C., Dijkman, N.A., Peene, J., Simis, S.G.H., and Gons, H.J. (2008). Estimating phytoplankton primary production in Lake IJsselmeer (The Netherlands) using variable fluorescence (PAM-FRRF) and C-uptake techniques. *Eur. J. Phycol.* 43, 327–344.
- Kromkamp, J.C., Peene, J., and Silsbe, G. (2011). A comparison between primary production estimates based on fluorometry and C-fixation. In *European Journal of Phycology*, (Taylor & Francis, England), pp. 53–53.
- Laney, S.R. (2006). Seconds to hour scale photosynthetic responses in marine microalgae. Thesis. Oregon State University.
- Laureau, C., DE Paepe, R., Latouche, G., Moreno-Chacón, M., Finazzi, G., Kuntz, M., Cornic, G., and Streb, P. (2013). Plastid terminal oxidase (PTOX) has the potential to act as a safety valve for excess excitation energy in the alpine plant species *Ranunculus glacialis*. *Plant Cell Environ.*
- Lavaud, J., and Lepetit, B. (2013). An explanation for the inter-species variability of the photoprotective non-photochemical chlorophyll fluorescence quenching in diatoms. *Biochim. Biophys. Acta BBA - Bioenerg.* 1827, 294–302.

- Lawrenz, E., Silsbe, G., Capuzzo, E., Ylöstalo, P., Forster, R.M., Simis, S.G.H., Prášil, O., Kromkamp, J.C., Hickman, A.E., Moore, C.M., et al. (2013). Predicting the Electron Requirement for Carbon Fixation in Seas and Oceans. *PLoS ONE* 8, e58137.
- Laws, E.A. (1991). Photosynthetic quotients, new production and net community production in the open ocean. *Deep Sea Res. Part Oceanogr. Res. Pap.* 38, 143–167.
- Lee, Y.J., Matrai, P.A., Friedrichs, M.A.M., Saba, V.S., Antoine, D., Ardyna, M., Asanuma, I., Babin, M., Bélanger, S., Benoit-Gagné, M., et al. (2015). An assessment of phytoplankton primary productivity in the Arctic Ocean from satellite ocean color/in situ chlorophyll-a based models. *J. Geophys. Res. Oceans* 120, 6508–6541.
- Lee, Y.W., Park, M.O., Kim, Y.S., Kim, S.S., and Kang, C.K. (2011). Application of photosynthetic pigment analysis using a HPLC and CHEMTAX program to studies of phytoplankton community composition. *J Korean Soc Ocean.* 16, 117–124.
- Lewis, M., and Smith, J. (1983). A small volume, short-incubation-time method for measurement of photosynthesis as a function of incident irradiance. *Mar. Ecol. Prog. Ser.* 13, 99–102.
- Lewis, K.M., Mitchell, B.G., van Dijken, G.L., and Arrigo, K.R. Regional chlorophyll a algorithms in the Arctic Ocean and their effect on satellite-derived primary production estimates. *Deep Sea Res. Part II Top. Stud. Oceanogr.*
- Li, T., Xu, J., Gao, B., Xiang, W., Li, A., and Zhang, C. (2016). Morphology, growth, biochemical composition and photosynthetic performance of *Chlorella vulgaris* (Trebouxiophyceae) under low and high nitrogen supplies. *Algal Res.* 16, 481–491.
- Li, W.K., McLaughlin, F.A., Lovejoy, C., and Carmack, E.C. (2009). Smallest algae thrive as the Arctic Ocean freshens. *Science* 326, 539–539.
- Lohrenz, S.E., Weidemann, A.D., and Tuel, M. (2003). Phytoplankton spectral absorption as influenced by community size structure and pigment composition. *J. Plankton Res.* 25, 35–61.
- Lovejoy, C., Vincent, W.F., Bonilla, S., Roy, S., Martineau, M.-J., Terrado, R., Potvin, M., Massana, R., and Pedrós-Alió, C. (2007). Distribution, phylogeny, and growth of cold-adapted picoprasinophytes in Arctic seas. *J. Phycol.* 43, 78–89.
- MacCaull, W.A., and Platt, T. (1977). Diel variations in the photosynthetic parameters of coastal marine phytoplankton. *Limnol. Oceanogr.* 22, 723–731.
- Macey, A.I., Ryan-Keogh, T., Richier, S., Moore, C.M., and Bibby, T.S. (2014). Photosynthetic protein stoichiometry and photophysiology in the high latitude North Atlantic. *Limnol. Oceanogr.* 59, 1853–1864.
- MacIntyre, H.L., Kana, T.M., Anning, T., and Geider, R.J. (2002). Photoacclimation of Photosynthesis Irradiance Response Curves and Photosynthetic Pigments in Microalgae and Cyanobacterial. *J. Phycol.* 38, 17–38.

- Mackey, K.R.M. (2010). On the response of marine phytoplankton to changing nutrient and light conditions. Thesis. Stanford University.
- Mackey, K.R.M., Paytan, A., Grossman, A.R., and Bailey, S. (2008). A photosynthetic strategy for coping in a high-light, low-nutrient environment. *Limnol. Oceanogr.* *53*, 900–913.
- Maldonado, M.T., Allen, A.E., Chong, J.S., Lin, K., Leus, D., Karpenko, N., and Harris, S.L. (2006). Copper-dependent iron transport in coastal and oceanic diatoms. *Limnol Ocean.* *51*, 1729–1743.
- Marchetti, A., Sherry, N.D., Juneau, P., Strzepek, R.F., and Harrison, P.J. (2006). Phytoplankton processes during a mesoscale iron enrichment in the NE Subarctic Pacific: Part III—Primary productivity. *Deep Sea Res.* *53*, 2131–2151.
- Marra, J. (2009). Net and gross productivity: weighing in with  $^{14}\text{C}$ . *Aquat Microb Ecol* *56*, 123–131.
- Martin, J., Tremblay, J.É., and Price, N.M. (2012). Nutritive and photosynthetic ecology of subsurface chlorophyll maxima in Canadian Arctic waters. *Biogeosciences* *9*, 5353–5371.
- Martin, J., Dumont, D., and Tremblay, J.-É. (2013). Contribution of subsurface chlorophyll maxima to primary production in the coastal Beaufort Sea (Canadian Arctic): A model assessment. *J. Geophys. Res. Oceans* *118*, 5873–5886.
- Matrai, P.A., Olson, E., Suttles, S., Hill, V., Codispoti, L.A., Light, B., and Steele, M. (2013). Synthesis of primary production in the Arctic Ocean: I. Surface waters, 1954–2007. *Prog. Oceanogr.* *110*, 93–106.
- Mauzerall, D., and Greenbaum, N.L. (1989). The absolute size of a photosynthetic unit. *Biochim. Biophys. Acta BBA - Bioenerg.* *974*, 119–140.
- McDonald, A.E., Ivanov, A.G., Bode, R., Maxwell, D.P., Rodermel, S.R., and Hüner, N.P.A. (2011). Flexibility in photosynthetic electron transport: The physiological role of plastoquinol terminal oxidase (PTOX). *Biochim. Biophys. Acta BBA - Bioenerg.* *1807*, 954–967.
- McKew, B.A., Davey, P., Finch, S.J., Hopkins, J., Lefebvre, S.C., Metodiev, M.V., Oxborough, K., Raines, C.A., Lawson, T., and Geider, R.J. (2013). The trade-off between the light-harvesting and photoprotective functions of fucoxanthin-chlorophyll proteins dominates light acclimation in *Emiliana huxleyi* (clone CCMP 1516). *New Phytol.* *200*, 74–85.
- Melrose, D.C., Oviatt, C.A., O'Reilly, J.E., and Berman, M.S. (2006). Comparisons of fast repetition rate fluorescence estimated primary production and  $^{14}\text{C}$  uptake by phytoplankton. *Mar. Ecol. Prog. Ser.* *311*, 37–46.
- Milligan, A.J., Halsey, K.H., and Behrenfeld, M.J. (2015). Advancing interpretations of  $^{14}\text{C}$ -uptake measurements in the context of phytoplankton physiology and ecology. *J. Plankton Res.* *37(4)*, 692–698.

- Mitchell, B.G., Kahru, M., Wieland, J., and Stramska, M. (2002). Determination of spectral absorption coefficients of particles, dissolved material and phytoplankton for discrete water samples. *Ocean Opt. Protoc. Satell. Ocean Color Sens. Valid. Revis.* 3, 231–257.
- Miyake, C., and Asada, K. (2003). The Water-Water Cycle in Algae. In *Photosynthesis in Algae*, A.W.D. Larkum, S.E. Douglas, and J.A. Raven, eds. (Springer Netherlands), pp. 183–204.
- Moore, C., Suggett, D., Holligan, P., Sharples, J., Abraham, E., Lucas, M., Rippeth, T., Fisher, N., Simpson, J., and Hydes, D. (2003). Physical controls on phytoplankton physiology and production at a shelf sea front: a fast repetition-rate fluorometer based field study. *Mar. Ecol. Prog. Ser.* 259, 29–45.
- Moore, C.M., Suggett, D.J., Hickman, A.E., Kim, Y.N., Tweddle, J.F., Sharples, J., Geider, R.J., and Holligan, P.M. (2006). Phytoplankton photoacclimation and photoadaptation in response to environmental gradients in a shelf sea. *Limnol. Oceanogr.* 936–949.
- Moore, J.K., Doney, S.C., Glover, D.M., and Fung, I.Y. (2001). Iron cycling and nutrient-limitation patterns in surface waters of the World Ocean. *Deep Sea Res. Part II Top. Stud. Oceanogr.* 49, 463–507.
- Morel, A., and Bricaud, A. (1981). Theoretical results concerning light absorption in a discrete medium, and application to specific absorption of phytoplankton. *Deep Sea Res. Part Oceanogr. Res. Pap.* 28, 1375–1393.
- Morel, A., Gentili, B., Claustre, H., Babin, M., Bricaud, A., Ras, J., and Tièche, F. (2007). Optical properties of the “clearest” natural waters. *Limnol. Oceanogr.* 52, 217–229.
- Morgan-Kiss, R.M., Priscu, J.C., Pockock, T., Gudynaite-Savitch, L., and Huner, N.P.A. (2006). Adaptation and Acclimation of Photosynthetic Microorganisms to Permanently Cold Environments. *Microbiol. Mol. Biol. Rev.* 70, 222–252.
- Morrison, J.R., and Goodwin, D.S. (2010). Phytoplankton photocompensation from space-based fluorescence measurements. *Geophys. Res. Lett.* 37, L06603.
- Murata, N., Takahashi, S., Nishiyama, Y., and Allakhverdiev, S.I. (2007). Photoinhibition of photosystem II under environmental stress. *Biochim. Biophys. Acta BBA - Bioenerg.* 1767, 414–421.
- Myers, J. (1980). On the Algae: Thoughts about Physiology and Measurements of Efficiency. In *Primary Productivity in the Sea*, P.G. Falkowski, ed. (Springer US), pp. 1–16.
- Napoléon, C., and Claquin, P. (2012). Multi-Parametric Relationships between PAM Measurements and Carbon Incorporation, an In Situ Approach. *PloS One* 7, e40284.
- Napoléon, C., Raimbault, V., and Claquin, P. (2013). Influence of Nutrient Stress on the Relationships between PAM Measurements and Carbon Incorporation in Four Phytoplankton Species. *PloS One* 8, e66423.

- Nawrocki, W.J., Tourasse, N.J., Taly, A., Rappaport, F., and Wollman, F.-A. (2015). The Plastid Terminal Oxidase: Its Elusive Function Points to Multiple Contributions to Plastid Physiology. *Annu. Rev. Plant Biol.* 66, 49-74.
- Niyogi, K.K. (2000). Safety valves for photosynthesis. *Curr. Opin. Plant Biol.* 3, 455–460.
- Niyogi, K.K., and Truong, T.B. (2013). Evolution of flexible non-photochemical quenching mechanisms that regulate light harvesting in oxygenic photosynthesis. *Curr. Opin. Plant Biol.* 16, 307–314.
- Öquist, G., Chow, W.S., and Anderson, J.M. (1992). Photoinhibition of photosynthesis represents a mechanism for the long-term regulation of photosystem II. *Planta* 186, 450–460.
- Öquist, G., Hurry, V.M., and Huner, N.P.A. (1993). The temperature dependence of the redox state of  $Q_A$  and susceptibility of photosynthesis to photoinhibition. *Plant Physiol. Biochem.* 31, 683–691.
- Ort, D.R., and Baker, N.R. (2002). A photoprotective role for  $O_2$  as an alternative electron sink in photosynthesis? *Curr. Opin. Plant Biol.* 5, 193–198.
- Ottesen, E.A., Young, C.R., Gifford, S.M., Eppley, J.M., Marin, R., Schuster, S.C., Scholin, C.A., and DeLong, E.F. (2014). Multispecies diel transcriptional oscillations in open ocean heterotrophic bacterial assemblages. *Science* 345, 207–212.
- Oxborough, K. (2004). Imaging of chlorophyll a fluorescence: theoretical and practical aspects of an emerging technique for the monitoring of photosynthetic performance. *J. Exp. Bot.* 55, 1195–1205.
- Oxborough, K., and Baker, N.R. (1997). Resolving chlorophyll a fluorescence images of photosynthetic efficiency into photochemical and non-photochemical components – calculation of  $qP$  and  $F_v'/F_m'$ ; without measuring  $F_o'$ . *Photosynth. Res.* 54, 135–142.
- Oxborough, K., Moore, C.M., Suggett, D.J., Lawson, T., Chan, H.G., and Geider, R.J. (2012). Direct estimation of functional PSII reaction center concentration and PSII electron flux on a volume basis: a new approach to the analysis of Fast Repetition Rate fluorometry (FRRf) data. *Limnol Ocean. Methods* 10, 142–154.
- Pabi, S., van Dijken, G.L., and Arrigo, K.R. (2008). Primary production in the Arctic Ocean, 1998–2006. *J. Geophys. Res. Oceans* 113, C08005.
- Palmer, M.A., Arrigo, K.R., Mundy, C.J., Ehn, J.K., Gosselin, M., Barber, D.G., Martin, J., Alou, E., Roy, S., and Tremblay, J.-É. (2011). Spatial and temporal variation of photosynthetic parameters in natural phytoplankton assemblages in the Beaufort Sea, Canadian Arctic. *Polar Biol.* 34, 1915–1928.
- Palmer, M.A., van Dijken, G.L., Mitchell, B.G., Seegers, B.J., Lowry, K.E., Mills, M.M., and Arrigo, K.R. (2013). Light and nutrient control of photosynthesis in natural phytoplankton

populations from the Chukchi and Beaufort seas, Arctic Ocean. *Limnol. Oceanogr.* 58, 2185–2205.

Papageorgiou, G., and Govindjee (2004). Chlorophyll a Fluorescence - A Signature of Photosynthesis. (Springer, Dordrecht.)

Pedros-Alió, C., Potvin, M., and Lovejoy, C. (2015). Diversity of planktonic microorganisms in the Arctic Ocean. *Prog. Oceanogr.* 139, 233–243.

Pei, S., and Laws, E.A. (2013). Does the  $^{14}\text{C}$  method estimate net photosynthesis? Implications from batch and continuous culture studies of marine phytoplankton. *Deep Sea Res. Part Oceanogr. Res. Pap.* 82, 1–9.

Peltier, G., Tolleter, D., Billon, E., and Cournac, L. (2010). Auxiliary electron transport pathways in chloroplasts of microalgae. *Photosynth. Res.* 106, 19–31.

Pemberton, K.L., Clarke, K.R., and Joint, I. Quantifying uncertainties associated with the measurement of primary production. *Mar. Ecol. Prog. Ser.* 322, 51–59.

Perrette, M., Yool, A., Quartly, G.D., and Popova, E.E. (2011). Near-ubiquity of ice-edge blooms in the Arctic. *Biogeosciences* 8, 515–524.

Peterson, B.J. (1980). Aquatic Primary Productivity and the  $^{14}\text{C}$ - $\text{CO}_2$  Method: A History of the Productivity Problem. *Annu. Rev. Ecol. Syst.* 11, 359–385.

Petrenko, D., Pozdnyakov, D., Johannessen, J., Counillon, F., and Syrov, V. (2013). Satellite-derived multi-year trend in primary production in the Arctic Ocean. *Int. J. Remote Sens.* 34, 3903–3937.

Petrou, K., Hassler, C.S., Doblin, M.A., Shelly, K., Schoemann, V., van den Enden, R., Wright, S., and Ralph, P.J. (2011). Iron-limitation and high light stress on phytoplankton populations from the Australian Sub-Antarctic Zone (SAZ). *Deep Sea Res. Part II Top. Stud. Oceanogr.* 58, 2200–2211.

Pinckney, J. L. (2013) HPLC Method - Technical - Estuarine Ecology, available from: <https://sites.google.com/site/jaypinckney/home/protocols-reports>

Platt, T., and Sathyendranath, S. (1993). Estimators of primary production for interpretation of remotely sensed data on ocean color. *J. Geophys. Res. Oceans* 98, 14561–14576.

Pope, R.M., and Fry, E.S. (1997). Absorption spectrum (380–700 nm) of pure water. II. Integrating cavity measurements. *Appl. Opt.* 36, 8710.

Popova, E.E., Yool, A., Coward, A.C., Dupont, F., Deal, C., Elliott, S., Hunke, E., Jin, M., Steele, M., and Zhang, J. (2012). What controls primary production in the Arctic Ocean? Results from an intercomparison of five general circulation models with biogeochemistry. *J. Geophys. Res. Oceans* 117, C00D12.

- Prasil, O., Kolber, Z., Berry, J.A., and Falkowski, P.G. (1996). Cyclic electron flow around Photosystem II; *Photosynth. Res.* 48, 395–410.
- Prézelin, B.B. (1992). Diel periodicity in phytoplankton productivity. *Hydrobiologia* 238, 1–35.
- Price, N.M., Harrison, G.I., Hering, J.G., Hudson, R.J., Nirel, P.M.V., Palenik, B., and Morel, F.M.M. (1989). Preparation and Chemistry of the Artificial Algal Culture Medium Aquil. *Biol. Oceanogr.* 6, 443–461.
- Prieto, L., Vaillancourt, R.D., Hales, B., and Marra, J. (2008). On the relationship between carbon fixation efficiency and bio-optical characteristics of phytoplankton. *J. Plankton Res.* 30, 43–56.
- Quay, P.D., Peacock, C., Björkman, K., and Karl, D.M. (2010). Measuring primary production rates in the ocean: Enigmatic results between incubation and non-incubation methods at Station ALOHA. *Glob. Biogeochem. Cycles* 24, GB3014.
- Raateoja, M.P. (2004). Fast repetition rate fluorometry (FRRF) measuring phytoplankton productivity: a case study at the entrance to the Gulf of Finland, Baltic Sea. *Boreal Environ. Res.* 9, 263–276.
- Raateoja, M., Seppl, J., and Kuosa, H. (2004). Bio-optical modelling of primary production in the SW Finnish coastal zone, Baltic Sea: fast repetition rate fluorometry in Case 2 waters. *Mar. Ecol. Prog. Ser.* 267, 9–26.
- Rao, D.S., and Platt, T. (1984). Primary production of Arctic waters. *Polar Biol.* 3, 191–201.
- Raven, J.A., Evans, M.C.W., and Korb, R.E. (1999). The role of trace metals in photosynthetic electron transport in O<sub>2</sub>-evolving organisms. *Photosynth. Res.* 60, 111–150.
- Ribalet, F., Swalwell, J., Clayton, S., Jiménez, V., Sudek, S., Lin, Y., Johnson, Z.I., Worden, A.Z., and Armbrust, E.V. (2015). Light-driven synchrony of *Prochlorococcus* growth and mortality in the subtropical Pacific gyre. *Proc. Natl. Acad. Sci.* 112(26), 8008-8012.
- Roach, T., and Krieger-Liszkay, A.K. (2014). Regulation of Photosynthetic Electron Transport and Photoinhibition. *Curr. Protein Pept. Sci.* 15, 351–362.
- Robinson, C., Tilstone, G.H., Rees, A.P., Smyth, T.J., Fishwick, J.R., Tarran, G.A., Luz, B., Barkan, E., and David, E. (2009). Comparison of in vitro and in situ plankton production determinations. *Aquat. Microb. Ecol.* 54, 13–34.
- Robinson, C., Suggett, D.J., Cherukuru, N., Ralph, P.J., and Doblin, M.A. (2014). Performance of Fast Repetition Rate fluorometry based estimates of primary productivity in coastal waters. *J. Mar. Syst.* 139, 299–310.
- Rochaix, J.D. (2011). Regulation of photosynthetic electron transport. *Biochim. Biophys. Acta BBA-Bioenerg.* 1807, 375–383.

- Roháček, K. (2002). Chlorophyll Fluorescence Parameters: The Definitions, Photosynthetic Meaning, and Mutual Relationships. *Photosynthetica* 40, 13–29.
- Röttgers, R., and Gehnke, S. (2012). Measurement of light absorption by aquatic particles: improvement of the quantitative filter technique by use of an integrating sphere approach. *Appl. Opt.* 51, 1336–1351.
- Roy, S., Llewellyn, C.A., Egeland, E.S., and Johnsen, G. (2011). *Phytoplankton Pigments: Characterization, Chemotaxonomy and Applications in Oceanography* (Cambridge University Press).
- Ruban, A.V. (2014). Evolution under the sun: optimizing light harvesting in photosynthesis. *J. Exp. Bot.* eru400.
- Ruban, A.V., and Mullineaux, C.W. (2014). Non-Photochemical Fluorescence Quenching and the Dynamics of Photosystem II Structure. In *Non-Photochemical Quenching and Energy Dissipation in Plants, Algae and Cyanobacteria*, B. Demmig-Adams, G. Garab, W.A. III, and Govindjee, eds. (Springer Netherlands), pp. 373–386.
- Ruban, A.V., and Murchie, E.H. (2012). Assessing the photoprotective effectiveness of non-photochemical chlorophyll fluorescence quenching: A new approach. *Biochim. Biophys. Acta BBA - Bioenerg.* 1817, 977–982.
- Ruban, A.V., Johnson, M.P., and Duffy, C.D.P. (2012). The photoprotective molecular switch in the photosystem II antenna. *Biochim. Biophys. Acta BBA - Bioenerg.* 1817, 167–181.
- Ryan-Keogh, T.J., Macey, A.I., Cockshutt, A.M., Moore, C.M., and Bibby, T.S. (2012). The Cyanobacterial Chlorophyll-Binding-Protein IsiA Acts To Increase The In Vivo Effective Absorption Cross-Section Of PSI Under Iron Limitation. *J. Phycol.* 48(1), 145-154.
- Ryan-Keogh, T.J., Macey, A.I., Nielsdóttir, M.C., Lucas, M.I., Steigenberger, S.S., Stinchcombe, M.C., Achterberg, E.P., Bibby, T.S., and Mark Moore, C. (2013). Spatial and temporal development of phytoplankton iron stress in relation to bloom dynamics in the high-latitude North Atlantic Ocean. *Limnol. Oceanogr.* 58, 533–545.
- Ryther, J.H. (1956). Photosynthesis in the ocean as a function of light intensity. *Limnol. Oceanogr.* 61–70.
- Sakshaug, E., Bricaud, A., Dandonneau, Y., Falkowski, P.G., Kiefer, D.A., Legendre, L., Morel, A., Parslow, J., and Takahashi, M. (1997). Parameters of photosynthesis: definitions, theory and interpretation of results. *J. Plankton Res.* 19, 1637–1670.
- Saroussi, S.I., Wittkopp, T.M., and Grossman, A.R. (2016). The Type II NADPH Dehydrogenase Facilitates Cyclic Electron Flow, Energy-Dependent Quenching, and Chlororespiratory Metabolism during Acclimation of *Chlamydomonas reinhardtii* to Nitrogen Deprivation. *Plant Physiol.* 170, 1975–1988.
- Scheibe, R. (2004). Malate valves to balance cellular energy supply. *Physiol. Plant.* 120, 21–26.

- Schofield, O., Grzymiski, J., Bissett, W.P., Kirkpatrick, G.J., Millie, D.F., Moline, M., and Roesler, C.S. (1999). Optical Monitoring and Forecasting Systems for Harmful Algal Blooms: Possibility or Pipe Dream? *J. Phycol.* *35*, 1477–1496.
- Schrader, P.S., Milligan, A.J., and Behrenfeld, M.J. (2011). Surplus Photosynthetic Antennae Complexes Underlie Diagnostics of Iron Limitation in a Cyanobacterium. *PLoS ONE* *6*, e18753.
- Schreiber, U. (2004). Pulse-amplitude-modulation (PAM) fluorometry and saturation pulse method: an overview. *Chlorophyll Fluoresc.* 279–319.
- Schreiber, U., Endo, T., Mi, H., and Asada, K. (1995). Quenching analysis of chlorophyll fluorescence by the saturation pulse method: Particular aspects relating to the study of eukaryotic algae and cyanobacteria. *Plant Cell Physiol.* *36*, 873–882.
- Schuback, N., Schallenberg, C., Duckham, C., Maldonado, M.T., and Tortell, P.D. (2015). Interacting Effects of Light and Iron Availability on the Coupling of Photosynthetic Electron Transport and CO<sub>2</sub>-Assimilation in Marine Phytoplankton. *PLoS ONE* *10*, e0133235.
- Schuback, N., Flecken, M., Maldonado, M.T., and Tortell, P.D. (2016). Diurnal variation in the coupling of photosynthetic electron transport and carbon fixation in iron-limited phytoplankton in the NE Subarctic Pacific. *Biogeosciences* *13*, 1019–1035.
- Shinopoulos, K.E., and Brudvig, G.W. (2012). Cytochrome b559 and cyclic electron transfer within photosystem II. *Biochim. Biophys. Acta BBA - Bioenerg.* *1817*, 66–75.
- Silsbe, G.: Phytotools: Phytoplankton Production Tools, an R package available on CRAN: <https://cran.r-project.org/web/packages/phytotools/index.html>, 2015.
- Silsbe, G.M., and Kromkamp, J.C. (2012). Modeling the irradiance dependency of the quantum efficiency of photosynthesis. *Limnol. Oceanogr. Methods* *10*, 645–652.
- Silsbe, G.M., Oxborough, K., Suggett, D.J., Forster, R.M., Ihnken, S., Komárek, O., Lawrenz, E., Prášil, O., Röttgers, R., Šicner, M., Simis, S.G.H., Van Dijk, M.A., Kromkamp, J.C. (2015). Toward autonomous measurements of photosynthetic electron transport rates: An evaluation of active fluorescence-based measurements of photochemistry. *Limnol. Oceanogr. Methods* *13*(3), 138-155.
- Smith Jr, W.O., and Sakshaug, E. (2013). Polar Phytoplankton. *Polar Oceanogr. Chem. Biol. Geol.* *477*.
- Smyth, T.J., Pemberton, K.L., Aiken, J., and Geider, R.J. (2004). A methodology to determine primary production and phytoplankton photosynthetic parameters from Fast Repetition Rate Fluorometry. *J. Plankton Res.* *26*, 1337–1350.
- Steemann-Nielsen, E. (1951). Measurement of the Production of Organic Matter in the Sea by means of Carbon-14. *Nature* *167*, 684–685.

Steemann-Nielsen, E.S. (1952). The use of radio-active carbon (C14) for measuring organic production in the sea. *J. Cons.* *18*, 117–140.

Stomp, M., J. Huisman, L. Vörös, F. R. Pick, M. Laamanen, T. Haverkamp, and L. J. Stal. (2007). Colourful coexistence of red and green picocyanobacteria in lakes and seas. *Ecol. Lett.* *10*: 290–298.

Streb, P., and Cornic, G. (2012). *Photosynthesis and antioxidative protection in alpine herbs* (Springer).

Streb, P., Josse, E.-M., Gallouët, E., Baptist, F., Kuntz, M., and Cornic, G. (2005). Evidence for alternative electron sinks to photosynthetic carbon assimilation in the high mountain plant species *Ranunculus glacialis*. *Plant Cell Environ.* *28*, 1123–1135.

Stross, R.G., Chisholm, S.W., and Downing, T.A. (1973). Causes of Daily Rhythms in Photosynthetic Rates of Phytoplankton. *Biol. Bull.* *145*, 200–209.

Strzepek, R.F., and Harrison, P.J. (2004). Photosynthetic architecture differs in coastal and oceanic diatoms. *Nature* *431*, 689–692.

Strzepek, R.F., Maldonado, M.T., Hunter, K.A., Frew, R.D., and Boyd, P.W. (2011). Adaptive strategies by Southern Ocean phytoplankton to lessen iron limitation: Uptake of organically complexed iron and reduced cellular iron requirements. *Limnol. Oceanogr.* *56*, 1983–2002.

Suggett, D., Kraay, G., Holligan, P., Davey, M., Aiken, J., and Geider, R. (2001). Assessment of photosynthesis in a spring cyanobacterial bloom by use of a fast repetition rate fluorometer. *Limnol. Oceanogr.* *46*, 802–810.

Suggett, D.J., MacIntyre, H.L., and Geider, R.J. (2004). Evaluation of biophysical and optical determinations of light absorption by photosystem II in phytoplankton. *Limnol Ocean. Methods* *2*, 316–332.

Suggett, D.J., Maberly, S.C., and Geider, R.J. (2006). Gross photosynthesis and lake community metabolism during the spring phytoplankton bloom. *Limnol. Oceanogr.* 2064–2076.

Suggett, D.J., MacIntyre, H.L., Kana, T.M., and Geider, R.J. (2009a). Comparing electron transport with gas exchange: parameterising exchange rates between alternative photosynthetic currencies for eukaryotic phytoplankton. *Aquat. Microb. Ecol.* *56*, 147–162.

Suggett, D.J., Moore, C.M., Hickman, A.E., and Geider, R.J. (2009b). Interpretation of fast repetition rate (FRR) fluorescence: signatures of phytoplankton community structure versus physiological state. *Mar Ecol Prog Ser* *376*, 1–19.

Suggett, D.J., Prášil, O., and Borowitzka, M.A. (2010a). *Chlorophyll a Fluorescence in Aquatic Sciences: Methods and Applications* (Springer).

Suggett, D.J., Moore, C.M., and Geider, R.J. (2010b). Estimating aquatic productivity from active fluorescence measurements. *Chlorophyll Fluoresc. Aquat. Sci. Methods Appl.* 103–127.

- Suzuki, L., and Johnson, C.H. (2001). Algae Know the Time of Day: Circadian and Photoperiodic Programs. *J. Phycol.* 37, 933–942.
- Taylor, R.L., Semeniuk, D.M., Payne, C.D., Zhou, J., Tremblay, J.-É., Cullen, J.T., and Maldonado, M.T. (2013). Colimitation by light, nitrate, and iron in the Beaufort Sea in late summer. *J. Geophys. Res. Oceans* 118, 3260–3277.
- Thamatrakoln, K., Bailleul, B., Brown, C.M., Gorbunov, M.Y., Kustka, A.B., Frada, M., Joliot, P.A., Falkowski, P.G., and Bidle, K.D. (2013). Death-specific protein in a marine diatom regulates photosynthetic responses to iron and light availability. *Proc. Natl. Acad. Sci.* 110, 20123–20128.
- Timmermans, K.R., Davey, M.S., Wagt, B. van der, Snoek, J., Geider, R.J., Veldhuis, M.J.W., Gerringa, L.J.A., and Baar, H.J.W. de (2001). Co-limitation by iron and light of *Chaetoceros brevis*, *C. dictyota* and *C. calcitrans* (Bacillariophyceae). *Mar. Ecol. Prog. Ser.* 217, 287–297.
- Tremblay, J.-É., and Gagnon, J. (2009). The effects of irradiance and nutrient supply on the productivity of Arctic waters: a perspective on climate change. In *Influence of Climate Change on the Changing Arctic and Sub-Arctic Conditions*, J.C.J. Nihoul, and A.G. Kostianoy, eds. (Springer Netherlands), pp. 73–93.
- Tremblay, J.-É., Anderson, L.G., Matrai, P., Coupel, P., Bélanger, S., Michel, C., and Reigstad, M. (2015). Global and regional drivers of nutrient supply, primary production and CO<sub>2</sub> drawdown in the changing Arctic Ocean. *Prog. Oceanogr.* 139, 171–196.
- Tripathy, S.C., Ishizaka, J., Fujiki, T., Shibata, T., Okamura, K., Hosaka, T., and Saino, T. (2010). Assessment of carbon- and fluorescence-based primary productivity in Ariake Bay, southwestern Japan. *Estuar. Coast. Shelf Sci.* 87, 163–173.
- Uitz, J., Huot, Y., Bruyant, F., Babin, M., Claustre, H., and Claustre, H. (2008). Relating Phytoplankton Photophysiological Properties to Community Structure on Large Scales. *Limnol. Oceanogr.* 53, 614–630.
- Vancoppenolle, M., Bopp, L., Madec, G., Dunne, J., Ilyina, T., Halloran, P.R., and Steiner, N. (2013). Future Arctic Ocean primary productivity from CMIP5 simulations: Uncertain outcome, but consistent mechanisms. *Glob. Biogeochem. Cycles* 27, 605–619.
- Varela, D.E., Crawford, D.W., Wrohan, I.A., Wyatt, S.N., and Carmack, E.C. (2013). Pelagic primary productivity and upper ocean nutrient dynamics across Subarctic and Arctic Seas. *J. Geophys. Res. Oceans* 118, 7132–7152.
- Vass, I. (2011). Role of charge recombination processes in photodamage and photoprotection of the photosystem II complex. *Physiol. Plant.* 142, 6–16.
- Vass, I. (2012). Molecular mechanisms of photodamage in the Photosystem II complex. *Biochim. Biophys. Acta BBA - Bioenerg.* 1817, 209–217.

- Vass, I., and Cser, K. (2009). Janus-faced charge recombinations in photosystem II photoinhibition. *Trends Plant Sci.* *14*, 200–205.
- Vassiliev, I.R., Kolber, Z., Wyman, K.D., Mauzerall, D., Shukla, V.K., and Falkowski, P.G. (1995). Effects of Iron Limitation on Photosystem II Composition and Light Utilization in *Dunaliella tertiolecta*. *Plant Physiol.* *109*, 963–972.
- Wang, J., Cota, G.F., and Ruble, D.A. (2005). Absorption and backscattering in the Beaufort and Chukchi Seas. *J. Geophys. Res. Oceans* *110*.
- Wassmann, P. (2015). Overarching perspectives of contemporary and future ecosystems in the Arctic Ocean. *Prog. Oceanogr.* *139*, 1–12.
- Wassmann, P., Duarte, C.M., Agusti, S., and Sejr, M.K. (2011). Footprints of climate change in the Arctic marine ecosystem. *Glob. Change Biol.* *17*, 1235–1249.
- Webb, W.L., Newton, M., and Starr, D. (1974). Carbon Dioxide Exchange of *Alnus rubra*. A Mathematical Model. *Oecologia* *17*, 281–291.
- Welschmeyer, N.A. (1994). Fluorometric analysis of chlorophyll a in the presence of chlorophyll b and pheopigments. *Limnol. Oceanogr.* *39*, 1985–1992.
- Westberry, T.K., and Behrenfeld, M.J. (2014). Oceanic Net Primary Production. In *Biophysical Applications of Satellite Remote Sensing*, J.M. Hanes, ed. (Springer Berlin Heidelberg), pp. 205–230.
- Williams, P.J. le B., Thomas, D.N., and Reynolds, C.S. (2008). *Phytoplankton Productivity: Carbon Assimilation in Marine and Freshwater Ecosystems* (John Wiley & Sons).
- Wilson, K.E., Ivanov, A.G., Öquist, G., Grodzinski, B., Sarhan, F., and Huner, N.P. (2006). Energy balance, organellar redox status, and acclimation to environmental stress. *Botany* *84*, 1355–1370.
- Yeremenko, N., Kouřil, R., Ihalainen, J.A., D’Haene, S., van Oosterwijk, N., Andrizhiyevskaya, E.G., Keegstra, W., Dekker, H.L., Hagemann, M., Boekema, E.J., et al. (2004). Supramolecular Organization and Dual Function of the IsiA Chlorophyll-Binding Protein in Cyanobacteria. *Biochemistry (Mosc.)* *43*, 10308–10313.
- Yruela, I. (2013). Transition metals in plant photosynthesis. *Met. Integr. Biometal Sci.* *5*, 1090–1109.
- Zaks, J., Amarnath, K., Sylak-Glassman, E.J., and Fleming, G.R. (2013). Models and measurements of energy-dependent quenching. *Photosynth. Res.* *116*, 389–409.
- Zehr, J.P., and Kudela, R.M. (2009). Photosynthesis in the Open Ocean. *Science* *326*, 945–946.
- Zhao, Y., and Quigg, A. (2015). Study of photosynthetic productivity in the Northern Gulf of Mexico: Importance of diel cycles and light penetration. *Cont. Shelf Res.* *102*, 33–46.

Zhu, Y., Ishizaka, J., Tripathy, S.C., Wang, S., Mino, Y., Matsuno, T., and Suggett, D.J. (2016). Variation of the photosynthetic electron transfer rate and electron requirement for daily net carbon fixation in Ariake Bay, Japan. *J. Oceanogr.* 1–16.

## Appendices

### Appendix A : Supplementary material for chapter 2

#### A.1 Spectral distribution of light sources and phytoplankton absorption spectra

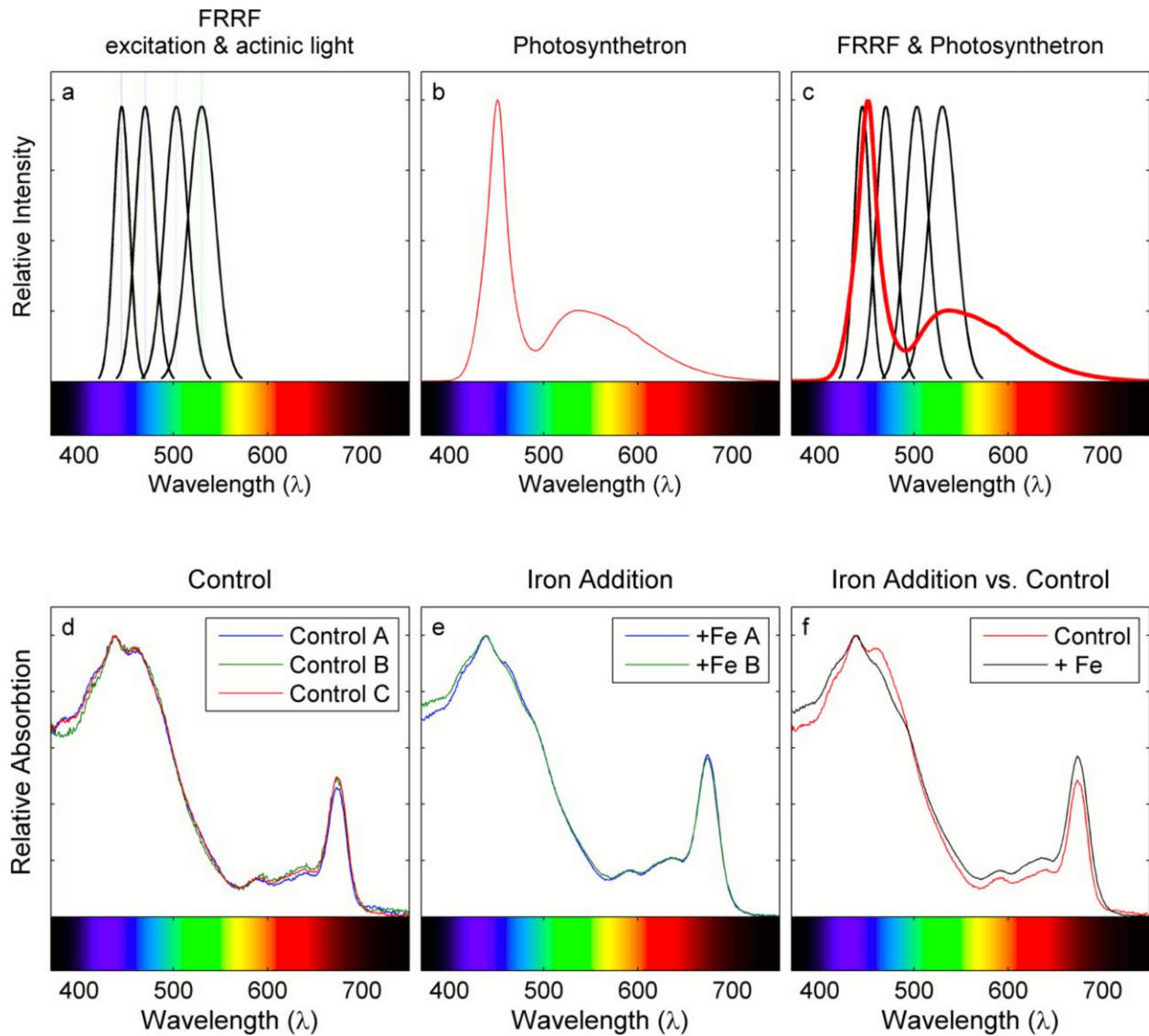


**Figure A1: Spectral distribution of light sources used for FRRF and Photosynthetron assays, and absorption spectra of phytoplankton assemblages on day 6 of the iron-addition experiment.** (a) The FRRF instrument used during this study contains LEDs with peak output at four wavelengths (445 nm, 470 nm, 503 nm, 530 nm). In our FRRF instrument, excitation as well as actinic background irradiance is applied from the same LEDs. (b) Spectral distribution of the LEDs used in the photosynthetron used for  $^{14}\text{C}$ -uptake experiments. (c) Spectral overlap of the two

light sources. The overlap is good in the region of maximal light absorption by photosynthetic pigment (ca. 450 nm). However, in direct comparison with the photosynthetron, the FRRF instrument provides a higher proportion of photons in the region  $> 480$  nm. This could have led to an underestimation of  $ETR_{RCII}$  values relative to  $CO_2$ -assimilation values measured in the photosynthetron, resulting in an under-estimate of  $\Phi_{e,C}/n_{PSII}$ . In addition to knowledge of spectral differences in the light sources used (a-c), spectral correction of our data would require light absorption spectra of the phytoplankton assemblages examined. Relative absorption spectra of the phytoplankton communities on day 6 after iron-addition (measured using the quantitative filter technique (Mitchell et al., 2002) are shown in (d-f). Spectra from 3 biological replicates of the control (d) and two biological replicates of the iron addition treatment (e) were averaged, and these spectra are shown together in panel (f). The results show relatively small changes in the relative light absorption between the two treatments, and it is unlikely that these changes would have significantly influenced the large iron and light-dependent effects in  $\Phi_{e,C}/n_{PSII}$ . Because we did not measure absorption spectra for all sampling points of the iron addition experiment and stations along the transect, we were unable to spectrally correct our data. Furthermore, because we are not deriving absolute values for  $\Phi_{e,C}/n_{PSII}$ , we did not apply a constant correction factor (estimated from *e.g.* the data shown in a-f).

## A.2 Phytoplankton assemblage composition

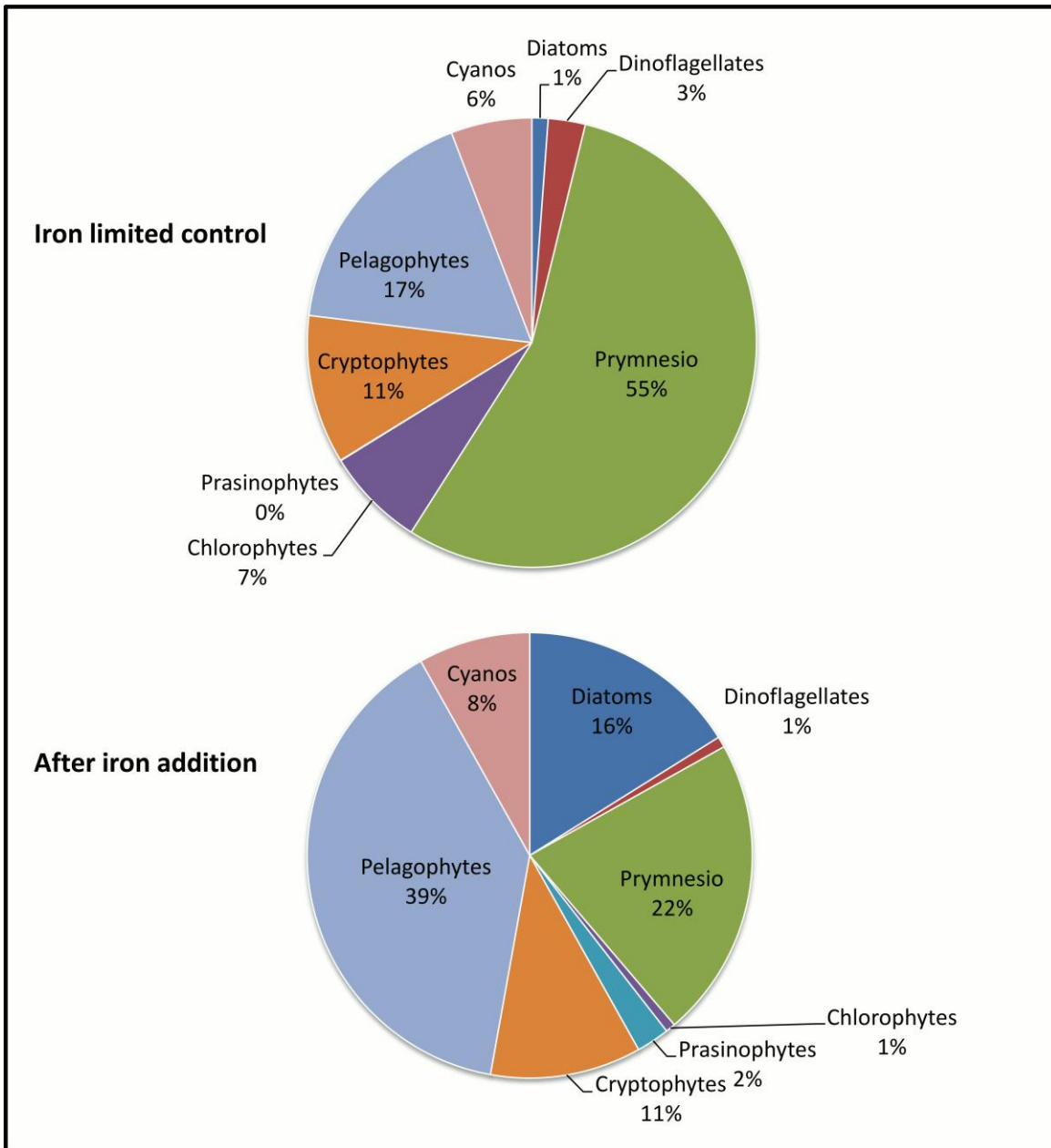


**Figure A2: Phytoplankton assemblage composition on day 6 of the iron addition experiment conducted at P20.** The taxonomic composition of phytoplankton assemblages (% of total chl *a*) was derived from HPLC analysis of accessory photosynthetic pigment. Average values are shown from three biological replicates for the iron-limited control and the iron addition treatment on day 6 of the experiment. One to 1.5 L of water were filtered on 25 mm GF/F and stored at -80 °C until analysis. Pigments were extracted and quantified as described by Taylor et al. (Taylor et al., 2013). Pigment ratios were then used to estimate phytoplankton assemblage composition using CHEMTAX as described by Taylor et al. (Taylor et al., 2013). The initial pigment ratio matrix used for our data was taken from Lee et al. (Lee et al., 2011), table 5, which is specific to North Pacific phytoplankton isolates.

### A.3 Volume normalized rates of CO<sub>2</sub>-assimilation

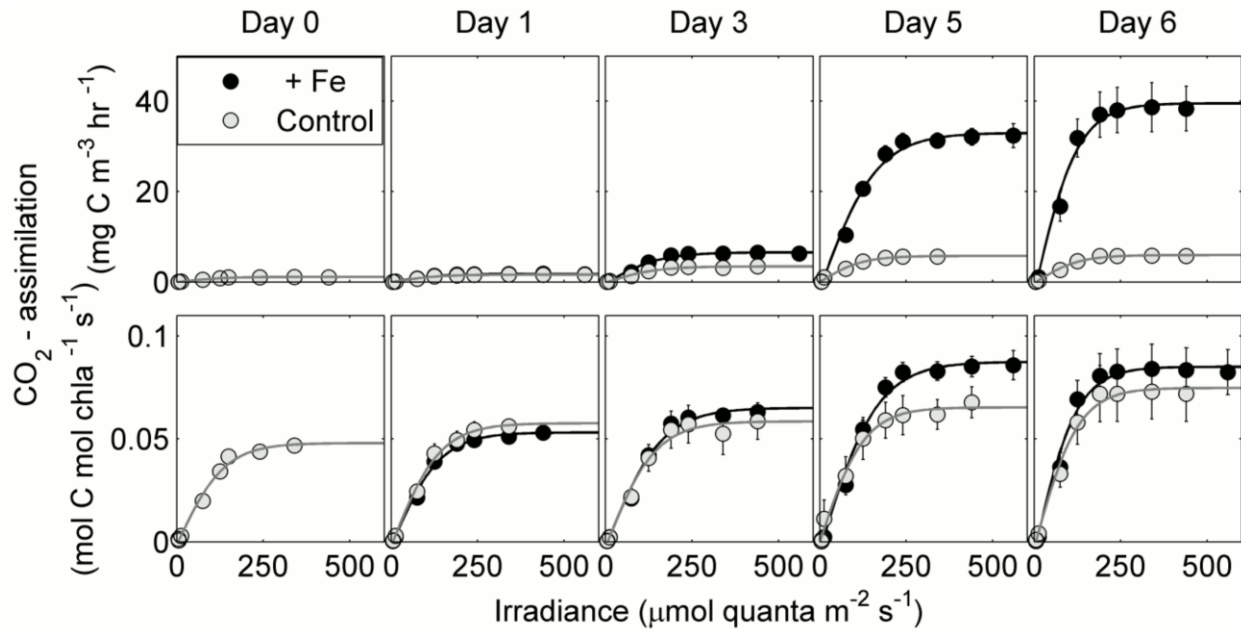


**Figure A3: Response of volume normalized rates of CO<sub>2</sub>-assimilation (mol C m<sup>-3</sup> hr<sup>-1</sup>) during the iron addition experiment.** The rates were measured as a function of irradiance, and PvsE curves were fit with the exponential model of Webb et al. (1974). Shown are mean values from three biological replicates where error bars represent standard error of mean and are sometimes smaller than symbols. Results shown in this figure confirm a strong stimulatory effect of iron additions on primary productivity in the experimental bottles.

## Appendix B : Supplementary material for chapter 4

### B.1 Final pigment ratio matrices from CHEMTAX analysis of HPLC pigments

**Table B2: Final pigment ratio matrices from CHEMTAX analysis of HPLC pigments.** Two different matrices were used for ML and sub-ML phytoplankton assemblages. *chl<sub>c1c2</sub>* stands for chlorophyllide *c1c2*; *perid* stands for peridinin; *19'BF* stands for 19'butanoyloxyfucoxanthin; *fuco* stands for fucoxanthin; *19'HF* stands for 19'hexanoyloxyfucoxanthin; *neo* stands for 9'cis-neoxanthin; *prasino* stands for prasinoxanthin, *chl<sub>b</sub>* stands for chlorophyll *b*; *chl<sub>a</sub>* stands for chlorophyll *a*.

| ML (high light)    |                           |              |              |             |              |            |                |              |               |                        |                        |
|--------------------|---------------------------|--------------|--------------|-------------|--------------|------------|----------------|--------------|---------------|------------------------|------------------------|
|                    | <i>chl<sub>c1c2</sub></i> | <i>perid</i> | <i>19'BF</i> | <i>fuco</i> | <i>19'HF</i> | <i>neo</i> | <i>prasino</i> | <i>allox</i> | <i>lutein</i> | <i>chl<sub>b</sub></i> | <i>chl<sub>a</sub></i> |
| Diatom             | 3.98                      |              |              | 0.57        |              |            |                |              |               |                        | 1.00                   |
| Dino               |                           | 0.45         |              |             |              |            |                |              |               |                        | 1.00                   |
| Chlorophytes       |                           |              |              |             |              | 0.03       |                |              | 0.14          | 0.23                   | 1.00                   |
| Prasino-3          |                           |              |              |             |              | 0.23       | 0.31           |              | 0.02          | 0.56                   | 1.00                   |
| Prasino-2          |                           |              |              |             |              | 0.05       |                |              | 0.13          | 2.07                   | 1.00                   |
| Cryptophytes       | 0.09                      |              |              |             |              |            |                | 0.23         |               |                        | 1.00                   |
| Chryso-Pelago      | 0.35                      |              | 0.90         | 0.22        |              |            |                |              |               |                        | 1.00                   |
| c3-flagellates     | 0.11                      |              | 0.04         | 0.12        | 0.05         |            |                |              |               |                        | 1.00                   |
| Hapto-7            | 0.17                      |              | 0.02         | 0.33        | 1.15         |            |                |              |               |                        | 1.00                   |
| sub-ML (low light) |                           |              |              |             |              |            |                |              |               |                        |                        |
| Diatom             | 4.57                      |              |              | 0.92        |              |            |                |              |               |                        | 1.00                   |
| Dino               |                           | 1.36         |              |             |              |            |                |              |               |                        | 1.00                   |
| Chlorophytes       |                           |              |              |             |              | 0.03       |                |              | 0.10          | 0.04                   | 1.00                   |
| Prasino-3          |                           |              |              |             |              | 0.08       | 0.15           |              | 0.00          | 0.23                   | 1.00                   |
| Prasino-2          |                           |              |              |             |              | 0.03       |                |              | 0.03          | 1.07                   | 1.00                   |
| Cryptophytes       | 0.10                      |              |              |             |              |            |                | 0.12         |               |                        | 1.00                   |
| Chryso-Pelago      | 1.08                      |              | 0.52         | 0.27        |              |            |                |              |               |                        | 1.00                   |
| c3-flagellates     | 0.08                      |              | 0.05         | 0.15        | 0.09         |            |                |              |               |                        | 1.00                   |
| Hapto-7            | 0.09                      |              | 0.01         | 0.22        | 0.43         |            |                |              |               |                        | 1.00                   |

**B.2 Phytoplankton assemblage composition**

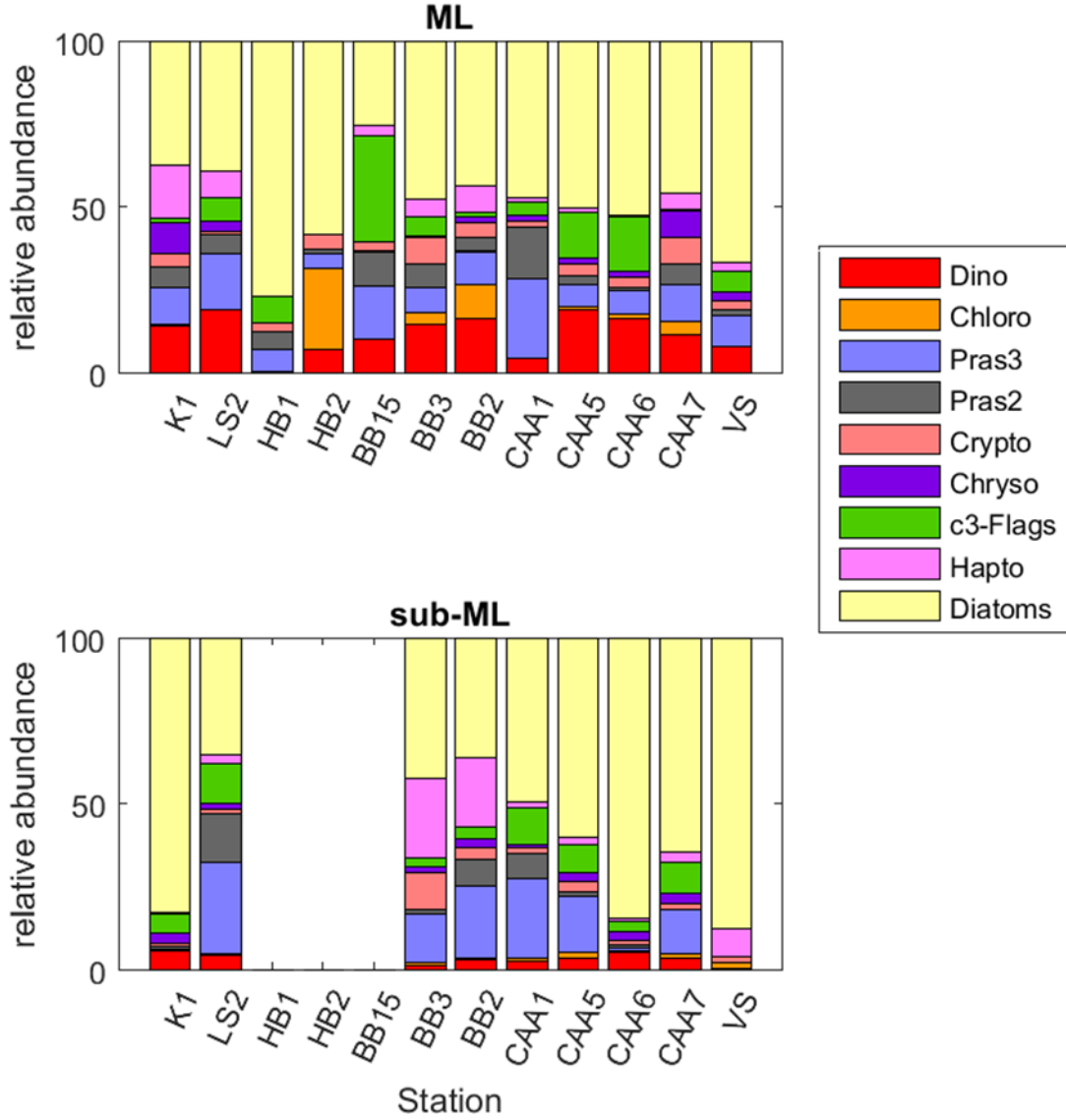


**Figure B1: CHEMTAX analysis of HPLC pigments.** Values present the contribution of each group to total chl*a* biomass.

### B.3 PvsE curves for $^{14}\text{C}$ -uptake

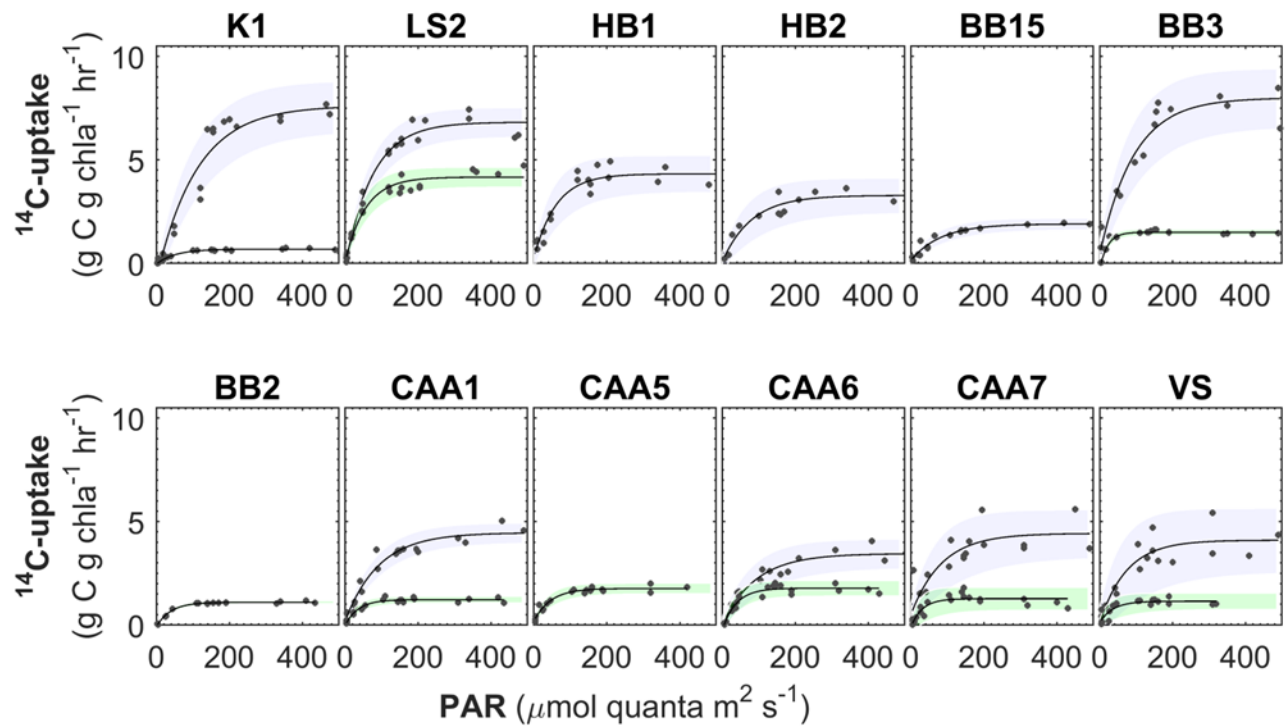


**Figure B2: PvsE curves for  $^{14}\text{C}$ -uptake.** Data from both depths sampled at each station are plotted on the same axes. ML samples have blue shaded areas and sub-ML samples have green shaded areas. The shaded area represents the 95 % confidence interval.

#### B.4 PvsE curves for $ETR_{RCII}$

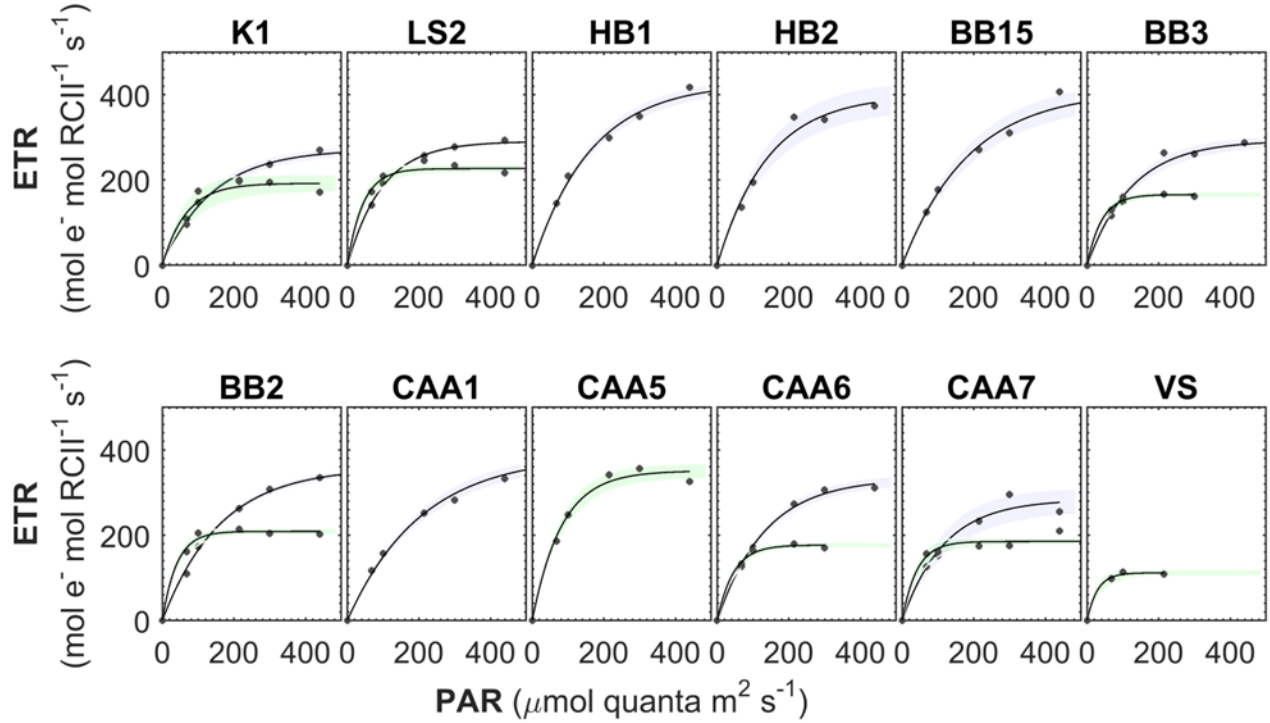


**Figure B3: PvsE curves for  $ETR_{RCII}$ .** Data from both depths sampled at each station are plotted on the same axes. ML samples have blue shaded areas and sub-ML samples have green shaded areas. The shaded area represents the 95 % confidence interval.

## B.5 Phytoplankton absorption spectra

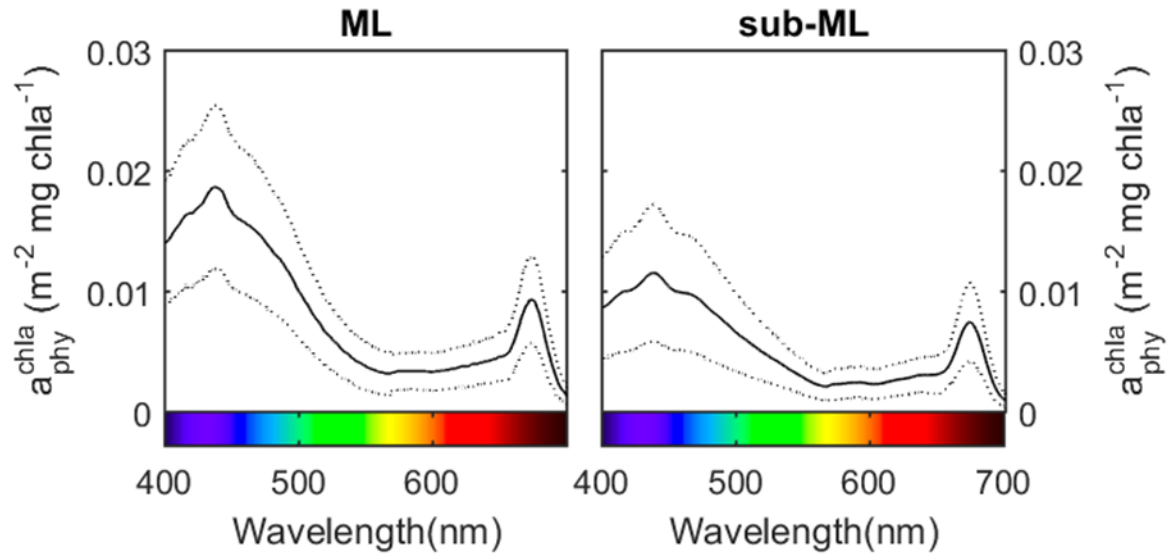


**Figure B4: Mean light absorption spectra normalized to [chl a] for phytoplankton assemblages sampled within (ML) and below (sub-ML) the mixed layer.** The solid line presents the mean absorption spectrum for (a) all ML samples and (b) all sub-ML samples, while the dotted line presents one standard deviation from the mean.

## B.6 Spectral distribution of light and phytoplankton absorption spectra

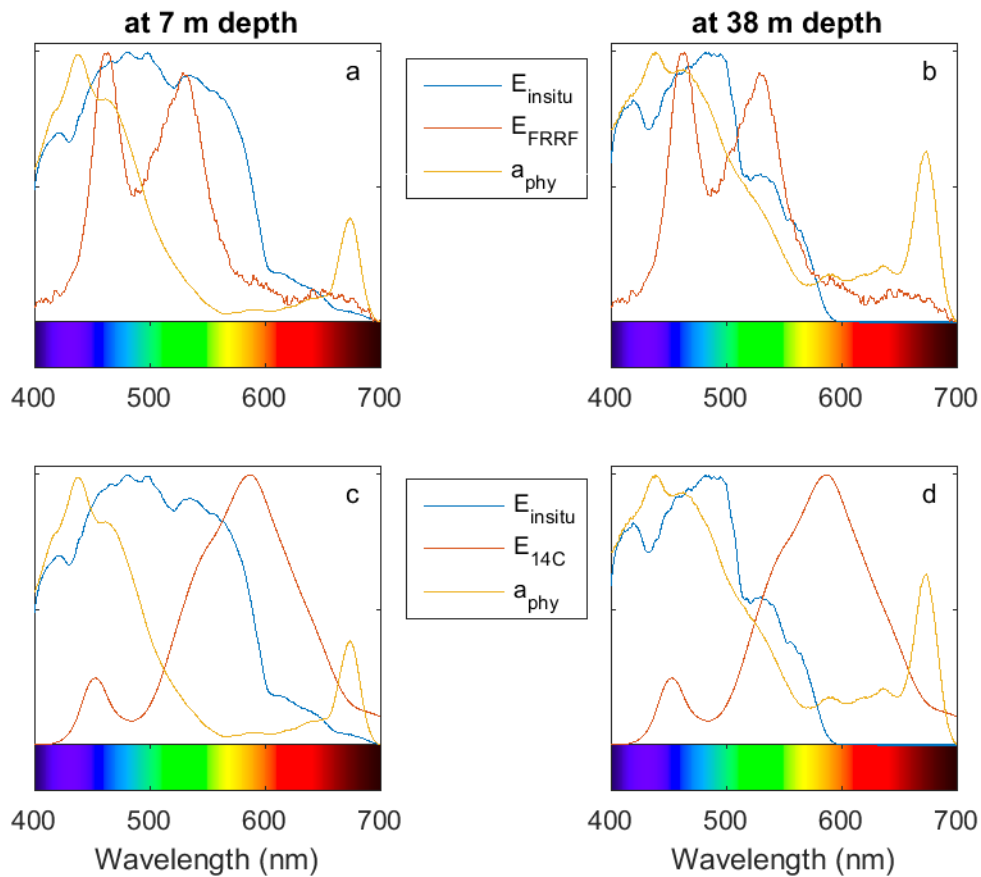


**Figure B5: Relative spectral distribution of transmission of *in situ* light ( $E_{\text{insitu}}$ ) and phytoplankton absorption spectra ( $a_{\text{phy}}$ ) from two depths at station K1 in relation to the spectral distribution of light in the FRRF instrument ( $E_{\text{FRRF}}$ ) and light from the LEDs used during  $^{14}\text{C}$ -uptake incubations ( $E_{14\text{C}}$ ). All spectra are normalized to 1. (a)  $E_{\text{insitu}}$  at 7 m depth,  $a_{\text{phy}}$  at 7 m depth and  $E_{14\text{C}}$ ; (b)  $E_{\text{insitu}}$  at 38 m depth,  $a_{\text{phy}}$  at 38 m depth and  $E_{\text{FRRF}}$ ; (c)  $E_{\text{insitu}}$  at 7 m depth,  $a_{\text{phy}}$  at 7 m depth and  $E_{14\text{C}}$ ; (d)  $E_{\text{insitu}}$  at 38 m depth,  $a_{\text{phy}}$  at 38 m depth and  $E_{\text{LED}}$ .**